

Environment and Properties of Submillimeter Galaxies

Dissertation

zur

Erlangung des Doktorgrades (Dr. rer. nat.)

der

Mathematisch-Naturwissenschaftlichen Fakultät

der

Rheinischen Friedrich-Wilhelms-Universität Bonn

vorgelegt von

Manuel Aravena

aus

Santiago, Chile

Bonn, Januar 2009

Angefertigt mit Genehmigung
der Mathematisch-Naturwissenschaftlichen Fakultät
der Rheinischen Friedrich-Wilhelms-Universität Bonn

1. Gutachter: Prof. Dr. Frank Bertoldi
2. Gutachter: Prof. Dr. Karl Menten

Tag der Promotion: 13 März 2009

Erscheinungsjahr: 2009

Diese Dissertation ist auf dem Hochschulschriftenserver der ULB Bonn unter:
http://hss.ulb.uni-bonn.de/diss_online elektronisch publiziert.

Para Constanza, Nora y Julio

Abstract

Extra-galactic surveys with large submillimeter bolometer cameras discovered a population of dust obscured starbursting galaxies at high redshifts. These submillimeter galaxies (SMGs) are crucial in the stellar build up of the Universe, and their abundance and epoch of formation place important constraints in models of galaxy evolution.

Using the Max-Planck Millimeter Bolometer Array (MAMBO) on the IRAM 30 m telescope, we mapped the central $20' \times 20'$ of the COSMOS field at 1.2 mm to an rms level of 1 mJy per $11''$ beam. We found 15 significant ($> 4\sigma$) millimeter sources, 11 of which have a reliable 1.4 GHz Very Large Array (VLA) radio counterpart. Ten more lower significance millimeter sources were identified based on a radio association. We used 24 μm data to complement the radio identifications. Using a stacking analysis on the MAMBO map, we estimated that radio ($S_\nu > 45 \mu\text{Jy}$), 24 μm ($S_\nu > 550 \mu\text{Jy}$) and millimeter sources ($S_\nu > 4 \text{ mJy}$) contribute with about 12% of the total cosmic background radiation at 1.2 mm.

About 70% of these SMGs could be classified as high-redshift star-forming galaxies based on the ($B - z$) and ($z - K$) colors and $\sim 35\%$ have mid-infrared (IR) colors consistent with the presence of a powerful active galactic nuclei (AGN). We find a median radio/millimeter and optical/IR photometric redshifts of 2.3 and 2.6, respectively, and a median stellar mass of $10^{11.4 \pm 0.4} M_\odot$, in agreement with previous studies of SMGs. This suggests that these galaxies are among the most massive at high-redshift.

We studied the environment of our MAMBO sources by constructing projected density maps of low-redshift and high-redshift K -band selected galaxies. We found that four MAMBO sources are located at the center of strong overdensities of high-redshift galaxies. These associations are statistically likely to be real. The photometric redshifts of the galaxies in these structures are consistent with the ones of their associated SMGs, all of them being in the range $z = 1.5 - 2.0$. They do not appear to be forming a red-sequence in the color-magnitude diagrams, but the SMGs are among the brightest K -band selected objects in these overdense galaxy groups. The overdensities are compact in size, typically with a diameter of $\sim 20''$, or $\sim 170 \text{ kpc}$ at $z = 1.5 - 2.0$. This provides evidence supporting that SMGs are the progenitors of local spheroidals.

Using the Plateau-du-Bureau Interferometer (PdBI), we obtained 1.3 mm continuum maps centered at the position of three significant MAMBO sources. Two of them lack significant counterparts ($> 4\sigma$) in the radio maps (J100007+021149 and J100026+021529). The other MAMBO source (J100008+02130) is embedded in a strong overdensity of high-redshift galaxies. Each of the former two MAMBO sources could be identified with single $> 3.5\sigma$ PdBI 1.3 mm sources. They could be associated with $\sim 3\sigma$ radio peaks and faint optical counterparts. Their optical/IR and radio/millimeter photometric redshifts indicate that these sources are at $z > 3$. This suggests that an important fraction of the SMGs is located at redshifts higher than the standard median value of 2.3 estimated from spectroscopic surveys of radio-selected SMGs. The MAMBO source in the strong overdensity appears to be associated with more than two PdBI 1.3 mm sources, however only one of them showed a radio counterpart. The detection of multiple millimeter components supports the picture that obscured galaxies do appear in galaxy groups.

Using the IRAM 30 m telescope, we detected four carbon monoxide (CO) emission lines in one of our brightest MAMBO sources (J100038+020822). This source is a bright type-1 AGN at $z = 1.8275$. Large velocity gradient modeling of the CO line intensities yields molecular gas (H_2) densities in the range $10^{3.5-4.0} \text{ cm}^{-3}$ and kinetic temperatures between 50 K and 200 K. We find a dust mass of $1.2 \times 10^9 M_\odot$, and a cold and hot dust temperatures of $42 \pm 5 \text{ K}$ and $160 \pm 25 \text{ K}$, respectively. A comparison of its multi-wavelength SED and morphology indicates that this object shares properties of both starburst and AGN, being likely in the transition between a starbursting SMG to a QSO.

Contents

Contents	i
List of Figures	v
List of Tables	vii
List of Acronyms	ix
1 Introduction	1
1.1 Continuum emission of starburst galaxies	3
1.2 Spectroscopy and line emission	7
1.3 Galaxy counts	11
1.4 Clustering properties	12
1.5 Galaxy evolution	12
1.6 Outline of the Thesis	13
2 MAMBO imaging of the COSMOS field	15
2.1 Introduction	15
2.2 The COSMOS field	16
2.2.1 X-ray imaging	17
2.2.2 Optical Imaging	17
2.2.3 Mid-infrared imaging	17
2.2.4 Radio imaging	19
2.3 Millimeter observations of COSMOS	21
2.3.1 MAMBO observations	22
2.3.2 Source extraction	23
2.4 Multi-wavelength counterpart identification	27
2.4.1 Radio counterparts	27
2.4.2 MIPS 24 μ m counterparts	28
2.4.3 IRAC and optical counterparts	29
2.4.4 X-ray identification	30
2.4.5 Comparison with the Bolocam 1.1 mm detections	30
2.4.6 Comments on identifications	30
2.5 Stacking analysis	34
3 Properties of MAMBO galaxies	47
3.1 Introduction	47
3.2 Results	48
3.2.1 BzK selection	48
3.2.2 Starburst or AGN ?	50

3.2.3	Radio-millimeter photometric redshifts	51
3.2.4	Optical/IR photometric redshifts	53
3.2.5	Stellar Masses	55
3.3	Discussion	57
3.3.1	The nature of SMGs	57
3.3.2	Massive galaxies at $z = 2$	59
4	Environment of submillimeter galaxies	61
4.1	Introduction	61
4.2	Observations	62
4.2.1	K band selected catalog	62
4.2.2	K band counterparts to MAMBO sources	65
4.2.3	BzK selection	65
4.3	Results	66
4.3.1	Searching for overdensities of high-redshift galaxies around SMGs	66
4.3.2	BzK galaxy overdensities around SMGs	69
4.3.3	Large scale structure of low-redshift galaxies	75
4.3.4	Probability of chance association	75
4.3.5	Color-magnitude diagrams	76
4.3.6	Photometric redshifts	77
4.3.7	Comments on photometric redshifts and more	83
4.3.8	Extended structure around COSBO-6?	85
4.3.9	The case of COSBO-29	85
4.4	Discussion	87
5	Interferometric continuum imaging of MAMBO sources	89
5.1	Introduction	89
5.2	Observations	90
5.2.1	Sample selection	90
5.2.2	PdBI millimeter continuum imaging	90
5.2.3	Image deconvolution	92
5.3	Results	94
5.3.1	Flux discrepancy	94
5.3.2	Multi-wavelength counterparts	95
5.3.3	Photometric redshifts	96
5.4	Discussion	100
5.4.1	Pinpointing the highest redshift SMGs	100
5.4.2	A group of SMGs at $z = 1.5$?	101
6	Properties of the molecular gas in a starbursting QSO	103
6.1	Introduction	103
6.2	Observations	106
6.2.1	Source selection	106
6.2.2	CO observations	106
6.3	Results and Analysis	106
6.3.1	Large Velocity Gradient model	107
6.3.2	CO Size and Mass	108
6.3.3	Dust Continuum	110
6.3.4	Star Formation Rates and Efficiencies	111
6.3.5	Optical Morphology	112
6.3.6	Spectral Energy Distribution	113

6.3.7	Black Hole Mass Estimate	113
6.4	Discussion	114
6.4.1	Comparison of Excitation Conditions	114
6.4.2	A Starburst-QSO Composite	115
7	Summary and Outlook	117
7.1	Summary	117
7.2	Perspectives	119
	References	121
	Acknowledgments	131
	Curriculum Vitae	133
	Publications	135

List of Figures

1.1	History of star formation and energy generation in the Universe	4
1.2	Observed intensity of the cosmic background radiation from radio to the far-UV wavebands	5
1.3	<i>UBI</i> true colour image of the galaxy cluster field Abell 1835	6
1.4	Observed restframe SEDs of starburst galaxies	7
1.5	Predicted flux density of a dusty starburst galaxy as a function of redshift at some relevant wavelengths	8
1.6	Redshift distribution of SMGs	9
1.7	Cumulative submillimeter and millimeter source number counts	10
1.8	Redshift evolution of galaxy clustering as a function of redshift	11
2.1	Filter transmission profiles for the COSMOS data sets	18
2.2	<i>Br'z'</i> color image of the COSMOS field	20
2.3	Schematic view of the coverage of the optical, IR and millimeter data sets in COSMOS	21
2.4	Root mean square noise map for the MAMBO survey of COSMOS	22
2.5	Flux deboosting for the MAMBO sources	23
2.6	Inner section of the COSBO map	24
2.7	Distribution of the corrected probability of chance association (P_C) for radio selected counterparts	28
2.8	Distribution of the corrected probability of chance association (P_C) for the 24 μm counterparts	29
2.9	Stacked MAMBO images centered at the position of radio and 24 μm sources, and random positions in the field	34
2.10	Optical and IR postage stamp images ($10'' \times 10''$) centered on the MAMBO sources	39
3.1	<i>BzK</i> color-color diagram for the MAMBO galaxies	48
3.2	$S_{24 \mu\text{m}}/S_{8.0 \mu\text{m}}$ vs. $S_{8.0 \mu\text{m}}/S_{3.6 \mu\text{m}}$ color-color diagram for the MAMBO galaxies	49
3.3	$r - (3.6)$ vs. $(3.6) - (8.0)$ color diagram for the MAMBO galaxies	51
3.4	Redshift estimates based on the radio to millimeter spectral index	52
3.5	Spectral Energy Distributions (SEDs) for the MAMBO counterparts	54
3.6	Photometric redshift distribution of MAMBO galaxies	56
3.7	Stellar masses for the reliable counterparts to the MAMBO sources	57
3.8	Stellar mass as a function of redshift	59
4.1	Comparison of our own photometry with the COSMOS catalog	63
4.2	Comparison of the <i>K</i> -band galaxy counts with those of recent near-IR surveys	64
4.3	<i>BzK</i> diagram for MAMBO galaxies from our <i>K</i> -band catalog.	66
4.4	Normalized distribution of galaxy number counts around MAMBO sources	67
4.5	Projected number density of galaxies around MAMBO sources as a function of their <i>K</i> -band magnitude	68

4.6	Density of low redshift <i>BzK</i> galaxies in the COSBO field.	70
4.7	Density of high-redshift <i>BzK</i> galaxies in the COSBO field.	71
4.8	Normalized distribution of galaxy number counts around MAMBO sources	72
4.9	Density maps for low redshift <i>BzK</i> galaxies in the fields of MAMBO sources.	73
4.10	Density maps for high redshift <i>BzK</i> galaxies in the fields of MAMBO sources.	78
4.11	<i>BzK</i> true color images of some MAMBO galaxy fields	81
4.12	Comparison of low-redshift density maps	82
4.13	Color-magnitude diagrams for some MAMBO source fields	83
4.14	Redshift distribution for galaxies in overdensities around some MAMBO galaxies	84
4.15	<i>BzK</i> true color image covering the position of COSBO-2 and COSBO-6 and the redshift distribution of the <i>K</i> -band selected galaxies in this field	86
4.16	Spectroscopic redshifts for galaxies around COSBO-29	87
5.1	Clean and residual 1.3 mm maps for COSBO-4	91
5.2	Clean and residual 1.3 mm maps for COSBO-6	91
5.3	Clean and residual 1.3 mm maps for COSBO-9	92
5.4	Continuum 1.3 mm to 1.2 mm flux ratio as a function of redshift.	94
5.5	Multi-waveband images around MAMBO source 4	96
5.6	Multi-waveband images around COSBO-6	97
5.7	Multi-waveband images around COSBO-9	98
5.8	Close-up Subaru <i>i</i> ⁺ band image around the 1.3 mm detections	98
5.9	Optical/near-IR SEDs for the likely counterparts to the millimeter sources	99
5.10	χ^2 distribution for the likely counterparts to the millimeter sources	99
6.1	Observed CO emission lines	104
6.2	CO line SED	107
6.3	$\log\chi^2$ distribution for the single component LVG model	108
6.4	Multi-frequency SED	109
6.5	Optical morphology of J100038	112
6.6	Optical spectrum of J100038	114

List of Tables

2.1	Data quality for the optical observations.	19
2.2	MAMBO sources and their Bolocam counterparts.	25
2.3	X-ray <i>XMM-Newton</i> identifications.	30
2.4	Radio and 24 μm counterparts to the MAMBO sources.	36
2.5	IRAC and optical counterparts to the MAMBO sources.	38
3.1	Properties of MAMBO galaxies	58
4.1	Significance of overdensities	76
5.1	PdBI 1.3 mm continuum observations.	93
5.2	Multiwavelength counterparts to the 1.3 mm detections.	93
6.1	Observed line parameters for J100038.	105
6.2	Infrared and radio fluxes of J100038.	110
6.3	Summary of derived properties of J100038	115

List of Acronyms

<i>ACIS</i>	Advanced CCD Imaging Spectrometer	17
<i>ACS</i>	Advanced Camera for Surveys	16
<i>AGN</i>	Active galactic nuclei	2
<i>AIPS</i>	Astronomical Imaging Processing System	20
<i>ALMA</i>	Atacama Large Millimeter Array	16
<i>BLR</i>	Broad line region	113
<i>CDF-N</i>	Chandra Deep Field North	16
<i>CFHT</i>	Canada-France-Hawaii telescope	17
<i>CIB</i>	Cosmic infrared background	2
<i>CMB</i>	Cosmic microwave background	2
<i>CO SED</i>	Spectral energy distribution of the CO emission	107
<i>COBE</i>	Cosmic Background Explorer satellite	2
<i>COSBO</i>	COSMOS MAMBO	21
<i>COSMOS</i>	Cosmic evolution survey	16
<i>CO</i>	Carbon monoxide	10
<i>CSO</i>	Caltech Submillimeter Observatory	21
<i>CTIO</i>	Cerro Tololo Inter-American Observatory	17
<i>DIRBE</i>	Diffuse Infrared Background Experiment instrument	2
<i>DRG</i>	Distant red galaxy	59
<i>ERO</i>	Extremely red objects	12
<i>EVLA</i>	Extended Very Large Array	16
<i>FIRAS</i>	Far Infrared Absolute Spectrophotometer	2
<i>FWHM</i>	Full-width half maximum	23
<i>GEMS</i>	Galaxy Evolution from Morphology and SEDs survey	16
<i>GOODS</i>	Great Observatories Origins Deep Survey	16
<i>HDF-N</i>	Hubble Deep Field North	16
<i>HST</i>	Hubble Space telescope	16
<i>H_zRG</i>	High-redshift radio galaxies	61
<i>IMF</i>	Initial mass function	53
<i>IRAC</i>	Infrared Array Camera	18
<i>IRAM</i>	Institut de Radioastronomie Millimetrique	2
<i>IRAS</i>	Infrared Astronomical Satellite	2
<i>IRS</i>	Infrared Spectrograph	9
<i>IR</i>	Infrared	1
<i>ISM</i>	Interstellar medium	1
<i>ISO</i>	Infrared Space Observatory	2
<i>JCMT</i>	James-Clerk Maxwell telescope	2
<i>KPNO</i>	Kitt Peak National Observatory	17
<i>LBG</i>	Lyman-break galaxy	3
<i>LTE</i>	Local thermodynamical equilibrium	107

<i>LVG</i>	Large velocity gradient	107
<i>MAMBO</i>	Max-Planck Millimetre Bolometer Camera	2
<i>MIPS</i>	Multiband Imaging Photometer	18
<i>NRAO</i>	National Radio-Astronomy Observatory	19
<i>PAH</i>	Poly-aromatic hydrocarbon	8
<i>PSF</i>	Point spread function	17
<i>QSO</i>	Quasi-stellar object	2
<i>SCUBA</i>	Submillimeter Common User Bolometer Camera	2
<i>SDSS</i>	Sloan Digital Sky Survey	17
<i>SED</i>	Spectral energy distribution	2
<i>SFE</i>	Star formation efficiency	111
<i>SFR</i>	Star formation rate	1
<i>SMBH</i>	Super massive black holes	4
<i>SMG</i>	Submillimeter Galaxy	3
<i>SSC</i>	Spitzer Science Center	18
<i>SWIRE</i>	Spitzer Wide-Area Infrared Extra-galactic	18
<i>TERAPIX</i>	Traitement Élémentaire, Réduction et Analyse des Pixels	62
<i>UKIRT</i>	United Kingdom Infrared 3.8 m telescope	17
<i>ULIRG</i>	Ultra luminous infrared galaxy	2
<i>UV</i>	Ultraviolet	1
<i>VLA</i>	Very Large Array	19

Introduction

To understand how stars form and how star formation relates to the evolution of galaxies through cosmic time and in relation to the formation of large scale structures has been a major focus of cosmological research. To address these issues, global star formation processes must be investigated in nearby and distant galaxies, and compared with analytical models and numerical simulations of galaxy formation. The work documented in this thesis adds to the empirical data on the star formation processes of distant starburst galaxies.

The Star Formation History of the Universe

Much of our current knowledge about the evolution and properties of distant galaxies has come from the study of their optical ($\lambda = 0.1 - 1.0 \mu\text{m}$), near-infrared (IR; $\lambda = 1.0 - 3.0 \mu\text{m}$) and radio ($\lambda > 0.7 \text{ cm}$) emission. A remarkable step in our understanding of the history of star formation through cosmic time has been the determination of the unobscured star formation rate (SFR) in galaxies over a wide range of redshift, $0 < z < 6$ (see Fig. 1.1; Lilly et al., 1996; Madau et al., 1996; Cowie et al., 1996; Connolly et al., 1997; Steidel et al., 1999; Iwata et al., 2003; Bouwens et al., 2003, 2004; Giavalisco et al., 2004a). The combination of spectroscopic redshift surveys at $z < 1$ (Lilly et al., 1996) and deep photometric surveys (Williams et al., 1996), together with effective photometric techniques to either select galaxies in narrow redshift ranges (e.g. Madau et al., 1996; Steidel et al., 1999) or provide accurate estimates of their redshifts, has indicated that the volume-averaged density of ultraviolet (UV; $\lambda < 0.1 \mu\text{m}$) luminosity in the Universe (which is directly related to the SFR) increases from redshift 6 to 3, with a peak at $z = 1 - 3$, and a steady decline at $z < 1$ (Fig. 1.1). Albeit such findings are in agreement with the SFR density derived from radio observations of galaxies and quasars for $z < 1$ (Cram, 1998; Haarsma et al., 2000; Cowie et al., 2004; Smolcic et al., 2008), extinction by interstellar dust is very significant in the luminous star forming galaxies at higher redshifts ($z > 1$), so that UV and optical observations cannot provide a good measure of the SFR in these systems. Corrections for dust obscuration are subject to large uncertainties, particularly for the most luminous systems (Hopkins et al., 2001).

Infrared Galaxies

A substantial fraction of the ultraviolet emission produced by young stars is absorbed and re-radiated at the rest frame mid-IR ($\lambda \sim 5 - 50 \mu\text{m}$), far-IR ($\lambda \sim 50 - 200 \mu\text{m}$) and submillimeter ($\lambda \sim 200 - 1000 \mu\text{m}$) wavelengths by dust grains in the interstellar medium (ISM). Continuum and spectral line observations in these spectral regimes efficiently trace the dust and gas content, providing a crucial tool in the study of the star formation process, and the chemical and dynamical composition of the ISM in distant galaxies (Weiß et al., 2008).

In the local Universe, observations with the Infrared Astronomical Satellite (IRAS) discovered a class of luminous galaxies that emit about 90% of their energy at IR wavelengths (see the review by Sanders & Mirabel, 1996). These luminous IR galaxies (LIRGs) and ultraluminous IR galaxies (ULIRGs) have typical bolometric luminosities of $\sim 10^{11-12} L_{\odot}$ and $\sim 10^{12-13} L_{\odot}$, respectively, and are more numerous than quasi-stellar objects (QSOs) at similar luminosities. These IR luminous galaxies are typically associated with strong interactions and/or mergers. The fraction of active galactic nuclei (AGN) in these galaxies was found to increase with IR luminosity, implying that the emission of the most luminous galaxies is powered by a mixture of circumnuclear starburst and AGN accretion. Large amounts of molecular gas are funneled towards their inner regions through nuclear bars, providing the fuel to sustain massive star formation.

The Cosmic Infrared Background

The “extragalactic background” is the faint diffuse light of the sky, consisting of the combined flux of all extragalactic sources, including the (almost) isotropic “Cosmic Microwave Background” (CMB) that was shaped early on, when the photons created during the Big Bang decoupled from matter. The extragalactic background contains much information about the history and formation of galaxies, and of the large-scale structure of the universe.

Quantitative observations of the “Cosmic Infrared Background” (CIB) began with the first astronomical satellites working in the IR, starting with IRAS, and followed by the Cosmic Background Explorer (COBE), the Infrared Space Observatory (ISO), and the Spitzer Space Observatory. The first and most extensive direct CIB measurements were performed by the Diffuse Infrared Background Experiment (DIRBE) instrument of the COBE satellite (Hauser et al., 1998; Dwek et al., 1998; Dwek & Arendt, 1998; Fixsen et al., 1998; Gorjian et al., 2000; Wright & Reese, 2000). DIRBE was a multi-wavelength IR detector designed to map dust emission. At a low angular resolution of 0.7° (that did not allow the identification of individual sources), DIRBE provided the first large-scale measurement of the spectral energy distribution (SED) of the far-IR to submillimeter CIB. After the removal of the zodiacal emission and the galactic cirrus emission (from a comparison with neutral hydrogen maps), the CIB was originally detected in the two longest DIRBE wavelength bands, $140 \mu\text{m}$ and $240 \mu\text{m}$, and in the short-wavelength end of the COBE Far Infrared Absolute Spectrophotometer (FIRAS) spectrum (Puget et al., 1996; Fixsen et al., 1996; Mather et al., 1999).

About half the integrated energy of the extragalactic background emerges in the optical to UV spectral range, and the other half in the IR (Fig. 1.2). As a result of the cosmic redshift and the reprocessing of short-wavelength radiation by dust, the CIB was thought to possibly contain a large fraction of the (individually unresolved) cumulative emission of stars and galaxies, dating back to the epoch when these objects first began to form. To confirm the origin of the CIB in objects at cosmological distances, it was necessary to resolve the CIB on a scale that allows a unique identification with galaxies whose distance could be measured. The understanding of the evolution of star formation in the Universe requires the systematic and detailed study of those high-redshift galaxies that produce the far-IR and submillimeter background (Blain et al., 1999).

Submillimeter Galaxies

With this important aim in mind, the Submillimeter Common User Bolometer Camera (SCUBA) on the James-Clerk Maxwell telescope (JCMT) in Hawaii and the Max-Planck Millimetre Bolometer Camera (MAMBO) at the Institut de Radioastronomie Millimetrique (IRAM) 30 m telescope were built (Holland et al., 1999; Kreysa et al., 1998). The first SCUBA maps at $850 \mu\text{m}$ ($14''$ resolution) were able to resolve the CIB into individual sources, which were soon found to be high redshift galaxies (Smail et al., 1997).

Since the commissioning of SCUBA and MAMBO about 10 years ago, a number of groups have conducted deep surveys of the (sub)millimeter sky, although mostly of small areas, and yielding small numbers of sources (Smail et al., 1997; Hughes et al., 1998; Barger et al., 1998; Eales et al., 1999; Bertoldi et al., 2000; Eales et al., 2000; Scott et al., 2002; Borys et al., 2003; Greve et al., 2004; Laurent et al., 2005; Voss et al., 2006; Coppin et al., 2006; Bertoldi et al., 2007; Greve et al., 2008; Scott et al., 2008).

“Blank field” bolometer surveys in the sky discovered a population of very luminous ($\sim 10^{12-14} L_{\odot}$) high-redshift galaxies (most are probably between 1.5 and 3) that contribute a large fraction of the far-IR and submillimeter background and that were not accounted for in previous optical and near-IR studies (e.g., Smail et al., 1997; Hughes et al., 1998; Barger et al., 1998; Lilly et al., 1999; Eales et al., 1999, 2000; Bertoldi et al., 2000). Their luminous thermal dust emission most likely arises from massive starbursts. The SFRs implied by their IR luminosity ($> 1000 M_{\odot} \text{ yr}^{-1}$) together with their number density could account for a large fraction of all star formation at these epochs (Smail et al., 2000; Tan et al., 1999; Blain et al., 1999). Apparently, high obscuration makes these sources inconspicuous at optical and near-IR wavelengths, although most of them can be detected in very deep (rms noise level $< 10 \mu\text{Jy}$ at 1.4 GHz) radio images (Barger et al., 2000). The difficulty of a unique optical identification or the difficulty to study in detail the faint optical counterpart galaxies has for a long time left unclear what known class of objects, if any, these submillimeter galaxies (SMGs) correspond to: extreme Lyman-break galaxies (LBGs), interacting galaxies, spheroidal galaxies or stellar bulges in their formation stages.

Compared to local starburst systems such as Arp 220 ($\sim 4 \times 10^{12} L_{\odot}$), the best studied and most IR luminous local starburst galaxy known, SMGs are more luminous and more numerous per comoving volume by about a factor of 30 (Smail et al., 1997; Scott et al., 2002), suggesting that a large fraction of all stars ever formed in the Universe were born in short and intense bursts at high redshifts (Blain et al., 1999).

With about 200 SMGs discovered to date, it has become clear that their number density implies a large population of hitherto unknown dust-enshrouded galaxies at high redshift, with star-formation rates $> 1000 M_{\odot} \text{ yr}^{-1}$, sufficient to assemble a giant elliptical galaxy in less than 10^9 years. The discovery of SMGs has had a strong impact on our understanding of the history of star and galaxy formation.

Although important progress has been made in the understanding of SMGs since their discovery, there are many issues that need to be investigated in order to place this population into the cosmological context of galaxy formation. In the following, we discuss some of their most important properties (Sections 1.1 to 1.5). In Section 1.6, we give a brief outline of this thesis.

1.1 Continuum emission of starburst galaxies

Since very deep exposures are necessary to detect the faint X-ray, optical, IR and radio emission from SMGs, submillimeter surveys have been preferentially conducted in regions of the sky where these data have already been obtained, such as the Hubble Deep Field (HDF) north and south, the Great Observatories Origins Survey (GOODS) fields, or various popular galaxy cluster fields (Fig. 1.3).

Optical and X-rays

The first identifications of submillimeter sources with optical and IR counterparts showed that they tend to be strongly obscured and therefore relatively optically faint, with typical optical *I*-band magnitudes > 25 (Fig. 1.3). In these systems, most of the light produced by young massive stars is obscured by dust. Their rest-frame continuum SEDs resemble those of local starbursts (e.g. Arp 220, M82), but with much higher bolometric luminosities (Fig. 1.4).

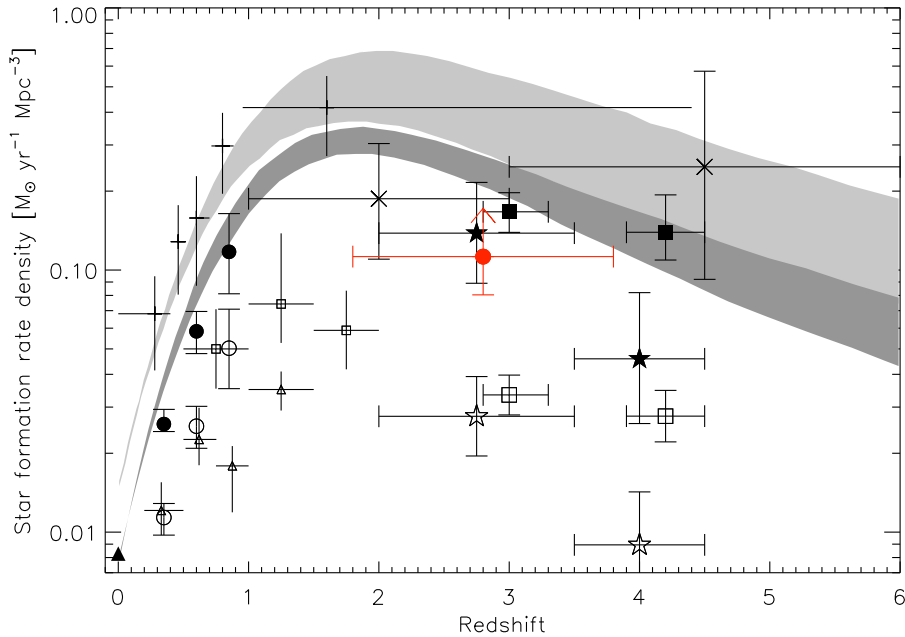


Figure 1.1: History of star formation and energy generation in the Universe (adapted from Smail et al. 2002). The dark grey and the light grey shaded areas represent 68% uncertainty in a simple parametric luminosity evolution model and a hierarchical model from Smail et al. (2002), respectively. The data points are taken from the UV, optical and near-IR observations of Gallego et al. (1996, filled triangle), Lilly et al. (1996, open circles), Cowie et al. (1999, small open triangles and error bars without hat), Connolly et al. (1997, small open squares and error bars without hat), Flores et al. (1999, filled circles – Lilly et al. values corrected for extinction), Madau et al. (1996, open stars), Pettini et al. (1998, filled stars – Madau et al. values corrected for extinction), Steidel et al. (1999, large open squares), Steidel et al. (1999, large filled squares – extinction corrected). From radio observations, Haarsma et al. (2000) infer values represented by the solid crosses with no terminators. From radio and submillimeter observations, Barger et al. (2000) derive star formation rates shown by the diagonal crosses at $z > 2$. The red circle represents a lower limit derived from submillimeter observations (Smail et al., 2002; Hughes et al., 1998)

X-ray emission in the center of galaxies is produced by accretion disks around super massive black holes (SMBHs). Even though absorption and Compton scattering through large column densities ($> 10^{22} \text{ cm}^{-2}$) of gas typically suppress the soft X-ray ($< 2 \text{ keV}$) emission, being visible only through the most energetic photons in the hard bands ($> 2 \text{ keV}$). If the gas column densities exceed $> 10^{24} \text{ cm}^{-2}$, the hard X-ray emission is also absorbed, and the AGN cannot be detected (e.g. Véron-Cetty & Véron, 2000).

The large obscuration of SMGs in the X-rays makes them difficult to observe, requiring very deep exposures. The detection of submillimeter-bright galaxies in the hard X-ray bands with the Chandra satellite has indicated that for about 30% of them the bolometric emission is dominated by AGN activity. It is likely that most of them ($\sim 70\%$), however, host obscured AGN (Fabian et al., 2000; Alexander et al., 2003, 2005).

Radio and IR

Observations of nearby star-forming galaxies have shown a tight correlation between their radio and far-IR luminosities, suggesting that both, radio and IR emission, are related to the star-

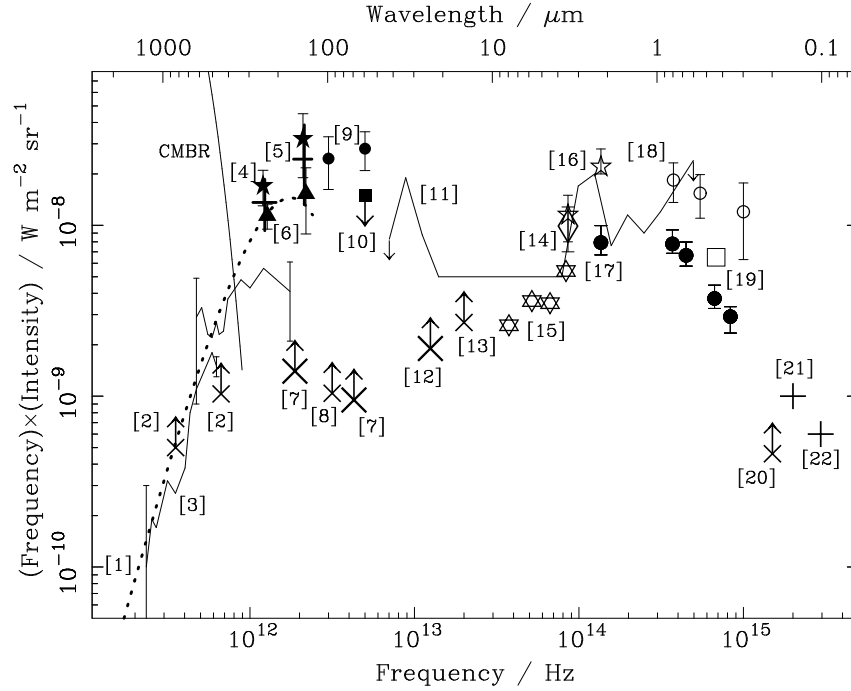


Figure 1.2: Observed intensity of the cosmic background radiation from radio to the far-UV wavebands (Adapted from Blain et al. 2002; Kraiberg-Knudsen, private communication). The observations are from: [1] Fixsen et al. (1998); [2] Smail et al. (2002); [3] Puget et al. (1996); [4] Schlegel et al. (1998); [5] Hauser et al. (1998); [6] Lagache & Puget (2000); [7] Dole et al. (2004); [8] Kawara et al. (1998); [9] Finkbeiner et al. (2000); [10] Dwek & Krennrich (2005); [11] Stanev & Franceschini (1998); [12] Papovich et al. (2004); [13] Altieri et al. (1999); [14] Dwek & Arendt (1998); [15] Fazio et al. (2004); [16] Wright & Johnson (2001); [17] Pozzetti et al. (1998); [18] Bernstein et al. (2002); [19] Toller et al. (1987); [20] Armand et al. (1994); [21] Lampton et al. (1990); and [22] Murthy et al. (1999). Lagache & Puget (2000) claim that Finkbeiner points [9] could be contaminated by diffuse zodiacal light. Where multiple results are available in the literature, the most sensitive result is quoted.

formation rate (Condon, 1992). The radio emission is produced by thermal Bremsstrahlung in ionized hydrogen regions (HII) and by non-thermal synchrotron emission from relativistic electrons created in supernova explosions. The far-IR emission is produced by dust grains heated by UV photons coming from star-forming regions or the accretion disk of an AGN. In the study of SMGs, the radio to far-IR correlation has become an important tool to provide rough redshift estimates (see Chapters 2 and 3).

The bulk of the dust thermal emission is produced at far-IR wavelengths. It is usually modeled as a modified black-body spectrum of the form $S_\nu \propto \tau_\nu B_\nu(T_d)$, with $B_\nu(T_d)$ the Planck function and τ_ν the optical depth. The exact frequency at which the far-IR SED peaks is determined by the dust temperature, T_d , and the strength of the far-IR emission by the temperature and mass of dust, through $\tau_\nu \propto M_d$.

Little is known about the dust properties of SMGs. Detailed modeling of the SED for some sources imply dust temperatures similar to that of local starbursts (Fig. 1.4) but with dust masses at least an order of magnitude higher. There is some evidence that, compared to high-redshift QSOs, SMGs seem to have colder dust temperatures (Blain et al., 2004a).

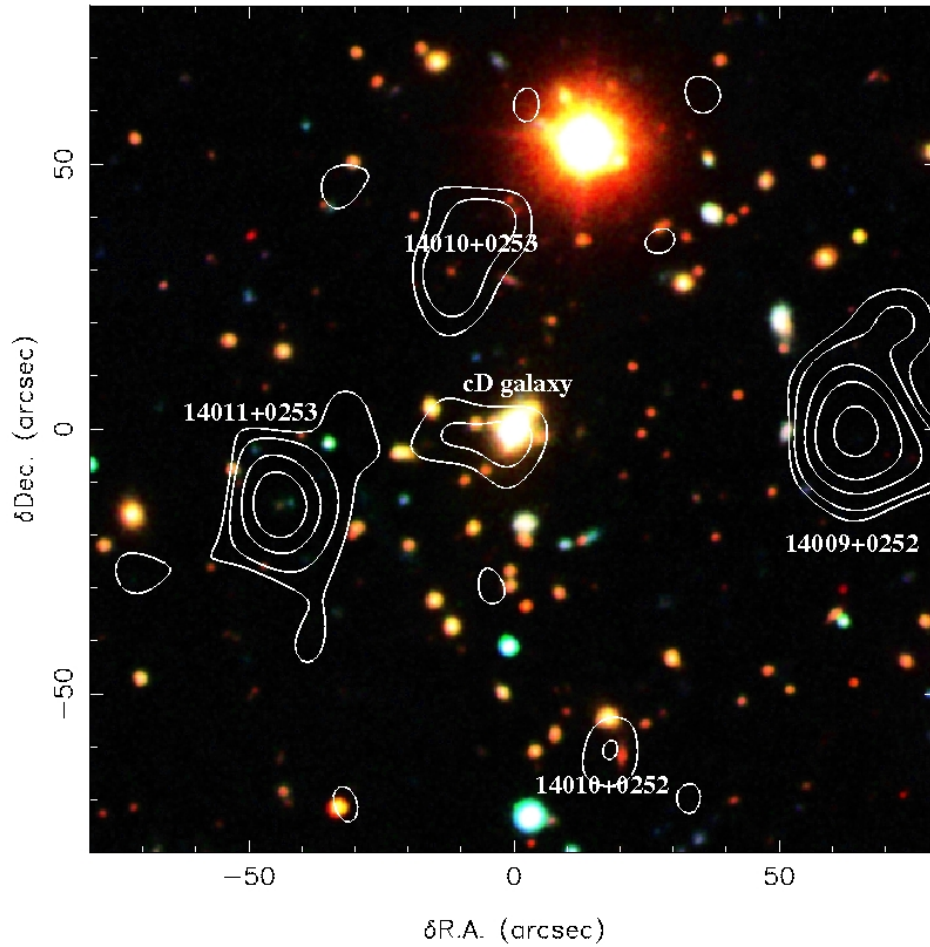


Figure 1.3: UBI true colour image of the galaxy cluster field Abell 1835 (Image and caption from Ivison et al. (2000b)). The large masses of galaxy clusters are related to deep gravitational potentials that magnify the light that we observe from background objects in the line of sight. The faint optical emission received from background SMGs is boosted and they can be detected more easily. The 850 μm SCUBA map is overlaid as a contour plot. There are possible optical counterparts to at least four of the submm sources, with the brightest submillimeter source having none. Compared to field galaxies, the possible optical counterparts to SMGs are very faint, likely due to the obscuration by dust.

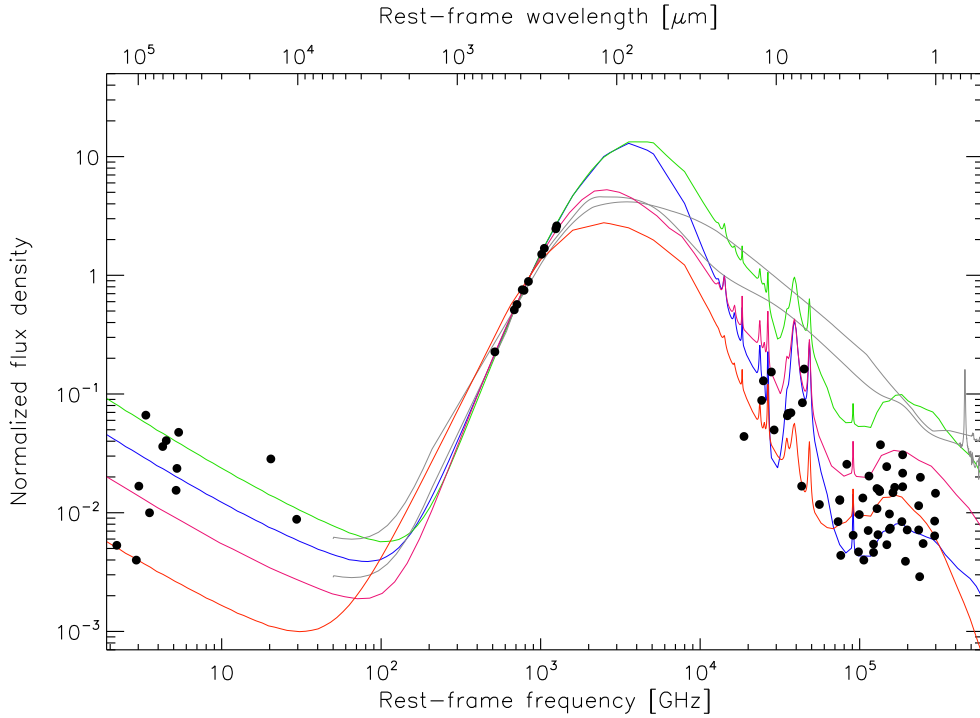


Figure 1.4: Various observed restframe spectral energy distributions (SEDs) of starburst galaxies and QSOs from the radio to the optical wavebands normalized to unity at $350 \mu\text{m}$. Solid curves represent model SEDs for three luminous low-redshift starburst galaxies Arp220 (blue), M82 (green) and NGC6090 (magenta), and for an extremely red object (ERO) at $z = 1.44$, HR10 (red), from Silva et al. (1998). The grey curves show the model SEDs for a QSO type-1 and type-2 from Polletta et al. (2007). Filled circles show the multi-frequency SED for SMGs detected in the Hubble Deep Field North (HDF-N), from Pope et al. (2006).

Negative K-correction

At large distances ($z > 1$), the effect of the flux decline with the square of the distance (cosmic distance dimming) is mostly offset as we trace a strongly rising (due to redshift) part of the far-IR SED, an effect known as “negative K-correction”. This means that, for a fixed far-IR luminosity, the flux density from galaxies observed in the submillimeter regime remains almost constant between redshift 1 and 10 (Fig. 1.5), unlike the radio or optical flux, which drops rapidly with redshift and thereby produces a strong variation of the selection function for galaxies at high redshifts (Blain & Longair, 1993).

1.2 Spectroscopy and line emission

The spectra of galaxies contain important information about their evolutionary state, distance, conditions of star-formation and kinematics.

Optical Emission lines

Several emission lines related to star-formation or AGN accretion disks are seen in the optical spectra of starburst galaxies ($\text{H}\alpha$, CIV, MgII, [NII], [SII], [OII], [OIII], etc). For instance, the

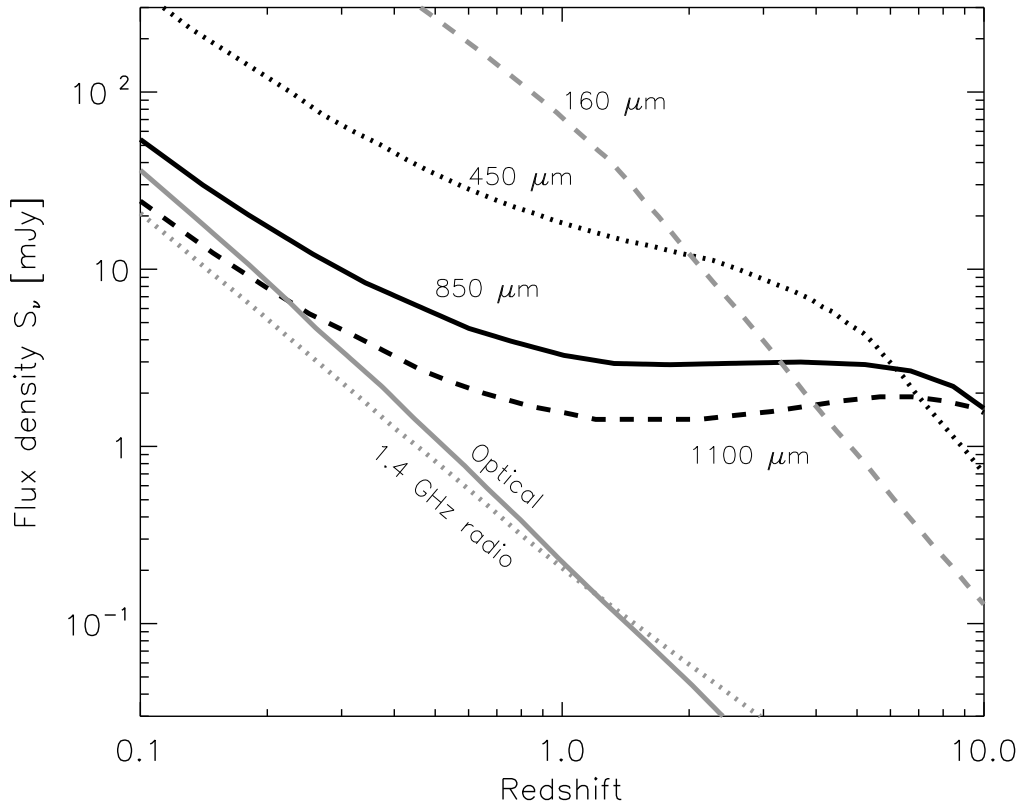


Figure 1.5: Predicted flux density of a dusty starburst galaxy as a function of redshift at some relevant wavelengths (adapted from Blain et al. 2002). The galaxy has a luminosity of $5 \times 10^{13} L_{\odot}$ and dust temperature of 38 K. While the optical and radio emission drop rapidly, the long wavelength submillimeter flux remains almost constant up to $z \sim 10$. The effects of CMB heating were not included.

strength of recombination lines (e.g. $H\alpha$, $H\beta$, CIV, $P\alpha$) or forbidden lines (particularly [OII]) provide an almost direct measure of the SFR in galaxies (Kennicutt, 1998). A comparison of the line-widths of permitted and forbidden lines allows to determine whether they host an AGN: in Seyfert 1 galaxies permitted lines are broader than forbidden lines, whereas in Seyfert 2 galaxies permitted and forbidden lines have similar widths.

Although some galaxies could be strongly extinguished and inconspicuous in the optical continuum (e.g., in some SMGs), the brightest emission lines ($H\alpha$, CIV, [NII]) can still be detected with deep spectroscopy (Chapman et al., 2003). The spectra of SMGs suggest that star-formation is generally the dominant power source, albeit mild AGN activity might be present (in agreement with X-ray observations), and the dynamics of their central regions appears to be baryon-dominated (Swinbank et al., 2006), in the form of dense molecular gas (Greve et al., 2005; Tacconi et al., 2006) and stars (Borys et al., 2005; Dye et al., 2008).

IR Emission Lines

At near and mid-IR wavelengths, the emission of galaxies is less affected by extinction and the most important features are the H_2 emission lines and atomic fine structure lines, and the polycyclic aromatic hydrocarbon (PAH) emission bands. Also present are silicate and H_2O ice absorption

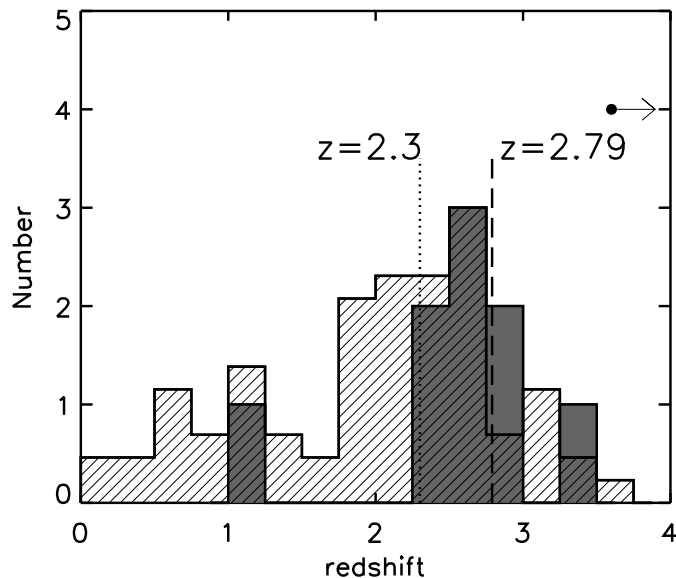


Figure 1.6: Redshift distribution for SMGs (from Valiante et al. 2007). The grayscale shaded histogram represents the mid-IR spectroscopic redshifts derived by Valiante et al. (2007). The hatched line shaded histogram shows the optical spectroscopic redshifts for the submillimeter flux-limited (and radio selected) sample of Chapman et al. (2005), normalized to the peak of the Valiante et al. distribution. The dashed and dotted vertical lines represent the median redshift for both samples, respectively. The median value for the Valiante et al. redshifts is calculated assuming $z > 3.6$ for undetected sources.

features. H_2 emission lines directly trace the bulk of gas in the interstellar medium (mostly composed of H_2 itself), however at the normal temperatures ($\sim 10 - 100$ K) the excited rotational levels are weakly populated and the emission is correspondingly faint. PAH dust grains, on the other hand, dominate the mid-IR radiation and provide an efficient tracer of the star-formation rate in luminous galaxies (Roussel et al., 2001; Dale et al., 2007). The typical mid-IR spectra of SMGs appears to be similar to those of local starburst galaxies, generally showing strong PAH emission, but with higher luminosities (Valiante et al., 2007; Menéndez-Delmestre et al., 2007).

Redshifts of SMGs

The determination of the redshift distribution of SMGs places important constraints on models of galaxy formation. The identification of radio counterparts is a common method to locate accurate positions that allow to obtain optical spectra of SMG. From a sample of about 75 radio-selected galaxies, optical spectroscopic redshifts show a redshift distribution that peaks at about $1.7 - 2.8$ (Fig. 1.6; Chapman et al., 2005). Nevertheless, the radio selection is prone to a likely bias against high redshifts (Fig. 1.5). A more reliable way to obtain accurate redshifts is provided by the identification of the PAH and silicate features in the mid-IR spectra of SMGs. The positional accuracy of submillimeter sources ($\sim 8''$) is good enough to match the relatively large field of view of the Infrared Spectrograph (IRS) on board of the Spitzer satellite at $\lambda > 20 \mu\text{m}$ ($11'' \times 22''$), and therefore mid-IR spectra can be obtained without a prior radio association.

Mid-IR spectroscopy of SMGs has indicated higher values for their redshifts. Valiante et al. (2007) derives a median of 2.8, compared to 2.3 derived from the optical spectra of Chapman et al. (2005). This implies that an important fraction of high-redshift sources is missed if a

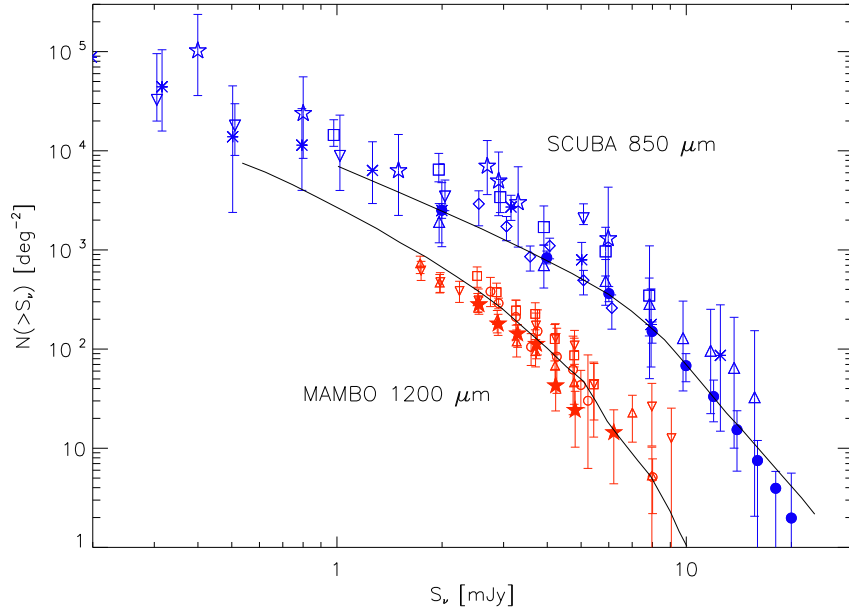


Figure 1.7: Cumulative source number counts determined from various blank-field and cluster lensing (corrected for lensing) SCUBA and MAMBO surveys (adapted from Coppin et al. 2006). SCUBA data points (in blue) are from Smail et al. (2002, open circles), Cowie et al. (2002, up-side down triangles), Chapman et al. (2002, squares), Borys et al. (2003, triangles), Webb et al. (2003, diamonds), Knudsen et al. (2006, stars), Coppin et al. (2006, filled circles) and Knudsen et al. (2008, asterisks). MAMBO data points (in red) are from Bertoldi et al. (2000); Dannerbauer et al. (2002, up-side down triangles), Greve et al. (2004, squares and triangles), Voss et al. (2006, open circles) and Bertoldi et al. (2007, filled stars). Solid lines represent models for the SCUBA and MAMBO number counts from Coppin et al. (2006) and Voss et al. (2006), respectively.

pre-selection based on radio detection is made (Fig. 1.6).

Molecular Emission Lines in the Far-IR

In the far-IR and (sub)millimeter wavelength ranges, molecular lines can be used to study the ISM of galaxies. After H_2 , the main constituent of molecular clouds in galaxies is carbon monoxide (CO). This molecule is easily excited by collisions and UV radiation in low to medium density gas, and its emission lines are bright and provides the best available proxy for H_2 .

Despite its importance, fewer than 20 SMGs have been studied in emission from CO (Frayser et al., 1998, 1999; Andreani et al., 2000; Sheth et al., 2004; Hainline et al., 2004; Neri et al., 2003; Greve et al., 2005; Frayer et al., 2008; Coppin et al., 2008; Tacconi et al., 2008) and only two have been observed in more than two CO transitions for a derivation of their molecular gas properties (this work; Aravena et al., 2008; Weiß et al., 2005a). These studies have indicated that SMGs host large amounts of gas ($M(H_2) = 3 \times 10^{10} M_\odot$) comparable to their dynamical and stellar masses, and similar to the molecular gas masses found for high-redshift QSOs. The CO linewidths and morphologies often suggest merging systems, similar to what is observed in local starburst galaxies, but with CO luminosities about 2 orders of magnitude higher.

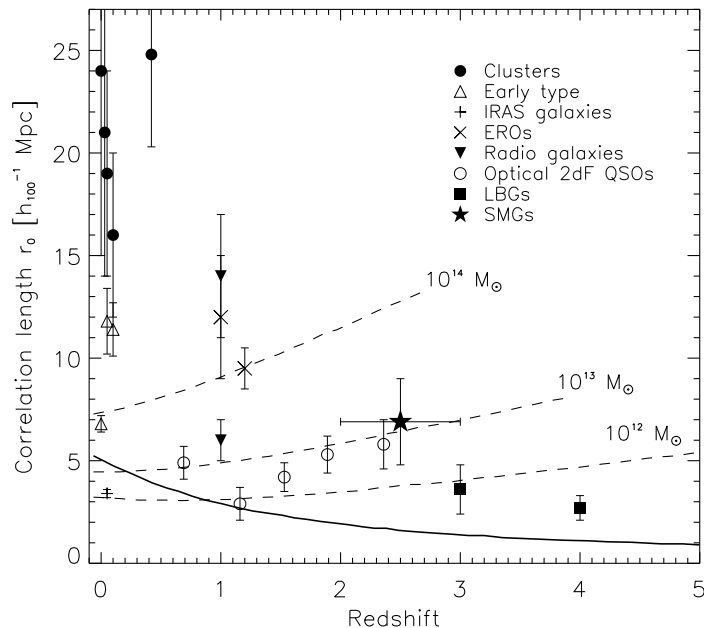


Figure 1.8: Redshift evolution of the galaxy clustering as a function of redshift. The solid line represents a model of clustering of dark matter halos from Jenkins et al. (1998). The dashed lines show the clustering evolution as a function of dark matter halo mass with $M_{\min} = 10^{12-14} M_{\odot}$ from the models of Matarrese et al. (1997). Data points are from Overzier et al. (2003). The starred data point shows the inferred correlation length for SMGs (Blain et al., 2004b).

1.3 Galaxy counts

Counting the number of galaxies within a given region of the sky and within a range of fluxes at different redshifts provides a direct measure of their abundance evolution that places direct constraints to models of galaxy formation.

The comparison of the number counts of local starbursts (Saunders et al., 1990) and SMGs (Coppin et al., 2006) suggests that strong evolution has affected the most luminous galaxies from $z \sim 2$ to the present. SMGs appear to be about 3 orders of magnitude more abundant than local starbursts at similar luminosities (Blain et al., 2002).

Recent bolometer blank field surveys indicate that the luminosity function of SMGs can be well described by a Schechter function (Schechter, 1976) with a break at $S_{850 \mu\text{m}} = 5 - 13$ mJy (Coppin et al., 2006). A strong down-turn in the number counts of SMGs appears to exist at flux densities > 6 mJy (Fig. 1.7; Coppin et al., 2006). This drop in number counts could be produced by regulating feedback between the disk and the central AGN in starburst galaxies that prevents them to attain higher luminosities (Lehnert & Heckman, 1996; Scoville, 2003; Thompson et al., 2005), although the actual cause of the downturn and the physics behind any limiting process are not well understood.

Submillimeter surveys with SCUBA and MAMBO have mapped relatively small patches of the sky, leading to poor statistics of the bright-end of the luminosity function, which is much affected by cosmic variance (Fig. 1.7). Wider and deeper surveys are necessary to study the evolution of the rarest, most luminous galaxies with bright flux densities and to better study the population of less luminous galaxies ($< L^*$) to flux densities < 0.1 mJy at $850 \mu\text{m}$.

1.4 Clustering properties

SMGs are among the most massive systems at high redshifts (Greve et al., 2005). Their comoving number density was found to be compatible with that of galaxy clusters (Scott et al., 2002; Almaini, 2002; Swinbank et al., 2006) and their properties suggest they may evolve into spheroidal galaxies at later epochs (Dunlop, 2001). Supporting evidence has arisen from the detection of galaxy pairs around known SMGs at similar redshifts (Ivison et al., 1998; Santos et al., 2004; Kneib et al., 2004), the presence of SMGs in a large scale structure of LBGs (Steidel et al., 2000), and their association with proto-cluster fields around radio galaxies (Ivison et al., 2000a; Stevens et al., 2003), which are good candidates as progenitors of cD galaxies.

Direct measurements of the clustering properties of SMGs (Blain et al., 2004b) suggest that they have a correlation length greater than that of LBGs at $z \sim 3-4$, similar to optically selected QSOs at $z \sim 2$, but somewhat smaller than extremely red objects (EROs) at $z \sim 1$ (Fig. 1.8). Due to cosmic variance and the small number statistics of SMG counts available for such estimates, the degree of clustering is poorly constrained, and it is not entirely clear whether SMGs evolve into bright ellipticals at later epochs. Larger submillimeter surveys covering areas of at least 1 deg^2 and providing $\gtrsim 100$ sources are necessary to assess this issue.

1.5 Galaxy evolution

From optical galaxy counts it had been known even prior to the discovery of SMGs that the cosmic star formation activity, as well as the QSO activity, peaked at $z > 1$. All evidence now suggests that star and galaxy formation had its period of highest activity at $z \sim 2$, that most stars seen in the local universe had formed before $z = 1$, and that SMGs play a major role in the formation of stars and the evolution of galaxies.

An intuitive explanation for the higher star formation rate in the early universe is the higher merger rate of smaller galaxies, which, according to the hierarchical picture of structure formation, formed first. By $z = 1$, most of the smaller galaxies had merged to form large spheroidal galaxies, and in the course of this cosmic consolidation, most of the stars formed in short ($10^7 - 10^8$ years) bursts during merger events. It is suggested by numerical simulations that during these mergers, some fraction of the gas mass is concentrated into very dense regions, usually toward the galaxy nucleus, and that this high concentration leads to a rapid conversion of the gas into stars.

In the course of such mergers, the central SMBHs are also fed by the gas concentrating toward the galactic nuclei, leading to QSO activity. It is believed that this kind of activity is a common, but short-lived phenomenon in galaxy evolution (McLeod et al., 1999). The formation of SMBHs and their relation to star formation in their host galaxies is one of the key issues of modern cosmology. Although it is still an open question how the host galaxy and merging affects the feeding of a QSO, there is statistical evidence for preceding mergers or current interaction of QSO host galaxies with a companion galaxy (Sanders et al., 1988a; McLeod & Rieke, 1994; Lim & Ho, 1999).

It is observationally confirmed that QSOs tend to have enhanced star formation activity in their host galaxies, and the transition between ULIRGs and AGN seems to be continuous (e.g., Sanders et al., 1988a), as they all show enhanced star-formation in their nuclear regions (McLeod et al., 1999). Observations of X-ray selected QSOs at $z \sim 2$ indicate that their submillimeter emission swiftly increases for the most obscured X-ray sources, revealing that this evolutionary scenario holds for the most massive and luminous systems in the early universe (Stevens et al., 2005). The molecular gas masses of transitional SMGs suggest that the evolution may be fast and the central black holes may grow more rapidly than the bulge component (Coppin et al., 2008).

One of the most important findings over the past years in this respect is that the centers of

early-type galaxies and of local spheroidals contain super-massive black holes, and that the black hole mass correlates tightly with the stellar bulge velocity dispersion, which in turn, is a measure for the mass of the bulge. This correlation suggests a coeval formation of a galaxy's bulge and SMBH (Gebhardt et al., 2000; Ferrarese & Merritt, 2000). The relation between the growth of SMBHs and massive starbursts is therefore a fundamental aspect of the galaxy formation process.

1.6 Outline of the Thesis

This Thesis is organized as follows:

In Chapter 2, we introduce the MAMBO 1.2 mm survey of the COSMOS field. We describe the COSMOS project data set and the millimeter observations that we use throughout this Thesis. We identify multi-wavelength counterparts to the millimeter sources and estimate the average contribution of radio and IR selected sources to the cosmic IR background using a stacking analysis.

In Chapter 3, we investigate the intrinsic properties of the identified SMGs. We study their relation to optically selected star-forming galaxies at high-redshift (BzK). Using their IR colors, we separate those SMGs that are likely dominated by AGN activity from those purely driven by star formation. We estimate radio/millimeter and optical/IR photometric redshifts, and stellar masses based on SED fitting.

In Chapter 4, we study the environments of the MAMBO galaxies. We use deep K -band data to investigate the possibility that SMGs are related to structures or overdensities of high-redshift star-forming galaxies. We study their projected number density distribution, optical/IR photometric redshifts and the presence of a color-magnitude relation typical of galaxy clusters.

In Chapter 5, we present interferometric continuum millimeter imaging of three of our MAMBO sources. We explore the possibility that two radio-faint MAMBO sources are located at high redshift, and study the millimeter emission of a MAMBO source that is embedded in a strong overdensity of high-redshift star-forming galaxies. We extract optical/IR photometry, locate the most likely multi-wavelength counterparts, and compute photometric redshifts for all detected millimeter sources.

In Chapter 6, we report the detection of four CO emission lines in one of the brightest MAMBO galaxies. We study the properties of the molecular gas, the star-formation conditions and dust properties. Through a detailed analysis of its multi-wavelength SED and morphology, we investigate the possibility that this source represents a transitional case between starburst and QSO

Finally, we summarize the topics covered, list the most important results and mention the ongoing projects related to this work.

MAMBO imaging of the COSMOS field

2.1 Introduction

Deep extra-galactic surveys with SCUBA (Holland et al., 1999) and MAMBO (Kreysa et al., 1998) were able to resolve part of the far-IR and (sub)millimeter background, discovering a population of dusty and massive star-forming galaxies at high redshifts (Smail et al., 1997; Barger et al., 1998; Eales et al., 1999, 2000; Bertoldi et al., 2000). This SMG population was found to contribute as much as 30% to the far-IR cosmic background detected by the COBE satellite using the FIRAS instrument (Puget et al., 1996; Fixsen et al., 1998).

Extra-galactic (sub)millimeter surveys have attempted to detect the typically faint emission from high redshift star forming galaxies either producing deep maps of blank field regions in the sky (Hughes et al., 1998; Eales et al., 1999, 2000; Scott et al., 2002; Borys et al., 2003; Greve et al., 2004; Laurent et al., 2005; Coppin et al., 2006; Bertoldi et al., 2007; Scott et al., 2008) or constructing maps that take advantage of gravitational lensing magnification by galaxy clusters (Smail et al., 1997, 2002; Chapman et al., 2002; Webb et al., 2005; Knudsen et al., 2006, 2008). These surveys demonstrated that a significant fraction of obscured star forming galaxies are missing in optical waveband studies and therefore the inclusion of this dusty galaxy population is necessary to build comprehensive and consistent models of galaxy formation and evolution in the early Universe (Blain et al., 1999).

Several imaging surveys have been performed in the (sub)millimeter regime, covering, however, small areas ($< 300 \text{ arcmin}^2$; Hughes et al., 1998; Eales et al., 1999, 2000; Scott et al., 2002; Borys et al., 2003) that lead to low number statistics and do not allow to study the large scale distribution and bright end of the submillimetre luminosity function.

Given the importance of having statistically meaningful samples of SMGs, new attempts to cover larger regions in the sky ($> 300 \text{ arcmin}^2$) have been made (Greve et al., 2004; Laurent et al., 2005; Mortier et al., 2005; Coppin et al., 2006; Bertoldi et al., 2007; Scott et al., 2008). Not only large submillimeter maps to the sub-mJy level are necessary, but also extensive multi-wavelength follow-up that permits a comprehensive study of the nature of the SMG population.

A number of blank field surveys have been conducted using MAMBO at the IRAM 30m telescope, aiming at fields in the sky that had prior, deep imaging at other wavelengths: Lockman Hole (Greve et al., 2004), NTT Deep Field (Dannerbauer et al., 2004), ELAIS-N2 (Greve et al., 2004), Abell 2125 (Bertoldi et al., 2000; Voss et al., 2006) and GOODS-North (Greve et al., 2008). Some of these fields (Lockman, ELAIS-N2) have overlapping SCUBA coverage, allowing an analysis of the 0.85 to 1.2 mm flux ratio for a limited number of SMGs.

In this Chapter, we present a new millimeter blank-field survey: the MAMBO 1.2 mm imaging of the COSMOS field (Bertoldi et al., 2007). In Section 2.2 we introduce the COSMOS project and describe the properties of its unique data set that will be used throughout this work. We

present the X-ray, optical, mid-IR and radio data, with emphasis in the last three wavelength ranges as they represent the primary data sets used in the next chapters. In Section 2.3, we present the millimeter observations, data reduction and source extraction carried out by Bertoldi et al. (2007). In Section 2.4, we show the multi-wavelength counterpart identification to the MAMBO sources. Finally, in Section 2.5 we present a stacking analysis that permits to estimate the contribution of radio and mid-IR sources to the submillimeter background.

2.2 The COSMOS field

The Cosmic Evolution survey, COSMOS, is the first survey comprising enough area ($1.5^\circ \times 1.5^\circ$) and depth to address the co-evolution of large scale structure, black holes and star formation in the early Universe (Scoville et al., 2007c). It is the largest Hubble Space telescope (HST) program ever, reaching a 10σ sensitivity limit of 27.3 magnitudes with the Advanced Camera for Surveys (ACS) I_{F814W} band (Scoville et al., 2007a; Koekemoer et al., 2007). Space and ground-based observations, some of them currently underway, span over nearly the entire electromagnetic spectrum from X-rays, UV, optical, near and mid-IR, millimeter, to the radio wavelengths, including imaging and spectroscopy (Hasinger et al., 2007; Taniguchi et al., 2007; Capak et al., 2007; Lilly et al., 2007; Sanders et al., 2007; Bertoldi et al., 2007; Schinnerer et al., 2007).

COSMOS is an equatorial field that permits access from all astronomical facilities, in particular the next generation of 20 – 30 m class optical/IR telescopes, the Expanded Very large Array (VLA) and the Atacama Large Millimeter Array (ALMA), placing a significant advantage compared to other much studied high declination fields such as the Hubble Deep Field North (HDF-N), Chandra Deep Field North (CDF-N), Groth strip and Lockman hole (Scoville et al., 2007c).

Other deep multi-wavelength projects, such as the Great Observatories Origins Deep Survey (GOODS; Giavalisco et al., 2004b) and the Galaxy Evolution from Morphology and SEDs survey (GEMS; Rix et al., 2004), are designed to study the earliest epoch of galaxy formation ($z > 4$) by means of ultra-deep imaging over small patches in the sky. Their pencil-beam design allows them to trace halo masses only up to $\sim 10^{13} M_\odot$ since they are not specifically pointed towards galaxy cluster regions. COSMOS, on the other hand, due to its large area coverage and deep exposures, is able to sample the largest structures up to halo masses of $\sim 10^{14} M_\odot$ (Scoville et al., 2007c) over the crucial epoch of galaxy formation ($1 < z < 4$).

The major science goals of the COSMOS project are: (1) The study of the assembly of galaxies, clusters and dark matter; (2) The reconstruction of the dark matter distribution on large scales up to $z < 1.5$; (3) The study of galaxy mergers, morphology, AGN activity and star formation as a function of environment, luminosity and redshift; (4) Trace the mass and luminosity distribution of galaxies over statistically significant samples overcoming cosmic variance; (5) Provide significant samples of very high redshift galaxies ($z > 2 - 3$), selected by optical/IR color criteria or direct detection of Lyman- α emission or IR and radio emission.

COSMOS is an international project and its different data sets have been acquired, reduced and analyzed by several working groups, as described in detail elsewhere (e.g. Scoville et al., 2007c; Capak et al., 2007; Schinnerer et al., 2007; Hasinger et al., 2007; Sanders et al., 2007; Koekemoer et al., 2007; Bertoldi et al., 2007; Scott et al., 2008). Below, we give a brief introduction to these data sets, their data reduction and source extraction, with emphasis on the optical and IR data as they are used in this work. Since part of the millimeter imaging of COSMOS (i.e. the MAMBO survey of COSMOS) is the main subject of this Thesis, we describe it in detail in the next section. The MAMBO data reduction and source extraction were performed by Bertoldi et al. (2007).

2.2.1 X-ray imaging

X-ray observations are of crucial importance due to their ability to locate emission from AGNs and galaxy clusters. X-ray imaging in the COSMOS field was performed by Hasinger et al. (2007) using a total of 25 overlapping pointings with the XMM-Newton satellite, to map an area of $1.4^\circ \times 1.4^\circ$, most of which (85%) has also been observed with the HST. Individual exposures times vary between the different pointings and lie in the range 30 – 62 ks, making a total net integration time of 504 ks. Including both point-like and extended, the number of sources detected in the 0.5–2 keV, 2–10 keV and 5–10 keV bands are 1307, 735 and 187, down to fluxes 7.2×10^{-16} erg s $^{-1}$ cm $^{-2}$, 4.0×10^{-15} erg s $^{-1}$ cm $^{-2}$ and 9.7×10^{-15} erg s $^{-1}$ cm $^{-2}$, respectively (Cappelluti et al., 2007; Hasinger et al., 2007).

A recent new X-ray survey of the central part of the COSMOS field was performed using the Chandra satellite (Elvis et al., 2008, in preparation). This survey consist of 36 overlapping pointings of 50 ks exposure time made with the Advanced CCD Imaging Spectrometer (ACIS). This overlap gives uniform exposure over the whole area, and a sharply defined limiting flux. The survey reaches an average exposure time of 200 ks and a total exposure time of 1.8 Ms over the central 0.8 deg 2 of COSMOS. A preliminary catalog in the 0.5 – 2 keV band includes 1758 sources to a limiting flux of $\sim 2 \times 10^{-16}$ erg s $^{-1}$ cm $^{-2}$, half of which are not detected by the XMM-Newton satellite. The better resolution of Chandra allows for a improved counterpart selection and allows to reach about 3 times deeper than the XMM-Newton survey of COSMOS.

2.2.2 Optical Imaging

An extensive ground based imaging program was undertaken. Using the Suprime-Cam instrument on the Subaru 8.3 m telescope, the COSMOS field was imaged by Taniguchi et al. (2007) using 6 broad bands filters, B_j, V_j, g^+, r^+, i^+ and z^+ . These data were complemented with deep u^* band imaging and shallow i^* band imaging using the Megaprime camera on the Canada–France Hawaii Telescope (CFHT). Shallow near-IR K_S band imaging was also undertaken using the FLAMINGOS camera on the Kitt Peak National Observatory (KPNO) 4 m telescope and the ISPI camera on the Cerro Tololo Inter–American Observatory (CTIO) 4 m telescope. Since COSMOS is an equatorial field, it has also been imaged in the course of the Sloan Digital Sky Survey (SDSS), although at much shallower depths, in 5 broad band filters, u', g', r', i' and z' . The optical and IR transmission filters are shown in Fig. 2.1.

The data reduction and creation of an optical/near-IR source catalog was done by Capak et al. (2007). All images were point spread function (PSF) homogenized and optimized for photometric measurements using a 3'' aperture. The i^+ band was used for detection, reaching a 50% completeness at $i^+ = 27.4$. Table 2.1 summarizes the relevant observational parameters for the optical data and Fig. 2.2 shows an optical color composite image for the whole extension of the COSMOS field.

Deeper near-IR imaging is currently underway in the Y, J and K_S bands using the WFCAM instrument on the United Kingdom Infrared 3.8 m telescope (UKIRT) and the WIRCAM instrument on the CFHT. The description of the K_S band data is given in Chapter 4.

2.2.3 Mid-infrared imaging

The acquisition of deep mid-IR continuum maps over the range $3.6 \mu\text{m} - 24 \mu\text{m}$ is crucial to understand the stellar mass assembly of galaxies as a function of redshift and environment. The peak light emission produced in old stars is typically observed in the rest-frame K band ($\sim 2.2 \mu\text{m}$). At redshifts $z > 0.5$ this component is observed at longer wavelengths ($> 3.3 \mu\text{m}$) and mid-IR data becomes an important tool to provide reliable estimates of the stellar mass and accurate photometric redshifts at $z > 1$.

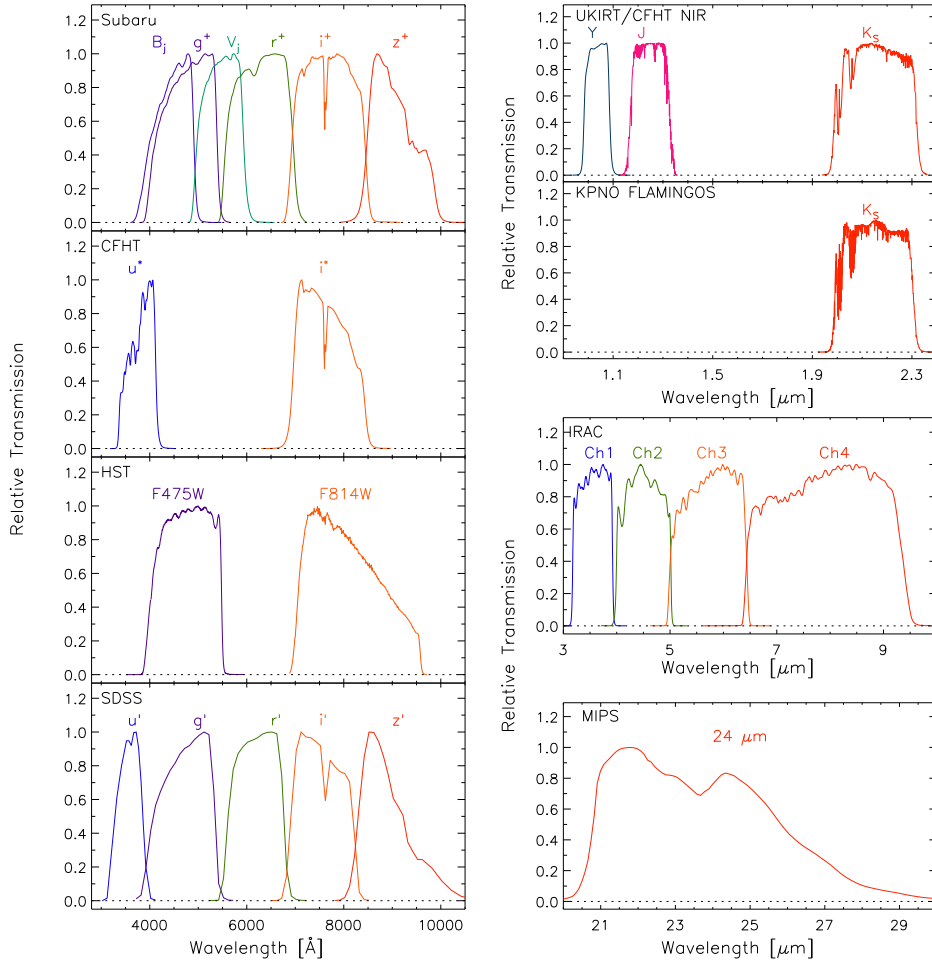


Figure 2.1: Filter transmission profiles for the COSMOS optical, and near and mid-IR data sets (Capak et al., 2007). All profiles have been normalized to 1 and include the atmosphere, the telescope, the camera optics, the detector and the filter transmissions. The left column show the optical broad band filters and the right column shows the near and mid-IR filters. The SDSS filters are shown for comparison.

The COSMOS field was imaged at 3.6, 4.5, 5.8 and 8.0 μm using the Infrared Array Camera (IRAC) and at 24 μm using the Multiband Imaging Photometer (MIPS) on board of the Spitzer satellite (Fig. 2.1). The data acquisition, reduction and obtention of source catalog were performed by Sanders et al. (2007).

A primary data reduction and calibration of the IRAC data was provided by the Spitzer Science Center (SSC). These corrections include dark subtraction, flat-fielding, and linearization. An adapted reduction pipeline from the Spitzer Wide-Area Infrared Extra-galactic (SWIRE) project was applied and is described in Surace et al. (in preparation). Image co-adding was performed with the SSC MOPEX software (Makovoz et al. 2005). Source extraction was carried out using SExtractor in all IRAC bands simultaneously using 1.9'' apertures and corrected to obtain total fluxes. Measured sensitivities reach 5σ levels of 0.9, 1.7, 11.3 and 14.6 μJy in the 3.6, 4.5, 5.8 and 8.0 μm bands, respectively.

MIPS 24 μm observations of COSMOS were performed to a shallow depth (*Cycle 2*). They

Table 2.1: Data quality for the optical observations.

Filter	Central Wavelength (\AA)	Filter Width (\AA)	Depth ^{ab}	Saturation ^b Magnitude	Offset from ^c Vega System
u'	3591.3	550	22.0	12.0	0.921
u^*	3797.9	720	26.4	15.8	0.380
B_J	4459.7	897	27.3	18.7	-0.131
g'	4723.1	1300	22.2	12.0	-0.117
g^+	4779.6	1265	27.0	18.2	-0.117
V_J	5483.8	946	26.6	18.7	-0.004
r'	6213.0	1200	22.2	12.0	0.142
r^+	6295.1	1382	26.8	18.7	0.125
i'	7522.5	1300	21.3	12.0	0.355
i^+	7640.8	1497	26.2	20.0	0.379
i^*	7683.6	1380	24.0	16.0	0.380
F814W	8037.2	1862	24.9	18.7	0.414
NB816	8151.0	117	25.7	16.9	0.458
z'	8855.0	1000	20.5	12.0	0.538
z^+	9036.9	856	25.2	18.7	0.547
K_S	21537.2	3120	21.6	10.0	1.852

^a 5σ in a $3''$ aperture; ^b In AB magnitudes; ^c AB = Vega + Offset. This offset does not include the color conversions to the Johnsons-Cousins system used by Landolt (1992).

cover a net area of $1.75^\circ \times 1.97^\circ$, slightly larger than the optical and radio coverages of COSMOS (Fig. 2.3). Deeper $24\ \mu\text{m}$ observations were taken over a $30' \times 20'$ region (“test area”). One of the main reasons to carry out combined shallow and deep observations was to check the quality of the COSMOS field to be integrated deeper in future observations. As COSMOS proved to be a “good” field for IR observations (e.g. low cirrus contamination), further measurements were performed during *Cycle 3* and their data reduction is currently underway (Frayer et al., in preparation). The *Cycle 3* data cover an area of $\sim 1.5^\circ \times 1.64^\circ$ to a depth comparable to the *Cycle 2* test region (Sanders et al., 2007). *Cycle 3* data is not included in this Thesis.

MIPS $24\ \mu\text{m}$ data taken in *Cycle 2* were reduced using a pipeline that combines IDL routines and the MOPEX software (Sanders et al., 2007). Contamination from cirrus emission was found to be negligible, far below the background level of the deep test area. Measured sensitivities reach 5σ levels of $420\ \mu\text{Jy}$ and $71\ \mu\text{Jy}$ for the shallow and deep $24\ \mu\text{m}$ maps, respectively (Sanders et al., 2007). A preliminary source extraction was performed for the shallow and deep images using the IDL version of the DAOPHOT package (Stetson, 1987). Finally, aperture photometry and PSF fitting were performed on the detected objects.

2.2.4 Radio imaging

Deep radio imaging down to the sub-mJy level is necessary to study the contribution of the different galaxy populations (e.g. starburst, AGN) to the radio emission at different redshifts. Given the tight correlation between the radio and far-IR outputs from star forming regions, radio imaging becomes a particularly important tool for the study of galaxies detected in the (sub-)millimeter regime (Section 2.4).

The COSMOS field was imaged in the 1.4 GHz (20 cm) continuum by Schinnerer et al. (2007) using the *L*-band receiver on the National Radio-Astronomy Observatory (NRAO) Very Large Array (VLA) interferometer. Observations were performed in the most extended A-configuration and reach an angular resolution of $1.5'' \times 1.4''$, matching the resolution of the optical imaging. A



Figure 2.2: *Br'z'* color image of the COSMOS field from Taniguchi et al. (2007). The image size is $1.5^\circ \times 1.5^\circ$.

total of 23 pointings were used to map the complete COSMOS field (2 deg^2).

Data reduction and extraction of the source catalog were performed by Schinnerer et al. (2007). The data were reduced using the standard routines of the Astronomical Imaging Processing System (AIPS; Greisen 2003). Noise maps were produced using SExtractor and source extraction was performed using a combination of the SAD, MAXFIT and JMFIT AIPS routines. The mean rms level for the inner 1 deg^2 is $10.5 \mu\text{Jy beam}^{-1}$, and the mean rms over the whole 2 deg^2 area $15.0 \mu\text{Jy beam}^{-1}$. The final catalog includes 3563 single component sources and 80 sources with more than one fitted component, with signal-to-noise (S/N) > 4.5 .

An additional very deep VLA 1.4 GHz map was obtained for the central $30' \times 30'$. This map reaches an rms level of $7 \mu\text{Jy}$ with a nearly round beam of $1.35''$. This deeper radio coverage of the COSMOS field is intended to probe the faintest population of radio emitters at the highest redshifts, being crucial for the identification of SMGs (Section 2.4.1).

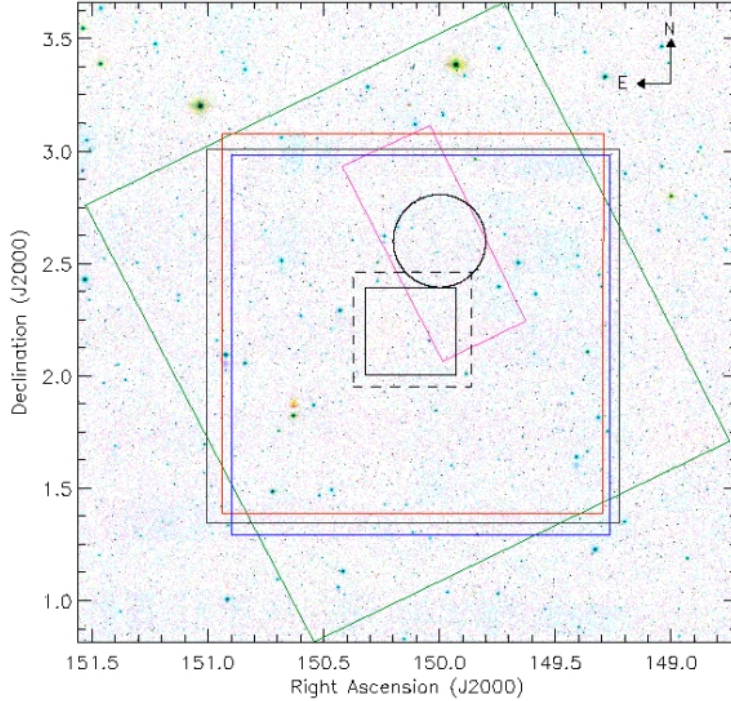


Figure 2.3: Schematic view of the coverage of the optical, IR and millimeter data sets in COSMOS. The background image is an inverted color composite from the SDSS. The gray square shows the region covered by the optical data (i.e. Subaru, CFHT). The green box represents the region comprised by the MIPS $24\ \mu\text{m}$ shallow survey, whereas the magenta rectangle indicates the section covered by the MIPS $24\ \mu\text{m}$ deep survey. The red box shows the region mapped by the IRAC 3.6 and $4.5\ \mu\text{m}$ bands, and the blue box shows the coverage of the IRAC 4.5 and $8.0\ \mu\text{m}$. The solid square and circle represent the sector covered by the MAMBO $1.2\ \text{mm}$ and AzTEC $1.1\ \text{mm}$ surveys, while the dashed square indicates the coverage of the Bolocam $1.1\ \text{mm}$ survey.

2.3 Millimeter observations of COSMOS

A significant fraction of the COSMOS field has been imaged at millimeter wavelengths by 3 independent surveys. Using the AzTEC camera (Wilson et al., 2008) on the JCMT, Scott et al. (2008) mapped a region occupied by a prominent large scale structure overdensity (Scoville et al., 2007b) that includes a rich X-ray cluster at $z = 0.73$ (Guzzo et al., 2007; Finoguenov et al., 2007). The AzTEC $1.1\ \text{mm}$ survey covers an area of $30' \times 30'$, centered at (R.A., Decl.)= $(10^{\text{h}}\ 00^{\text{m}}\ 00^{\text{s}}, +02^{\circ}\ 36'\ 00'')$, to a depth of $1.3\ \text{mJy}$ per $18''$ beam.

A larger field of $30.6' \times 30.6'$ was mapped at $1.1\ \text{mm}$ by Aguirre et al. (in preparation) using the Bolocam instrument (Glenn et al., 2003; Haig et al., 2004) on the Caltech Submillimeter Observatory (CSO). The Bolocam survey encompasses a blank field region centered at (R.A., Decl.)= $(10^{\text{h}}\ 00^{\text{m}}\ 28.6^{\text{s}}, +02^{\circ}\ 12'\ 21.0'')$ to a depth of $1.9\ \text{mJy}$ per $31''$ beam.

The inner part of the COSMOS field was imaged at $1.2\ \text{mm}$ by Bertoldi et al. (2007) using MAMBO (Kreysa et al., 1998) on the IRAM 30 m telescope in Pico Veleta, Spain. The COSMOS-MAMBO (COSBO) survey was designed to cover a moderate-size blank field, taking advantage of the complete and deeper multi-wavelength coverage available in the central region of COSMOS.

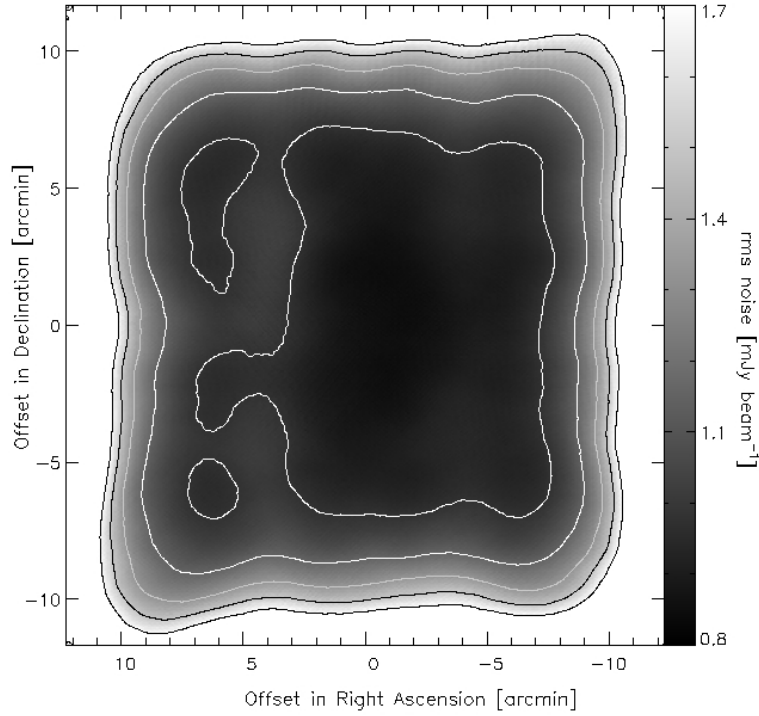


Figure 2.4: Root mean square noise map for the MAMBO survey of COSMOS. Contour levels are 0.85, 1.1, 1.3 and 1.6 mJy per beam. Offset positions are measured from $(RA, DEC) = (10^{\text{h}} 00^{\text{m}} 30^{\text{s}}, +02^{\circ} 12' 00'')$.

Since this survey is the main subject of this work, we describe its observations, data reduction and source extraction in the rest of this Section.

2.3.1 MAMBO observations

Our observations of the COSMOS field cover a region of $20' \times 20'$, centered at $(R.A., Decl.) = (10^{\text{h}} 00^{\text{m}} 30^{\text{s}}, +02^{\circ} 12' 00.0'')$ and reach a nearly uniform depth of 1 mJy per $11''$ beam. This survey overlaps with the wider Bolocam survey, however it provides a much deeper coverage (see below) under the better resolution supplied by the IRAM 30 m telescope, being able to pick up the emission from the more distant and fainter SMGs.

The observations were performed within the winter semester 2003 – 2004 in good weather conditions, with 250 GHz opacities ranging between 0.1 to 0.3 and stable atmospheric conditions (low sky-noise).

To obtain an uniform depth coverage of the entire field, the standard on-the-fly scan-map observing mode was used with a regular grid of offset positions. Each scan-map is typically formed by a $\sim 300'' \times 320''$ grid and mapped at a velocity $5'' \text{ s}^{-1}$. A full map implies 41 azimuthal sub-scans of 60 s length. The wobbler secondary was chopped in azimuth at a frequency of 2 Hz, with a wobbler throw of $42'' - 46''$, that eliminates most systematics and residual effects from the double beam profile.

The telescope pointing and focus were checked approximately every scan-map with the nearby bright point source J0909+014. The pointing was found to be stable within $3''$. The flux estimates

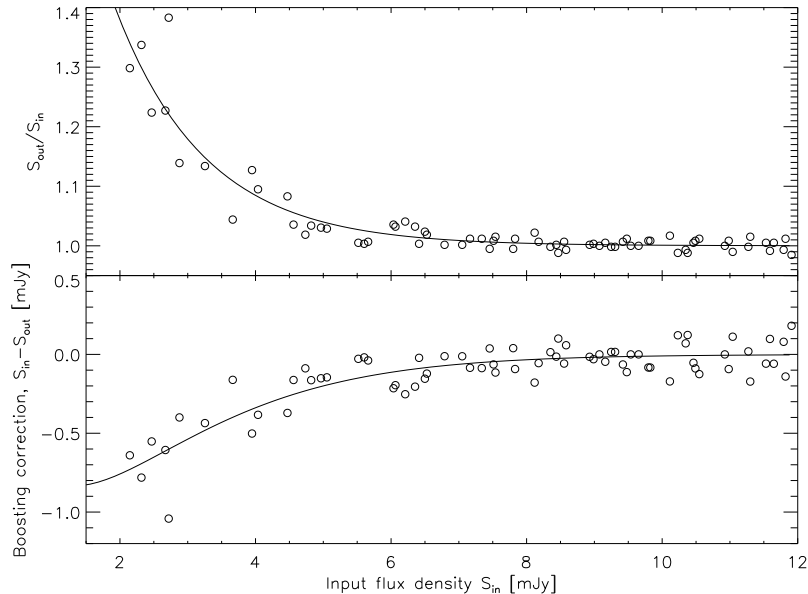


Figure 2.5: The top panel shows the result of the flux extraction of artificial point sources in the randomized MAMBO maps (open circles). The solid line represents the best fitting model to the measured ratio between the output and input flux. The bottom panel shows the respective flux deboosting correction that has to be applied for a given flux.

have an uncertainty of $\sim 10\%$ based on observations of standard calibrators (planets, bright point sources).

The data were reduced by Bertoldi et al. (2007) using standard pipeline procedures of the MOPSI and MOPSIC software packages, written by R. Zylka (IRAM). This involves de-spiking, removal of correlated noise and correction for the atmospheric opacity. The final map has a nearly uniform rms of $\sim 1 \text{ mJy beam}^{-1}$ in the central $\sim 250 \text{ arcmin}^2$ and increases toward the edges, reaching $< 2 \text{ mJy beam}^{-1}$ for a total area of $\sim 450 \text{ arcmin}^2$ (Fig. 2.4).

2.3.2 Source extraction

As described by Bertoldi et al. (2007), sources were extracted using a combination of the MOPSIC's `gfit` routine and IDL procedures. First, a signal-to-noise (S/N) map is created from the MAMBO signal and noise maps. All the peaks above a certain S/N threshold are selected. For each peak, the surrounding pixels are located and exposed to a second lower threshold. Sources above this second threshold are considered as significant sources (e.g. $S/N > 4$). This procedure sets, for each peak found, the initial guess parameters and the area in which to perform an elliptical Gaussian fit. The computed intensity obtained from this fit is thereafter re-normalized to a circular Gaussian corresponding to the full-width half maximum (FWHM) of the $10.7''$ beam (Bertoldi et al., 2007).

Using this procedure, we find a total of 15 sources having integrated flux densities with $S/N > 4$ (note that all the sources have sizes much smaller than the MAMBO FWHM). Some of these significant COSBO sources show fragmented or double-peaked structure in the S/N maps that can be attributed to noise or pointing errors. It is also possible that the double-peaked structures are real associations (see Chapter 5). In these cases each peak has $S/N < 4$, however

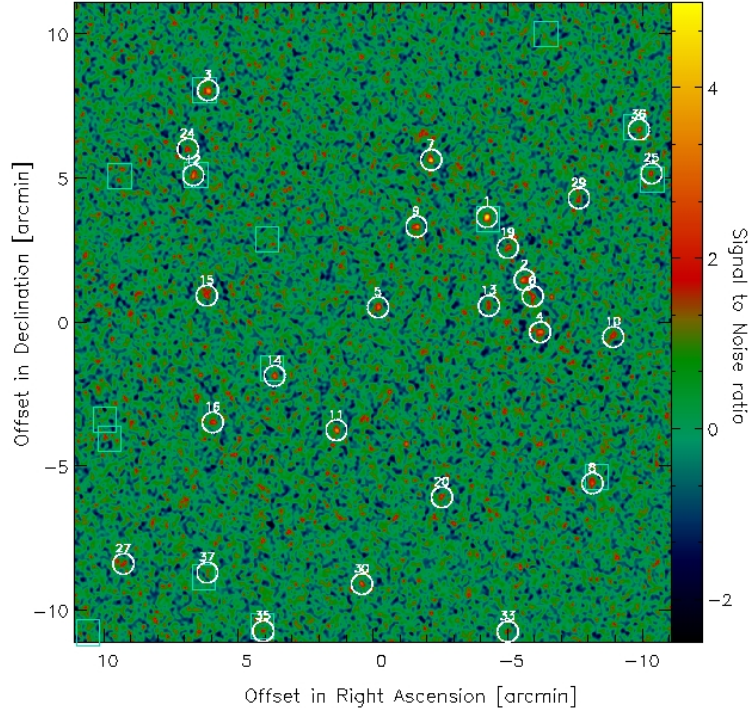


Figure 2.6: Inner section of the COSMOS map smoothed to $12''$ resolution. Extracted MAMBO sources are marked with white circles and their IDs. Bolocam sources within the MAMBO map region are shown in cyan boxes, for comparison. Offset positions are measured from $(R.A., Decl.) = (10^{\text{h}} 00^{\text{m}} 30^{\text{s}}, +02^{\circ} 12' 00'')$.

the integrated flux density is above the $S/N = 4$ threshold.

A problem that arises in low significance flux limited surveys (as it is generally the case for cosmological submillimeter surveys) is the so called flux-boosting. As a result of the joint contribution of instrumental noise from the array and/or confusion noise from faint sources below the detection threshold, the fluxes of low S/N sources are scattered upward, potentially significantly affecting and biasing the faint source number counts.

To account for this effect, the amount of “boosted” flux (or flux correction) as a function of flux density was modeled, following the approach of Greve et al. (2004). Random maps were generated, altering the array parameters (e.g. time streams) from the original MAMBO map. This ensures the conservation of the original MAMBO map noise features and the loss of all information of the individual source intensities. After this, point sources were arbitrarily inserted at different flux density levels on the simulated maps and extracted using the procedure described above (Bertoldi et al., 2007). Next, the extracted flux densities, S_{out} , were compared with the input flux densities, S_{in} . The boosting factor thereby modeled,

$$S_{\text{out}}/S_{\text{in}} = 1 + 1.7 e^{-0.75S_{\text{in}}}, \quad (2.1)$$

increases strongly as the input flux densities approach to the noise background level (Fig. 2.5). Finally, this model was used to correct the original MAMBO source fluxes (Table 2.2).

Table 2.2: MAMBO sources and their Bolocam counterparts.

ID	Name (MM J)	MAMBO			Bolocam				Offset (")
		R.A. (J2000)	Decl. (J2000)	$S_{1.2\text{mm}}$ (mJy)	ID	R.A. (J2000)	Decl. (J2000)	$S_{1.1\text{mm}}$ (mJy)	
1.....	100016+021549	10 00 15.7	+02 15 49	$6.3 - 0.10 \pm 0.9$	4	10 00 15.5	02 15 45	$7.8 - 1.9 \pm 1.9$	5
2.....	100010+021338	10 00 10.1	+02 13 38	$5.9 - 0.13 \pm 0.9$				3.7	
2W.....		10 00 09.7	+02 13 33	$2.2 - 0.83 \pm 0.9$					
2E.....		10 00 10.4	+02 13 37	$4.2 - 0.37 \pm 0.9$					
3.....	100057+022013	10 00 57.2	+02 20 13	$7.5 - 0.05 \pm 1.1$	33	10 00 57.8	02 20 13	$5.9 - 2.4 \pm 1.9$	9
4.....	100007+021149	10 00 07.8	+02 11 49	$5.7 - 0.15 \pm 0.9$				4.1	
5.....	100031+021241	10 00 31.9	+02 12 41	$5.3 - 0.19 \pm 0.9$				3.5	
6.....	100008+021304	10 00 08.9	+02 13 04	$5.2 - 0.20 \pm 0.9$				3.7	
7.....	100024+021748	10 00 24.0	+02 17 48	$5.2 - 0.20 \pm 0.9$				1.3	
8.....	100000+020634	10 00 00.0	+02 06 34	$5.6 - 0.15 \pm 1.0$	12	09 59 59.4	02 06 48	$7.1 - 2.2 \pm 1.9$	17
9.....	100026+021529	10 00 26.2	+02 15 29	$4.9 - 0.24 \pm 0.9$				3.1	
10.....	095956+021139	09 59 56.9	+02 11 39	$6.0 - 0.12 \pm 1.1$				1.8	
11.....	100038+020825	10 00 38.1	+02 08 25	$4.8 - 0.25 \pm 0.9$				5.6	
12.....	100059+021716	10 00 59.4	+02 17 16	$5.0 - 0.22 \pm 1.0$	24	10 00 58.9	02 17 17	$6.1 - 2.4 \pm 1.9$	8
13.....	100015+021244	10 00 15.4	+02 12 44	$4.4 - 0.32 \pm 0.9$				4.3	
13N.....		10 00 15.5	+02 12 53	$2.3 - 0.83 \pm 0.9$					
13S.....		10 00 15.3	+02 12 40	$2.2 - 0.83 \pm 0.9$					
14.....	100047+021018	10 00 47.3	+02 10 18	$4.4 - 0.32 \pm 1.0$	29	10 00 47.7	02 10 33	$6.0 - 2.4 \pm 1.9$	
15.....	100057+021305	10 00 57.4	+02 13 05	$4.4 - 0.32 \pm 1.0$				2.2	
16.....	100056+020841	10 00 56.5	+02 08 41	$3.8 - 0.45 \pm 1.0$				0.6	
19.....	100012+021445	10 00 12.6	+02 14 45	$3.5 - 0.55 \pm 0.9$					
20.....	100022+020605	10 00 22.4	+02 06 05	$3.5 - 0.55 \pm 0.9$				1.1	
24.....	100100+021811	10 01 00.2	+02 18 11	$3.4 - 0.58 \pm 1.0$				-0.0	
25.....	095951+021720	09 59 51.2	+02 17 20	$4.5 - 0.30 \pm 1.3$	19	09 59 51.1	02 17 08	$6.5 - 2.3 \pm 1.9$	12
27.....	100109+020346	10 01 09.8	+02 03 46	$4.2 - 0.37 \pm 1.4$				0.8	
29.....	100002+021628	10 00 02.0	+02 16 28	$3.6 - 0.51 \pm 1.2$				3.2	
30.....	100034+020304	10 00 34.3	+02 03 04	$3.5 - 0.54 \pm 1.2$				-0.9	
33.....	100012+020125	10 00 12.6	+02 01 25	$5.2 - 0.20 \pm 2.0$				4.7	
35.....	100048+020125	10 00 49.0	+02 01 26	$4.4 - 0.32 \pm 1.5$	15	10 00 49.1	02 01 36	$6.7 - 2.3 \pm 1.9$	10
36E.....	095953+021851	09 59 53.9	+02 18 51	$2.2 - 0.83 \pm 0.9$	9	09 59 53.7	02 18 56	$7.5 - 2.1 \pm 1.9$	6
36W.....		09 59 53.1	+02 18 51	$3.5 - 0.54 \pm 0.9$					
37.....	100057+020228	10 00 57.3	+02 03 28	$2.8 - 0.74 \pm 1.1$	6	09 59 29.0	02 22 53	$7.7 - 2.0 \pm 1.9$	12
.....				<5.2	2	10 01 9.4	02 00 56	$8.7 - 1.6 \pm 1.9$	
.....				<4.3	10	10 00 6.9	02 22 09	$7.3 - 2.1 \pm 1.9$	
.....				<5.3	11	10 01 12.6	02 08 47	$7.2 - 2.2 \pm 1.9$	
.....				<6.7	16	09 59 46.2	02 12 17	$6.6 - 2.3 \pm 1.9$	
.....				<5.2	18	10 01 11.9	02 08 07	$6.5 - 2.3 \pm 1.9$	
.....				<8.4	25	10 00 4.4	02 00 23	$6.1 - 2.4 \pm 2.0$	

Continued.

ID	Name (MM J)	MAMBO			Bolocam				Offset ($''$)
		R.A. (J2000)	Decl. (J2000)	$S_{1.2\text{mm}}$ (mJy)	ID	R.A. (J2000)	Decl. (J2000)	$S_{1.1\text{mm}}$ (mJy)	
.....				<8.4	28	10 01 15.1	02 01 23	$6.0 - 2.4 \pm 1.9$	
.....				<2.9	30	10 00 48.4	02 15 03	$6.0 - 2.4 \pm 1.9$	
.....				<4.0	31	10 01 10.4	02 17 13	$6.0 - 2.5 \pm 1.9$	

Extracted MAMBO sources are listed with their respective MAMBO and Bolocam fluxes. For those MAMBO sources with no significant Bolocam detection, the Bolocam flux at the MAMBO position is listed. Conversely, for Bolocam sources with no significant MAMBO counterpart, a 3σ upper limit is provided. Listed flux densities are source integrated normalized to $10.7''$ beam, followed by the flux boosting correction and background level around the source.

2.4 Multi-wavelength counterpart identification

The identification of the optical counterparts responsible for the far-IR emission is crucial to properly investigate the properties of SMGs. Due to the large beams provided by current telescopes in the millimeter regime ($\sim 10'' - 30''$), resolving millimeter peaks into discrete sources whose positions can be compared with sources detected at other wavelengths (e.g. in the optical) constitutes a difficult task. The direct identification of counterparts in optical images is not practical. To detect the faint signal from these obscured sources long integration times are needed, leading to a high number density of optical sources (not necessarily related to the submillimeter emission) and making the counterpart identification ambiguous.

The standard way to find counterparts to the millimeter sources is to use deep high resolution radio imaging (e.g. Ivison et al., 2002, 2005, 2007). The well-established relation between the radio and far-IR emission (Condon, 1992) and the low density of radio sources compared with optical/IR radio sources, makes this selection technique the most appropriate, given the unlikely chance of alignments between radio and millimeter sources. Even though, the radio flux drops rapidly with redshift and therefore, at current radio surveys depths ($\sim 10 \mu\text{Jy}$), this method turns to be useful up to $z \sim 3$.

A different approach has been the selection of counterparts in the mid-IR regime (Egami et al., 2004; Ivison et al., 2004; Pope et al., 2006; Ashby et al., 2006). This selection technique has proven to be successful to disentangle sources not detected in the radio, however its poor angular resolution ($\sim 2''$), the unprecise relation of the mid-IR (in particular at $24 \mu\text{m}$) to the far-IR emission and the larger number density of mid-IR sources compared to radio sources, can make this counterpart selection method ambiguous. A joint selection using both deep radio and mid-IR maps is currently the most reliable way to identify counterparts (Ivison et al., 2007).

2.4.1 Radio counterparts

To identify possible radio counterparts to the MAMBO sources, we used the deepest VLA 1.4 GHz map of the COSMOS field ($7 \mu\text{Jy}$ rms noise per $1.35''$ beam).

Radio sources lying within a search radius of $10''$ from the MAMBO position were considered as counterpart candidates. The chosen search radius is slightly larger than that the $8''$ radius that we used in Bertoldi et al. (2007) because it accounts for the MAMBO beam ($11''$), the pointing errors ($3''$), and accounts for both the VLA 1.4 GHz ($\sim 1''$) and MIPS $24 \mu\text{m}$ ($\sim 2''$) positional uncertainties.

For the 15 most significant MAMBO detections ($S/N > 4$), 11 can be associated with a faint radio source. Four sources (COSBO 4, 9, 14 and 15) do not show any radio counterpart to a 3σ level of $21 \mu\text{Jy}$.

Additionally, we identified 10 lower significance MAMBO sources ($S/N = 3.5 - 4.0$) that coincide with a radio source within $5''$ radius from the MAMBO peak. Although the selection of MAMBO sources based on their radio association is biased, these galaxies likely represent real and faint SMGs, given the known correlation between radio and far-IR emission in galaxies (Condon, 1992) and the low radio source density.

Furthermore, 2 low significance MAMBO peaks ($S/N < 4$) were added based on their joint identification with Bolocam and radio sources (e.g. COSBO 36 and 37).

To estimate the reliability of each association we computed the corrected Poisson probability of chance association, P_C . It corresponds to the probability that a radio source is, by chance, located within a radius $r = 10''$ from the millimeter position (Downes et al., 1986). We computed this Poisson probability as

$$P_C = 1 - e^{-P_s[1+\log(P_s/P)]}, \quad (2.2)$$

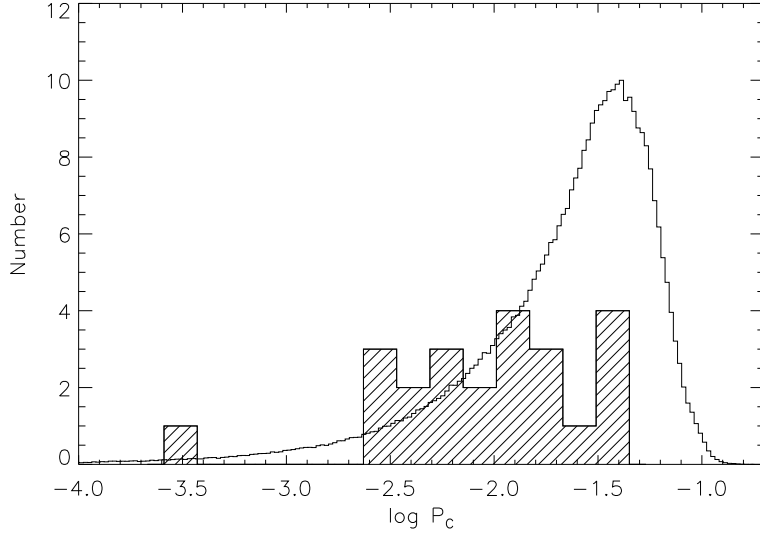


Figure 2.7: Distribution of the corrected probability of chance association (P_C) for radio selected counterparts. The hatched histogram shows the values of P_C for the most likely counterparts to the MAMBO sources. The solid histogram is the distribution of P_C found for randomly selected positions in the field.

where $P_S = 1 - \exp(-\pi n_S d^2)$ is the “raw” Poisson probability of finding a source brighter than S at a distance d from the millimeter position, and n_S is the local density of radio sources brighter than S. The value of P corresponds to the raw Poisson probability of finding a radio source brighter than the detection limit of our catalog within the $10''$ search radius. The P_C values for the radio associations to the MAMBO sources are listed in Table 2.4.

Figure 2.7 shows the distribution of the corrected Poisson probability for the radio associations to the MAMBO sources, compared with the distribution computed from a Monte Carlo simulation in which the reference positions were chosen randomly in the radio map. The probabilities for the identified MAMBO sources follow a distribution clearly different from that of the random galaxy sample and shifted to lower P_C values, suggesting that most of the identifications are real.

2.4.2 MIPS $24 \mu\text{m}$ counterparts

To complement the radio counterpart identification of the millimeter sources, we performed an independent search of counterparts to the MAMBO galaxies based on the MIPS $24 \mu\text{m}$ detections. As explained in Section 2.2.3, the *Cycle 2* $24 \mu\text{m}$ coverage of the COSMOS field consists of a shallow map that covers the entire 2 deg^2 , and a deeper map that covers $\sim 30 \times 20 \text{ arcmin}^2$. Due to its location and geometry in the COSMOS field, part of the deep MIPS region overlaps with the MAMBO map (Fig. 2.3), enclosing the position of 12 millimeter sources (COSBO 1, 2, 4, 6, 7, 8, 10, 13, 19, 25, 29 and 36). Thus, for the identification, we divided our MAMBO sample into those covered by the deep $24 \mu\text{m}$ map and those covered by the shallow $24 \mu\text{m}$ map, and looked for counterparts separately.

We followed a procedure similar to that used for the radio identifications. We looked for counterparts within a radius of $10''$ around each MAMBO position and accounted for the reliability of the associations using the corrected Poisson probability of chance association. The result of the identifications is summarized in Table 2.4.

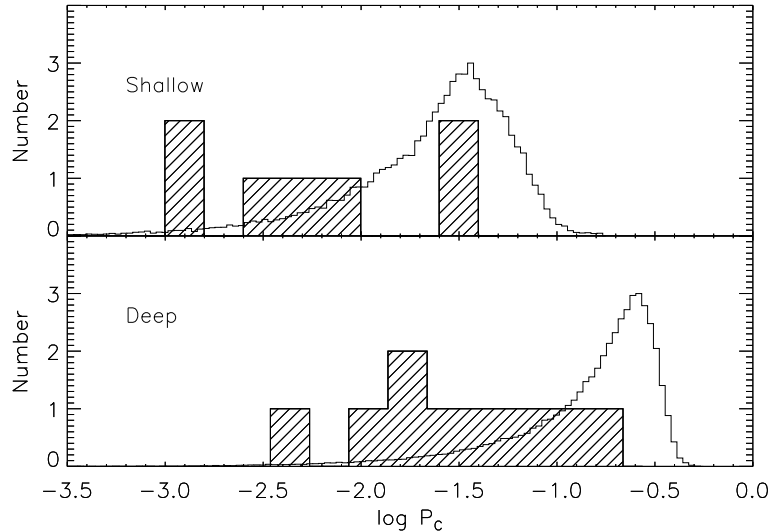


Figure 2.8: Distribution of the corrected probability of chance association (P_C) for the $24\ \mu\text{m}$ counterparts to the MAMBO sources. The hatched histogram shows the distribution of P_C for the most likely identifications. The solid line histogram shows the distribution found for randomly selected positions in the field. The bottom panel shows the distribution of MAMBO sources covered by the MIPS deep survey and the top panel shows the distribution of the rest of MAMBO sources, covered by the MIPS shallow survey.

2.4.3 IRAC and optical counterparts

To identify optical and near-IR counterparts to the radio and $24\ \mu\text{m}$ sources related with the MAMBO emission, we use the deep IRAC imaging data (Sanders et al., 2007) and the COSMOS source catalog (Capak et al., 2007) based on the Subaru, HST and K-band data.

For the radio-identified counterparts, we searched for $3.6\ \mu\text{m}$ sources lying within $1''$ from the radio peak position. For the $24\ \mu\text{m}$ -identified counterparts with no radio association, we searched for $3.6\ \mu\text{m}$ detections lying within a radius of $2.5''$ from the $24\ \mu\text{m}$ peak position. In all cases, this led to at most one IRAC counterpart per radio (or $24\ \mu\text{m}$) source.

To find optical counterparts, we looked for sources in the COSMOS catalog lying within $1''$ from the $3.6\ \mu\text{m}$ position. In cases with more than one optical counterpart, we chose the closer optical identification to the $3.6\ \mu\text{m}$ position. Conversely, in cases where there were no $3.6\ \mu\text{m}$ detections, we searched for optical counterparts to the radio or $24\ \mu\text{m}$ sources directly from the COSMOS point source catalog. Table 2.5 lists the optical/IR counterparts and the photometry for the radio and $24\ \mu\text{m}$ identifications.

Figure 2.10 shows IRAC $3.6\ \mu\text{m}$ cut-outs with radio and $24\ \mu\text{m}$ contours overlaid for all MAMBO sources. Many of the millimeter peak positions coincide with relatively strong emission at $24\ \mu\text{m}$. Even though, the radio and $24\ \mu\text{m}$ positions do not always match. We note that COSBO 1, 9, 14 and 15 do not show neither significant radio nor $24\ \mu\text{m}$ counterparts. Nonetheless, they all could be associated with faint IRAC emission. COSBO 1 and 9 have a single $3.6\ \mu\text{m}$ identification, each coincident with an optical source. COSBO 14 has a single $3.6\ \mu\text{m}$ counterpart, however does not show any optical association. COSBO 15 shows two $3.6\ \mu\text{m}$ counterparts, coincident with optical sources.

Table 2.3: X-ray XMM-Newton identifications.

ID	X-ID	R.A. (J2000)	Dec. (J2000)	Soft (10^{15} erg s $^{-1}$ cm $^{-2}$)	Hard	Hardness	X-radio ($''$)
11E	160	10 00 37.95	+02 08 22.5	2.39	10.2	-0.08	1.0
20	278	10 00 22.22	+02 06 04.3	1.46	undetected	-1	1.7
29	13	10 00 02.27	+02 16 31.3	21.1	29	-0.54	–

2.4.4 X-ray identification

We compared our catalog of MAMBO sources with the list of X-ray point sources from the COSMOS XMM-Newton observations (Brusa et al., 2007; Cappelluti et al., 2007). We find that two identified MAMBO galaxies, 11 and 20, coincide with X-ray detections (Table 2.3). A third association could be made for COSBO 29, however, the X-ray position lies at $8''$ from the MAMBO-VLA position, making the identification ambiguous.

2.4.5 Comparison with the Bolocam 1.1 mm detections

We used the Bolocam 1.1 mm map and source list (Aguirre et al., in preparation), to compare with our MAMBO survey.

Table 2.2 lists the detected MAMBO sources, and the Bolocam detections that lie within our MAMBO map. Fifteen of 35 Bolocam sources with $S/N > 3$ are covered by our MAMBO map. Four of the 8 most significant Bolocam sources ($> 3.5\sigma$) covered by the MAMBO survey coincide with one of the significant MAMBO sources. The other 4 significant Bolocam sources do not have a significant MAMBO counterpart, mainly because they lie at the edges of the MAMBO map where the noise increases strongly. For these, we list 3σ upper limits in the MAMBO map (Table 2.2). For the other 7 Bolocam sources ($S/N = 3.0 - 3.5$) covered by MAMBO, 4 coincide with MAMBO detections, and the rest are listed as upper limits. For the MAMBO sources with no significant Bolocam counterpart, we measured their flux density in the Bolocam map. For these 28 MAMBO sources, only 7 have Bolocam fluxes consistent with the MAMBO ones.

2.4.6 Comments on identifications

MAMBO sources with $S/N > 4$

These millimeter sources represent the most significant detections in our MAMBO survey. The following description of each identification is complemented with Fig. 2.10.

(1) *MMJ100016+021549*. This MAMBO source lies at $\sim 2''$ from a faint 3.5σ radio peak. The radio signal coincides with a faint optical counterpart near a brighter, irregular source. The latter shows IRAC emission in all bands, however, the $24 \mu\text{m}$ imaging of this area is not deep enough to associate this source with MIPS emission. Given the faintness of the radio emission, the IRAC source is the most likely counterpart, but we cannot exclude the possibility that the millimeter emission is related with a undetected high redshift galaxy.

(2) *MMJ100010+021338*. This MAMBO source is composed of two millimeter peaks separated by about $10''$. The weaker western component is clearly identified with a bright radio/ $24 \mu\text{m}$ source (COSBO-2W). The stronger eastern component (COSBO-2E) can either be associated with a radio peak that lies half a MAMBO beam west from the millimeter position and coincides with a faint optical source (COSBO-2E1), or with a faint $24 \mu\text{m}$ source that closely matches the MAMBO position (COSBO-2E2). The latter, however, has neither an IRAC nor an optical

counterpart. A third, rather unlikely, $24\ \mu\text{m}$ counterpart is found to the north of the MAMBO position, within the $10''$ search radius (COSBO-2E3).

(3) *MMJ100057+022013*. Two significant radio sources are found within $10''$ of the millimeter position. Given its proximity to the MAMBO peak, the radio source to the south-east (COSBO-3S) is the most likely counterpart. We note that the region surrounding this MAMBO source is crowded with IR sources (Chapter 4), and the emission at $24\ \mu\text{m}$ is faint and diffuse, making it difficult to associate the MAMBO emission with a significant MIPS source. Unlike the southern component, the radio source to the north-west (COSBO-3N) is related to faint $24\ \mu\text{m}$ emission. In this case, millimeter interferometry becomes crucial in order to decide which radio source, if not both, is the actual counterpart to the MAMBO emission.

(4) *MMJ100007+021149*. The VLA 1.4 GHz map does not show any significant radio signal ($> 3\sigma$) around the MAMBO position. However, the IR images show three possible $24\ \mu\text{m}$ counterparts, all of them lying at a similar distance from the MAMBO peak ($\sim 6.5'' - 7''$) and associated with optical counterparts. Based on the probability of chance association (P_C), the western $24\ \mu\text{m}$ source (COSBO-4W) is selected as the most likely counterpart. We note that it is possible that none of these MIPS sources is the real counterpart to the MAMBO source. This source has been followed-up with interferometric millimeter imaging to locate its position, as it could correspond to a high-redshift galaxy ($z > 3$; Chapter 5) due to its radio faintness.

(5) *MMJ100031+021241*. An isolated radio source that coincides with significant $24\ \mu\text{m}$ emission is seen $2''$ north of the MAMBO peak, representing a secure counterpart identification. The position of the identified radio/ $24\ \mu\text{m}$ source coincides with a faint optical source.

(6) *MMJ100008+021304*. This MAMBO source is divided into 2 peaks, as shown in Fig. 2.10. The stronger component can be associated with a significant radio source that coincides with strong MIPS $24\ \mu\text{m}$ and IRAC emission. A faint optical pair (blended in the Subaru optical image but separated in the ACS) lying $1''$ from the radio position is identified as the likely optical counterpart. This MAMBO source is embedded in a strong overdensity of blue and red galaxies at $z \sim 1.5$ (Chapter 4). Interferometric imaging was performed for this source in order to investigate other possible millimeter emitters in the neighborhood of this source (Chapter 5).

(7) *MMJ100024+021748*. An elongated radio source (deconvolved $3.1'' \times 0.5''$) is located at $\sim 2''$ from the MAMBO source. The radio signal coincides within $1''$ with a bright optical low redshift ($z = 0.3$) galaxy. However, a detailed view of the ACS image reveals a very faint optical point source at the edge of the bright optical galaxy that matches the radio position within $0.1''$. This suggests that the actual counterpart to the millimeter emission may be lensed by the low-redshift galaxy. Although MIPS $24\ \mu\text{m}$ and IRAC sources match the radio position, they are likely blended with the bright galaxy.

(8) *MMJ100000+020634*. A radio source at $1''$ from the MAMBO peak is identified as the likely counterpart. This radio peak is associated with emission at $24\ \mu\text{m}$ and $3.6\ \mu\text{m}$. The Subaru i^+ band image shows that the radio source coincides with a faint optical source that is blended with a bright elliptical galaxy $1''$ away. Due to the proximity of both, no reliable photometry was possible for the faint counterpart.

(9) *MMJ100026+021529*. This MAMBO source shows neither a radio nor a $24\ \mu\text{m}$ counterpart. This could imply that it is either a very high redshift galaxy or a spurious MAMBO source identification. Only a few sources are seen in the area around the millimeter source. A faint IRAC/optical source is the best guess counterpart to this MAMBO source. Interferometric millimeter imaging of this source has been performed as it is possible that it lies at high redshift (Chapter 5).

(10) *MMJ095956+021141*. The MAMBO emission is diffuse and two radio counterparts can be associated with the millimeter central peak. Both radio sources have low P_C values, being plausible counterparts. The western and fainter radio source (COSBO-10W) lies at the edge of an irregular low-redshift galaxy, as revealed by the optical image, while the eastern radio source (COSBO-10E) is matched by a significant $24\ \mu\text{m}$ source and by a very faint optical source with

color consistent with a starburst galaxy at high-redshift. We conclude that the eastern source is the most reliable counterpart.

(11) *MMJ100038+020825*. Significant radio and 24 μm sources can be associated to the millimeter emission. The radio source is centered in a relatively bright optical source (COSBO-11E), however it extends to the location of a fainter companion to the west (COSBO-11W) which also appears to have radio emission. The 24 μm peak is centered in the bright optical source (COSBO-11E), however, the poor resolution of MIPS does not allow to separate the emission from the western fainter source. The bright component is related to X-ray emission and likely hosts a faint QSO with $L_X \sim 10^{44} \text{ erg s}^{-1}$.

(12) *MMJ100059+021716*. Four possible counterparts are identified close to the MAMBO peak. A faint central radio source ($< 3\sigma$) previously identified by Bertoldi et al. (2007), neither shows an optical nor an IR counterpart. Therefore, we do not consider it as a real or even plausible counterpart. South-west of the MAMBO position, a weak radio peak with no signs of IR emission is found (COSBO-12S2). To the south-east, a faint radio source that coincides with faint 24 μm emission can be seen (COSBO-12S1). To the north of the MAMBO peak, a comparatively strong radio/24 μm source is found (COSBO-12N), with optical colors consistent with a starburst galaxy. This represents the most likely counterpart to the millimeter emission according to its assigned P_C value.

(13) *MMJ100015+021244*. This MAMBO source appears fragmented into two components. For the northern millimeter peak (COSBO-13N), no radio or 24 μm counterpart is found. For the southern peak (COSBO-13S), there are two possible counterparts. The first candidate is a bright radio source 0.7'' apart from the MAMBO position (COSBO-13S1), that coincides with a faint multiple optical/near-IR source. The second candidate is a strong 24 μm source that lies $\sim 3''$ north-east (COSBO-13S2) from the MAMBO source. It is possible that the galaxy responsible for the strong radio output (COSBO-13S1) also contributes to the 24 μm emission, however, the northern MIPS 24 μm source (COSBO-13S2) is much brighter at this wavelength and outshines it.

(14) *MMJ100047+021018*. No significant radio or 24 μm source is found in the region around this MAMBO source, although only shallow MIPS coverage is available in this part of the sky. The best guess for a counterpart candidate relies in a faint 3.6 μm source with no optical counterpart. This source is also detected with Bolocam representing a good candidate for a high redshift SMG.

(15) *MMJ100057+021305*. The MAMBO emission is elongated with two components. Neither component show significant radio or 24 μm counterpart. However, two IRAC counterparts (both with optical matches) are found within 10'' of the central MAMBO position. It is not clear whether these potential candidates are related to the millimeter emission.

MAMBO sources with $S/N = 3.5 - 4.0$ with radio association

The following lower significance MAMBO sources were selected based on the presence of a radio source within 5'' from the millimeter position. Since the match of a millimeter and a radio source likely indicates a real association, it allows the study of fainter galaxies that would be overlooked otherwise.

(16) *MMJ100056+020841*. A significant radio source 4'' apart is likely associated with the elongated MAMBO emission. The radio source matches the position of an elongated and faint optical counterpart with a likely photometric redshift of ~ 0.5 (Chapter 3), and another possible (less likely) photometric redshift of $\sim 2 - 3$. Although this lower significance MAMBO source was selected based on the existence of a radio detection, we note that a second plausible counterpart corresponds to a faint 24 μm source north-east from the MAMBO peak with photometric redshift $z \sim 1.3$. As we shall see in Chapter 4, this MAMBO source coincides with a group of galaxies at $z \sim 1.3$, hinting at a physical relation of the MAMBO source with the MIPS counterpart.

(19) *MMJ100002+021445*. A faint radio peak, coincident with a strong MIPS 24 μm /IRAC

source is identified as the counterpart to the millimeter emission. Another $24\ \mu\text{m}$ source is found farther away to the south, however it does not coincide with a radio emission peak.

(20) *MMJ100022+020605*. A significant radio source located at $1''$ from the millimeter position is recognized as the likely counterpart. The radio source coincides with a MIPS $24\ \mu\text{m}$ /IRAC source and the associated optical source is identified as a moderately luminous AGN, based on the X-ray detection (Table 2.3).

(24) *MMJ100100+021811*. This MAMBO source appears associated with a significant radio emission peak $3''$ north of the millimeter peak. Although no $24\ \mu\text{m}$ source is detected (likely due to the shallow coverage of this region), a $3.6\ \mu\text{m}$ match is identified. An extended and red optical/near-IR object is associated with the radio source, showing a bright unresolved nucleus at about $\sim 0.5''$ from the radio center.

(25) *MMJ095951+021720*. A faint radio source is identified as the likely counterpart to the millimeter source. While significant IRAC and $24\ \mu\text{m}$ emission are related to the radio source, no optical counterpart was found. This indicates that this source is strongly obscured at optical wavelengths.

(27) *MMJ100109+020346*. The MAMBO source is fragmented with two main components, probably due to noise. A significant radio source is found close to the central position, and coincides with an IRAC and a faint $24\ \mu\text{m}$ source. The radio source matches a faint multi-component optical source (as seen in the deep Subaru image) which is identified in the COSMOS catalog as two separate sources. The shallower ACS image shows only the brighter eastern component as a faint point source.

(29) *MMJ100002+021628*. Several radio and IR sources are grouped around the diffuse MAMBO emission. Three significant radio sources are found within $10''$ of the millimeter position. It is not clear which one is the real counterpart to the millimeter source. The closer radio source is located south-west of the MAMBO peak and is associated with an elongated optical source at $z \sim 0.5$. An IR bright interacting system, identified with a bright X-ray source, is seen north-east of the MAMBO center. However, it does not show evidence of radio emission. Given the redshift of this nearby galaxy group ($z \sim 0.5$), it is possible that the actual MAMBO galaxy is a lensed distant galaxy (Chapter 4).

(30) *MMJ100034+020304*. Two radio sources are found within $10''$ of the MAMBO peak. The closer and more significant radio source coincides with MIPS $24\ \mu\text{m}$ and IRAC emission, and with the south-western component of a double optical source.

(33) *MMJ100012+020125*. A faint radio source can be identified with this low S/N MAMBO source. The radio source lies at the edge of a bright elliptical galaxy. As revealed by the ACS images, the radio emission coincides with a faint optical point source which blends with a brighter galaxy in the Subaru and IR images. No reliable multi-band photometry is available for this source.

(35) *MMJ100048+020125*. A single radio source that coincides with a $3.6\ \mu\text{m}$ source is identified as the counterpart to the MAMBO signal. No $24\ \mu\text{m}$ emission was found for this source possibly due to the shallow coverage. The optical counterpart is faint and extended on $1''$ scale.

MAMBO sources associated with $> 4\sigma$ Bolocam sources

The following MAMBO sources were selected based on their coincidence with significant Bolocam sources. Since they are low significance MAMBO sources, they would not have been selected otherwise.

(36) *MMJ095953+021851*. This significant Bolocam source is associated with a fragmented MAMBO peak. The stronger western component (COSBO-36W) shows no signs of a significant radio or IR counterpart. The fainter eastern component (COSBO-36E), however, lies $3''$ apart from a significant radio peak. A faint optical counterpart is identified with this radio source,

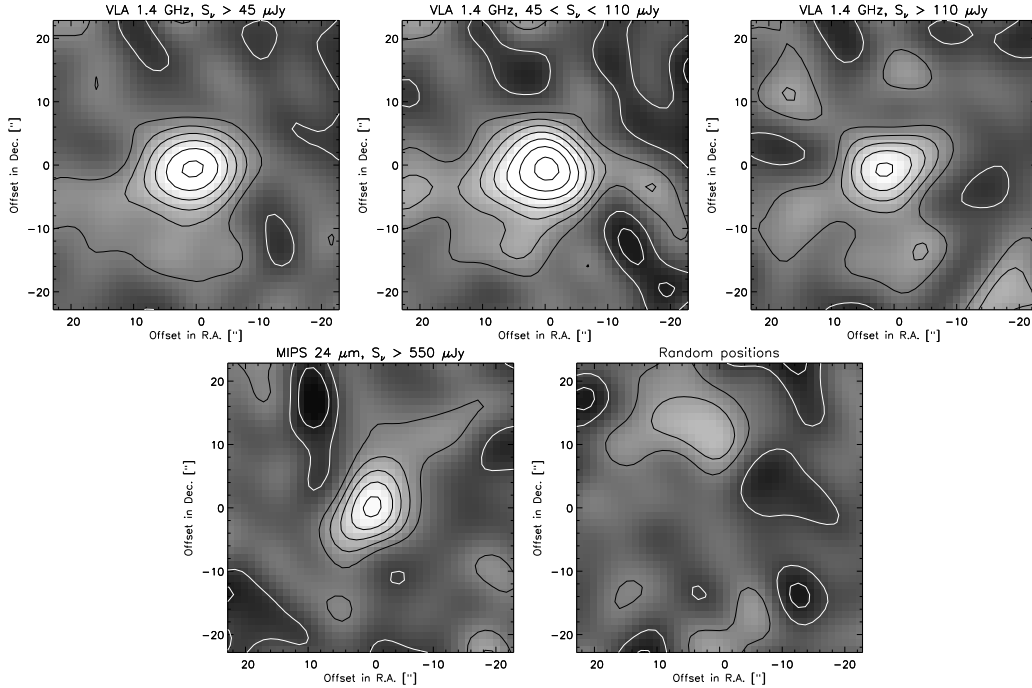


Figure 2.9: Stacked MAMBO images centered at the position of radio and $24\ \mu\text{m}$ sources, and random positions in the field. On top, from left to right, the average of the stacked images of all radio sources within the MAMBO coverage region, those in the flux range $45\ \mu\text{Jy} < S_{1.4\text{GHz}} < 110\ \mu\text{Jy}$ and those with fluxes $S_{1.4\text{GHz}} > 110\ \mu\text{Jy}$ are shown. On the bottom, the stacked image produced by centering each subimage on the position of a MIPS $24\ \mu\text{m}$ source with $S_{24\mu\text{m}} > 550\ \mu\text{Jy}$ is shown (left), and the stacked image of 1000 random positions in the field is shown for comparison (right). As expected, no signal is present in the latter.

however, no multi-band photometry is possible due to its proximity to a bright nearby galaxy. The strong IR emission at the radio source position is likely due to the bright galaxy.

(37) *MMJ100057+020228*. The $> 4\sigma$ Bolocam source is again associated with a two component MAMBO source. No radio or IR source is seen close to the northern millimeter peak. However, a strong radio source which also shows $24\ \mu\text{m}$, IRAC and optical emission, is identified with the southern MAMBO peak.

2.5 Stacking analysis

The (sub-)millimeter emission from the galaxies comprising the bulk of the submillimeter background as measured by FIRAS (Puget et al., 1996) cannot be detected at the sensitivity limits reached by current surveys. This emission is hidden below the noise and therefore cannot be disentangled for individual sources. However, it is possible to estimate the average (sub-)millimeter emission from these galaxies, or their average contribution to the (sub-)millimeter background, by means of a stacking analysis.

For a given class of object (e.g. faint radio or $24\ \mu\text{m}$ sources, X-ray selected, Lyman Break galaxies), the strategy is to coadd (variance weighted) the signal maps centered on the positions of sources confirmed at other wavelengths. Let S_i be the signal map around a given source, and

N_i the corresponding noise rms map, then the stacked image is

$$S_{\text{stack}} = \frac{\sum_i S_i/N_i^2}{\sum_i 1/N_i^2} \quad (2.3)$$

Thereby, the depth is increased, and the average signal of these objects can be computed.

Due to the strong correlation between radio and far-IR emission in star forming galaxies (Condon, 1992), it is likely that (sub-)millimeter galaxies just below the detection threshold are associated with faint radio sources.

Figure 2.9 shows the result of stacking MAMBO map postage stamps, $\sim 42'' \times 42''$ size, centered on 313 radio source positions that lie within the MAMBO map boundary. In order to provide an estimate of the contribution of radio sources to the faint MAMBO emission, we excluded radio sources that lie within $10''$ from $S/N > 4$ millimeter peaks or $S/N < -4$. We find that radio sources with $S_\nu > 45 \mu\text{Jy}$ have an average millimeter flux of $401 \pm 64 \mu\text{Jy}$. If we split the radio source catalog, we find that radio sources with $45 \mu\text{Jy} < S_\nu < 110 \mu\text{Jy}$ (163 out of 313 sources) are detected with $473 \pm 94 \mu\text{Jy}$, while radio sources with $S_\nu > 110 \mu\text{Jy}$ (150 out of 313) contribute with $335 \pm 71 \mu\text{Jy}$.

Additionally, we stacked equally sized ($\sim 42'' \times 42''$) MAMBO map postage stamps centered on $24 \mu\text{m}$ sources taken from the MIPS-shallow survey. We restricted the MIPS sources to flux densities $> 550 \mu\text{Jy}$ ($S/N > 5$) and, as in the case of radio sources, excluded those sources in the vicinities of $S/N > 4$ or $S/N < -4$ MAMBO sources. We find that $24 \mu\text{m}$ sources have an average 1.2 mm flux of $384 \pm 71 \mu\text{Jy}$, being similar to the average flux density of radio sources.

This kind of analysis can be further used to give an estimate of the residual systematics and rms pointing errors in the MAMBO map. From the radio source stacked image we obtain that the peak signal is systematically shifted by $+1.1''$ in R. A. and at $-1.2''$ in Decl., which is well within the $3''$ typical pointing error of the IRAM 30 m telescope at 1.2 mm .

The contribution of the radio sources to the MAMBO flux density is somewhat lower than that to the AzTEC map at the same 1.4 GHz limiting flux level ($S_\nu > 45 \mu\text{Jy}$; Scott et al., 2008). Radio sources have an average AzTEC 1.1 mm flux density of $487 \pm 60 \mu\text{Jy}$, being $\sim 100 \mu\text{Jy}$ higher than for MAMBO. This difference is mostly explained by the slightly different frequencies of both MAMBO and AzTEC surveys. Due to the negative slope of the SED at submillimeter wavelengths, the flux measured at 1.1 mm is about $20\% - 30\%$ higher than the flux at 1.2 mm , regardless the redshift and the far-IR emission model chosen (see Chapter 5). Scaling down the AzTEC 1.1 mm flux to 1.2 mm , we get $405 \pm 50 \mu\text{Jy}$, comparable to the MAMBO flux.

The stacked AzTEC 1.1 mm signal for $24 \mu\text{m}$ sources is $324 \pm 24 \mu\text{Jy}$ using the MIPS deep survey of COSMOS ($S_\nu > 60 \mu\text{Jy}$). By scaling the AzTEC flux to 1.2 mm , we obtain that the MAMBO flux is about 1.4 times higher than the implied by AzTEC, $270 \pm 20 \mu\text{Jy}$. This indicates that fainter $24 \mu\text{m}$ sources ($60 \mu\text{m} < S_\nu < 550 \mu\text{m}$) contribute much less to the millimeter background than brighter $24 \mu\text{m}$ sources ($S_\nu > 550 \mu\text{Jy}$).

Finally, we estimate the contribution to the cosmic IR background radiation by the resolved sources in the MAMBO survey. The background intensity at 1.2 mm is $\approx 20.3 \text{ Jy deg}^{-2}$ as revealed by the FIRAS instrument in the COBE satellite (Fixsen et al., 1998). By summing up the fluxes of the fifteen $S/N > 4$ MAMBO sources, we find that their integrated flux is 0.65 Jy deg^{-2} , while including all MAMBO sources gives 1.00 Jy deg^{-2} , representing $\sim 4.9\%$ of the total extragalactic background at this wavelength. The integrated 1.2 mm flux for radio sources is $1.02 \pm 0.16 \text{ Jy deg}^{-2}$ and for $24 \mu\text{m}$ sources, $0.49 \pm 0.09 \text{ Jy deg}^{-2}$, accounting for 5.0% and 2.4% of the cosmic IR background, respectively. In total, we resolve $\sim 12.3\%$ of the total extragalactic millimeter background radiation. This result is consistent with the $18 - 24\%$ found by Scott et al. (2008) in the AzTEC map of COSMOS given the different frequency, or the $13 - 19\%$ found by Wang et al. (2006) in the SCUBA map of the GOODS-N field.

Continued.

ID ^a	MAMBO position		VLA 1.4 GHz position		Offset	P_c	$S_{1.4\text{GHz}}$	MIPS 24 μm position		Offset	P_c	$S_{24\mu\text{m}}$
	RA (J2000)	DEC (J2000)	RA (J2000)	DEC (J2000)				RA (J2000)	DEC (J2000)			
37	10 00 57.3	+02 03 28	10 00 57.21	+02 03 22.4	5.8	0.0230	121 \pm 7.5	10 00 57.30	+02 03 22.7	5.26	0.026	328 \pm 111

^a Boldfaced IDs represent the most likely counterparts to the MAMBO sources.

Table 2.5: IRAC and optical counterparts to the MAMBO sources.

ID	IRAC 3.6 μm position		AB magnitudes											
	RA (2000)	DEC (2000)	u^*	B	V	g^+	r^+	i^+	z^+	K_S^a	[3.6]	[4.5]	[5.8]	[8.0]
1.....	10 00 15.48	+02 15 50.72	25.01	24.53	24.57	24.83	24.33	23.89	23.27	21.67	20.68	20.51	20.89	20.74
2W.....	10 00 09.68	+02 13 34.16	24.93	24.25	23.68	24.31	23.30	22.40	21.76	20.29	19.78	20.08	20.18	20.68
2E1.....	10 00 10.15	+02 13 34.93	99	99	28.24	99	99	26.70	27.20	22.95	22.20	21.68	21.66	21.03
2E3.....	10 00 10.27	+02 13 46.11	24.23	23.53	23.15	23.60	22.62	22.07	21.76	20.84	20.74	21.14	21.00	21.09
3S ^b	10 00 57.26	+02 20 12.62	28.74	27.20	99	27.09	26.62	26.21	25.48	21.85	99	99	99	99
3N.....	10 00 57.01	+02 20 17.65	26.39	25.68	26.22	25.86	25.47	24.64	23.99	21.73	20.56	20.23	20.16	19.98
4W.....	10 00 07.45	+02 11 51.97	27.00	26.05	25.53	26.15	25.26	24.79	24.07	21.36	20.75	20.64	20.31	20.70
4E.....	10 00 08.18	+02 11 53.65	28.56	27.91	27.91	28.82	27.05	25.98	25.90	22.99	21.96	21.61	21.39	21.79
4S.....	10 00 08.10	+02 11 42.26	26.89	25.81	25.10	26.03	24.58	23.45	22.69	20.90	20.56	20.98	21.46	21.40
5.....	10 00 31.84	+02 12 42.89	26.79	26.14	25.47	26.56	25.55	25.02	24.43	21.95	20.32	19.91	19.39	19.22
6.....	10 00 08.81	+02 13 04.38	26.62	26.07	25.76	26.37	25.44	24.74	23.92	21.06	19.88	19.55	19.45	19.85
10E.....	09 59 57.10	+02 11 36.40	99	28.76	27.97	28.70	26.82	25.92	25.32	99	20.49	20.15	19.82	19.92
10W.....	09 59 56.87	+02 11 37.46	25.47	24.42	23.47	24.27	22.67	21.71	21.17	19.64	19.23	19.60	19.46	20.01
11E.....	10 00 38.01	+02 08 22.43	21.19	20.77	20.67	20.94	20.73	-99	20.33	19.81	18.76	18.32	17.90	17.56
11W ^b	10 00 37.89	+02 08 22.00	24.02	23.47	23.35	23.68	23.38	-99	22.70	21.61	-99	-99	-99	-99
12N.....	10 00 59.26	+02 17 19.07	25.41	24.96	24.91	25.11	24.79	24.18	23.65	21.12	19.96	19.68	19.57	19.69
12S1.....	10 00 59.26	+02 17 10.72	27.53	26.67	25.55	26.72	25.17	24.93	24.81	99	22.29	22.11	21.97	21.24
12S2.....	10 00 59.68	+02 17 08.82	26.03	25.37	24.51	25.37	23.95	22.70	22.03	20.09	19.41	19.72	19.96	20.39
13S1.....	10 00 15.28	+02 12 40.23	25.97	25.46	25.49	25.69	25.11	24.58	24.03	21.74	20.53	20.34	20.08	20.07
13S2.....	10 00 15.47	+02 12 43.40	24.51	24.11	23.86	24.23	23.66	22.97	22.45	21.01	19.67	19.43	19.18	19.23
16 ^b	10 00 56.31	+02 08 39.33	27.21	26.40	26.00	26.43	25.09	24.55	24.10	22.52	99	99	99	99
19.....	10 00 12.58	+02 14 44.07	26.51	25.54	25.14	25.79	24.82	24.53	23.86	21.56	20.07	19.85	19.69	19.99
20.....	10 00 22.33	+02 06 05.08	28.43	27.20	26.59	26.88	26.31	25.78	25.45	22.19	20.62	19.97	19.17	18.58
24.....	10 01 00.27	+02 18 13.15	26.86	25.85	25.77	26.09	25.48	25.43	25.51	22.86	21.67	21.27	21.17	20.54
25 ^c	09 59 51.11	+02 17 15.03	99	99	99	99	99	99	99	99	21.68	21.25	20.66	21.24
27.....	10 01 09.83	+02 03 45.90	28.79	27.24	26.83	27.25	26.38	25.79	25.45	99	21.44	20.98	20.36	20.93
29.....	10 00 01.80	+02 16 27.44	25.02	24.09	23.26	24.07	22.62	21.94	21.40	19.76	19.71	19.77	19.86	18.99
30.....	10 00 34.29	+02 03 02.31	99	26.62	25.91	26.51	25.45	25.15	24.65	22.26	20.14	19.86	19.59	19.41
35.....	10 00 48.90	+02 01 25.65	99	28.62	27.91	28.81	99	27.40	26.93	99	22.00	21.40	20.80	20.70
37.....	10 00 57.23	+02 03 22.78	24.40	23.85	23.87	24.07	23.55	22.98	22.24	20.85	19.96	19.91	20.03	19.67

^a K_S magnitudes are from the shallow coverage with CTIO and KPNO.^b Either no IRAC counterparts were detected (magnitude flag: 99) or blended with a brighter source (magnitude flag: -99), and the quoted positions correspond to the optical counterparts from the COSMOS catalog.^c No optical counterpart found.

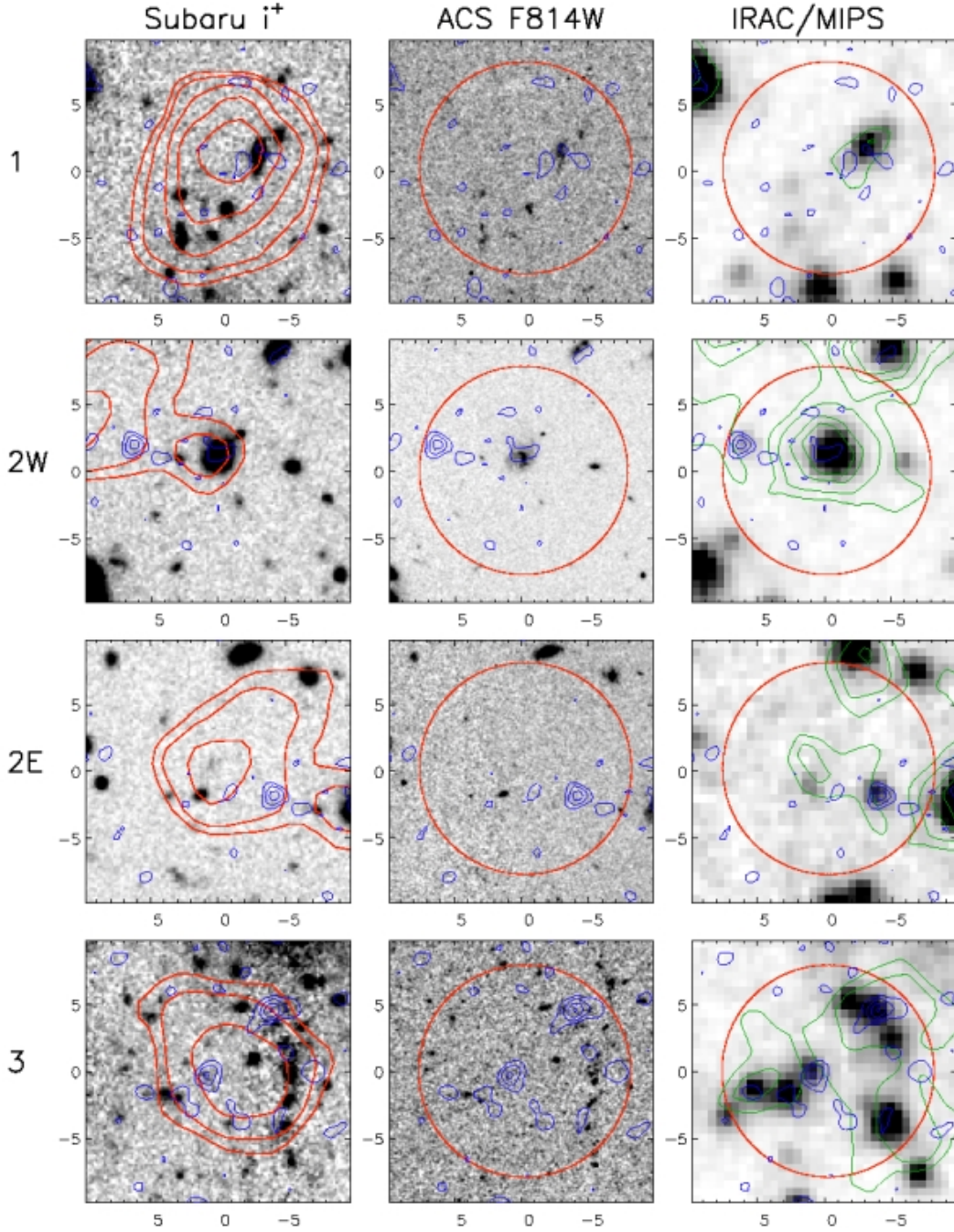
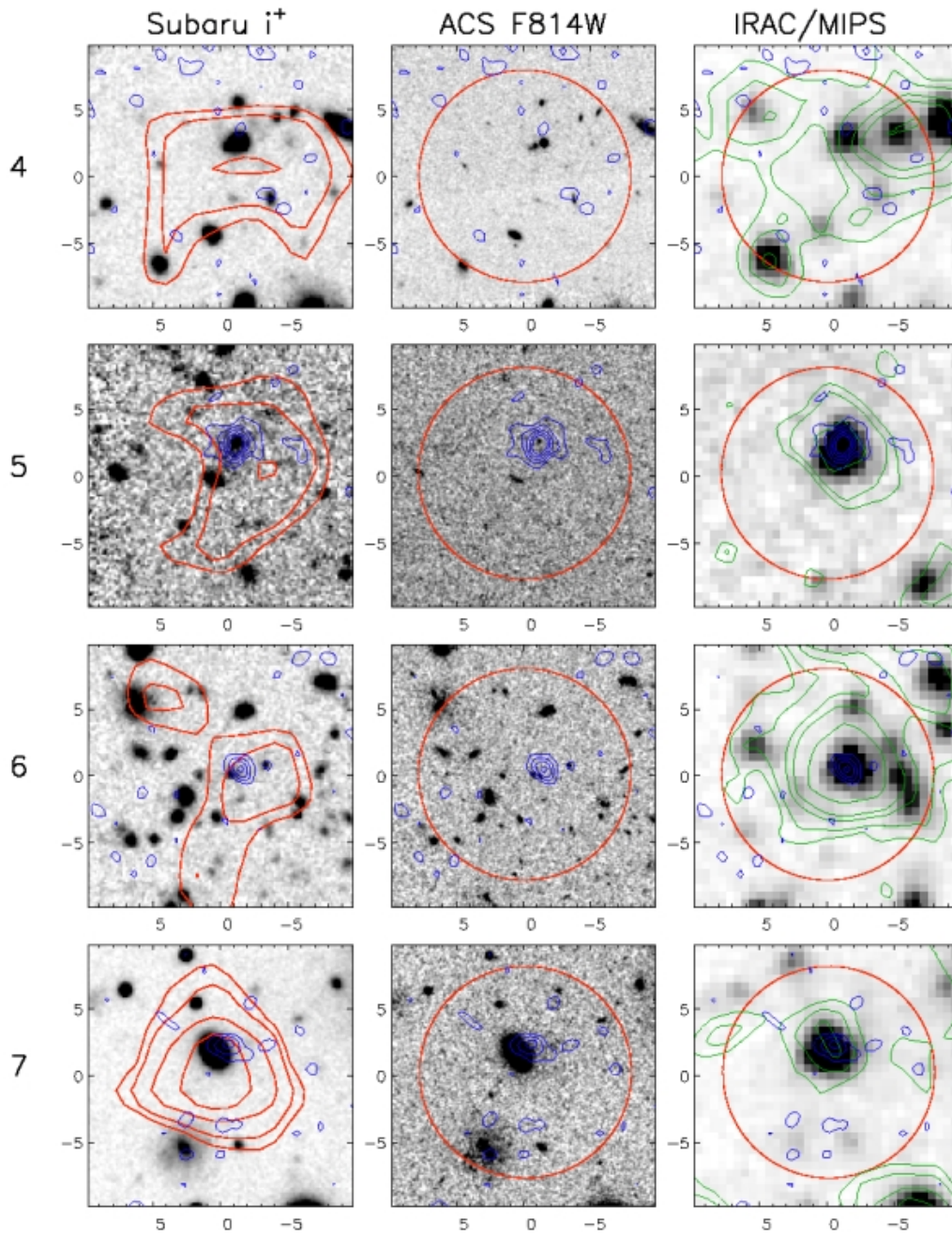
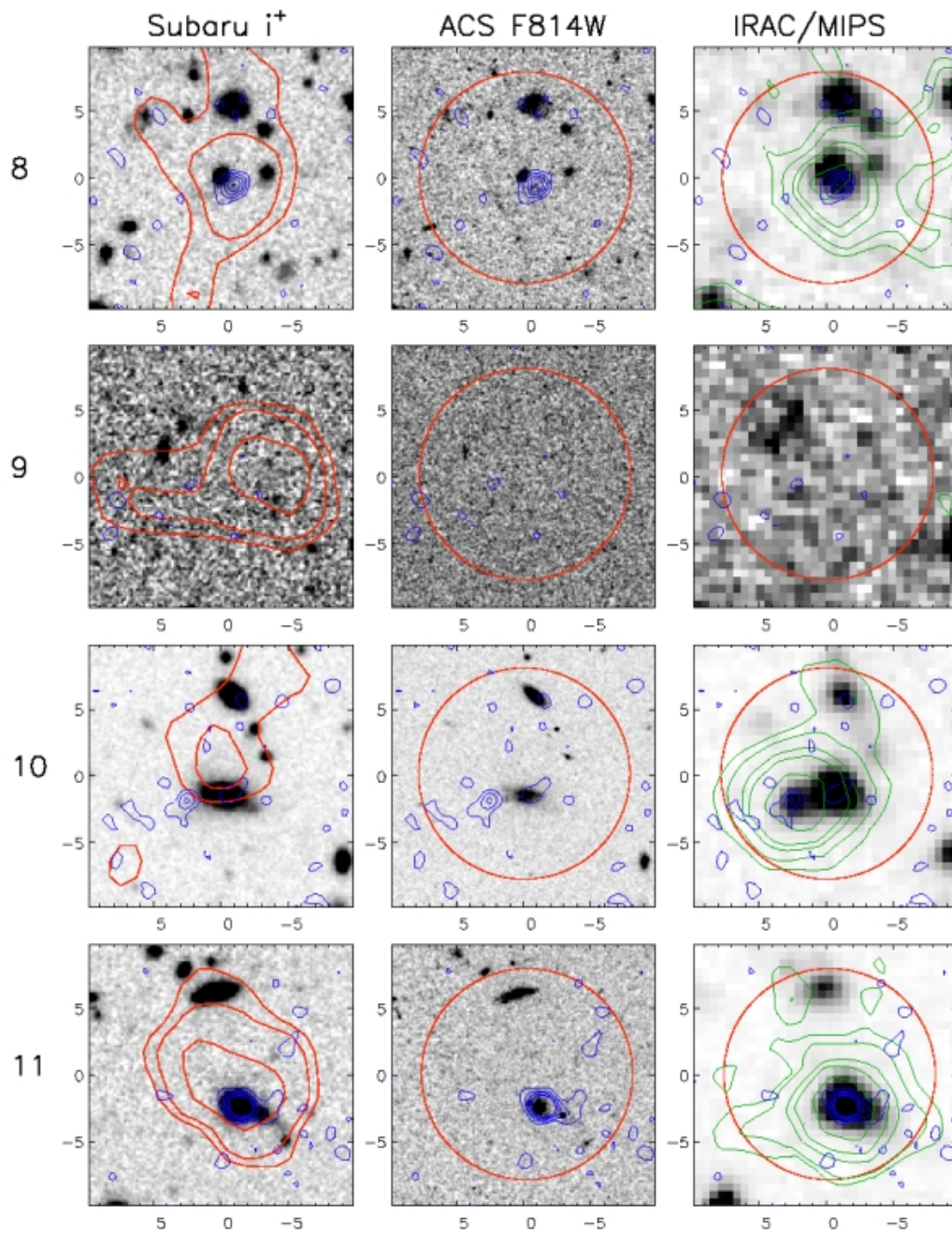
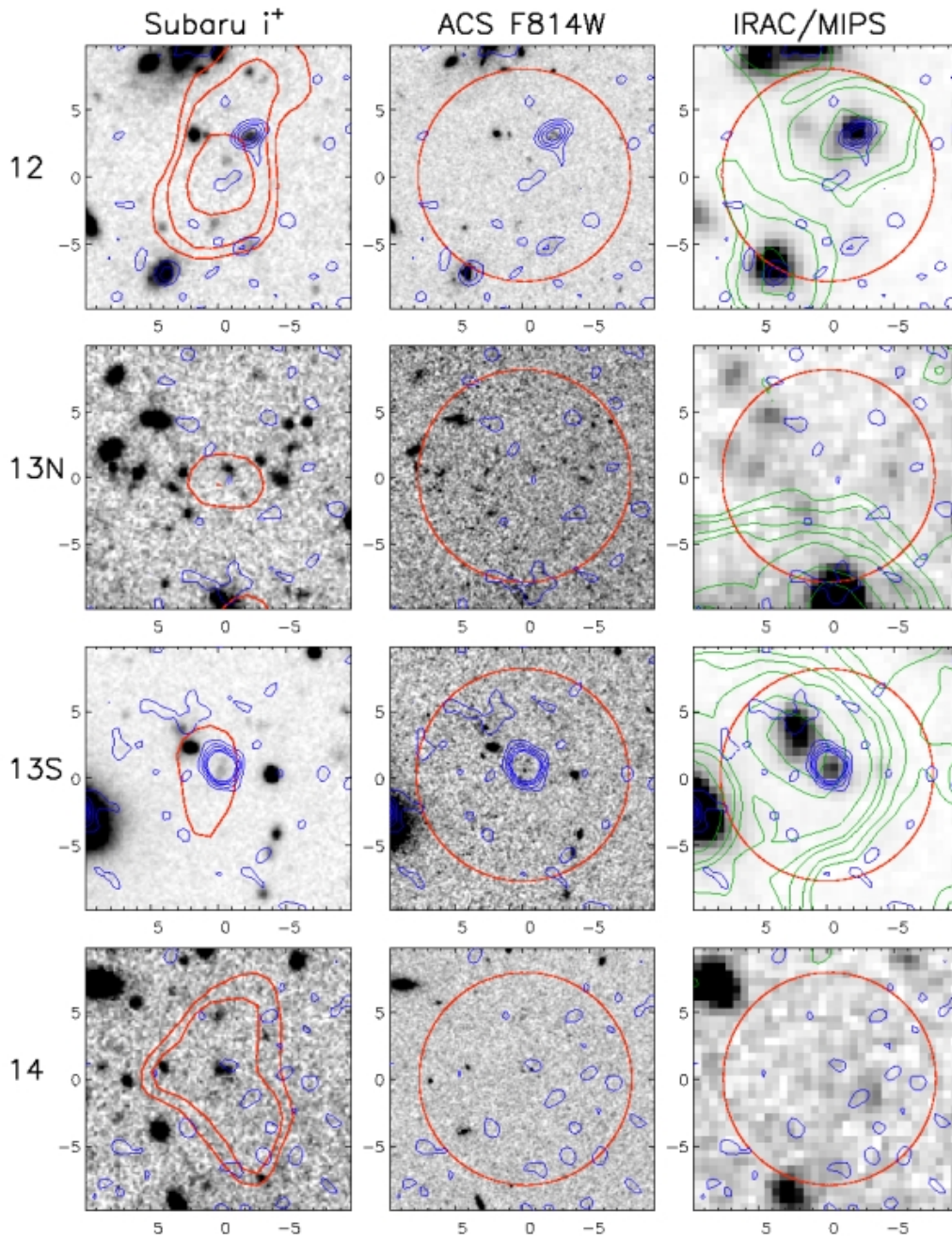
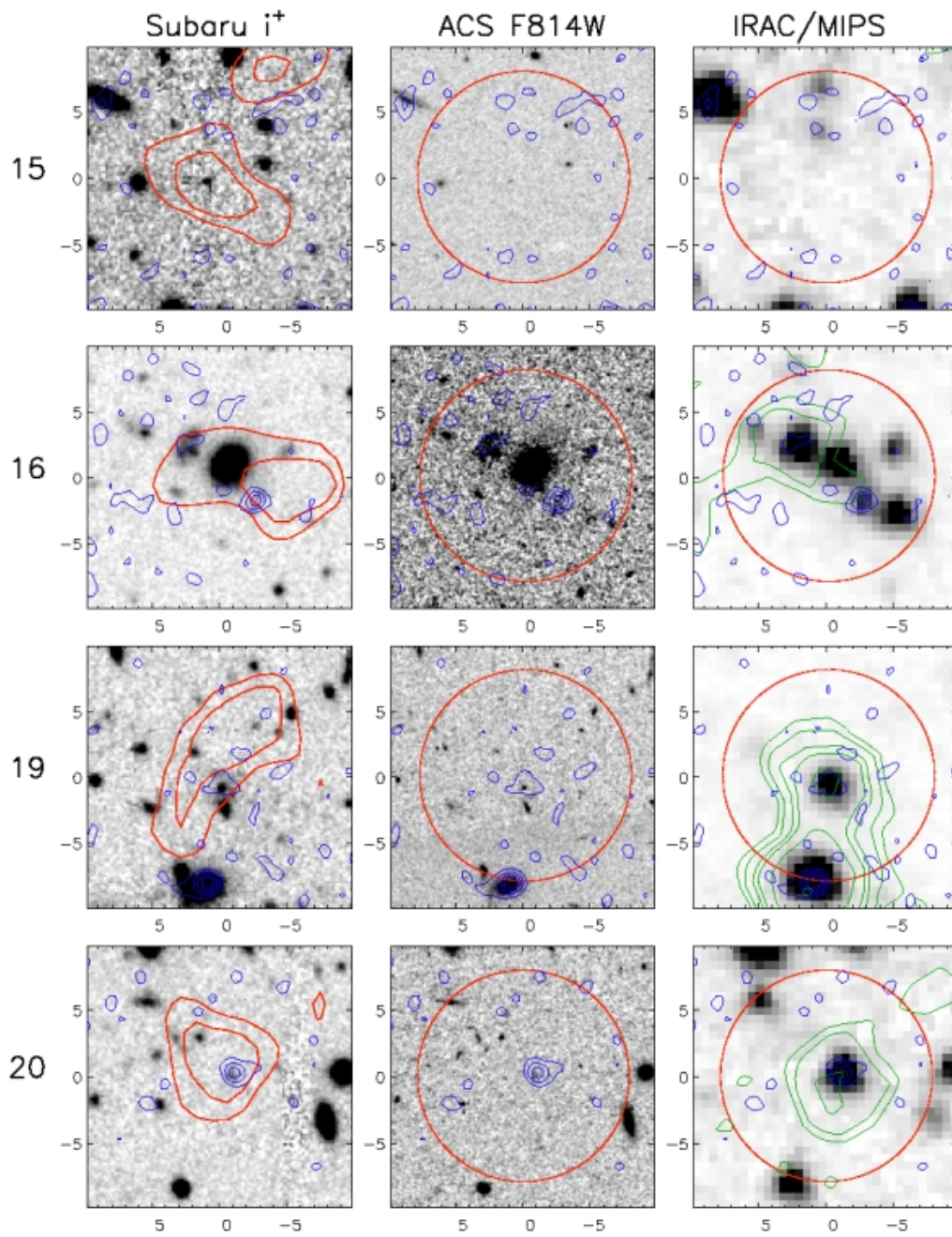


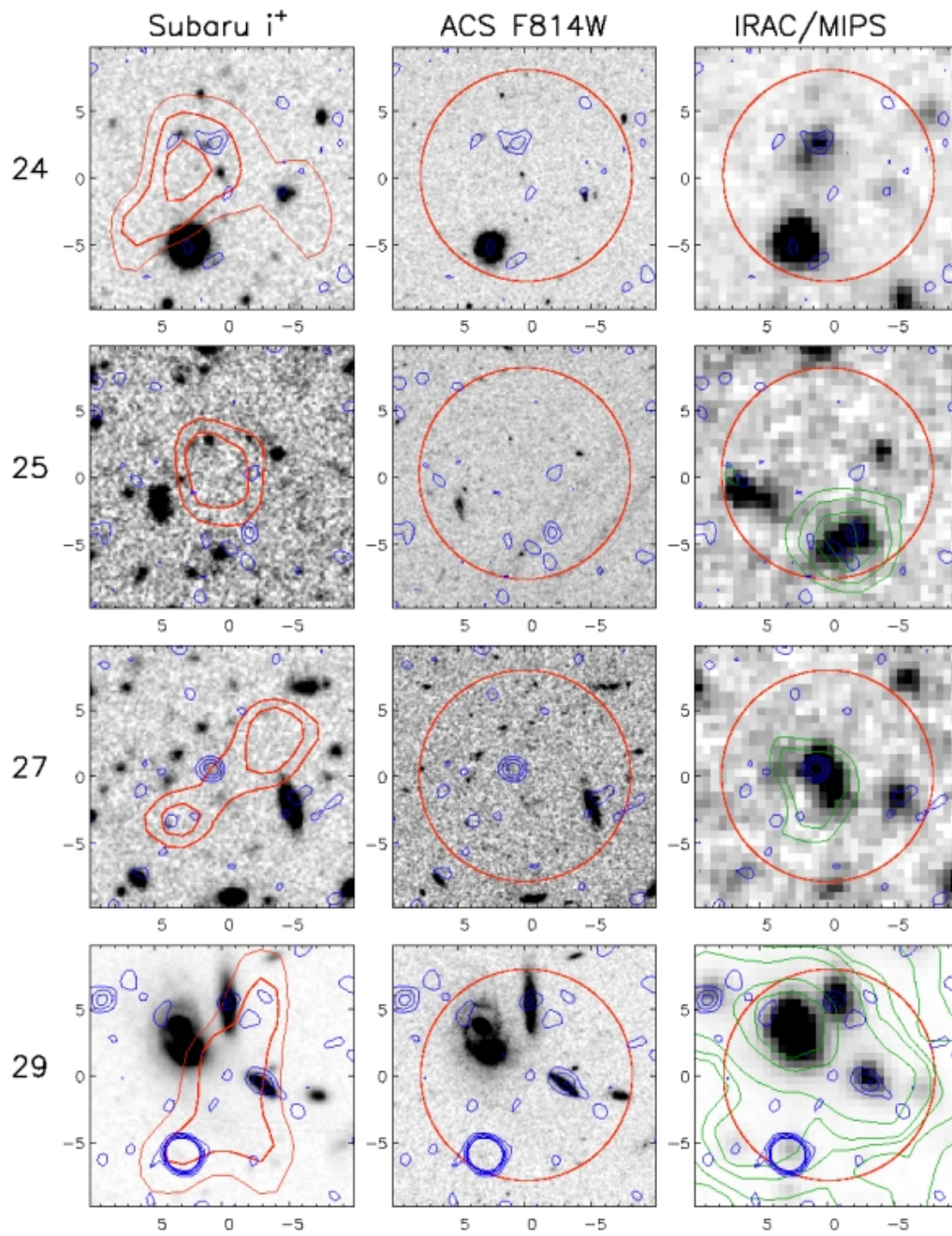
Figure 2.10: Optical and IR postage stamp images ($10'' \times 10''$) centered on the MAMBO source centroid position and labeled with their MAMBO ID. The background images are for the Subaru i^+ band ($0.8 \mu\text{m}$), ACS F814W band ($0.8 \mu\text{m}$) and IRAC $3.6 \mu\text{m}$ band. The red (thick) contours represent the MAMBO S/N levels of 2.5, 3.5, 4.5 and 5.5. For COSBO 24, 29, 35, 36 and 37 the MAMBO S/N level 1.5 is shown as a thinner contour. The MAMBO positions are represented by a $8''$ red circle in the central and right images, for clarity. Blue contours represent the VLA 1.4 GHz flux at levels of 15, 30, 45, 60 and $75 \mu\text{Jy}$. Green contours are the MIPS $24 \mu\text{m}$ emission at 14, 21, 42, 56 and 85 mJy for those MAMBO sources covered by the MIPS shallow survey, whereas for sources covered by the MIPS deep survey the contours are 4, 7, 11, 14, 21, 42 and 85 mJy .

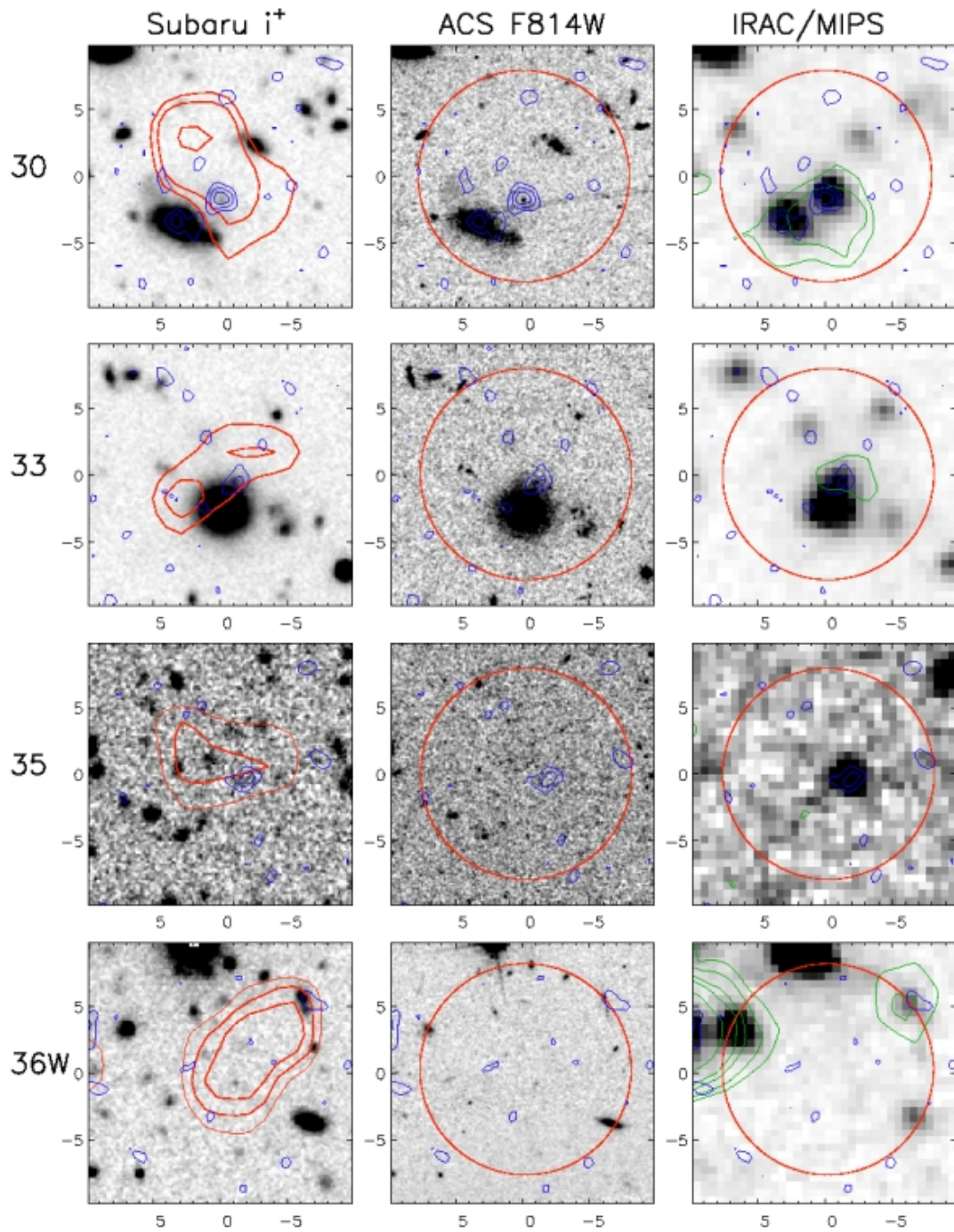
Figure 2.10: *Continued.*

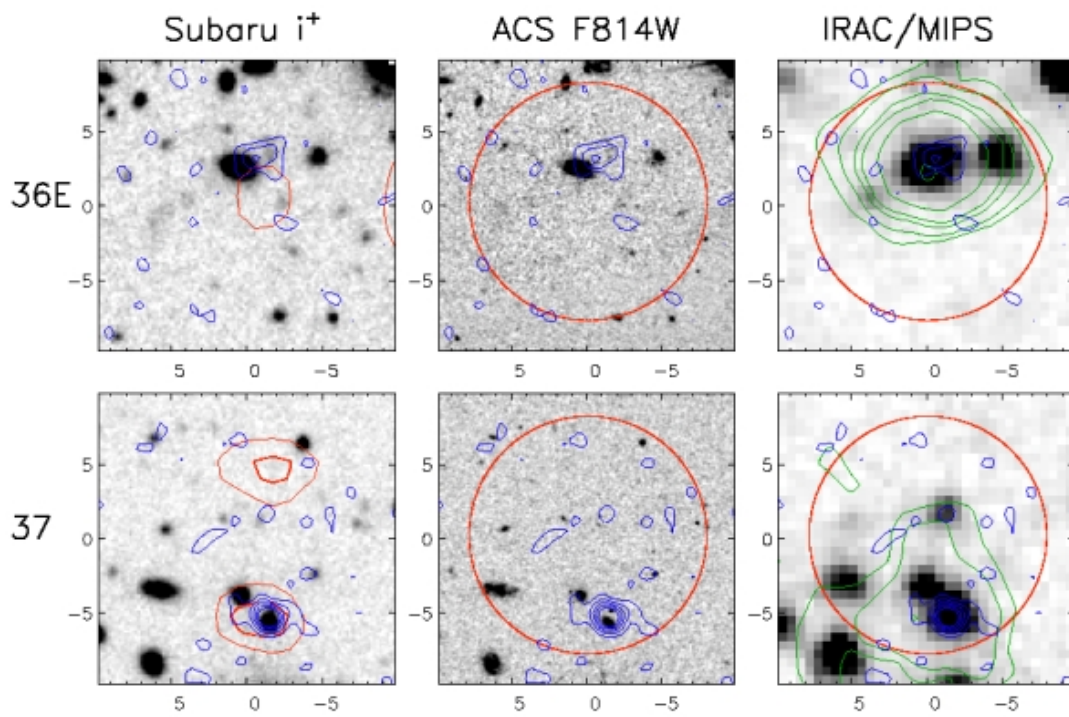
Figure 2.10: *Continued.*

Figure 2.10: *Continued.*

Figure 2.10: *Continued.*

Figure 2.10: *Continued.*

Figure 2.10: *Continued.*

Figure 2.10: *Continued.*

Properties of MAMBO galaxies

3.1 Introduction

The SEDs of galaxies have features that allow to decipher the galaxy's activity, properties and history. Such attributes are used in the study of high-redshift galaxies in order to measure the cosmic star formation history of the universe, the growth of cosmic stellar mass density and its relation to the growth of supermassive black holes.

Since it is not yet possible to carry out unbiased deep spectroscopic surveys over large areas of the sky, efforts have so far focused on the study of objects selected in specific spectral bands. For instance, X-ray and radio observations are used to select powerful AGN. Radio and (sub)millimeter observations are used to detect extreme starburst galaxies at high redshifts.

Different galaxy types can be selected through their colors in either color-color or color-magnitude diagrams. This selection technique has been used to select massive high redshift star forming galaxies, e.g., by detecting the Lyman break at $z > 3$ (LBGs; Steidel et al., 1996, 2003) or the Balmer break at $1 < z < 3$ (e.g., Thompson et al., 1999; Daddi et al., 2000, 2004; Franx et al., 2003; van Dokkum et al., 2003). These color selection criteria have further been exploited in the IR to reliably identify obscured AGN. Color selection has been very effective to disentangle a population of obscured AGN that is not easily detected in the X-rays or optical wavelengths (e.g., Lacy et al., 2004; Hatziminaoglou et al., 2005; Stern et al., 2005; Hickox et al., 2007; Wilson et al., 2007).

The compilation of complete multi-wavelength SEDs (from X-rays to the far-IR) has permitted the computation of reliable photometric redshift and stellar mass estimates that, in turn, allow the study of the growth and evolution of galaxies (Cimatti et al., 2002; Dickinson et al., 2003; Glazebrook et al., 2004; Fontana et al., 2006; Daddi et al., 2007; Grazian et al., 2007; Pérez-González et al., 2008).

Detailed studies of the stellar mass density as a function of galaxy mass and redshift suggest that a differential evolution of low mass ($< 10^{11} M_{\odot}$) and high mass ($> 10^{11} M_{\odot}$) galaxies took place. While massive galaxies appear to have evolved more rapidly and grown at high redshifts ($z > 1.5$), less massive galaxies are found to dominate the average stellar content at later epochs ($z < 1.5$). This effect has become known as galaxy downsizing (Cowie et al., 1996).

Our understanding of the properties of SMGs is not yet very deep, but progress is being made as the number of detected SMGs increases and the dedicated follow-up observations of individual SMGs yield detailed information on their properties. For instance, the question of whether SMGs are the progenitors of massive ellipticals and trace the formation of large structures (e.g. galaxy clusters) still remains unresolved. Submillimeter selected galaxies appear to lie at a median redshift of $z = 2.3$ (Chapman et al., 2005) and to have large stellar masses $\sim 10^{11} M_{\odot}$, about 10 times larger than those found in UV-selected star-forming systems at similar redshifts (Borys

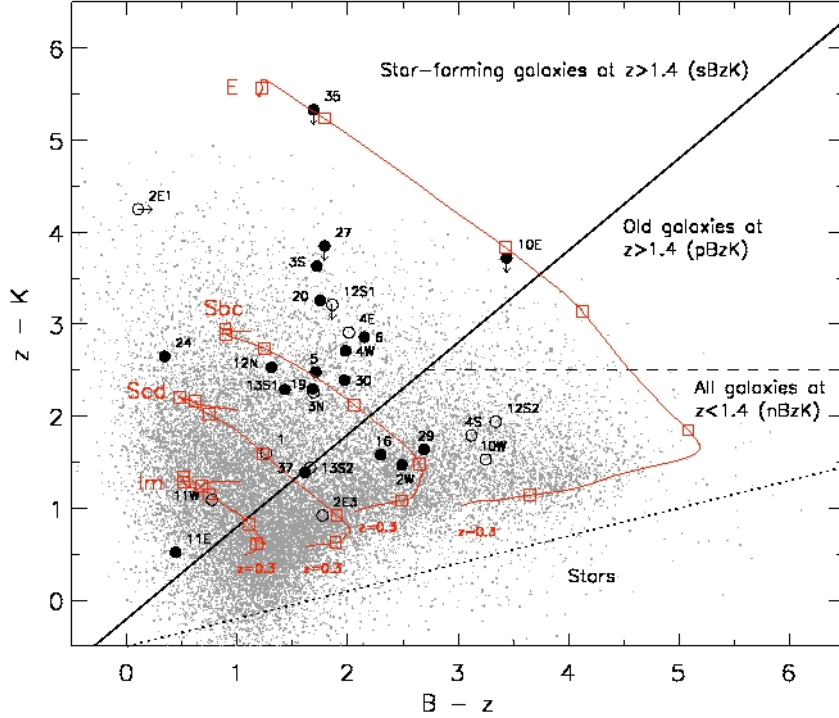


Figure 3.1: *BzK* color-color diagram. Filled circles show the most likely identifications to the MAMBO sources. Open circles show the unlikely or ambiguous associations to the MAMBO sources. Small dots represent galaxies from the field. The solid and dashed lines separate star-forming and old passive elliptical galaxies at redshift $z > 1.4$ from low redshift objects. The dotted line separates stars from galaxies. The red lines show the redshift tracks followed by the Coleman et al. (1980) templates (Elliptical, Spiral bc, Spiral cd and Irregular), starting at redshift $z = 0.3$. Open squares represent the value of the template color for redshift $z = 0.5, 1.0, 1.5, 2.0, 2.5$ and 3.0 .

et al., 2005; Dye et al., 2008). They have been found to host large molecular gas reservoirs in their inner regions (< 4 kpc), with molecular gas masses in the range $10^{10} - 10^{11} M_{\odot}$ (Neri et al., 2003; Greve et al., 2005; Tacconi et al., 2006). SMGs appear like scaled-up versions of local ULIRGs (Sanders & Mirabel, 1996). These findings are still rather uncertain due to the low number of SMGs known and therefore studies of larger and homogeneous samples are needed.

In this Chapter, we study the optical properties of the MAMBO SMGs found in COSMOS. In Sections 3.2.1 and 3.2.2 we analyse the optical/IR colors in order to characterize the nature of their optical counterparts. In Sections 3.2.3 and 3.2.4 we compute photometric redshifts for our MAMBO SMGs and compare their redshift distribution with previous spectroscopic redshift studies. In Section 3.2.5 we estimate stellar masses based on their multi-wavelength SEDs. In Section 3.3 we discuss the main implications of our results.

3.2 Results

3.2.1 BzK selection

Daddi et al. (2004) found that by using the combination of galaxy colors $BzK \equiv (z - K) - (B - z)$

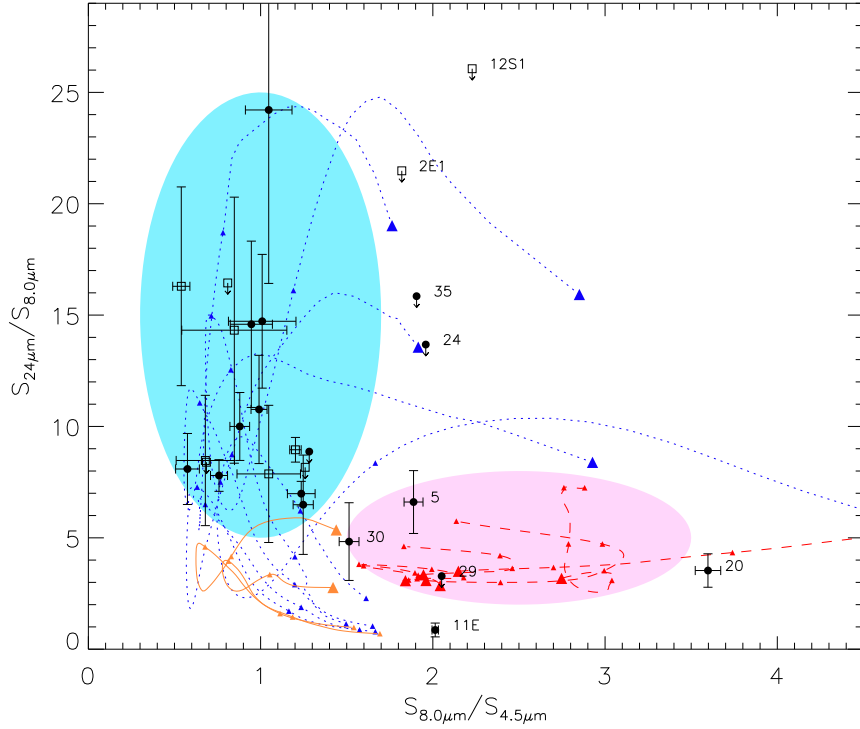


Figure 3.2: $S_{24\mu m}/S_{8.0\mu m}$ vs. $S_{8.0\mu m}/S_{4.5\mu m}$ color-color diagram for the reliable (filled circles) and ambiguous (open squares) MAMBO counterparts. For comparison the tracks of some of the SWIRE template SEDs (Polletta et al., 2007) are also shown: 5 starburst galaxies corresponding to the SEDs of Arp220, M82, NGC 6090, IRAS 22491-1808, and IRAS 20551-4250 (blue, short dashed curves), 6 QSO-like SEDs, 3 type-1 and 2 type-2 and Mrk 231 (red, long dashed) and the template SEDs of a Seyfert 1.8 and a Seyfert 2 galaxy (orange, solid). The turquoise area marks the zone likely occupied by star-forming galaxies. The pink area represents the region where QSOs likely reside. The triangles along the template tracks mark the position in redshift, $z = 1, 2, 3$ and 4. The large triangles represent the starting redshift 0.5 in each track.

(where B, z and K correspond to the photometric bands centered at $\sim 4.4, 9.0$ and $2.2\ \mu\text{m}$, respectively), it is possible to separate galaxies at low and high redshift nearly independently of dust extinction.

According to this selection criterion, objects with color index $BzK > -0.2$ are star-forming galaxies with redshifts > 1.4 ($sBzK$). Objects with color index $BzK < -0.2$ and color $(z - K) > 2.5$ are old passive evolving galaxies at redshifts > 1.4 ($pBzK$), while sources with $BzK < -2.5$ and $(z - K) < 2.5$ are a mixture of star-forming and old galaxies at redshifts < 1.4 ($nBzK$). The additional restriction $(z - K) < 0.3(B - z) - 0.5$ allows a reliable separation of stars.

Figure 3.1 shows the BzK color-color diagram for the MAMBO and field galaxies in the COSMOS field. For comparison we also show the redshift tracks of the standard galaxy templates of Coleman et al. (1980). The crucial feature of this selection criterion is that at redshift > 1 all template tracks turn towards bluer ($B - z$) colors, mainly because the $4000\ \text{\AA}$ break in the galaxy SEDs enters the z band. This implies that the galaxy tracks cross almost perpendicular to any $BzK = \text{const.}$ line and, at redshift ~ 1.4 , the tracks align with $BzK = -0.2$.

The bulk of field galaxies is located in the lower left part of the diagram, with colors $(B - z)$ and $(z - K)$ in the range between 1 and 2, where we find only few MAMBO SMGs.

Interestingly, 20 of the 29 MAMBO SMGs (68%), or 14 of the 18 secure identifications (77%), lie in the high-redshift star-forming section of the BzK diagram, and almost half the sources with ambiguous or non-secure counterparts lie in the low redshift section. Given the most likely redshift for SMGs ($z \sim 2$; Chapman et al., 2005), this would be consistent that the ambiguous identifications are indeed false.

3.2.2 Starburst or AGN ?

From near to mid-IR wavelengths, the SEDs of galaxies are different depending on the nature of their emission. At wavelengths longer than $\simeq 1.6 \mu\text{m}$ (rest-frame), where the emission of the stellar population peaks, the spectra of elliptical and normal galaxies decline rapidly, whereas the spectra of star-forming galaxies generally show hot dust emission and prominent PAH features. Conversely, AGN dominated galaxies show strong continuum emission (from the powerful central source) typically with monotonically increasing flux densities toward longer wavelength. At redshifts $z > 0.3$, the $1.6 \mu\text{m}$ stellar peak and PAH emission features are shifted to the *Spitzer* IRAC and MIPS $24 \mu\text{m}$ bands, which allows to trace and separate the activity of galaxies by comparing their IR colors.

Several mid-IR color based diagnostics have been used to separate AGN and starburst galaxies at different redshifts. The most common diagnostic criteria has been the comparison of the $S_{24 \mu\text{m}}/S_{8.0 \mu\text{m}}$ and $S_{8.0 \mu\text{m}}/S_{3.6 \mu\text{m}}$ galaxy colors (Ivison et al., 2004; Pope et al., 2006; Ivison et al., 2007; Beelen et al., 2008).

Figure 3.2 shows the respective diagram for our sample of COSBO sources, comparing their colors with the ones derived from the SED templates of Polletta et al. (2007). The redshift tracks for starburst galaxies, represented by blue lines, are located in the well defined turquoise-colored region of the diagram, while AGN, shown by red lines, occupy the pink square. Little or no overlap is seen between the tracks of starbursts and AGN. Most of the MAMBO galaxies can thereby be classified as star-formation dominated. We note that this diagnostic successfully identifies those galaxies previously observed to host AGN revealed by their X-ray emission (COSBO 11 and 20; Bertoldi et al., 2007).

Since there are sources with no detection in the shallow $24 \mu\text{m}$ coverage, it is difficult to decide whether they are AGN or low redshift starbursts. To complement this diagram, we compared the $r - [3.6]$ and $[3.6] - [8.0]$ galaxy colors (Wilson et al., 2007) with the SED templates of Polletta et al. (Fig. 3.3). We included the same SEDs from Fig. 3.2, but added two new templates representing elliptical galaxies (also from Polletta et al.). This diagram, in addition to be helpful to separate starburst and AGN when $24 \mu\text{m}$ data is not available, can be used to identify old passive evolving galaxies at high redshift, provided that the color cut $r - [3.6] > 4$ selects objects at $z > 1$ (Wilson et al., 2004).

The $r - [3.6]$ vs. $[3.6] - [8.0]$ diagram is very effective for discriminating between old passive evolving galaxies, AGN and starbursts, as their redshift tracks clearly occupy different regions in the diagram. Indeed, this selection is in very good agreement with the one presented in Fig. 3.2, suggesting that both methods are consistent and reliable. COSBO 12S1 and 24 are marked as $24 \mu\text{m}$ non-detections, and thereby classified as AGN, while COSBO-30 is ambiguously classified by both criteria as it lies in between the tracks of AGN and starbursts.

A total of 6 of the 18 secure counterparts to the MAMBO sources ($\sim 33\%$) are classified as AGN. By including COSBO-30 as an AGN, this fraction increases to 39%. Only two sources of the 6 classified as AGN are $S/N > 4$ MAMBO detections, while the other 4 sources are lower significance millimeter detections selected based on their radio association (Chapter 2). Although we need a larger number of sources to confirm this quantitatively, this could imply that the radio based selection of the low significance submillimeter sources preferentially selects AGN, whereas the optical/near-IR counterparts of the high significance (sub)millimeter sources are dominated by star formation rather than AGN activity.

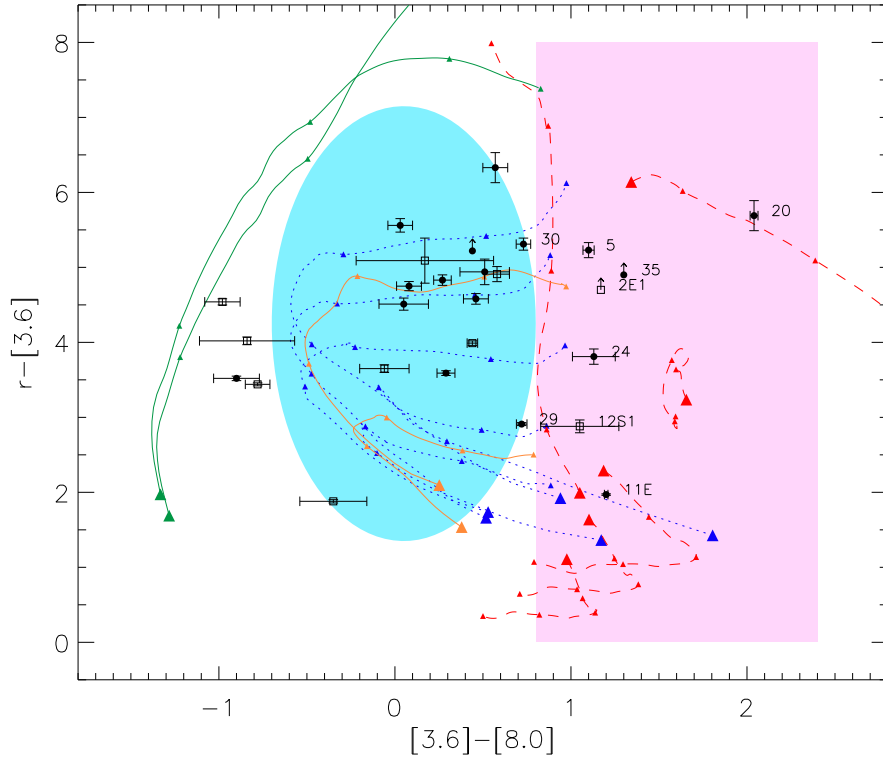


Figure 3.3: $r - [3.6]$ vs. $[3.6] - [8.0]$ color diagram for the reliable (filled circles) and ambiguous (open squares) MAMBO source counterparts. For comparison, we show the redshift tracks of template SEDs from Polletta et al. (2007), including the template SED tracks of 2 elliptical galaxies (3 and 5 Gyr old; green, solid curve). The light blue ellipse delimitates the region in the diagram where starburst galaxies are likely to reside and the light red rectangle the region the AGN-dominated sources are located. The triangles along the template tracks mark the position in redshift, $z = 1, 2, 3$ and 4. The large triangles represent the starting redshift 0.5 in each track.

3.2.3 Radio-millimeter photometric redshifts

For an estimate of the redshift of our MAMBO sources, we used the radio to millimeter spectral index as a redshift measure for starburst galaxies (Carilli & Yun, 1999). We computed the spectral index as

$$\alpha_{250}^{1.4} = \frac{\log(S_{250 \text{ GHz}}/S_{1.4 \text{ GHz}})}{\log(250 \text{ GHz}/1.4 \text{ GHz})}, \quad (3.1)$$

where $S_{250 \text{ GHz}}$ and $S_{1.4 \text{ GHz}}$ are the observed flux densities at 250 GHz and 1.4 GHz (measured with MAMBO and the VLA), respectively. We make use of the tight correlation between radio and far-IR luminosity observed in local starbursts (Condon, 1992), and assume the radio/far-IR SED of the prototypical starburst galaxy Arp220. Then, the spectral index is a strong function of redshift (Fig. 3.4). Although $\alpha_{250}^{1.4}$ is subject to uncertainties arising from the varying dust properties (temperature, mass, opacity) that starburst galaxies can have, perhaps even as a function of redshift, it provides a rough estimate of the redshift and helps to decide whether a particular source lies at low or high redshift.

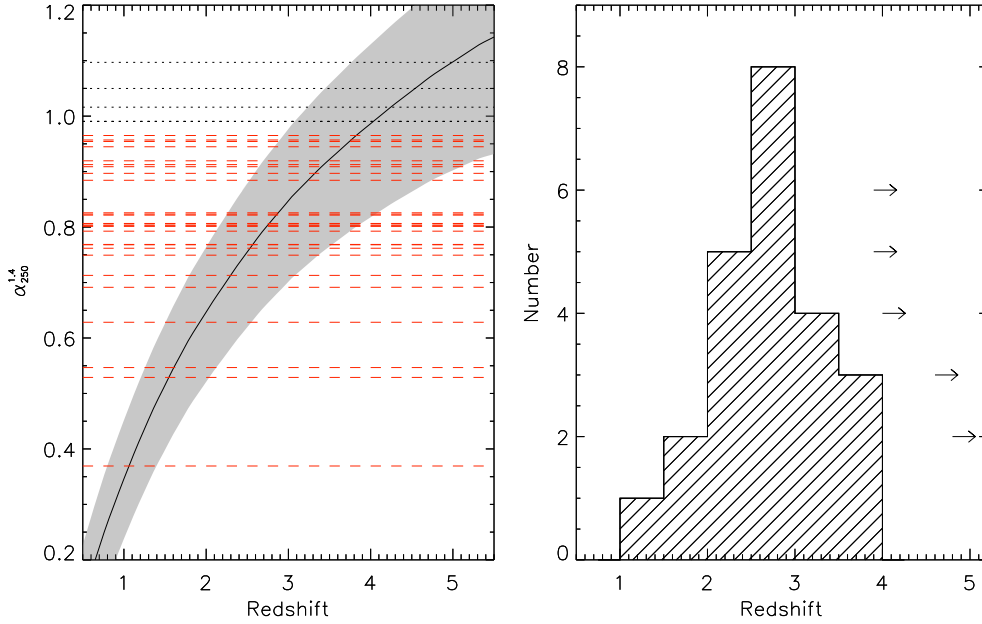


Figure 3.4: Redshift estimation based on the radio to millimeter spectral index. On the left, the relation between spectral index and redshift is shown. The solid line represents the spectral index computed for the IR luminous starburst galaxy Arp220 (which roughly has $T_d = 45$ K). The filled area shows the spectral index obtained for similar models with different dust temperatures, $T_d = 30$ K (lower limit) and $T_d = 60$ K (upper limit). Red dashed horizontal lines show the spectral index computed for the radio-identified MAMBO sources. Black dotted horizontal lines indicate lower limits for the spectral index (COSBO 1, 4, 9, 14 and 15). On the right, the respective redshift distribution of radio identified MAMBO galaxies is shown. Rightward pointing arrows indicate redshift lower limits for the MAMBO sources with no significant radio identification

Figure 3.4 (left) shows the relation between the radio to millimeter spectral index and redshift for Arp220 (which approximately has $T_d = 45$ K and $\beta = 1.0$), and illustrates the uncertainties introduced by using different dust temperatures. Figure 3.4 (right) shows the implied redshifts, most of them in the range $z = 2 - 3$. Here, we included COSBO 7, 8 and 33, which do not have a reliable optical/IR counterpart, but a reliable radio association. Their redshifts thereby computed are $3.1^{+0.9}_{-0.7}$, $2.7^{+0.4}_{-0.3}$ and $3.8^{+0.7}_{-0.5}$, respectively.

COSBO 4, 9, 14 and 15, which do not coincide with any significant radio source, are likely located at redshifts > 3 . Based on the 3σ limit in the radio map, we estimate a lower limit for their spectral indexes of 1.096, 1.049, 1.016, 0.991 and 0.991, respectively. They are represented as lower limits in Fig. 3.4 (right). We note that COSBO-4 can be associated with three possible radio-faint $24 \mu\text{m}$ counterparts that are likely at $z < 2$ (see below), as suggested by their optical/IR photometric redshifts. However, the radio to millimeter spectral index implies a high redshift ($z > 3$), indicating that the $24 \mu\text{m}$ sources may not be necessarily associated with the millimeter emission. As described in Chapter 5, we used millimeter interferometry to locate this MAMBO source.

We obtained a median redshift of 2.6 for the radio-identified MAMBO sources, consistent with the average $z = 2.3$ found by Chapman et al. (2005). Table 3.1 lists the computed redshifts and their errors. The uncertainty range for the redshifts in Table 3.1 only includes the error in the observed radio to millimeter spectral index but no the intrinsic uncertainty coming from the

assumption of an Arp220 model. This would add an uncertainty of $+1/-0.5$.

3.2.4 Optical/IR photometric redshifts

We computed optical/IR photometric redshifts for the MAMBO sources using the Hyperz code (Bolzonella et al., 2000) to find the best template SED that fits the photometric data points via χ^2 minimization.

We used the evolutionary synthesis models of Bruzual & Charlot (2003) to create a grid of template SEDs with 5 different star formation histories: a single burst, 3 exponentially decaying star formation rates ($\tau = 1, 2, 15$ Gyr) and one with constant star formation rate. Each set of templates consists of 50 different ages, which we limited to the age of the Universe at the source redshift. We adopted a Chabrier initial mass function (IMF; Chabrier, 2003) with lower and upper mass cut-offs at 0.1 and 100 M_{\odot} , respectively, and assuming solar metallicity.

To take into account those sources with QSO-like SED we included three QSO type-1 and two QSO type-2 templates, and the starburst/QSO Mrk231 template from Polletta et al. (2007).

We allowed for photometric redshifts in the range $z = 0-5$ and applied an extinction correction based on the model of Calzetti et al. (2000) for starburst galaxies. Since this extinction model has been calibrated in the range $0.12 - 2.2 \mu\text{m}$ (from UV to near-IR), we linearly extrapolated the ranges $0.12 - 0.13 \mu\text{m}$ and $0.21 - 0.22 \mu\text{m}$ to shorter (up to $0.1 \mu\text{m}$) and longer wavelengths (to $5 \mu\text{m}$), respectively. We assume that the behaviour of the extinction curve between $0.1 \mu\text{m}$ and $0.12 \mu\text{m}$ does not change drastically and note that the applied extrapolation has little effect in the mid-IR. We allowed for a broad range in the visual extinction based on the results of Dye et al. (2008) for SCUBA sources, $A_V = 0-2.5$. Objects not detected in a given band are assigned a zero flux and an error corresponding to the limiting magnitude in that filter.

Figure 3.5 shows the MAMBO source counterpart photometric data and the best fitting templates. Most sources are best fitted by young single burst templates. The photometric redshifts show good agreement with the spectroscopic redshift values for those sources for which the latter has been measured. COSBO 2W, 10W, 11E and 29 have spectroscopic redshifts of 1.032, 0.629, 1.829 and 0.472, respectively. Not surprisingly, most of the sources classified as AGN-dominated through their mid-IR colors (Figs. 3.2 and 3.3) were best fitted by QSO-like template SEDs. In some cases the fits yield low redshift solutions that are unlikely considering the average SMG redshift distribution (Chapman et al., 2005). For example, based on its optical spectra, COSBO-11E was found to host a type-1 AGN with redshift $z = 1.8288$ (Trump et al., 2007). The best fit to its photometry corresponds to a type-1 QSO, however the implied photometric redshift is $z = 0.71$. The second redshift solution in its χ^2 distribution is $z = 1.51$, in better agreement with the spectroscopic redshift. AGN-dominated objects are difficult to fit with templates because they lack sharp SED features, such as a 4000 \AA break. Template based optical photometric redshifts lead to wrong results in about 50% of the cases for AGN (Berta et al., 2007).

Figure 3.6 shows the optical photometric redshift distribution for the MAMBO source counterparts. For the reliable counterparts that we classified as starburst galaxies through their mid-IR colors, we find a median redshift of 2.1. Including those sources classified as QSOs, the median redshift is 1.99. Estimations based on the χ^2 minimization can produce, in the general case, wrong photometric redshifts. This arises from degeneracies in parameter space (redshift, template, extinction) and by the fact that our photometry does not trace the 4000 \AA break at $z \sim 2$ (for which we need deep J and H photometry). However, this can be partly overcome by using the galaxy redshift probability distributions. If a galaxy has two possible redshift solutions, this will be reflected in its redshift probability distribution as two strong peaks that maximize the likelihood (or minimize χ^2). Measuring the redshift distribution based on the best redshift solutions misses information about the secondary peaks. Instead, measuring the average probability distribution over all galaxies will use this information, weighting both peaks accordingly.

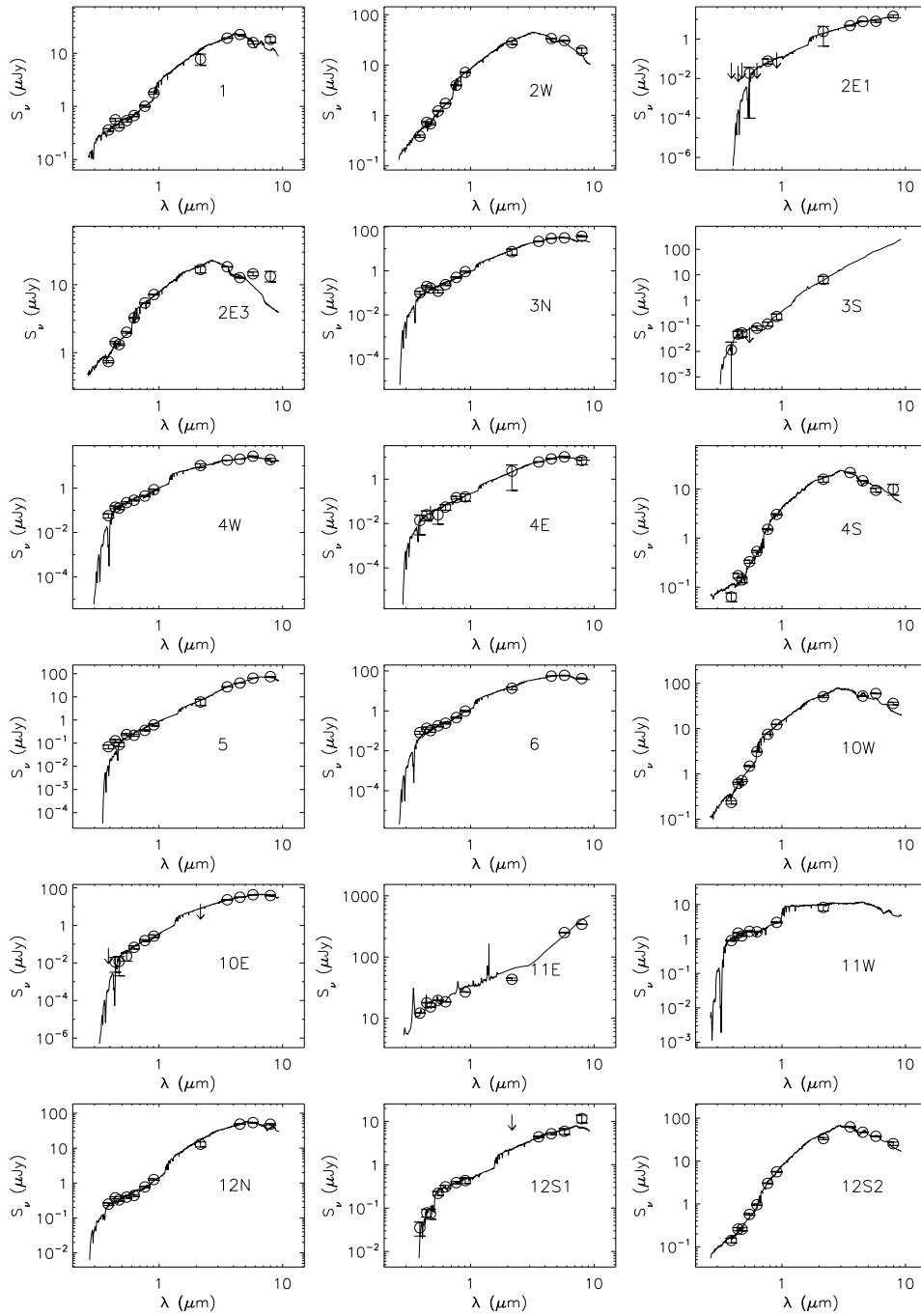
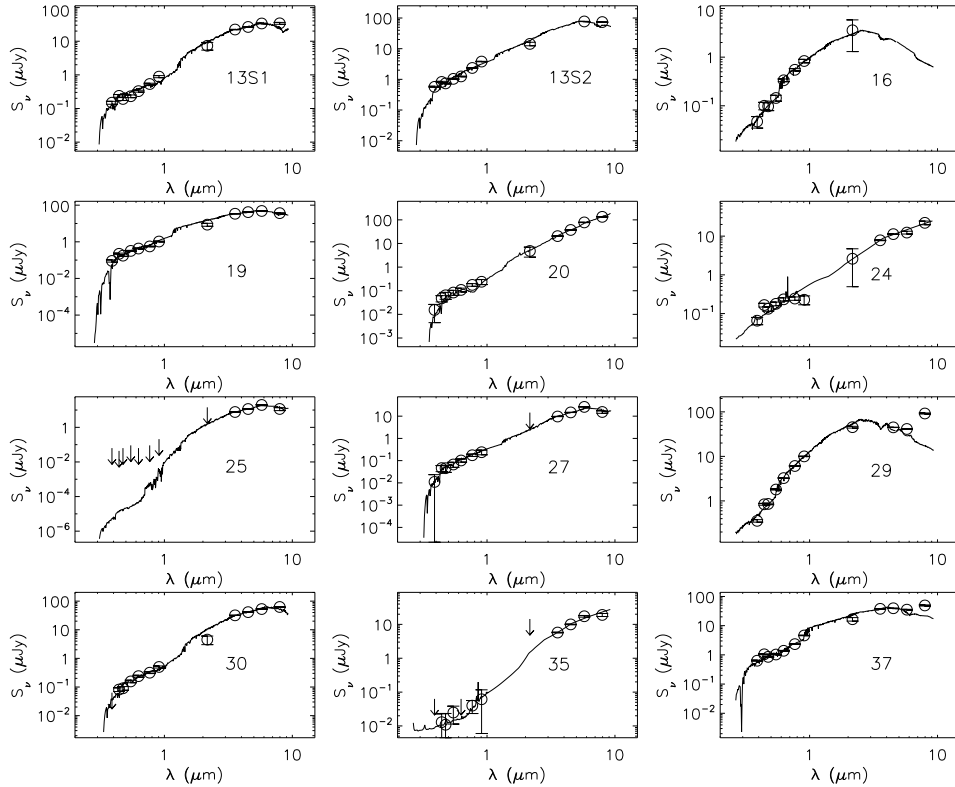


Figure 3.5: Spectral Energy Distributions (SEDs) for the MAMBO counterparts. Open circles are the multi-wavelength data points from the optical to the mid-IR. The solid lines correspond to the best template fits. Upper limits are represented by downward pointing arrows.

Figure 3.5: *Continued.*

For each redshift step z_i used in the χ^2 minimization procedure, we computed the average probability, $P(z_i)$, over all the reliable optical/near-IR counterparts to the MAMBO sources, N , as (Fig. 3.6),

$$P(z_i) = \sum_j P_j(z_i)/N, \quad j = 1 \dots N. \quad (3.2)$$

The probability values $P_j(z_i)$ are related to the χ^2 value at that redshift step through $P_j(z_i) \propto \exp(-\chi^2/2)$.

The average probability distribution shows a median redshift of 2.33 without including QSOs, and a median redshift of 2.41 including them. We note that the average probability distribution still shows an important contribution at low ($z < 1$) and high ($z > 3$) redshifts. This is mainly due to parameter space degeneracy explained before.

3.2.5 Stellar Masses

Each template SED from the Bruzual & Charlot (2003) library has been modeled to follow a stellar mass to light ratio $(M^*/L_K)_{\text{model}}$ that varies as a function of the galaxy template's age. M^* is the stellar mass and L_K is the luminosity in the K band, both quantities in solar units.

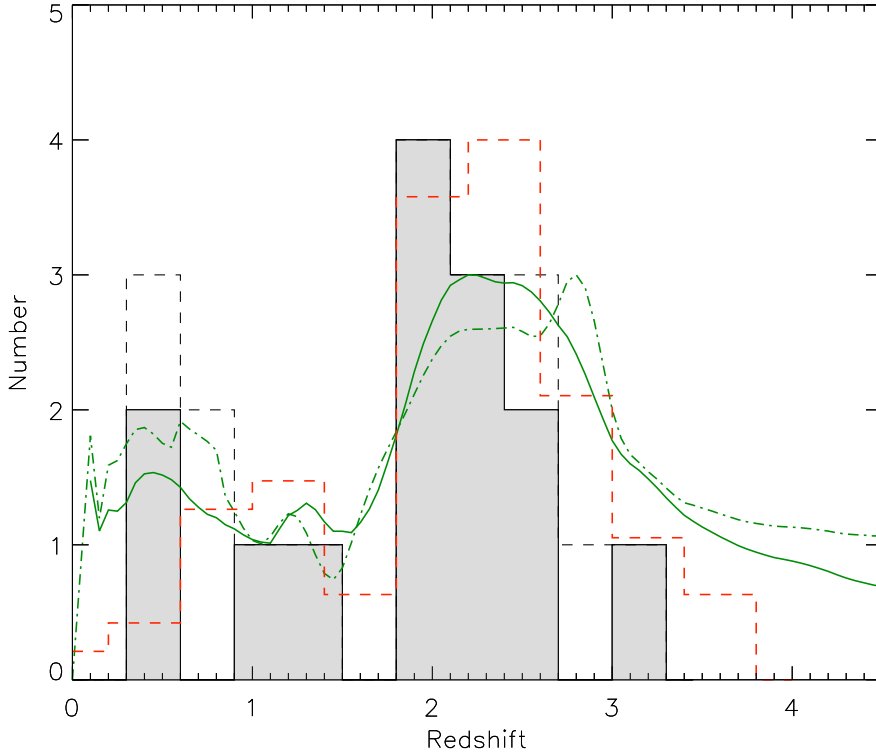


Figure 3.6: Redshift distribution of MAMBO sources. The shaded histogram shows the photometric redshift distribution excluding sources classified as QSOs. The dashed histogram includes the photometric redshifts for sources classified as QSOs. The green curves show the probability distribution averaged over non-QSOs (solid) and QSOs (dot-dashed) and normalized to 3 for comparison. The red dotted histogram shows the redshift distribution of SCUBA and MAMBO galaxies from Chapman et al. (2005).

Thus, using the absolute magnitude M_K it is possible to compute the stellar mass, for a given IMF, as:

$$M^* = (M^*/L_K)_{\text{model}} \times 10^{-0.4(M_K - M_{K,\odot})}. \quad (3.3)$$

Thus, the photometric redshift and the best fitting template computed via χ^2 minimization can be used to calculate the absolute magnitude and the galaxy stellar mass M^* . At the typical redshift of SMGs ($z \sim 2$), the rest-frame K band is shifted to the mid-IR and therefore the IRAC photometry is crucial to trace the stellar mass.

Using the procedure above, we computed stellar masses for the MAMBO counterparts. We excluded AGN-dominated objects as their SEDs were best fitted by QSO templates that produce very uncertain redshift estimates. Furthermore, their optical emission is likely to contain a strong AGN component.

We considered two sources of uncertainty in the mass estimation: the metallicity in the template SEDs and the error of the photometric data points (Dye et al., 2008). To estimate the error from an unknown metallicity, we created two new sets of template SEDs from the libraries of Bruzual & Charlot (2003). One with a metallicity of $Z = 0.4 Z_\odot$ and another with $Z = 2.5 Z_\odot$, and assuming the star formation rate histories described above. Then, we re-computed the stellar

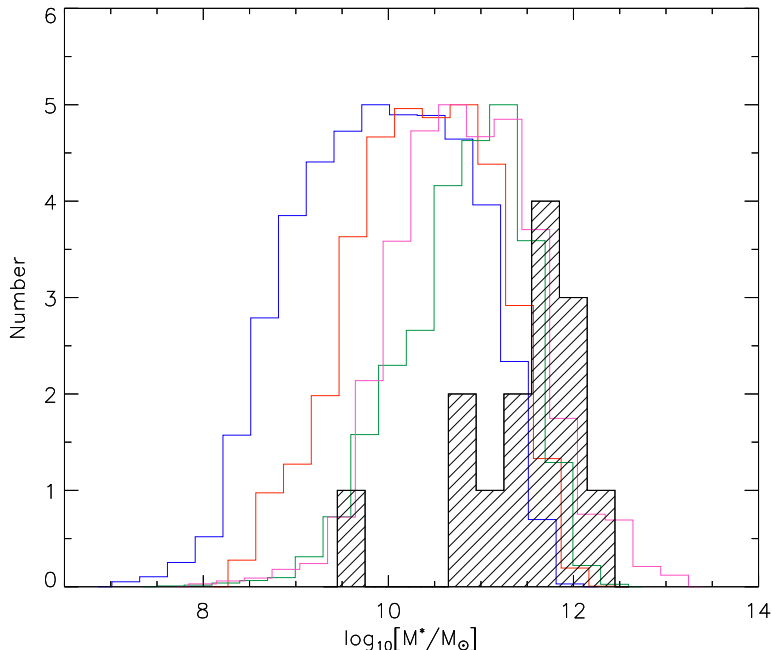


Figure 3.7: Stellar mass distribution of reliable MAMBO source counterparts (shaded histogram). The stellar mass distribution derived for optical/IRAC field galaxies, in the redshift ranges $z = 0.1 - 0.8$ (blue), $z = 0.8 - 1.5$ (red) and $z = 1.5 - 2.5$ (green) and scaled to a peak of 5 is also shown.

masses for the MAMBO galaxies using the two template SED sets and calculated the 1σ mass error (due to metallicity) as the difference between the 2 template sets.

To account for photometric errors, we carried out a Monte Carlo simulation of the optical/IR flux densities. For each MAMBO source, we randomly sampled the optical and IR flux densities 1000 times, assuming a Normal distribution around the measured flux density and a width given by the 1σ error of the observed flux. If the MAMBO source was undetected in a band, instead of randomly sampling its flux, we set it to zero and assigned an uncertainty corresponding to the sensitivity limit. Using the simulated flux densities, we re-computed the photometric redshifts and thereby the stellar masses, and estimated their stellar mass error as the 1σ scatter in the distribution of masses. Finally, we added both sources of error (metallicity and photometric errors) in quadrature to obtain the total uncertainty in the mass estimates.

3.3 Discussion

3.3.1 The nature of SMGs

Submillimeter selected galaxies are the strongest star-forming galaxies known ($\text{SFR} > 1000 M_{\odot} \text{yr}^{-1}$). Since they are heavily obscured, their optical appearance may not necessarily reflect their starbursting nature. For instance, optically selected QSOs are seen as bright AGN with blue colors in the optical, however some of them are seen as star-forming galaxies in the millimeter and radio regimes (see Chapter 6). Nevertheless, our results show that SMGs can be classified as star-forming galaxies through their millimeter/radio and optical properties.

We found that about 70 – 80% of galaxies in our MAMBO sample can be classified as star-forming high-redshift galaxies. This large overlap implies that a close link between these two

Table 3.1: Properties of MAMBO galaxies

ID	z_{radio}^a	$z(1)^b$	$z(2)^c$	Type ^d	Age ^e	A_V^f	M_K^g	$\log_{10} M^*^h$
1.....	$4.8^{+1.4}_{-0.9}$	$1.420^{+0.021}_{-0.022}$	0.200	Sa	1.700	1.4	-25.41	11.16 ± 0.22
2W.....	$2.1^{+0.2}_{-0.2}$	$0.930^{+0.004}_{-0.003}$	0.770	Burst	0.091	2.0	-25.33	10.94 ± 0.10
2E1.....	$3.1^{+0.5}_{-0.4}$	$3.395^{+0.483}_{-0.352}$	1.680	Burst	0.128	2.0	-26.69	11.49 ± 0.44
2E3.....	–	$0.615^{+0.007}_{-0.007}$	0.200	1	0.064	1.5	-23.61	10.14 ± 0.93
3N.....	$3.8^{+0.7}_{-0.5}$	$1.930^{+0.044}_{-0.087}$	0.150	Burst	0.045	2.3	-26.49	11.13 ± 0.31
3S.....	$3.8^{+0.6}_{-0.5}$	$1.810^{+1.046}_{-0.780}$	2.475	Burst	0.360	0.4	-25.00	11.00 ± 0.52
4W.....	–	$2.235^{+0.074}_{-0.072}$	1.355	Burst	0.181	1.5	-26.49	11.51 ± 0.09
4E.....	–	$2.095^{+0.630}_{-0.227}$	2.675	Burst	0.039	2.4	-25.44	10.65 ± 1.56
4S.....	–	$0.795^{+0.012}_{-0.016}$	0.600	E	4.500	0.9	-24.28	11.10 ± 0.34
5.....	$2.3^{+0.2}_{-0.2}$	$2.815^{+0.040}_{-0.042}$	0.150	Burst	0.026	2.4	-28.20	11.55 ± 0.84
6.....	$2.7^{+0.4}_{-0.3}$	$1.860^{+0.043}_{-0.023}$	0.285	Burst	0.128	2.4	-27.16	11.68 ± 0.34
10W.....	$4.6^{+0.3}_{-0.9}$	$0.660^{+0.003}_{-0.002}$	3.810	Burst	0.181	2.3	-25.19	10.99 ± 0.20
10E.....	$3.4^{+0.7}_{-0.4}$	$2.595^{+0.088}_{-0.089}$	3.740	Burst	0.181	2.4	-27.41	11.87 ± 0.26
11E.....	$1.8^{+0.2}_{-0.2}$	$0.705^{+0.001}_{-0.005}$	1.505	QSO1	–	0.4	-25.68	11.05 ± 0.03
11W.....	$3.5^{+0.6}_{-0.5}$	$1.650^{+0.066}_{-0.055}$	0.620	Burst	0.255	0.0	-24.79	10.86 ± 0.27
12N.....	$2.6^{+0.4}_{-0.4}$	$1.995^{+0.026}_{-0.052}$	2.515	E	2.000	1.5	-27.16	11.97 ± 0.25
12S1.....	$3.3^{+0.8}_{-0.6}$	$3.190^{+0.190}_{-0.395}$	2.855	Sa	1.015	1.1	-26.35	11.46 ± 0.38
12S2.....	$3.5^{+0.7}_{-0.5}$	$0.700^{+0.036}_{-0.006}$	1.390	E	2.600	2.1	-25.16	11.26 ± 0.32
13S1.....	$1.0^{+0.1}_{-0.1}$	$2.375^{+0.152}_{-0.064}$	2.225	E	2.600	1.1	-27.22	12.08 ± 0.10
13S2.....	–	$2.065^{+0.021}_{-0.010}$	0.185	Im	0.026	2.4	-27.60	11.17 ± 0.50
16.....	$2.5^{+0.5}_{-0.5}$	$0.540^{+0.078}_{-0.152}$	1.390	Burst	0.091	2.1	-21.60	9.45 ± 0.57
19.....	$3.6^{+1.3}_{-0.9}$	$2.100^{+0.031}_{-0.023}$	1.995	Burst	0.128	1.9	-27.13	11.67 ± 0.39
20.....	$2.4^{+0.5}_{-0.4}$	$2.530^{+0.103}_{-0.121}$	1.250	Mrk231	–	1.4	-28.38	12.16 ± 0.59
24.....	$2.7^{+0.7}_{-0.6}$	$0.350^{+0.036}_{-0.044}$	2.050	QSO1	–	1.9	-20.61	11.31 ± 1.41
25.....	$3.4^{+0.7}_{-0.4}$	$2.395^{+0.168}_{-0.120}$	4.905	Burst	3.500	2.4	-26.01	11.79 ± 0.12
27.....	$2.6^{+0.6}_{-0.6}$	$3.120^{+0.136}_{-0.083}$	0.150	Sa	2.300	1.9	-26.63	11.72 ± 0.12
29.....	$2.6^{+0.6}_{-0.6}$	$0.455^{+0.004}_{-0.003}$	3.170	Sa	2.000	2.3	-24.08	10.67 ± 5.72
30.....	$2.4^{+0.6}_{-0.5}$	$2.660^{+0.058}_{-0.053}$	0.150	E	2.600	1.6	-27.96	12.38 ± 0.33
35.....	$3.2^{+0.9}_{-0.7}$	$0.710^{+0.166}_{-0.138}$	3.510	QSO2	–	0.1	-22.42	10.75 ± 4.56
37.....	$1.5^{+0.3}_{-0.5}$	$1.420^{+0.003}_{-0.010}$	1.270	Burst	0.128	1.4	-26.28	11.33 ± 0.24

^a Radio photometric redshift based on the MAMBO 250 GHz to VLA 1.4 GHz spectral index.

^b Optical/IR best fit photometric redshift solution.

^c Optical/IR second photometric redshift solution.

^d Best fit template, Burst: Single burst; E: Elliptical; Sa: Spiral; Sc: Spiral; Im: Irregular; QSO1: Type-1 QSO; QSO2: Type-2 QSO; Mrk231: Starburst/QSO composite.

^e Best fit age, in 10^9 yrs.

^f Best fit optical extinction.

^g Absolute K-band magnitude.

^h Stellar mass.

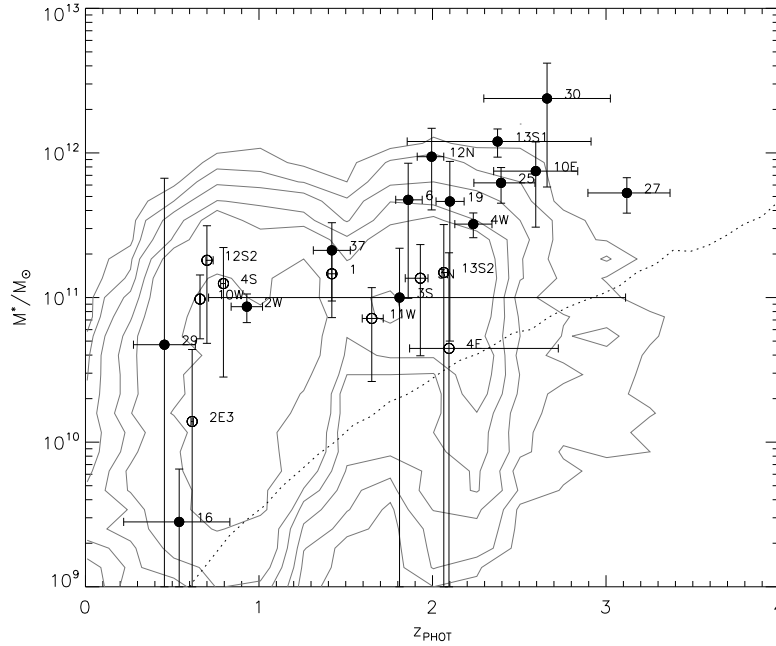


Figure 3.8: Stellar mass as a function of redshift for reliable (filled circles) and ambiguous (open circles) MAMBO source counterparts. The horizontal error bars show the 90% confidence range for the photometric redshifts and the vertical error bars correspond to the stellar mass errors explained in the text. The background contour plot represents the number density of optical/IRAC field galaxies as a function of stellar mass and redshift. The dotted curve corresponds to the mass limit implied by the K band sensitivity limit, assuming an elliptical galaxy template (conservative approach).

populations exists and that the BzK selection criteria might be used to select millimeter bright galaxies at high redshifts (Dannerbauer et al., 2006; Takagi et al., 2008). However, also distant red galaxies (DRGs) and redshift ~ 2 UV-selected (BX/BM) galaxies (Reddy et al., 2005) are identified as high-redshift star forming galaxies in the BzK diagram. Typically, $sBzK$ galaxies, DRGs and BX/BM galaxies have average colors $\langle z - K \rangle = 1.6$, 2.5 and 1.1, respectively (Reddy et al., 2005). Our MAMBO galaxies have an average color $\langle z - K \rangle = 2.6$, which is consistent with that found for a sample of SCUBA sources from Takagi et al. (2008) ($\langle z - K \rangle = 2.5$). The redder color observed in SMGs compared to other galaxy populations can be attributed to the strong extinction by dust.

Deep X-ray observations have shown that the majority ($\approx 75\%$) of radio-selected spectroscopically identified SMGs host obscured AGN (Alexander et al., 2003, 2005). The fraction of SMGs with AGN dominating the bolometric output is about $\sim 20 - 30\%$, as found in flux limited samples of (sub)millimeter sources (Chapman et al., 2003; Alexander et al., 2003, 2005; Ivison et al., 2004; Ashby et al., 2006). Our sample of MAMBO galaxies is consistent with previous studies, with $\sim 35\%$ being dominated by AGN. Overall, this indicates that most of the bolometric output in SMGs is provided by intense star formation rather than AGN activity.

3.3.2 Massive galaxies at $z = 2$

Spectroscopic studies of large samples of radio-selected SMGs have found that they are at median redshift $z \approx 2.3$ (Chapman et al., 2005). Studies based on radio, millimeter and far-IR colors are

consistent with this result, indicating a median redshift of ~ 2.4 for SCUBA sources (Aretxaga et al., 2007). These redshift estimates are considerably higher than the optical/IR photometric redshifts estimates of Dye et al. (2008), who find a median redshift of $z \sim 1.5$. From our radio/millimeter photometric redshift estimates we find a median redshift $z \sim 2.6$, and our optical/IR photometric redshifts imply $z \approx 2.1$, or $z \approx 2.3$ when based on the probability redshift distribution. Our estimates are therefore in agreement with the results of Chapman et al. (2005) and Aretxaga et al. (2007).

Interestingly, four MAMBO sources do not show a reliable radio counterpart. From their radio to millimeter spectral index, these galaxies should lie at a redshift > 3.5 . Although some of the MAMBO sources with no radio detection may also be spurious, a good fraction of these SMGs may well be at these high redshifts, as supported also by mid-IR spectroscopy (Lutz et al., 2005; Menéndez-Delmestre et al., 2007; Valiante et al., 2007) and millimeter continuum interferometry (see Chapter 5; Younger et al., 2007), which concluded that SMGs lie on average at higher redshifts, with a median redshift of 2.8.

We compared the stellar masses derived for the MAMBO sources with those derived for a sample of field galaxies selected in an area of $40' \times 40'$ enclosing the COSBO region. We selected IRAC point sources that had an optical counterpart within $1''$ (91% of IRAC sources) and computed their photometric redshifts and stellar masses in the same way that we did for the MAMBO galaxies, using the same template SEDs and HyperZ parameters. We rejected star-like objects using the neural-network-based star/galaxy SExtractor classifier, $\text{CLASS_STAR} > 0.95$. We also rejected objects that were masked in the optical images. We separated AGN dominated objects using a color selection, $([3.6] - [8.0]) > 0.8$ (Fig. 3.3) and did not consider them. This resulted in 19700 non-AGN galaxies detected in both the optical and IRAC point source catalogs.

Figure 3.7 compares the stellar mass distribution of the MAMBO and field galaxies in different redshift intervals. The average stellar mass derived for our sample of millimeter galaxies is $10^{11.4 \pm 0.4} M_{\odot}$, matching the average value found by Borys et al. (2005). This is also in good agreement with the larger sample of SCUBA sources studied by Dye et al. (2008), who find a slightly higher average value, $10^{11.8 \pm 0.1} M_{\odot}$.

Figure 3.8 shows the evolution of the stellar masses for the MAMBO galaxies. The direct comparison with field galaxies suggests that SMGs are among the most massive galaxies at all redshifts but also that SMGs at larger redshifts tend to have larger masses. This is consistent with findings of Pérez-González et al. (2008), who suggested that the most massive systems were already in place at redshifts > 2.5 , and most of the star formation activity at lower redshifts has been driven by less massive galaxies. A similar trend was found by Borys et al. (2005) and Dye et al. (2008) for SCUBA galaxies. They argue that two phases of stellar mass growth occurred. In a first stage, large amounts of stellar mass are built up, likely amounting for the large masses we observe in SMGs. In a second stage, galaxy mergers triggered stellar mass growth. This is supported by the fact that many SMGs are observed to be involved in massive galaxy mergers (Greve et al., 2005; Tacconi et al., 2006).

Environment of submillimeter galaxies

4.1 Introduction

In the hierarchical scenario of structure formation, galaxy clusters form by the gravitational collapse of primordial density peaks (Peacock, 1999). They form the most massive bound systems known and are good tracers of the large-scale structures of the Universe. The understanding of the conditions and the epoch at which galaxies formed in the first large scale structures can place strong constraints on current models of galaxy formation and evolution.

Searches for galaxy clusters have mostly been done at X-ray and optical wavelengths, either through the detection of hot gas emission from the intra-cluster medium (Rosati et al., 2002) or through the detection of a ‘red-sequence’ in optical/near-IR color-magnitude diagrams of the cluster galaxies (Larson et al., 1980; Gladders & Yee, 2000; Gladders, 2002). These methods have been successful in the detection of the most massive and evolved systems up to redshift ~ 1.3 (Stanford et al., 1997; Rosati et al., 1999; Mullis et al., 2005; Stanford et al., 2005, 2006; Brodwin et al., 2006; Elston et al., 2006; Castellano et al., 2007).

A different method that also works well at high redshifts has been to detect structures in the surroundings of high redshift radio galaxies (HzRG; for a review see Miley & De Breuck, 2008). Searches for distant galaxy overdensities, so-called “proto-clusters”, have been very successful, including the detection of large structures up to $z = 5.2$ (Venemans et al., 2004; Overzier et al., 2006). These studies covered a considerable range in redshift, $z \sim 1.5 - 5.0$, and have used different observational strategies such as the search for narrow emission lines in galaxy spectra (e.g. Lyman α or H α ; Kurk et al., 2004a; Venemans et al., 2004; Croft et al., 2005; Venemans et al., 2005, 2007) or strong continuum features in galaxy SEDs, including the Lyman break at 912 Å (Overzier et al., 2006; Intema et al., 2006) and the Balmer break at 4000 Å (Kurk et al., 2004b; Kajisawa et al., 2006; Kodama et al., 2007).

Studies of the environments of radio galaxies in the redshift range $z \sim 1 - 2$ have been difficult due to the lack of narrow spectral features to measure the galaxy redshifts. Nevertheless, significant overdensities of EROs or galaxies forming a red-sequence have been found in the fields of radio galaxies at $z \sim 1.5 - 2.0$ (Sánchez & González-Serrano, 1999; Best, 2000; Sánchez & González-Serrano, 2002; Best et al., 2003; Kurk et al., 2004b; Kajisawa et al., 2006; Kodama et al., 2007; Zirm et al., 2008). These observations have indicated that the structures formed around massive radio galaxies are pre-stages of today’s rich galaxy clusters (Miley & De Breuck, 2008; Overzier et al., 2008).

However, radio galaxies may not be the only kind of object tracing proto-clusters. Indeed, the large dynamical (Greve et al., 2005; Tacconi et al., 2006, 2008) and stellar masses observed in bright SMGs (Borys et al., 2005; Dye et al., 2008), their similar comoving number density compared to bright local ellipticals (Scott et al., 2002; Swinbank et al., 2006), as well as their

strong clustering (Blain et al., 2004b), have suggested that they are precursor of today's massive spheroidals, which are typically located in massive galaxy clusters (Dunlop, 2001).

Further evidence has arisen from near-IR observations, indicating that SMGs at $z > 2$ can evolve on to the Faber-Jackson relation of local early-type galaxies, and accounting for the formation of present luminous ellipticals (Swinbank et al., 2006). Moreover, some SMGs are known to be associated with galaxy clusters at high redshifts (Best, 2002; Webb et al., 2005), including the discovery of an extended group of SMGs at $z = 2$ (Chapman et al., 2008). Indications of the presence of SMGs in overdensities of LBGs and radio galaxy fields have also been found (Kneib et al., 2004; Stevens et al., 2003; Ivison et al., 2000b; Smail et al., 2003). These observations suggest an important role of SMGs in the formation of local ellipticals.

If SMGs are progenitors of massive clustered spheroids, they would likely show signs of clustering in the epoch when these galaxies had their peak in activity and luminosity ($z \sim 1 - 3$), similar to what is observed in powerful AGN. Attempts to measure the clustering of SMGs indicate that they are associated with massive dark matter halos and possibly trace the largest scale structures at high redshifts (Blain et al., 2004a). Even though, current submillimeter blank field surveys cover small areas in the sky, yielding a few tens of sources within contiguous fields (Scott et al., 2002; Webb et al., 2003; Greve et al., 2004; Coppin et al., 2006; Bertoldi et al., 2007; Scott et al., 2008). Hence, good quantitative studies of the large scale clustering of the SMG population are not feasible until large surveys comprising a few square degrees in the sky can be made.

However, studies of the environment of SMGs are possible, given the rich complementary data available for current (sub)millimeter fields. Whether SMGs are embedded in regions with an enhanced number of optical/near-IR detected high-redshift galaxies has yet not been quantified. In this chapter, we investigate to what extent (sub)millimeter selected galaxies are located in clustered fields. For this, we make use of deep near-IR imaging data in the COSMOS field to measure the density of K -band selected BzK galaxies in the surroundings of MAMBO galaxies (Section 4.2). Next, we examine the projected number density of low and high redshift BzK galaxies as a function of magnitude and distance to the millimeter source (Sections 4.3.1 and 4.3.2). We study the color-magnitude diagram (Section 4.3.5) and compute photometric redshifts for galaxies in those regions with the most prominent overdensities (Section 4.3.6). Finally, we discuss the implications of our findings (Section 4.4).

4.2 Observations

4.2.1 K band selected catalog

To complement the deep optical and shallow K band coverage of the COSMOS field (Capak et al., 2007), a new deep K band imaging survey was carried out using the WIRCAM instrument on the CFHT (McCracken et al, in prep.).

Both the observations and data reduction were performed by McCracken et al. (private communication). The data were taken between December 2005 and June 2007 with a seeing between $0.7''$ and $0.9''$. The images were pre-reduced using the standard Traitement Élémentaire, Réduction et Analyse des Pixels (TERAPIX) pipelines (Bertin et al., 2002). Weight maps, catalogues and quality assessment reports were generated using the TERAPIX software tool QualityFITS. An astrometric solution was obtained with the TERAPIX software tool SCAMP (Bertin, 2006) using the Subaru i^+ band image as reference. The final astrometric accuracy reaches $\sim 0.2''$. All images were combined using SWARP (Bertin et al., 2002) and corrected to match the astrometric grid of the other COSMOS images ($0.15''/\text{pixel}$).

Note that the publicly available i^+ band selected COSMOS catalog (Capak et al., 2007) does not include deep K band photometry and the newer version of this catalog (Capak et al., private communication), with 30 photometric narrow, intermediate and broad band photometry, was

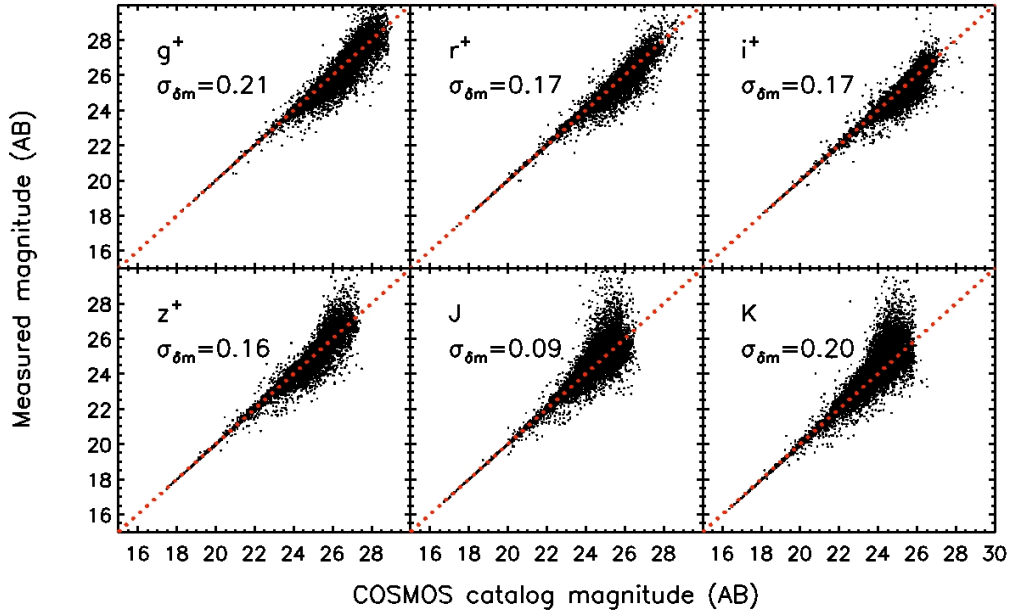


Figure 4.1: Comparison of our final extracted photometry with the values listed in the i^+ -band selected COSMOS catalog. Red dotted lines represent an exact match. Values for the dispersion of the difference of our magnitudes with that from the COSMOS catalog up to the 5σ limit in the respective band are shown.

restricted to $i^+ < 26.5$, not including the faintest and likely most obscured galaxies. The selection in the K band, on the other hand, is less prone to obscuration and can be directly compared with previous studies of radio galaxies. Since at the time when this work was written there was no multi-wavelength K -band selected catalog available in the COSMOS field, we extracted our own photometry using the deep K band images for detection.

From the final K band mosaic, we extracted a $\sim 24' \times 24'$ area image centered at the COSBO field position (R.A., Dec.) = $(10^{\text{h}} 00^{\text{m}} 30^{\text{s}}, 02^{\circ} 12' 00'')$, and complemented it with Subaru B , V , g^+ , r^+ , i^+ and z^+ , CFHT u^* , i^* and UKIRT J -band images of the same size and centered at the same reference position. Similarly, we extracted cutouts of the deep Spitzer IRAC $3.6 \mu\text{m}$, $4.5 \mu\text{m}$, $5.8 \mu\text{m}$ and $8.0 \mu\text{m}$ band images. All optical and near-IR images have the same size and pixel scale ($0.15''/\text{pixel}$). Spitzer images were modified accordingly to match these requirements.

All images were smoothed to match the PSF of the u^* band data, except for the IRAC data, which have much poorer resolution. For these, we computed aperture magnitudes and applied aperture corrections. The latter were derived by simulating the flux of 10000 stars across the whole COSMOS field and comparing the simulated and extracted flux (M. Salvato, private communication).

We performed aperture photometry in the optical and IR images using SExtractor (Bertin & Arnouts, 1996) in dual image mode with the K band images as reference and setting an aperture diameter of $3''$. A 5×5 convolution mask of a Gaussian PSF with a FWHM of 2.5 pixels was used for filtering. Small corrections (typically less than 0.2 magnitudes) were applied to correct the measured aperture magnitudes to total.

The COSBO region provides a sufficiently large area for comparison with the local fields around the MAMBO sources. As we explain later on, the overdensities of sources seen around some MAMBO galaxies appear on small scales ($< 20''$) and therefore do not affect the overall

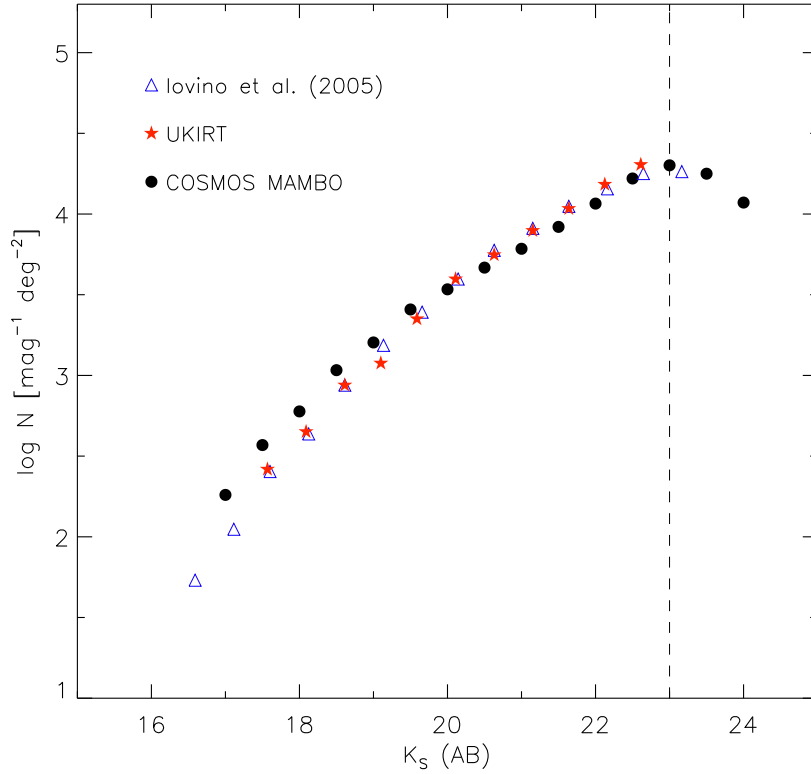


Figure 4.2: Comparison of the K -band galaxy counts from the COSBO field with those of recent large and deep near-IR surveys. The vertical dashed line shows where our number counts are complete at $K \sim 23$ magnitudes.

background source number density and the results reported here.

Small patches of the COSBO field were significantly affected by the presence of very bright stars that induced high flux density levels. Such regions were masked out and therefore do not influence the results exposed.

To check the reliability of the deep K band observations, we compared our measured magnitudes with those of the new i^+ band selected COSMOS catalog (Capak, priv. comm.). Figure 4.1 shows the comparison of our extracted photometry (corrected to total magnitudes) with that from the COSMOS catalog for some of our bands. Our measurements agree well with those listed in the COSMOS catalog, however some scatter exists, likely due to the different selection band used, which implies slightly different centroid source positions (therefore slightly different flux estimates), and the selection of different kind of objects (e.g. the K band selects objects at higher redshifts). This also means that some K -selected sources do not have a counterpart in the i^+ selected catalog, and vice versa.

Figure 4.2 shows the number counts of K band selected galaxies in the COSBO field compared with those recently observed in other wide deep fields. To isolate galaxies, we followed the BzK color criterion, which reliably separates galaxies from stars (see Section 4.3.2). Our number counts are in good agreement with the values derived in other fields up to our completeness limit (~ 23 magnitudes). Small differences can be seen, however, they are likely due to cosmic variance given the limited extent of our COSBO field ($\sim 24' \times 24'$).

Our K band catalog reaches a 5σ limit of 23.9 magnitudes. Objects located near bright stars,

including those with $K < 17$ (most of which are stars), or in the border of the images, were removed from the final catalogs or masked accordingly.

4.2.2 K band counterparts to MAMBO sources

We used the radio and $24\ \mu\text{m}$ identifications of the MAMBO sources (Chapter 2) to search for K band counterparts. For the radio identified counterparts to the MAMBO emission, we searched for K band sources within $1''$ from the radio peak position. For the $24\ \mu\text{m}$ selected counterparts, we looked for K band sources within a radius of $2''$ to match the resolution of the MIPS instrument on board of Spitzer ($\sim 2.5''$).

We thereby found K band counterparts for all the radio/ $24\ \mu\text{m}$ counterparts to the MAMBO sources except for COSBO 2E1, 33 and the unlikely identification COSBO 12S2. This suggests that the selection made in the near-IR is more effective than the search for counterparts in the optical, likely due to less extinction (Fig. 4.3).

4.2.3 BzK selection

In order to select galaxies that may be spatially related to SMGs, it is favourable to select those objects that match the redshift range typically occupied by the SMG population ($z = 1 - 3$), and therefore filter out foreground or background sources.

Several selection criteria can be applied for this. At redshifts > 2 , typical for most SMGs, the $4000\ \text{\AA}$ break in the SED of galaxies is shifted to the J , H and K bands. Therefore, a selection based in the color restriction $(J - K) > 2$ or of a combination of these near-IR bands, which generally pick DRGs (van Dokkum et al., 2003; Franx et al., 2003), is practical. However, our current J band coverage is relatively shallow and we do not have deep H band imaging to perform a complete and unbiased selection using these bands.

As we explain in Section 3.2.1, there is a close color similarity between high-redshift BzK galaxies and SMGs. They share a similar redshift distribution, and SMGs appear to be a subset of star-forming high-redshift BzK s. Moreover, the selection based on the $z - K$ color allows to pick old ellipticals at redshift $z > 1$ in a similar way than the standard $(r - K) > 5$ color criteria for EROs (Elston et al., 1988; McCarthy et al., 1992; Hu & Ridgway, 1994). An advantage of the BzK criteria is the selection of a mixture of galaxy populations at high redshift including old passive ellipticals and very red objects, which is best if we search for overdensities around SMGs.

Figure 4.3 shows the BzK color-color diagram for the K -band selected counterparts to the MAMBO sources and for objects in the COSBO field. According to this diagram, sources with $BzK \equiv (z - K) - (B - z) > -0.2$ are star-forming galaxies at redshift > 1.4 (s BzK), while objects with $BzK < -0.2$ but $(z - K) > 2.5$ are old passively evolving galaxies at redshift > 1.4 (p BzK). Objects with $BzK < -0.2$ and $(z - K) < 2.5$ correspond to a mixture of old and star-forming galaxies at redshift < 1.4 (n BzK). The restriction $(z - K) < 0.3(B - z) - 0.5$ allows the separation of stars whose colors significantly differ from those of galaxies.

The BzK diagram for MAMBO SMGs based on the K -band selected sample (Fig. 4.3) is rather similar to the diagram constructed from the i^+ band selected catalog (Fig. 3.1). Since we use a deeper K -band coverage now, more sources are included in the diagram. Small differences are seen in the colors of MAMBO galaxies compared to those shown in Fig. 3.1. Galaxies that are not reliable identifications to the MAMBO sources (red filled triangles) are mostly located in the low redshift part of the diagram. Conversely, objects that are likely counterparts to the MAMBO sources (black filled circles) generally lie in the high redshift part of the diagram, consistent with the typical redshift of SMGs ($z \sim 2$). Only one counterpart to the MAMBO sources (COSBO-10E) appears to be an old system at intermediate redshift ($z \sim 1.5$).

In order to study the environment of the MAMBO galaxies, we used the BzK criteria to divide our K -band selected galaxy sample into one of galaxies at low redshift ($z < 1.4$) and another

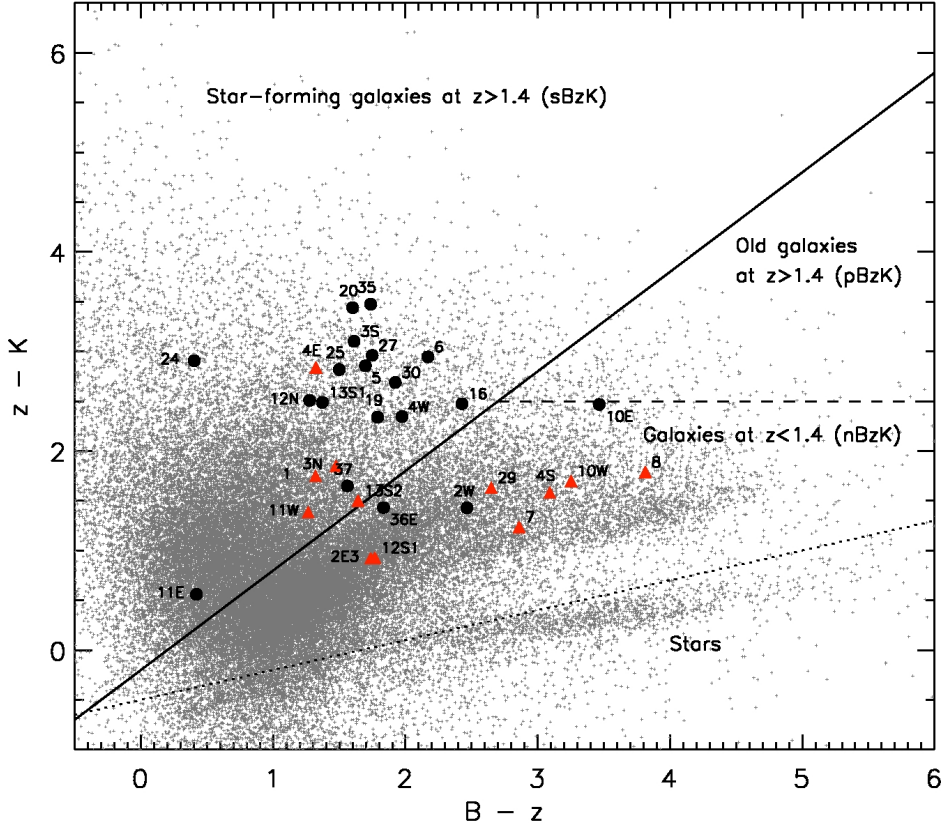


Figure 4.3: BzK diagram for MAMBO sources in the COSMOS field. Reliable K -band selected identifications are represented by filled black circles and ambiguous or unreliable identifications are shown as filled red triangles. The BzK loci for galaxies in the COSBO field are shown as small dots. The solid line separates star forming galaxies at $z > 1.4$, while the dashed line separates old passive evolving galaxies at $z > 1.4$. The dotted line separates stars.

containing a mixture of old ellipticals and star-forming galaxies at high redshift ($z > 1.4$). We constrained our sample to include objects in the magnitude range $K = 17 - 23$ and used the BzK criteria to reject stars.

4.3 Results

4.3.1 Searching for overdensities of high-redshift galaxies around SMGs

To check whether MAMBO galaxies lie in overdense environments, we computed the number of low and high redshift BzK galaxies that lie within $20''$ from each MAMBO galaxy position and down to our magnitude limit, $K = 23$ (Fig. 4.4). For comparison, we generated a Monte Carlo simulation with 4000 random positions across the COSBO field and counted the number of low and high redshift objects that lie in the surroundings of the random positions (Fig. 4.4). The number counts for the random sample nearly follow a Poisson distribution, with an average number density of low and high redshift BzK galaxies of $15 \pm 9 \text{ arcmin}^{-2}$ and $7 \pm 5 \text{ arcmin}^{-2}$, respectively. This translates into 5.3 ± 3.0 and 2.4 ± 1.9 galaxies within the $20''$ radius. The

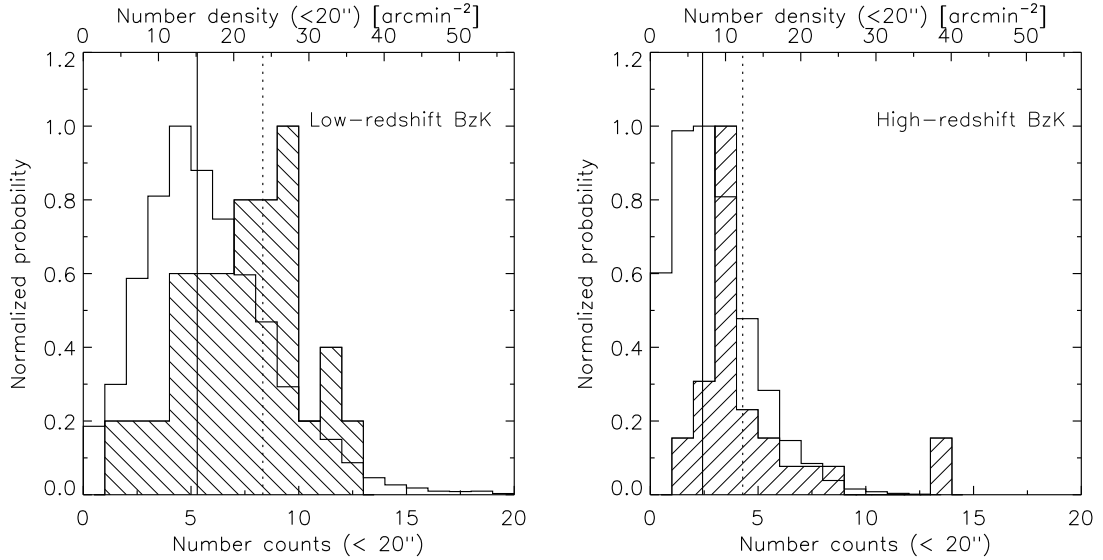


Figure 4.4: Normalized distribution of number counts of low (left) and high (right) redshift *BzK* galaxies that lie within $20''$ from the positions of MAMBO galaxies (shaded histogram) and randomly selected galaxies in the COSBO field (open histogram). The dotted and solid vertical lines represent the location of the mean number count for low and high redshift *BzK* galaxies, respectively.

quoted uncertainties are not statistical errors but reflect actual cosmic variance, being slightly larger than the error implied by Poisson statistics ($N^{1/2}$).

For some MAMBO galaxies, we find that their near environments have around 1.5 – 2 times more galaxies than the average value estimated from the random sampling of the COSBO field, implying statistical fluctuations of $\sim 2\sigma - 3\sigma$ over that average. The distribution of high-redshift *BzK* galaxies around MAMBO galaxies is consistent with that of the field, however the distribution of low-redshift *BzK* galaxies around MAMBO galaxies peaks at significantly higher densities than the average value in the field. This could possibly be explained by gravitational lensing of far away SMGs.

Figure 4.5 shows the cumulative number count distribution of low and high redshift *BzK* galaxies brighter than a given magnitude K and located within $20''$ from the MAMBO source counterpart position, compared with the distribution of accordingly selected galaxies in the COSBO field. While some MAMBO galaxies appear to be surrounded by a low number of galaxies compared to the field, there are at least 2 sources (i.e. COSBO 3 and 6) that show a strongly enhanced number of either low or high redshift galaxies at $K < 23$.

Overdensities of low-redshift galaxies could either be explained by the existence of a real low-redshift galaxy group acting as a gravitational lens for a background faint submillimeter source, or by a real association of the galaxy group with a SMG. The former is a more likely explanation since at the typical redshift of SMGs ($z \sim 2$), strong gravitational lensing is most likely produced by lenses at redshifts $z < 0.4$ (e.g. produced by lenses located at half the angular distance to the lensed galaxy; Schneider et al., 1992).

As discussed in Chapter 2, some MAMBO sources are identified with faint optical sources that lie at the edges of bright low-redshift galaxies, suggesting that they are lensed by the low-redshift galaxy. Whether MAMBO galaxies are lensed objects or are associated to low-redshift galaxy groups can only be discerned in cases where a proper identification of a radio/optical counterpart to the millimeter source has been made, which requires high resolution radio and optical imaging

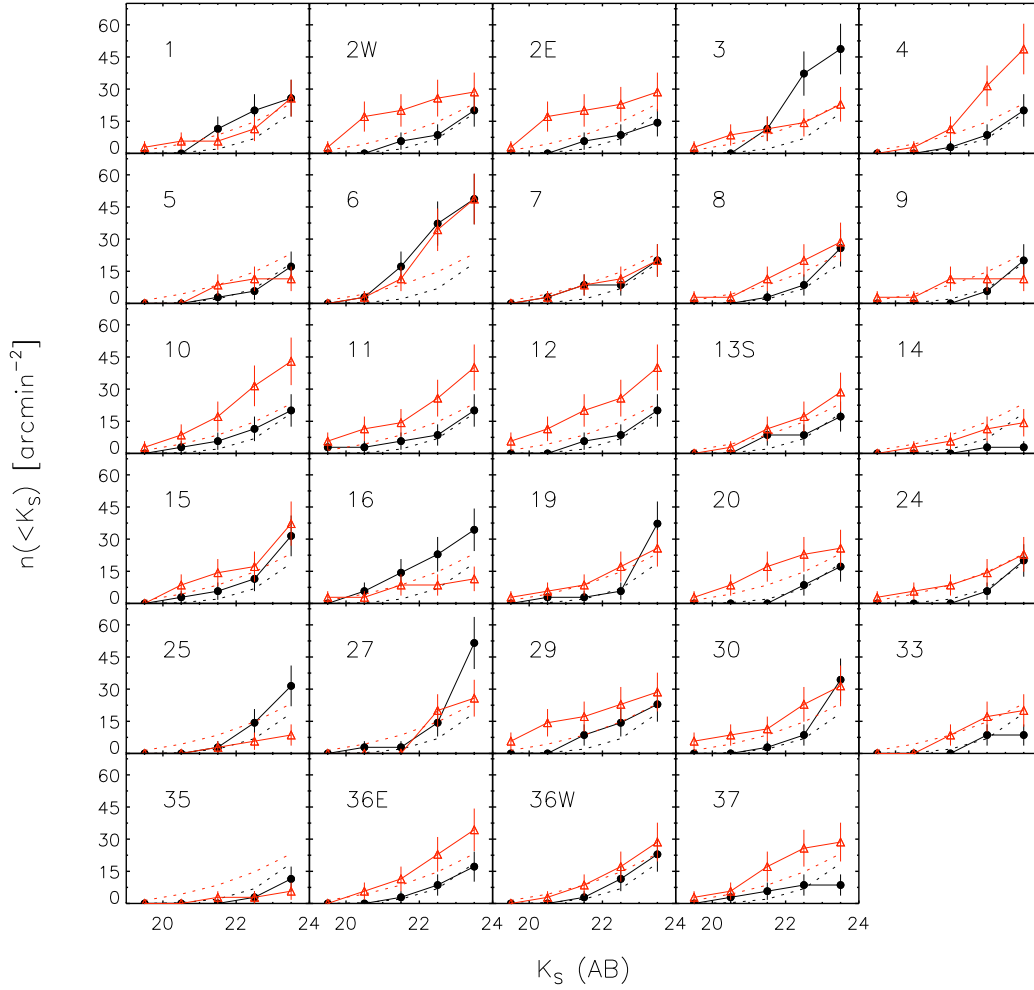


Figure 4.5: Projected number density of low-redshift (solid red) and high-redshift (solid black) *BzK* galaxies within $20''$ from the MAMBO galaxy position, compared to the projected number density of low-redshift (dotted red) and high-redshift (dotted black) *BzK* galaxies in the COSBO field. Error bars are computed from Poisson statistics.

(i.e. VLA and HST). It is also possible that the overdensities of low-redshift galaxies are produced by the chance projection of galaxies along the line of sight.

For overdensities of high-redshift galaxies around MAMBO sources, the gravitational lensing explanation is unlikely. The possibilities are either a real physical association between the SMG and the projected high-redshift *BzK* galaxies, or merely a chance projection along the line of sight. As we will see in Section 4.3.4, the latter is unlikely since this would imply the projection of a galaxy overdensity along with a bright SMG, which have a rather low surface density ($0.075 \text{ arcmin}^{-2}$).

4.3.2 *BzK* galaxy overdensities around SMGs

Some of our COSBO sources are located in overdensities of high-redshift galaxies. Such overdensities may suggest associated galaxy groups, and it is thus interesting to study their spatial extent and their possible relation to the MAMBO galaxy. It is possible that we are missing compact or lower significance overdensities due to our choice of the somewhat large $20''$ radius aperture (~ 160 kpc at $z = 1 - 3$).

The mere analysis of galaxy radial distributions of *BzK* galaxies around COSBO sources does not provide a complete picture of their environments. SMGs may not necessarily be at the center of galaxy groups, and therefore galaxy overdensities at, e.g., $10''$ from the SMG position will be diluted in radial distribution diagrams. Hence, we constructed a number density map of low and high redshift *BzK* galaxies in the COSBO field. For this, we created a grid of 200×200 equally spaced positions within the COSBO field, and computed the density as the 7th nearest neighbour *BzK* galaxy to each point (i, j) in the grid

$$n_7 = \frac{7}{\pi(d_7)^2}, \quad (4.1)$$

where d_7 is the distance of the 7th nearest neighbour *BzK* galaxy (low or high redshift). This procedure is similar to the one introduced by Dressler (1980). The choice of 7 is a compromise between accounting for structures on small scales and good statistics for each density value. Similar approaches have been applied to known rich galaxy clusters (e.g. Smith et al., 2005; Guzzo et al., 2007), but using photometric or spectroscopic information to compute the number density in redshift slices. The application of this method to redshift selected samples is limited by the accuracy of the photometric redshift estimation at redshifts $z > 1.5$ and by the significance of the forming galaxy cluster compared to the background.

Figures 4.6 and 4.7 show the projected number density maps of low and high redshift *BzK* galaxies, respectively, in the COSBO field. Each of these density maps is scaled to the average density across the COSBO field and is shown in terms of the standard deviation, σ . The average and standard deviation values were computed by using all grid points from our density maps of low and high redshift *BzK* galaxies in the COSBO field (Fig. 4.8). The average densities thus computed are 18 ± 12 and 8 ± 6 arcmin $^{-2}$, respectively, and the quoted uncertainties correspond to the actual cosmic variance. Figures 4.9 and 4.10 show density map close-ups around each MAMBO source.

Several MAMBO galaxies are located near significant ($> 4\sigma$) overdensities of low-redshift *BzK* galaxies (Fig. 4.9). This was already suggested by Figs. 4.4 and 4.8. In these cases (e.g. COSBO 2, 4, 6, 7, 10, 12, 16, 19, 29, 30, 36 and 37) the density structure is mostly fragmented and not always enhanced toward the central position of the map, where the millimeter emission is detected. Lower significance overdensities ($2\sigma - 4\sigma$) are also present, showing a similarly fragmented structure.

Interestingly, four MAMBO galaxies (COSBO 1, 3, 6 and 16) are embedded in significant overdensities ($> 4\sigma$) of high-redshift *BzK* galaxies (Fig. 4.10). Given the strength of these “detections” and the typical redshift of the SMG and high-redshift *BzK* populations, it is likely that these constitute real associations. Substantial density peaks ($\sim 4\sigma$) are also found within other MAMBO galaxy fields. However, they seem to be unrelated with the position of the SMGs (COSBO 12, 29, 35 and 36). The overdensity of galaxies around MAMBO sources is also seen directly on the optical and IR images (Fig. 4.11). Here, red galaxies are easily distinguished to be in excess toward the MAMBO source position (image center).

The typical radial extent of these overdensities is $\sim 10''$ (or $\sim 20''$ size). At a typical redshift of $z \sim 2$, this implies structures on scales of ~ 150 kpc, similar to what has been found in radio galaxy fields (Hall & Green, 1998; Hall et al., 2001; Best et al., 2003).

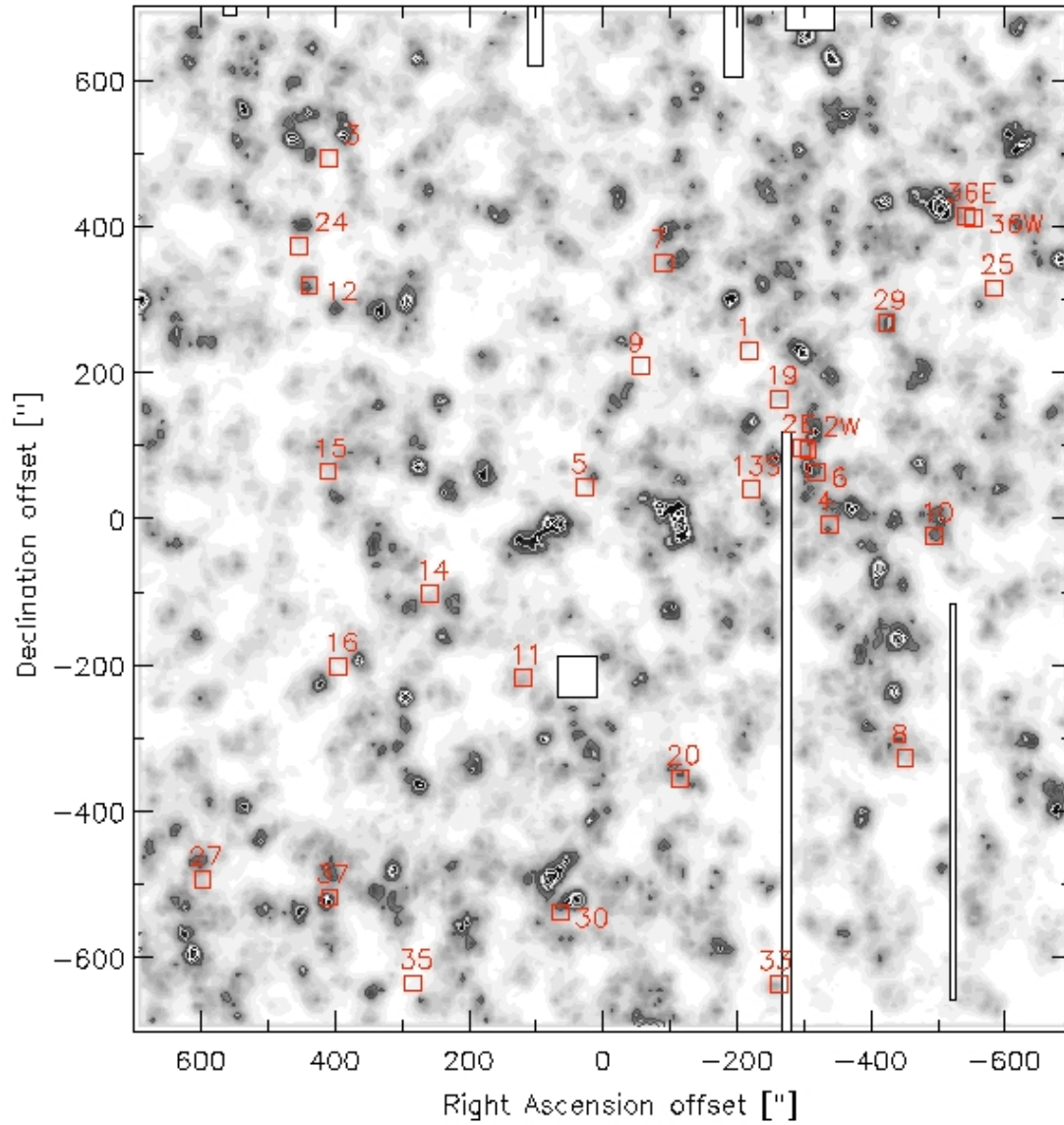


Figure 4.6: Projected number density of low-redshift BzK galaxies (n_{BzK}) in the COSBO field. Galaxies were chosen to have magnitudes in the range $K = 17 - 23$. Contour levels represent $S/N = 2\sigma, 4\sigma, 6\sigma, 8\sigma, 10\sigma$ and 15σ , where σ is the standard deviation over the local background level.

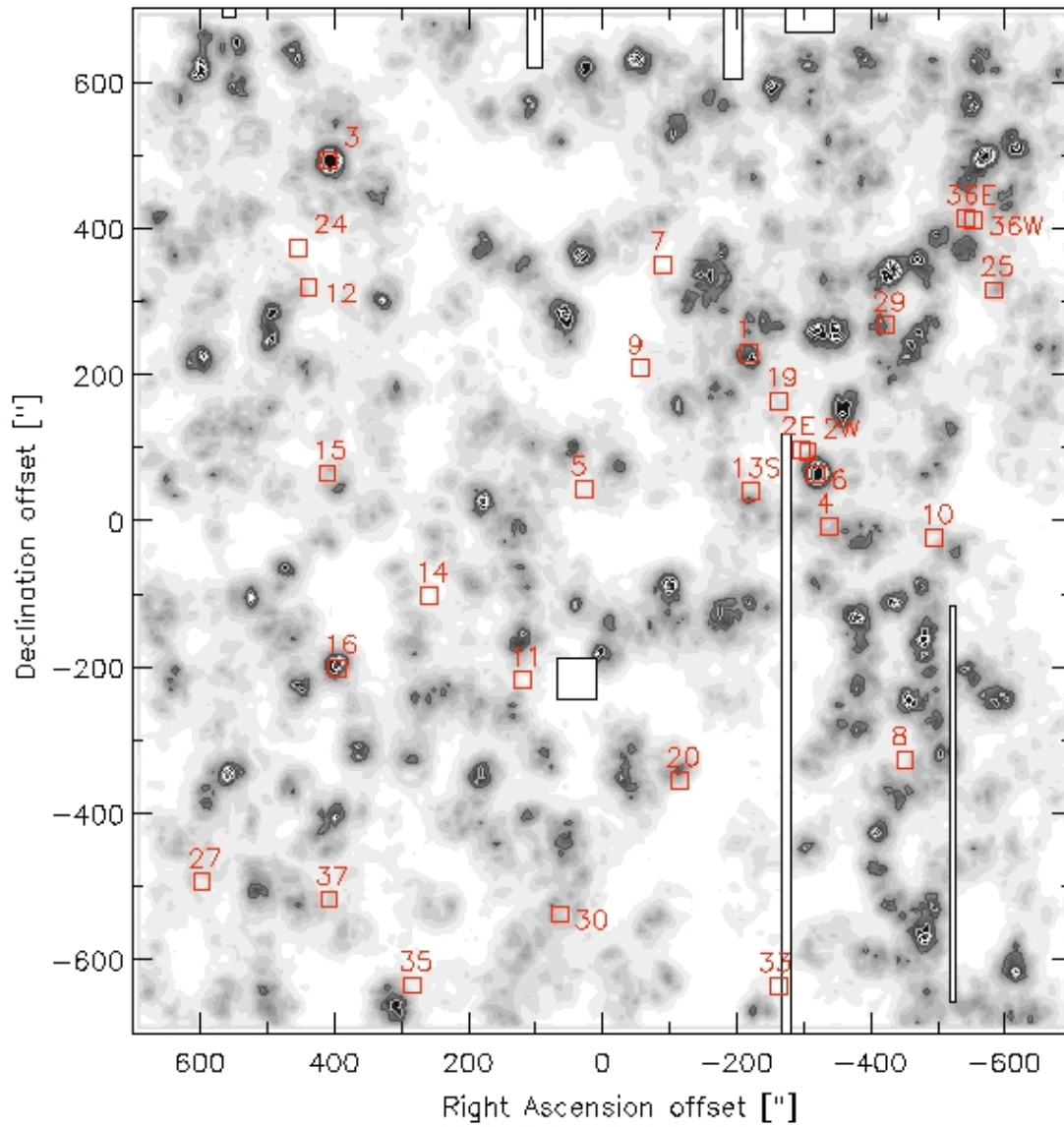


Figure 4.7: Projected number density of high-redshift BzK galaxies in the COSBO field. Galaxies were chosen to have magnitudes in the range $K = 17 - 23$. Contour levels represent $S/N = 2\sigma, 4\sigma, 6\sigma, 8\sigma, 10\sigma$ and 15σ , where σ is the standard deviation over the local background level.

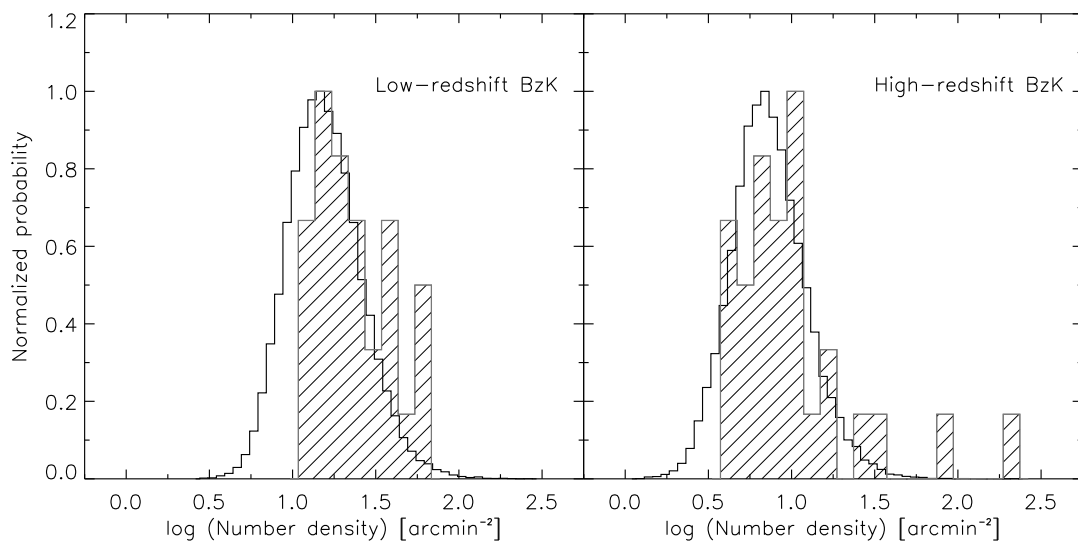


Figure 4.8: Normalized distribution of number counts of low-redshift (left) and high-redshift (right) BzK galaxies at the MAMBO source position (shaded histogram) compared to the distribution of number counts for all the 200×200 grid points in the COSBO density maps, based on the 7th nearest neighbour estimation.

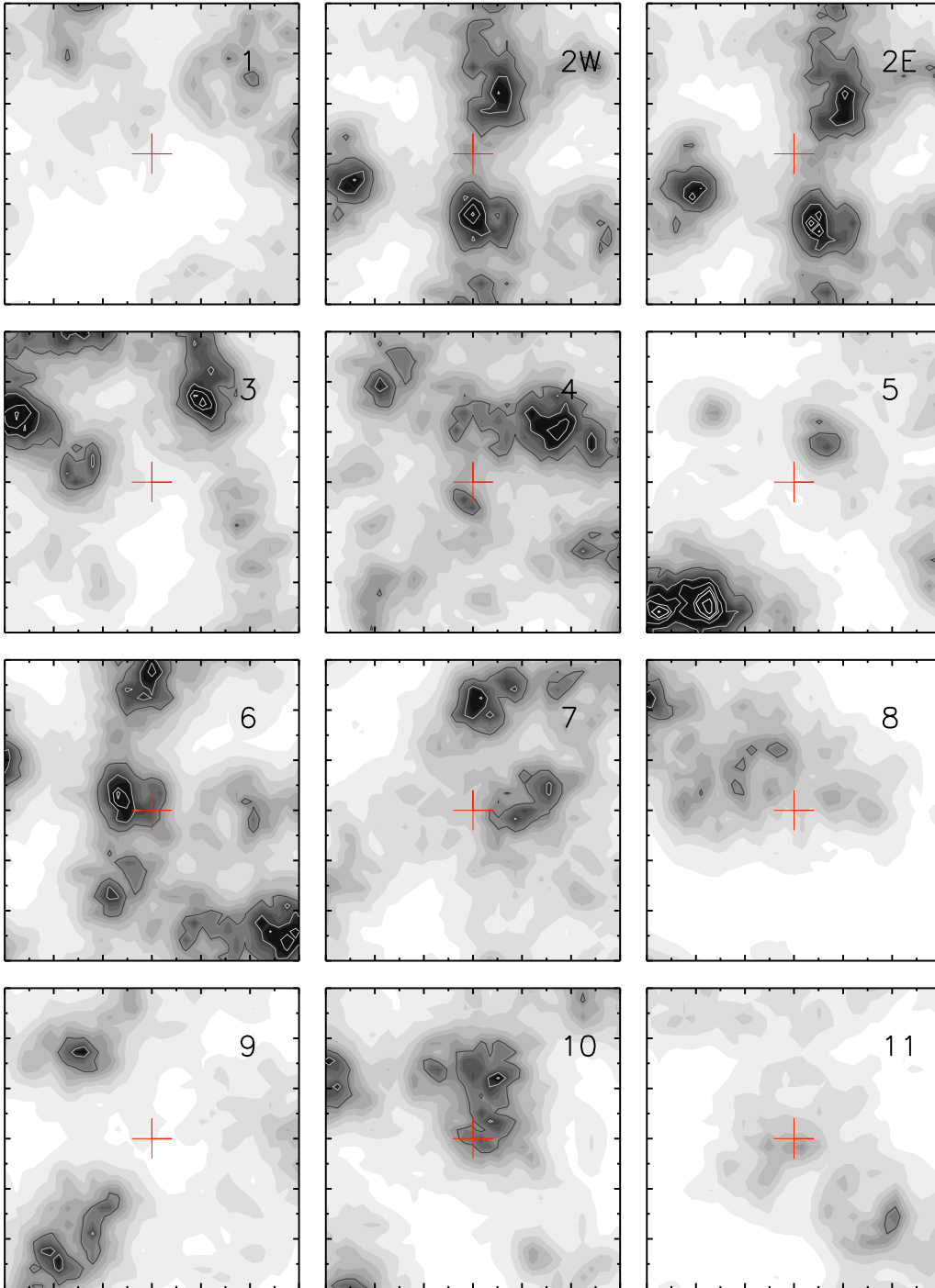


Figure 4.9: Projected number density maps ($2' \times 2'$ size) for low-redshift BzK galaxies (nBzK) in the fields of MAMBO sources. Galaxies were chosen to have magnitudes in the range $K = 17 - 23$. Contour levels represent $S/N = 2\sigma, 4\sigma, 6\sigma, 8\sigma, 10\sigma$ and 15σ , where σ is the standard deviation over the local background level. Maps are centered at the MAMBO source position (red crosses) and major ticks are in steps of $20''$.

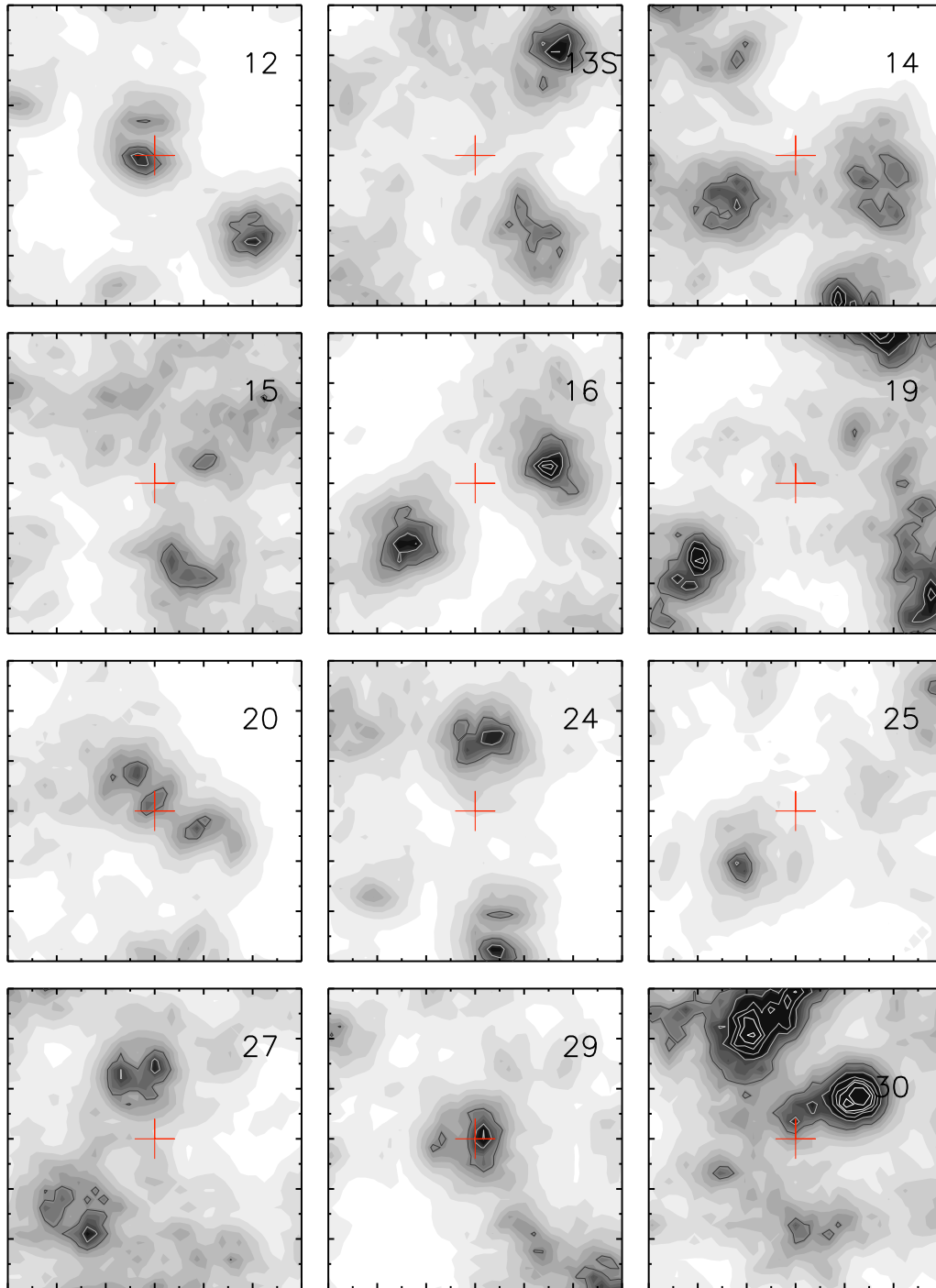
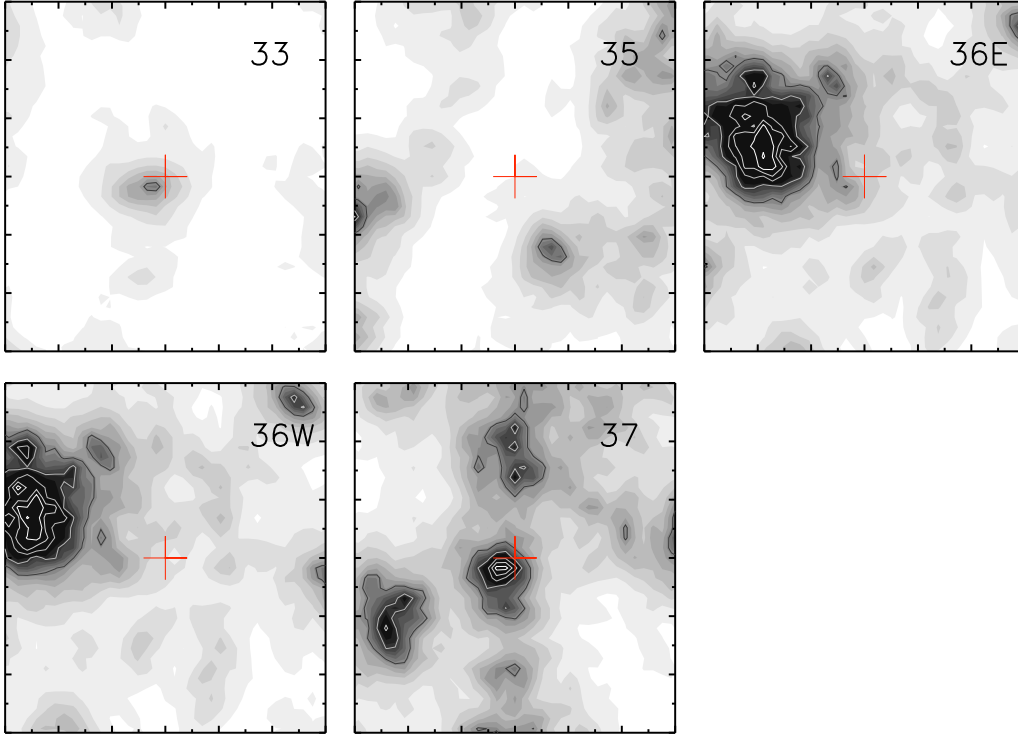


Figure 4.9: *Continued.*

Figure 4.9: *Continued.*

4.3.3 Large scale structure of low-redshift galaxies

We compared our projected density map of low-redshift BzK galaxies ($z < 1.4$) in the COSBO field with the density map of galaxies at $z < 1.4$ computed by (Scoville et al., 2007b). This allows a direct check of the reliability of our results. To match the resolution of the density map of Scoville et al. (2007b), we convolved our low-redshift BzK density map with a Gaussian kernel of FWHM = $0.9'$.

Figure 4.12 shows the result of this comparison. Despite the different selection bands in the catalogs used (i.e. Scoville et al. used the i^+ selected COSMOS catalog and here we use a K band selected catalog) and the different selection criterion used for low-redshift galaxies (i.e. Scoville et al. used photometric redshifts and we use the BzK color criterion), both density maps agree and appear to trace the same large scale structures.

The good match between both density distributions allows us to verify that our better resolution low-redshift density map is reliable and validates our results for high-redshift galaxies.

4.3.4 Probability of chance association

We estimated the significance of an association between a high-redshift galaxy overdensity and a millimeter source (for COSBO 1, 3, 6 and 16), by computing the Poisson probability that a significant number density peak is found by chance within a distance d from a millimeter source, in a background of randomly distributed high-redshift BzK number density peaks. This

Table 4.1: Significance of associations between high-redshift galaxy overdensities and millimeter sources

ID	$(S/N)_p^a$	$(S/N)_G^b$	N^c	$P(10'')^d$	$P(20'')^e$
COSBO-1	6.1	3.9	43	2.72	10.44
COSBO-3	38.5	38.2	0	$< 10^{-6}$	$< 10^{-6}$
COSBO-6	19.4	18.6	1	0.06	0.25
COSBO-16	9.3	7.7	10	0.64	2.53

^a Peak signal to noise computed directly from the density map.

^b Peak signal to noise derived from the Gaussian fit (see text).

^c Number of density peaks with a S/N greater than that of the overdensity associated to the COSBO source.

^d Poisson probability (in %) that an overdensity stronger than the observed one lies within $10''$ of the MAMBO source by chance.

^e Probability that such an overdensity lies within $20''$ of the MAMBO source by chance.

is similar to the criteria used in Chapter 2 to find the significance of radio source counterparts to the MAMBO emission. The Poisson probability is computed as

$$P(d) = 1 - \exp(-\pi d^2 N/A), \quad (4.2)$$

where N is the number of high-redshift galaxy density peaks with a density value larger than the candidate and within the area $A \sim 24' \times 24'$ of the COSBO field.

To find all the peaks in our high-redshift BzK density map, we used the IDL version of the DAOPHOT task FIND (Stetson, 1987). This routine finds the positive perturbations in the density map, and uses marginal Gaussian fits to locate the centroid and amplitude of the density peak. Although this Gaussian approximation may not be valid for fragmented density structure, it is reliable for the most significant overdensities which are typically non-fragmented.

Based on this procedure, we found 66 high-redshift galaxy density peaks with $S/N > 3$. We found that COSBO 1, 3, 6 and 16 coincide with $S/N = 3.9, 18.6, 38.2$ and 7.7 overdensities, respectively. This implies that the overdensities around COSBO 3 and 6 are the strongest within the COSBO region. Due to the high significance of the overdensities, the probability that such associations are produced by chance is negligible (Table 4.1).

4.3.5 Color-magnitude diagrams

Optical observations have shown that low-redshift galaxy clusters are dominated at their cores by a co-evolving population of bright galaxies that have similar colors. As a consequence, the brightest galaxies in clusters tend to form a “red-sequence” in color-magnitude diagrams. The formation of a red-sequence in clusters is believed to have started at redshifts $z = 1 - 2$, and has been effectively used to find proto-clusters at such redshifts (Castellano et al., 2007; Swinbank et al., 2007; Kodama et al., 2007; Zirm et al., 2008).

If galaxies in the surroundings of SMGs are physically linked to each other we might expect to see the formation of an early red-sequence. We constructed color-magnitude diagrams for those MAMBO fields that show the strongest overdensities of high-redshift BzK galaxies at the position of the MAMBO galaxies (Fig. 4.13; COSBO 1, 3, 6 and 16). We selected all galaxies located within $20''$ from the density peak and compared their colors with those of galaxies in the COSBO field. We filtered out stars by using the BzK criteria.

The high-redshift BzK galaxies selected within $20''$ from the density peak do not appear to follow a color-magnitude pattern in which galaxies share a similar color. The trend seen in this case seems to be related to the BzK criteria itself. A simple linear fit for these galaxies in the magnitude range $K = 21.5 - 24.5$ illustrates this fact. In the cases of MAMBO source fields 1 and

3, a clear bimodality exists between low and high redshift BzK galaxies (i.e low redshift galaxies are brighter and have bluer colors). For the COSBO-6 and COSBO-16 fields, both low and high redshift BzK galaxies are mixed, indicating that these galaxy groups are possibly located at an intermediate redshift $z \sim 1.4$.

Our results suggest that these structures have not yet evolved into the formation of a red sequence. However, massive MAMBO galaxies (Chapter 3) are already among the K -band brightest and reddest galaxies suggesting their important role in formation of these groups.

4.3.6 Photometric redshifts

In the previous sections we have found that significant overdensities of high-redshift star-forming galaxies, typically on scales of $\sim 20''$ radius, exist in the local environments of some millimeter selected galaxies.

To check the clustering of these galaxy groups in redshift space and their relation to the SMG, we derived photometric redshifts using the multi-wavelength extracted photometry around the stronger density peaks that are associated with the MAMBO galaxies.

To compute photometric redshifts we used the HyperZ code (Bolzonella et al., 2000) which uses a χ^2 minimization routine to find the galaxy template model that best fit the observed photometric data points. We used the whole broad band photometry available in the COSMOS field, including the optical/near-IR u^* , B^+ , V^+ , g^+ , r^+ , i^+ , i^* , z^+ , J and K_S bands and the IRAC 3.6, 4.5, 5.8 and 8.0 μm bands.

We created template SED models using the evolutionary synthesis models of Bruzual & Charlot (2003), including one constant and four exponentially decaying star-formation histories at 51 different ages, similar to the templates provided with HyperZ in its default configuration. We allowed a redshift range of $z = 0.1 - 5.0$ in steps of $\Delta z = 0.05$ and used a Calzetti et al. (2000) reddening model with optical extinction in the range $A_V = 0 - 2.5$, in steps of $\Delta A_V = 0.1$. Objects not detected in a given band were assigned a zero flux and a flux error corresponding to the 5σ magnitude limit in that band. A minimum error of 0.01 magnitudes in each photometric data point was applied to avoid infinite χ^2 values and ensure reliable results.

Figure 4.14 (left) shows the redshift distribution of K -band selected galaxies that lie within $20''$ from the high redshift BzK density peaks and that are likely associated with SMGs (COSBO 1, 3, 6 and 16). In all cases, the redshift distribution of BzK galaxies (dark-gray shaded histogram) shows a marked peak indicating a likely association of galaxies in redshift. The redshift implied for the SMGs (black histogram) is in all cases consistent with the peak of the redshift distribution. Note that most of the K -band selected galaxies in these fields are actually high-redshift BzK galaxies, unlike the low-redshift galaxies that we would expect from the field number counts at this depth.

Photometric redshifts were also computed by Ilbert et al. (2008) for the new COSMOS i^+ band selected catalog using 30 broad, intermediate and narrow photometric bands with the LePhare code (see Ilbert et al., 2006), which uses an optimized χ^2 minimization routine to find the best fitting template and redshift. The inclusion of 12 intermediate and 2 narrow bands from the COSMOS-20 survey (from Subaru imaging; Taniguchi et al. 2008, in preparation) greatly improves the redshift accuracy, as shown by a comparison with spectroscopic redshifts up to $z < 2$ (Ilbert et al., 2008). Figure 4.14 (right) show the redshifts computed by Ilbert et al. (2008) of i^+ band selected galaxies that lie within $20''$ from the high-redshift BzK density peaks, to a limiting magnitude $i^+ = 26.5$. For the COSBO-6 field, the galaxies from the i^+ band selected sample that have a high-redshift BzK match within $1.5''$ in our K band selected catalog (dark-gray shaded histogram) show a pronounced redshift peak. This is confirmed by the redshift distribution of high-redshift BzK i^+ -band selected galaxies (red histogram). For the other MAMBO source fields, this is not the case. Our photometric redshift estimates for the MAMBO galaxies are consistent with the estimation from the i^+ -band selected catalog, except for COSBO-16.

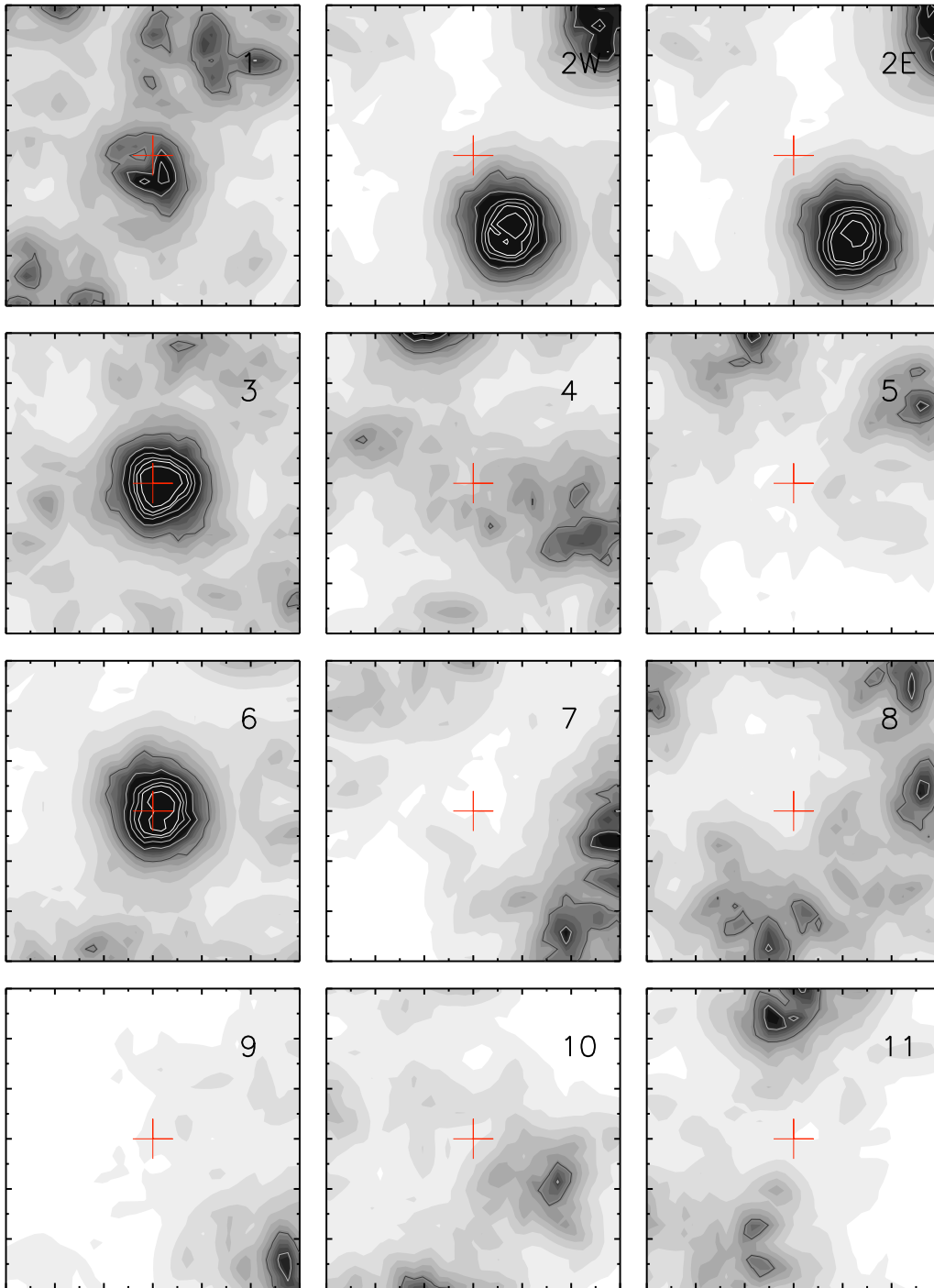
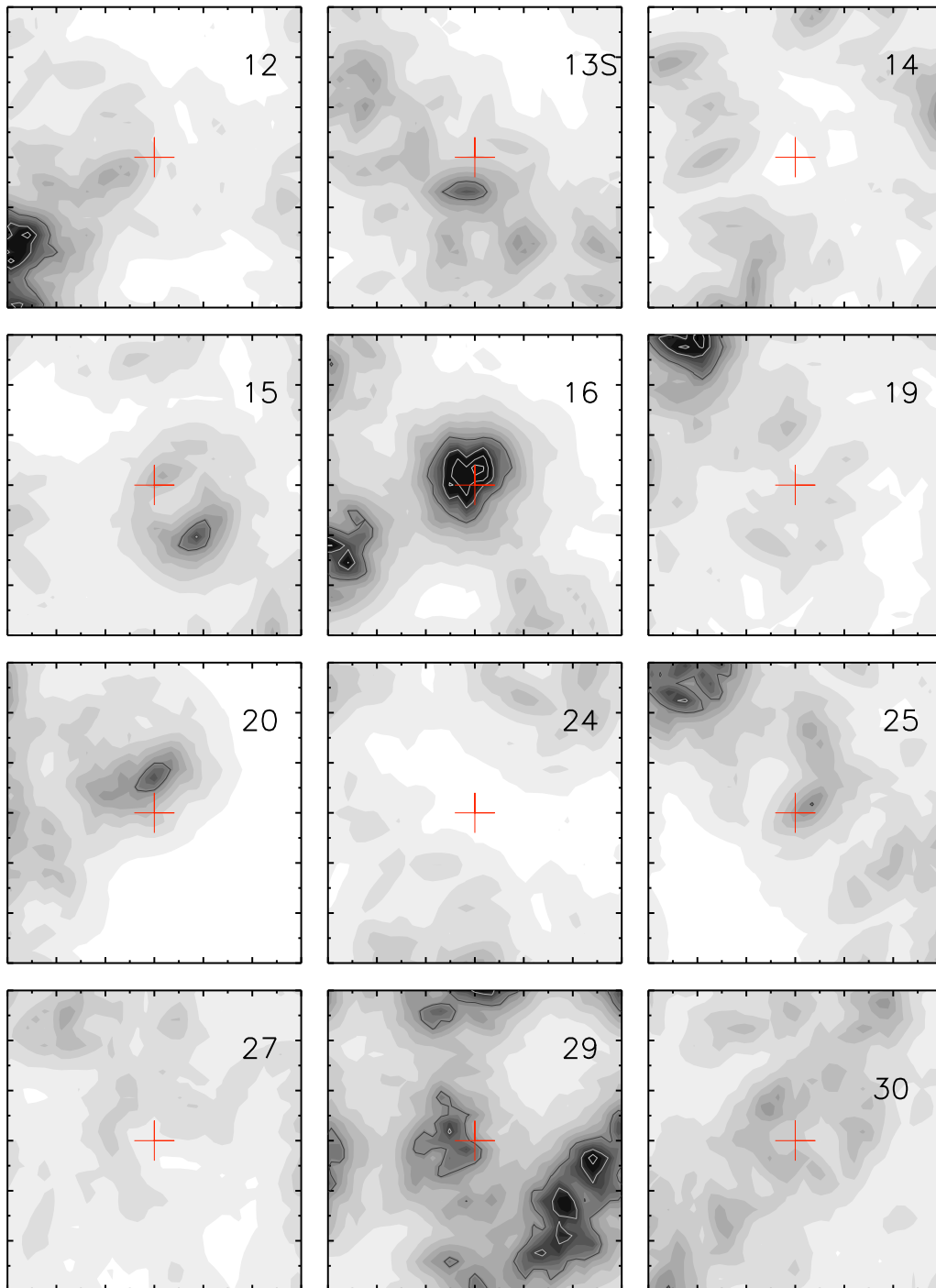


Figure 4.10: Projected number density maps ($2' \times 2'$ size) for high-redshift BzK galaxies in the fields of MAMBO sources. Contour levels are $S/N = 2\sigma, 4\sigma, 6\sigma, 8\sigma, 10\sigma$ and 15σ , where σ is the standard deviation over the local background level. Maps are centered at the MAMBO source position and major ticks are in steps of $20''$.

Figure 4.10: *Continued.*

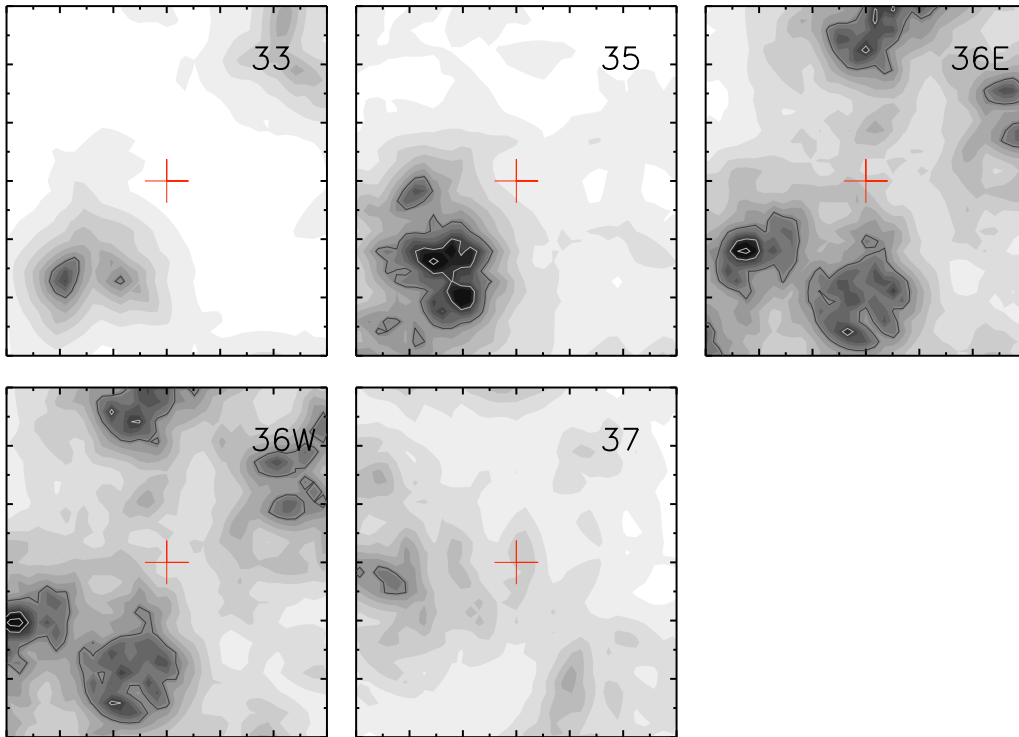


Figure 4.10: *Continued.*

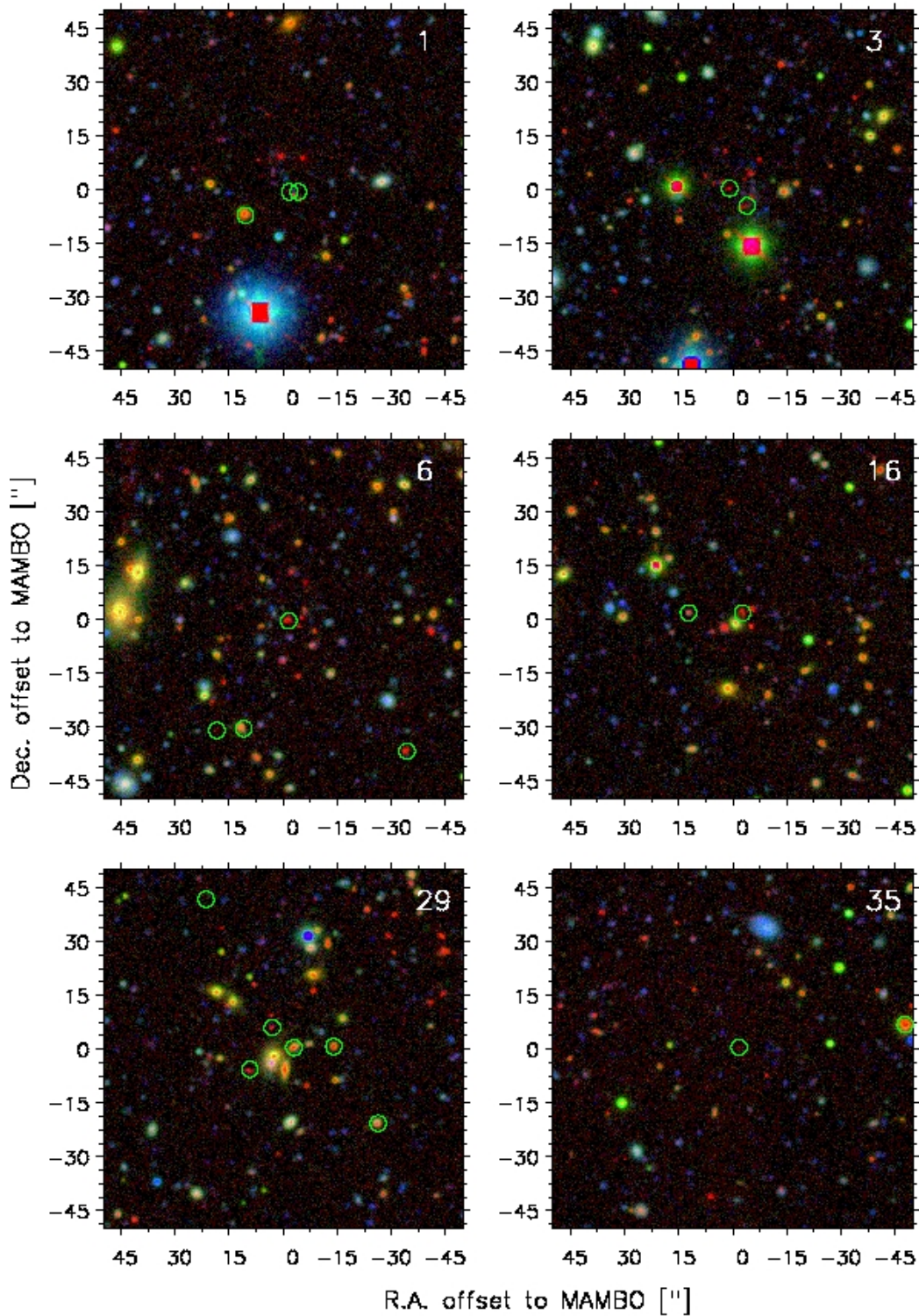


Figure 4.11: *BzK* true color images of some MAMBO galaxy fields centered at the MAMBO source position. The fields around the 4 strongest overdensities close to MAMBO sources are shown including the overdensity of low-redshift galaxies around COSBO-29. Also shown is COSBO-35, for which a group of blue high-redshift galaxies is seen to the south east of the MAMBO position. The images size is $100'' \times 100''$ and the green circles show the position of VLA 1.4 GHz sources.

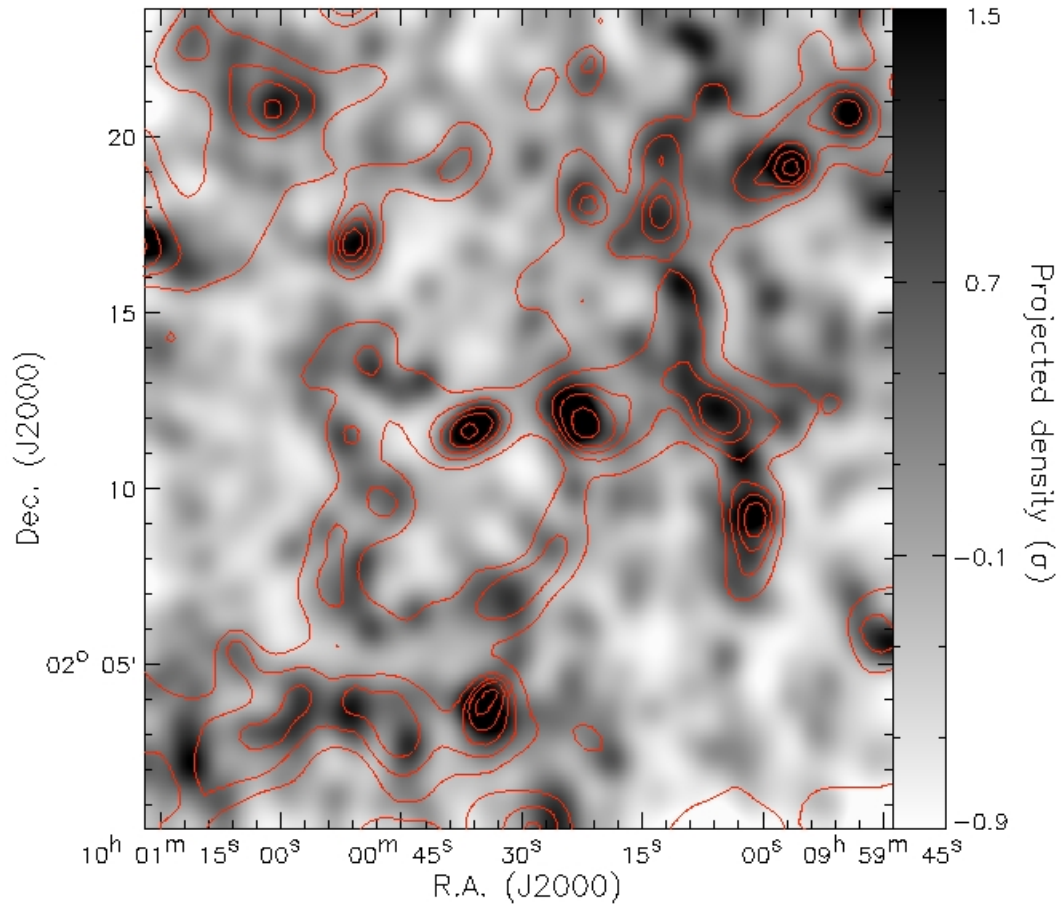


Figure 4.12: Comparison of density maps for galaxies at $z < 1.4$. The background image corresponds to our smoothed low-redshift BzK density map. Background levels are given in terms of the number of standard deviations above the average density across the field. Red contours represent the density distribution for galaxies at $z < 1.4$ computed by Scoville et al. (2007b). Red contour levels are at 30, 50, 60, 70, 80 and 100 galaxies per sq. arcmin.

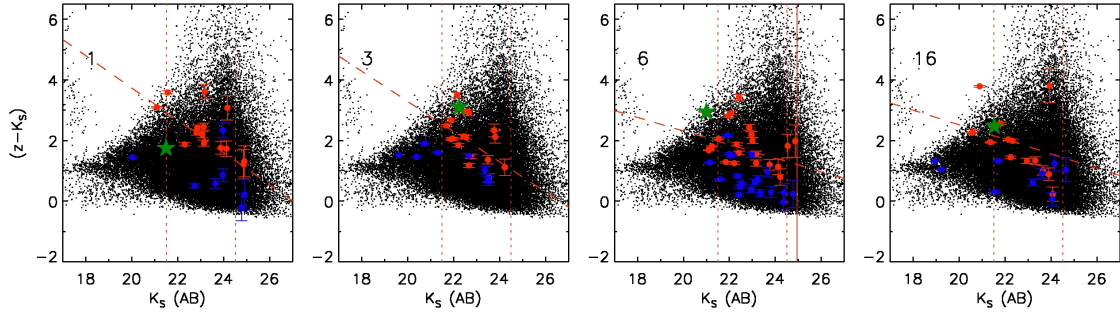


Figure 4.13: Color-magnitude diagrams for the five MAMBO source fields with strong overdensities associated. Red filled circles indicate high redshift galaxies ($z > 1.4$) selected with the BzK criteria. Blue filled circles represent low redshift galaxies ($z < 1.4$) selected likewise. Black dots show the color of typical galaxies taken from our COSBO field.

4.3.7 Comments on photometric redshifts and more

For COSBO-1, it is not clear whether the millimeter emission is produced by a radio and optically undetected high-redshift galaxy ($z > 3.5$, as implied by its radio to millimeter spectral index) or by a relatively bright IRAC/optical source with a photometric redshift of 1.4 (Table 3.1). Using our K -band selected catalog, we obtain a photometric redshift of 1.25 for the bright optical source. From the COSMOS i^+ band selected catalog we find that this source has a photometric redshift of 1.4, in agreement with the other estimates. If this is the correct counterpart, it would imply that this MAMBO source is embedded in a galaxy group at intermediate redshift. It would also imply that this source has a very cold dust temperature (< 15 K) in order to produce strong millimeter emission with a faint radio flux (Chapman et al., 2005).

COSBO-3 is embedded in a strong overdensity of high-redshift BzK galaxies. The redshift distribution of the galaxies in its close neighbourhood is consistent with most of them being at redshift $\sim 2.0 - 2.4$ (Fig. 4.14). The associated MAMBO source has a clear radio/IR/optical counterpart (COSBO-3S) with a photometric redshift of 1.8 (Table 3.1). Based on our K band selected catalog, we estimate a photometric redshift of 2.2. For the less likely radio/optical counterpart (COSBO-3N) we find a photometric redshift of 2.0 (Table 3.1), consistent with the redshift of the galaxy group and that of COSBO-3S.

COSBO-6 is also located in a very strong overdensity of high-redshift BzK galaxies. Most galaxies in this group lie at redshift $\sim 1.2 - 1.8$. We estimated a photometric redshift of 1.9 for the radio/optical identified counterpart to the millimeter emission based on the i^+ band selected catalog (Table 3.1). This agrees with our estimate based on the K band selected catalog, $z = 1.7$. Although the derived redshift for the likely counterpart is slightly larger than the one implied by the redshift distribution of the surrounding high-redshift BzK galaxies, it agrees within $\Delta z = 0.2$. The distribution of photometric redshifts from the COSMOS catalog for the surrounding BzK galaxies also shows the concentration at $z = 1.8$ (Fig. 4.14, left).

The overdensity of high-redshift galaxies surrounding COSBO-16 has a photometric redshift of ~ 1.4 . The photometric redshift derived for the likely radio/optical counterpart from the i^+ band selected catalog is 0.54 (Table 3.1), however the secondary solution implies $z = 1.4$. From the K -band selected catalog we estimate a primary solution for the photometric redshift of 1.4. The photometric redshift listed in the COSMOS catalog is, however, 2.55 which agrees better with that implied by the radio to millimeter spectral index. Because of the somewhat ambiguous redshift derivation for the millimeter source, it is difficult to relate it to the redshift peak in the surrounding galaxies, although we may be inclined to take $z = 1.4$ for the most likely case for either.

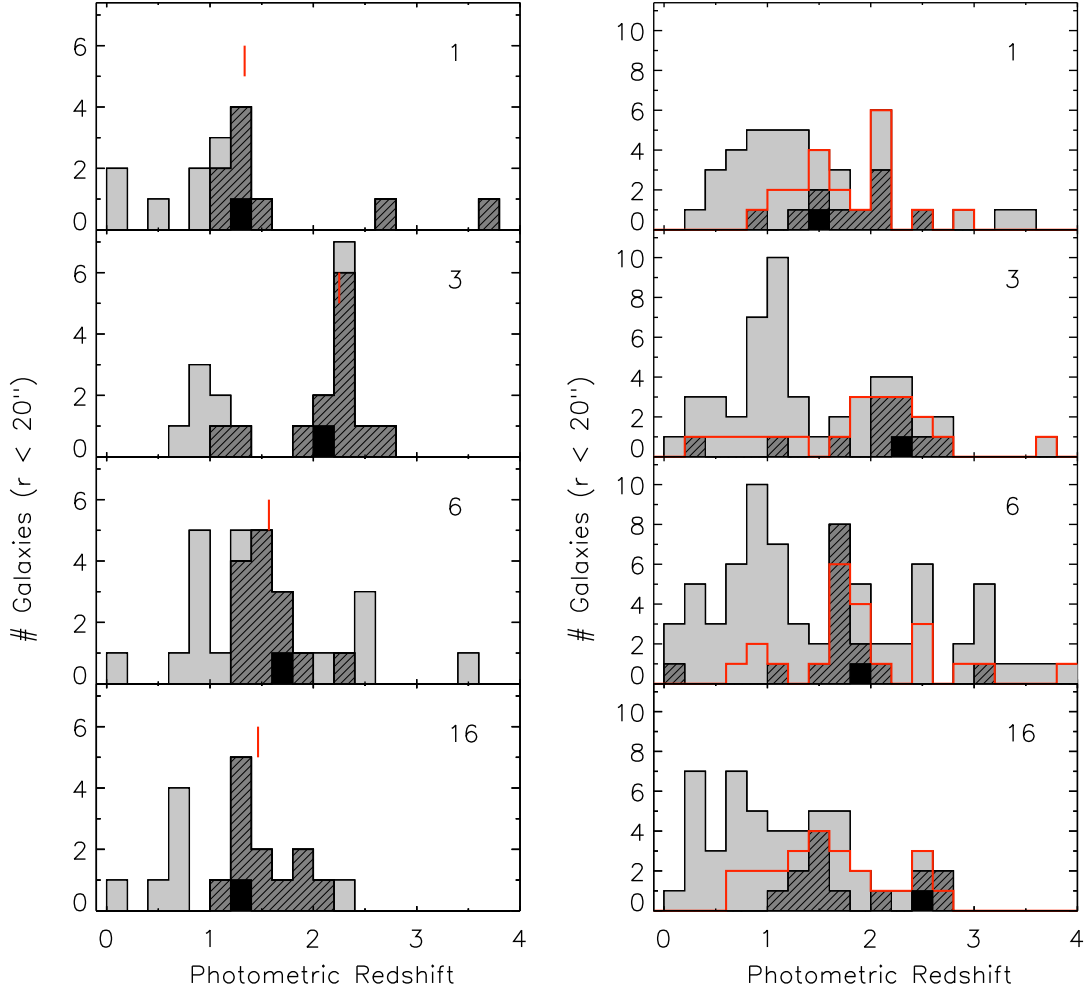


Figure 4.14: Redshift distribution for galaxies located within $20''$ from the density peak of high-redshift BzK galaxies near MAMBO sources. To the left, the light-gray histogram shows the photometric redshifts for all K-band selected objects, the dark-gray histogram shows the photometric redshifts of the K-band selected high-redshift BzK galaxies, the red mark represents the median redshift of high-redshift BzK galaxies and the black histogram shows the photometric redshift of the most likely counterpart to the MAMBO source. To the right, the light-gray histogram shows the COSMOS catalog photometric redshifts for all i^+ -band selected objects, the dark-gray histogram shows the COSMOS catalog redshifts for our K-band selected high-redshift BzK galaxies that account with it, the red histogram shows the COSMOS catalog redshifts for the i^+ -band selected high-redshift BzK galaxies and the black single object entry shows the COSMOS catalog redshift of the most likely counterpart to the MAMBO source.

4.3.8 Extended structure around COSBO-6?

COSBO sources 2 and 6 are located at $\sim 40''$ from each other (Fig. 4.9). Since the redshift derived for the galaxy group around COSBO-6 is at the edge of the redshift separation made by the BzK criteria ($z \sim 1.2 - 1.6$), it is possible that the extended structure of low-redshift BzK galaxies in the vicinity of COSBO 2E and 2W (Figure 4.10) may be connected to the overdensity around COSBO 6.

Figure 4.15 shows a color image of the region ($2.3' \times 2.3'$ size) encompassing the position of COSBO 2W, 2E and 6, and contours representing the density map. No evidence is found for an extended overdensity of high-redshift galaxies. A second density peak is found to the north-east even though it is not clear whether a link with the overdensity around COSBO-6 exists. Additionally, we marked the sources with spectroscopic redshifts from the zCOSMOS project (Lilly et al., 2007) along with the significant 1.4 GHz VLA detections, for reference. Since the current zCOSMOS survey only covers the brightest sources in the field, few $z > 1$ sources are shown. We find that four galaxies are located in the spectroscopic redshift range $z = 0.931 - 0.938$, within $\sim 60''$ distance from each other, likely being part of a galaxy group. The existence of such a group is reinforced by the strong peak in the photometric redshift distribution of this field at that redshift ($z \sim 0.9$; Fig. 4.15). This indicates that the compact overdensity of $z \sim 1.4$ galaxies seen around COSBO-6 is not related with the extended structure of low-redshift BzK galaxies in the surroundings of COSBO 2E and 2W. Note that a relatively significant fraction of the objects have photometric redshifts > 2.5 . This is likely due to the inaccuracy of photometric redshift calculations for faint optical sources (e.g. $I > 27$).

It is interesting to note, however, that the likely radio counterpart to COSBO-2E1 could not be associated with any Subaru i^+ band optical source (Chapter 2). Nevertheless, it does show a faint K -band detection for which we estimate a photometric redshift of $z = 1.31$, consistent with the redshift of the strong overdensity around COSBO-6. This could imply a larger extension for this galaxy group, although this can only be confirmed with spectroscopy.

4.3.9 The case of COSBO-29

Some SMGs coincide with low-redshift galaxy overdensities, allowing for the possibility that in these cases faint SMGs are lensed by nearby galaxy groups. Although less likely, it is also possible that some SMGs are part of these galaxy groups.

COSBO-29 can be associated with a significant overdensity of low-redshift galaxies (Fig. 4.9). Optical images show that this overdensity is related to a group of bright low-redshift galaxies, some of them clear galaxy mergers (Fig. 4.11). Based on a radio source identification, we selected one of the galaxies in this group as a possible counterpart. An overdensity of high-redshift BzK galaxies with somewhat bluer and redder colors can be seen to the south-west and north-west, respectively. However, they do not coincide with the position of the MAMBO emission.

Using the spectroscopic redshifts from the zCOSMOS project (Lilly et al., 2007), we are able to confirm the distance and link between some of the galaxies that are part of the low-redshift galaxy group. We derive an average spectroscopic redshift of 0.472, with five galaxies within 700 km s^{-1} from that redshift, and within a $1'$ radius.

This galaxy group includes a few luminous infrared galaxies as revealed by the $24 \mu\text{m}$ and radio images. Due to the multiplicity of IR and radio sources it was not possible to reliably identify the actual source of the MAMBO emission and therefore it has not been possible to decide whether the millimeter emission is produced by a source located within the galaxy group or whether it is produced by a distant galaxy.

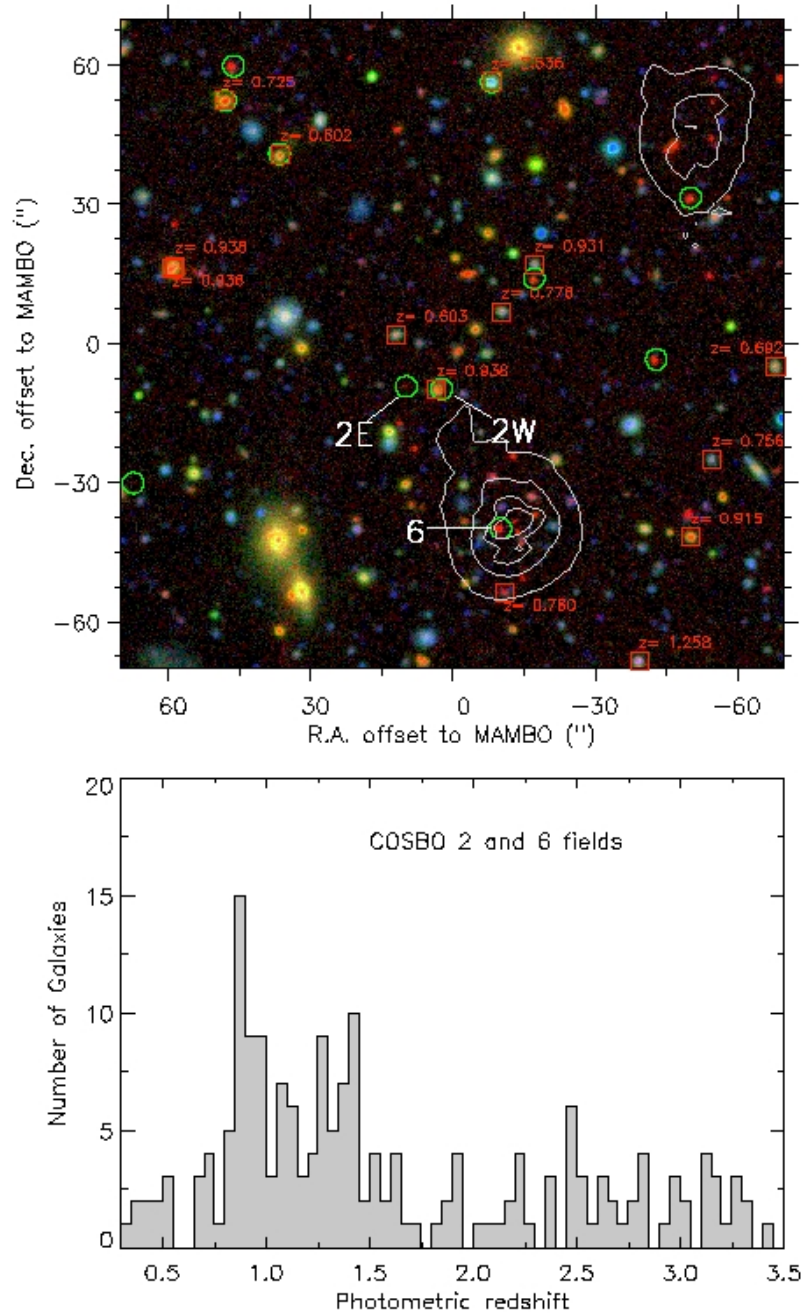


Figure 4.15: On top, we show the $2.3' \times 2.3'$ BzK color image covering the position of COSBO-2 and COSBO-6. White contours represent the density map at 2, 6, 12, and 18σ levels over the average across the field. Green circles mark the position of 1.4 GHz VLA sources and red circles indicate the position of spectroscopic redshift targets (zCOSMOS). On the bottom, the redshift distribution for the K band selected galaxies in this field is shown.

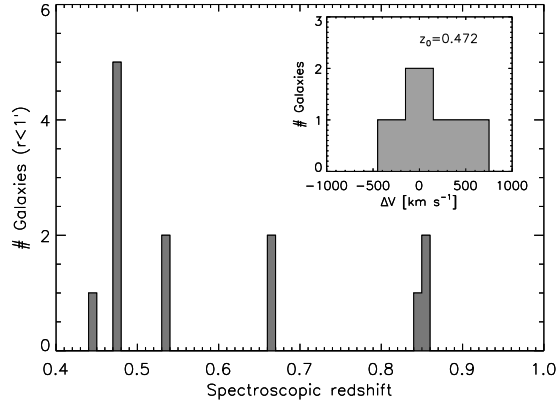


Figure 4.16: Spectroscopic redshifts for galaxies within $1'$ from COSBO-29. The embedded plot at the top right shows a close-up view around the redshift of the galaxy group, $z = 0.472$.

4.4 Discussion

Our main findings can be summarized as follows.

1. Significant overdensities of high redshift BzK galaxies ($K < 23$) appear to be associated with some MAMBO galaxies. In many cases, density enhancements of low-redshift galaxies are also present and the association may be due to gravitational lensing of a fainter background SMG.
2. The strongest galaxy overdensities of high-redshift galaxies are compact in size and very concentrated around the SMGs. We find typical sizes of $\sim 20''$, implying physical scales of ~ 170 kpc in the $1.5 - 2.0$ redshift range, similar to the overdensities found around radio galaxies at comparable redshifts.
3. The associations of significant overdensities of high-redshift galaxies and SMGs are unlikely to be produced by chance. Two of these associations correspond to the strongest overdensities of BzK galaxies in the COSBO field.
4. In the cases where strong overdensities are present, color-magnitude diagrams indicate that the galaxies do not share similar colors. A mixture of blue and red objects seem to compose some of these groups. In all cases, the SMG appears to be among the K -band brightest galaxies in such overdensities.
5. Photometric redshifts indicate that the galaxies in these overdensities are indeed clustered in redshift.

These facts provide substantial evidence for the formation of some SMGs in galaxy groups. Similar results have been found in radio loud QSO fields, with similar sizes and redshifts (e.g. Hall & Green, 1998; Hall et al., 2001; Best et al., 2003). In an evolutionary context, a question that arises is whether the enhanced galaxy clustering observed in some SMG fields represents a different pathway for galaxy cluster formation to that observed in radio galaxy fields or whether a connection between starbursting SMGs and powerful radio galaxies exists and what we observe are different stages of the same process of cluster formation.

Starbursting SMGs have been observed to be rich mergers with large amounts of dust and gas (Greve et al., 2005; Tacconi et al., 2006, 2008). Radio galaxies are evolved systems, generally

massive elliptical galaxies, that host powerful AGN. These two kind of activities (starburst and AGN) are connected, as suggested by observations, in both the distant (Carilli et al., 2001) and the local Universe (Sanders et al., 1988a), and numerical simulations (Mihos & Hernquist, 1994). According to this scenario, two gas-rich galaxies merge, funneling large amounts of gas and dust toward the nucleus, where a SMBH grows through accretion. When the SMBH has grown sufficiently, it is able to disperse the surrounding dust and gas and can be observed as an optically luminous QSO. Radio galaxies may evolve through this sequence as long as the central SMBH becomes sufficiently active to generate powerful radio jets. In the meantime, the host galaxy evolves passively and becomes a massive spheroidal galaxy.

If submillimeter and radio galaxies are the same kind of object in a different evolutionary stage, it may thus be that the formation of galaxy clusters at high redshifts is related to both submillimeter and radio galaxies. Since SMGs represent an earlier and short ($\sim 10 - 100$ Myr) phase in the formation of a massive galaxy, it may well be that the clustering observed in their environments constitute a stage in the formation of galaxy clusters that is earlier than that observed in the environments of radio galaxies. This is supported by the lack of a color-magnitude relation in SMG fields, which we might expect to observe in relatively evolved galaxy groups and clusters, and the mixture of blue and red galaxies in these diagrams, that points to a mixture of star-forming and passive galaxies.

The appearance of a color-magnitude relation in galaxy clusters requires the presence of sufficiently red and bright, and therefore massive galaxies (with stellar masses $\sim 10^{11} M_{\odot}$ at $z \sim 1 - 2$). Only a few galaxies at $z \sim 3$ were able to become massive enough at an age corresponding to $z \sim 1 - 2$. For galaxies with a stellar mass $\sim 10^{10} M_{\odot}$ at $z \sim 3$, extreme star formation rates ($> 100 M_{\odot} \text{ yr}^{-1}$) are needed to build up a galaxy stellar component of $\sim 10^{11} M_{\odot}$ at $z \sim 2$ (in about 1 Gyr Kodama et al., 2007). Such SFRs are only observed in ULIRGs (SFR $\sim 100 M_{\odot} \text{ yr}^{-1}$) and SMGs (SFR $\sim 1000 M_{\odot} \text{ yr}^{-1}$). In Chapter 3, we found that SMGs have already assembled a strong stellar component by $z \sim 2$ ($\sim 10^{11} M_{\odot}$). Here, we found that SMGs lying in high-redshift galaxy overdensities are among the K band brightest galaxies in each of the color-magnitude diagrams, suggesting that they are likely progenitors of the brightest and more massive galaxies in clusters.

We found that the observed overdensities near MAMBO SMGs are very compact, suggesting that they could be the cores of very young clusters. It is possible that the formation of structures related to SMGs is not merely restricted to small galaxy groups. Chapman et al. (2008) studied a larger association of SMGs ($\sim 7'$ size) at redshift $z = 1.99$. They find that the strong concentration of SMGs is not accompanied by a similar overdensity of UV selected galaxies. This implies that such systems may not have sufficient baryon mass to evolve into the rich galaxy clusters observed today. Chapman et al. (2008) suggest that this may also be the case for the galaxy overdensities observed around luminous AGNs. Nevertheless, their study did not include evolved quiescent or massive IR selected galaxies, which can account for a substantial contribution to the total stellar mass. On the other hand, Chapman et al. (2008) pointed out that associations of SMGs exist on small scales, as suggested by two relatively close SMG pairs (of $9''$ and $17''$, respectively), which is consistent with our results (see Chapter 5).

Although our results indicate the existence of compact overdensities that hint at the early formation of galaxy clusters at $z \sim 2$, similar studies over larger samples of submillimeter selected galaxies will provide better statistics and will help to understand the abundance of such SMG-cluster associations. We will need accurate spectroscopic redshifts and a proper computation of the two-point correlation function, from large scale submillimeter surveys with LABOCA, AzTEC, SCUBA2 and Herschel to discern whether structures around SMGs may evolve into massive galaxy clusters. We are currently performing a similar analysis over a likewise deep submillimeter blank field, the E-CDFS. This study, along with our COSBO survey will permit to study of such SMG-cluster associations.

Interferometric continuum imaging of MAMBO sources

5.1 Introduction

Submillimeter and millimeter wavelength blank field surveys with SCUBA and MAMBO, discovered a population of heavily dust-obscured starburst galaxies at high redshifts (Smail et al., 1997; Barger et al., 1998; Eales et al., 1999; Bertoldi et al., 2000). These (sub)millimeter galaxies (SMGs) contribute a large fraction to the cosmic IR background (Puget et al., 1996) and current models suggest that they likely represent the formation of massive spheroidal galaxies at redshifts between 2 and 5 (Dunlop, 2001; Baugh et al., 2005).

The identification of optical counterparts to the (sub)millimeter sources has mainly been based on the identification of radio sources, detected through deep VLA 1.4 GHz imaging ($\sim 5-15 \mu\text{Jy}$). The direct search for counterparts in the optical wavebands is not practical due to their common faintness and the high number density of optical sources within the positional uncertainty. For about 50% – 80% of all (sub)millimeter sources precise positions could be determined from an identification of faint radio counterparts (e.g. Ivison et al., 2002, 2005, 2007). This has allowed the study of the properties of the galaxies responsible for the (sub)millimeter emission through optical, near-IR, or X-ray imaging and spectroscopy, and once accurate spectroscopic redshifts became available, has enabled CO imaging (e.g. Chapman et al., 2005; Alexander et al., 2005; Borys et al., 2005; Dye et al., 2008; Kovács et al., 2006; Neri et al., 2003; Greve et al., 2005; Tacconi et al., 2006).

Despite the great advances achieved in the study of SMGs, the depth of radio observations limits the identification of typical (sub)millimeter sources to redshifts below ~ 3 , since due to the strong K-correction, the radio flux (unlike the submillimeter flux) drops rapidly with redshift (Carilli & Yun, 1999). For instance, radio-selected SMGs were found with a median redshift of 2.3 (Chapman et al., 2005). However, mid-IR spectroscopy has suggested that a higher redshift, significant fraction of SMGs at higher redshifts, and among them the brightest in the (sub)millimeter, have been missed in radio identified samples, shifting the mean redshift of the SMGs to a higher value of ~ 2.8 (Lutz et al., 2005; Menéndez-Delmestre et al., 2007; Valiante et al., 2007).

Massive starburst galaxies at the highest redshifts place tight constraints on galaxy formation models. Moreover, the flatness of the (sub)millimeter redshift selection function may allow to find sources even at very high redshifts ($z > 5$), touching the epoch of cosmic reionization. Good candidates for such high redshift objects are (sub)millimeter sources with very faint radio counterparts (Dannerbauer et al., 2002, 2004, 2008; Younger et al., 2007). Albeit it is also possible that some of the weakest (sub)millimeter “detections” may be spurious if their fluxes are boosted

by confusion noise, this is less likely for the more significant detections. To identify these sources in the optical/near-IR for spectroscopic follow-up, (sub)millimeter interferometry is the most reliable approach. It also constitutes an important tool in the identification of counterparts in cases where we suspect there may be more than one SMG within the typical beam of single dish (sub)millimeter telescopes.

In this chapter, we report on interferometric millimeter continuum imaging observations that were conducted to accurately locate the position of three of our MAMBO detections in the COSMOS field. Two of them were not significantly detected at radio wavelengths, thus making them good candidates for high redshift SMGs. The other MAMBO source is located in an overdense region of high redshift star-forming galaxies, suggesting that it could actually be a group of faint SMGs. In Section 2, we explain our source selection criteria and describe our observations and data reduction. In Section 3, we present the identification of optical counterparts to our millimeter detections, their SEDs and photometric redshifts. In Section 4, we discuss the implications of our findings.

5.2 Observations

5.2.1 Sample selection

We selected two sources from the MAMBO 1.2 mm survey of the COSMOS field that are good candidates to be at high redshifts. The other source was selected based on the enhanced number density of high-redshift *BzK* galaxies found in its environment.

MM J100007+021149 (hereafter COSBO-4) is one of the strongest MAMBO detections with a boosting corrected millimeter flux¹, $S_{1.2 \text{ mm}} = (5.7 - 0.15) \pm 0.9 \text{ mJy}$. We did not find any 1.4 GHz radio source to a $> 3.5\sigma$ level of $24 \mu\text{Jy}$ within $12''$ from the millimeter emission peak (Chapter 2). Using the radio to millimeter spectral index as a measure of redshift (see Section 5.3.3; Carilli & Yun, 1999), the upper limit in the VLA 1.4 GHz flux combined with the MAMBO 1.2 mm flux implies a redshift > 3 . We found three $24 \mu\text{m}$ sources within $10''$ from the MAMBO peak position (Chapter 2). Two of them are consistent with $z \sim 2$. However, since they all have comparable $24 \mu\text{m}$ intensities and lie at a similar distance ($\sim 7''$) from the millimeter peak, it is not clear which of them, if any, is the real counterpart to the millimeter source. The lack of radio emission hints at a higher redshift association that is not compatible with the $24 \mu\text{m}$ sources.

MM J100008+021304 (COSBO-6) is located in a strong overdensity of *BzK* galaxies at $z \sim 1.5$. It has a boosting corrected integrated flux density of $S_{1.2 \text{ mm}} = (5.2 - 0.2) \pm 0.9 \text{ mJy}$ (Chapter 2). A secure radio/optical counterpart exists for this MAMBO source and its redshift is consistent with that of galaxies in its surroundings ($z \sim 1.5$). Since most of the objects in its close environment appear to be star forming galaxies, it is likely that the MAMBO emission is not merely produced by a single SMG, but by two or more, as indicated by the fragmented millimeter emission found in the MAMBO map.

MM J100026+021529 (COSBO-9) is a significant millimeter source with a boosting corrected millimeter flux of $S_{1.2 \text{ mm}} = (4.9 - 0.24) \pm 0.9 \text{ mJy}$. It is located in a region devoid of radio and $24 \mu\text{m}$ sources (Chapter 2) and thus no counterpart candidates could be identified. The radio to millimeter spectral index implies a very high redshift ($z > 4$), unless this is a spurious millimeter detection.

5.2.2 PdBI millimeter continuum imaging

We performed 1.3 mm continuum (230 GHz) observations using the IRAM Plateau du Bureau Interferometer (PdBI) six elements array in its compact D-configuration in October and November

¹Including a statistical correction that accounts for the possible boost in flux due to confusion noise

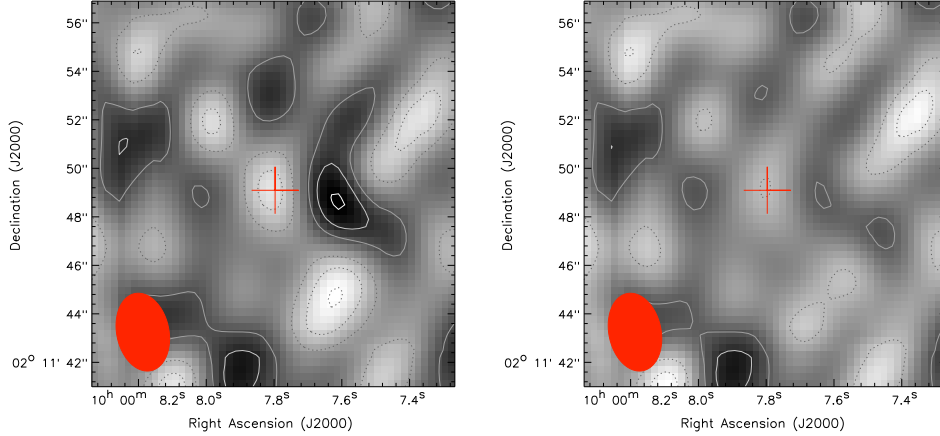


Figure 5.1: Clean (left) and residual (right) map of the 1.3 mm continuum emission toward COSBO-4. The contour step is 0.548 mJy/beam, corresponding to 1σ . Dotted contours are negative, solid contours are positive. The red ellipse represents the observed synthesized beam. The red cross indicates the phase tracking center (MAMBO source position).

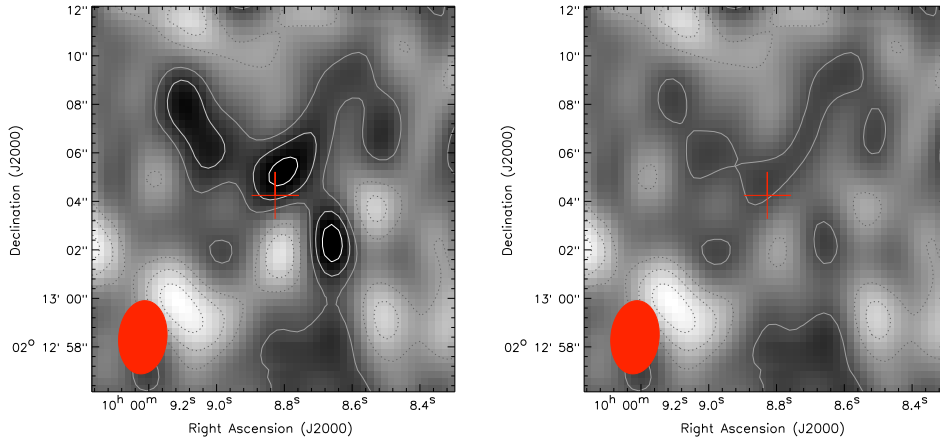


Figure 5.2: Clean (left) and residual (right) map of the 1.3 mm continuum emission toward COSBO-6. The contour step is 0.292 mJy/beam (1σ). Dotted contours are negative, solid contours are positive. The red ellipse represents the observed synthesized beam. The red cross indicates the phase tracking center (MAMBO source position).

2007. All observations were done in good millimeter weather conditions with precipitable water vapor values $\lesssim 5$ mm. We used the full 1 GHz bandwidth available in the 1.3 mm receivers. The beam size at this wavelength is typically between $2''$ and $3''$ with a field of view of $21.9'' \times 21.9''$ (FoV, i.e. the FWHM of a 15 m component antenna primary beam). The observing frequencies were 231.98 GHz for COSBO-4 and 231.52 GHz for COSBO 6 and 9.

We reduced the data using the CLIC package from the IRAM GILDAS software. This involves the calibration of flux amplitudes, phases and RF passbands for each source, flagging the data when necessary (e.g. when part of the data were taken under bad weather conditions), and the creation of data tables that contain the final visibility values for each frequency channel, spatial frequency (u, v) and time. Finally, we analyzed the data using the MAPPING package from the

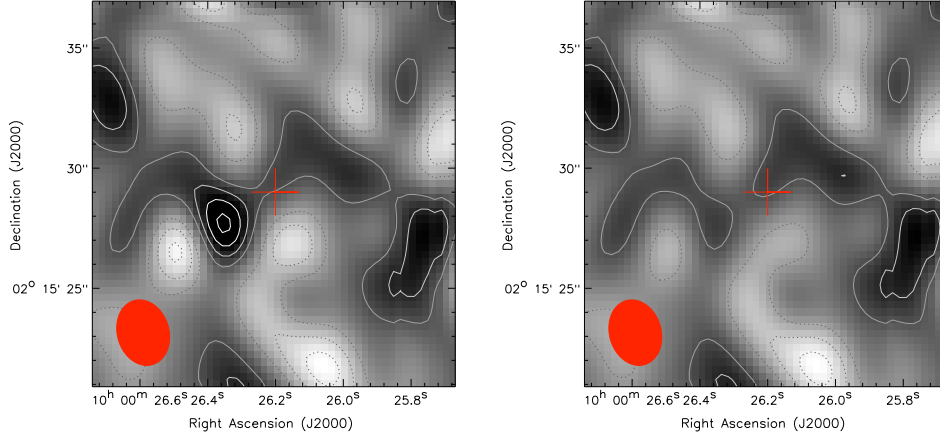


Figure 5.3: Clean (left) and residual (right) map of the 1.3 mm continuum emission toward COSBO-9. The contour step is 0.387 mJy/beam (1σ). Dotted contours are negative, solid contours are positive. The red ellipse represents the observed synthesized beam. The red cross indicates the phase tracking center (MAMBO source position).

GILDAS software. This implies imaging and deconvolution of the visibilities.

5.2.3 Image deconvolution

An important part in the creation of a meaningful astronomical “image” from interferometric data is the deconvolution of the visibilities. This implies to obtain a proper measure of the intensity distribution from the visibilities, using *a priori* information about the source intensity distribution, and knowledge about the dirty beam and noise².

Since our main goal is to locate the position of our MAMBO sources, and thereby to check whether these are real detections or spurious sources, it is crucial to deconvolve our interferometric images by using as little information as possible about the source spatial distribution without losing information about their intensity.

In order to deconvolve our images consistently, we used the CLEAN/HOGBOM cleaning algorithm (Högbom, 1974) in two steps. First, we applied the default HOGBOM algorithm that cleans the inner quarter of the dirty image, which is the region where the millimeter source should lie. The resulting cleaned image provides a hint about the possible location of the millimeter source. Next, we define a polygon comprising the most significant sources and deconvolve the dirty image again using HOGBOM and the newly defined region. The final images reach rms noise levels of 0.548 mJy/beam, 0.292 mJy/beam and 0.387 mJy/beam for COSBO 4, 6 and 9, respectively.

²IRAM GILDAS Documentation 2007, J. Pety, available at <http://www.iram.es/IRAMFR/GILDAS/>

Table 5.1: PdBI 1.3 mm continuum observations.

ID ^a	Name MMJ. . .	Major ^b (arcsec)	Minor ^c (arcsec)	P.A. ^d (deg)	ν_{obs} ^e (GHz)	rms noise ^f (mJy/beam)	R.A. ^g (J2000)	Dec. ^h (J2000)	S _{1.3mm} ⁱ (mJy)	S _{1.2mm} ^j (mJy)
4	100007+021149	3.26±0.01	2.30±0.01	14.31±0.34	231.98	0.548	10 00 07.608	+02 11 48.93	2.71±0.71	(5.7–0.15)±0.9
6	100008+021304	3.03±0.01	2.13±0.01	173.09±0.03	231.52	0.292				(5.2–0.20)±0.9
6C [†]							10 00 08.871	+02 13 04.97	0.87±0.52	
6S [†]							10 00 08.666	+02 13 02.43	0.94±0.52	
6N [†]							10 00 09.076	+02 13 07.33	1.14±0.52	
9	100026+021529	2.79±0.01	2.27±0.01	21.05±0.62	231.52	0.387	10 00 26.351	+02 15 27.52	2.02±0.58	(4.9–0.24)±0.9

[†] All sources detected in the same field. ^a MAMBO identification number. ^b Beam major axis. ^c Beam minor axis. ^d Position angle. ^e Observing frequency. ^f Root mean square noise level. ^g Right ascension. ^h Declination. ⁱ Integrated 1.3 mm continuum flux. ^j MAMBO 1.2 mm integrated flux

Table 5.2: Multiwavelength counterparts to the 1.3 mm detections.

ID	Radio					Optical				
	R.A. ^a (J2000)	Dec. ^b (J2000)	S _{1.4GHz} ^c (μ Jy)	$\alpha_{1.4}^{270}$ ^d	z_{radio} ^e	R.A. ^a (J2000)	Dec. ^b (J2000)	i^+ ^f (mag)	$z_{\text{phot}}(1)$ ^g	$z_{\text{phot}}(2)$ ^h
4.	10 00 07.56	+02 11 47.75	23.1±7	0.934	3.8 ^{+0.6} _{-0.5}	10 00 07.55	+02 11 47.23	24.61±0.01	3.26	0.63
6C.	10 00 08.80	+02 13 04.38	66.9±7	0.502	1.4 ^{+0.2} _{-0.2}	10 00 08.83	+02 13 04.11	24.86±0.02	1.89	1.78
6S.1.			< 21	> 0.74	> 2.4	10 00 08.70	+02 13 01.73	26.09±0.16	0.62	1.75
6S.2.			< 21	> 0.74	> 2.4	10 00 8.57	+02 13 01.83	25.66±0.11	0.62	0.98
6N.			< 21	> 0.78	> 2.7	10 00 09.02	+02 13 07.46	26.24±0.19	1.29	1.01
9.	10 00 26.36	+02 15 28.27	21.75±7	0.887	3.4 ^{+0.7} _{-0.5}	10 00 26.37	+02 15 28.38	28.56±0.34	1.15	0.95

^a Right ascension. ^b Declination. ^c VLA 1.4 GHz flux. ^d Radio to millimeter spectral index. ^e Radio photometric redshift. ^f Subaru i^+ band magnitude. ^g Optical photometric redshift (primary solution). ^h Optical photometric redshift (secondary solution).

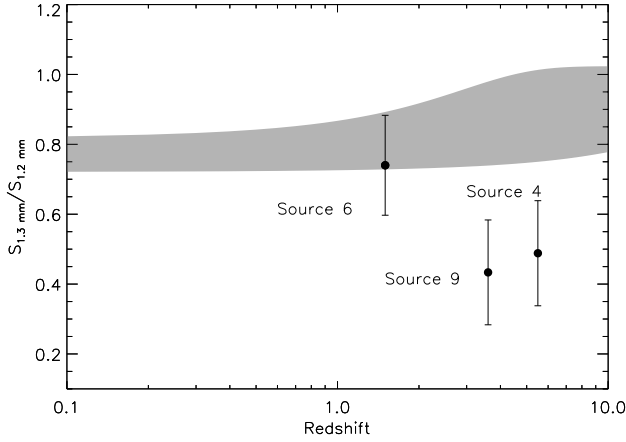


Figure 5.4: Continuum 1.3 mm to 1.2 mm flux ratios as a function of redshift. Black dots represent the values observed with PdBI and MAMBO (boosting corrected). The sources were placed at their most likely radio photometric redshift. The shaded region corresponds to the range of $S_{1.3 \text{ mm}}/S_{1.2 \text{ mm}}$ spanned by the gray bodies with $T_d = 10$ and $\beta = 1.0$ (lower limit) and $T_d = 70$ and $\beta = 2.0$ (upper limit).

5.3 Results

Figures 5.1, 5.2 and 5.3 show the clean and residual images for COSBO 4, 6 and 9, respectively. Table 5.1 summarizes our observations.

The PdBI map of COSBO-4 shows a single millimeter source with a peak S/N ratio of 3.8 lying at a distance of $2.86''$ from the MAMBO central position. No other significant source is seen in the map.

For COSBO-6 we find two PdBI sources with peak S/N ratios of 3.4 and 3.7 at a distance of $\sim 1''$ (COSBO-6C) and $\sim 3''$ (COSBO-6S) from the MAMBO original position, respectively. A third less significant 1.3 mm source is found $\sim 5''$ north-east (COSBO-6N), with a peak S/N = 2.78 from the MAMBO position.

COSBO-9 can be identified with a 3.5σ peak in the PdBI map. It lies at a distance of $2.5''$ from the MAMBO position.

To precisely measure the position and integrated fluxes of the possible PdBI source detections, we fitted single point source models directly to the visibilities. This method avoids the imaging and deconvolution steps that may introduce artifacts in the results. Table 5.1 presents the measured fluxes for the detected PdBI sources.

5.3.1 Flux discrepancy

The comparison of the fluxes measured at 1.3 mm and 1.2 mm with PdBI and MAMBO shows an evident inconsistency, particularly for COSBO-4 and COSBO-9. We might expect similar flux values given the similar observing frequencies. This difference, on one hand, could be explained by flux boosting of a faint millimeter source by noise in the MAMBO map, which would produce a larger measured 1.2 mm flux. On the other hand, it could be an effect of the far-IR SED passing through these bands at different redshifts.

In order to study the flux that we might expect for typical far-IR SEDs as a function of redshift, we compared the measured 1.3 mm to 1.2 mm flux ratios with the expected flux ratios derived from dust models at different redshifts (Fig. 5.4). Using an optically thin ($\tau \ll 1$) single

component gray-body spectrum dust model, the ratio between fluxes measured at ν_1 and ν_2 can be expressed as

$$\frac{S(\nu_1)}{S(\nu_2)} = \frac{[B(\nu_1, T_d) - B(\nu_1, T_{BG})] \kappa(\nu_1)}{[B(\nu_2, T_d) - B(\nu_2, T_{BG})] \kappa(\nu_2)}, \quad (5.1)$$

where $B(\nu, T_d)$ is the black body spectrum, $T_{BG} = 2.73 \times (1 + z)$ K is the cosmic background radiation temperature and T_d is the dust temperature. The dust absorption coefficient κ_d is given by (Kruegel & Siebenmorgen, 1994)

$$\kappa_d(\nu) = 0.4 \left(\frac{\nu}{250 \text{ GHz}} \right)^\beta [\text{cm}^2/\text{gr}] \quad (5.2)$$

and we allow the spectral index β to vary between 1 and 2 (Priddey & McMahon, 2001). As expected, the 1.3 mm to 1.2 mm flux ratios remain almost constant up to redshift $z = 3$, with little variation for larger redshifts. In any case, the modeled flux ratios are higher than the ones observed toward COSBO-4 and COSBO-9. Even if we compare with a model $T_d = 10$ K, $\beta = 1.0$, which is believed to be a fairly extreme case (Greve et al., 2008; Kovács et al., 2006), the measured flux ratios are lower by about a factor of 2. These results suggest that most of the difference is likely produced by flux boosting, although they are also consistent within the measurement uncertainties at the $\sim 2\sigma$ level.

For COSBO-6, at least three PdBI sources are found within the area covered by the MAMBO beam. The integrated MAMBO 1.2 mm flux over the whole region is $S_{1.2\text{mm}} = (5.2 - 0.2) \pm 0.9$ mJy, however the structure is fragmented. It is possible that some of the measured MAMBO flux is product of noise (i.e. the northern spike in the MAMBO map; see Chapter 2 – Fig. 2.10). Even though, the integrated flux across the entire region covering the millimeter source candidates in the PdBI map gives $S_{1.3\text{mm}} = 3.7 \pm 0.26$ mJy, which is consistent at the $< 1\sigma$ level with the MAMBO flux estimate as shown in Fig. 5.4.

5.3.2 Multi-wavelength counterparts

Figures 5.5, 5.6 and 5.7 show optical/IR images around COSBO 4, 6 and 9, respectively. It is evident that the galaxies responsible for the millimeter emission are very faint at optical and IR wavelengths. The VLA 1.4 GHz map (blue contours) indicates that the PdBI sources for COSBO-4 and COSBO-9 are associated with 3.2σ and 3.1σ radio emission peaks, respectively. COSBO-6C is associated with the significant radio source that had previously been identified as the likely counterpart to the MAMBO emission, however, no radio association can be made for the COSBO-6N and COSBO-6S down to a 2σ level.

In order to properly locate the faint optical counterparts to our PdBI detections, we extracted multi-band photometry in the region around to the millimeter sources ($16'' \times 16''$; Figs. 5.5, 5.6 and 5.7) using SExtractor (Bertin & Arnouts, 1996) and the Subaru i^+ band images for detection. We measured fluxes in the u^* , B , V_j , g^+ , r^+ , i^+ , i^* , z^+ , J and K_S bands using an aperture of $3''$ and in the IRAC bands using an aperture of $1.9''$. Small corrections were applied to convert the aperture fluxes to total fluxes.

In Fig. 5.8 we see that three faint optical sources are found toward the PdBI detection of COSBO-4. The faint radio peak can be associated with the brightest of these optical sources, making it the most likely counterpart (Fig. 5.5).

Three PdBI sources are detected toward COSBO-6. The central PdBI and VLA source (COSBO-6C) is associated with a bright optical/IR counterpart (Fig. 5.6). Although we do not detect any significant optical source coincident with COSBO-6S and COSBO-6N, the COSMOS point source catalog (Capak et al., 2007) lists two faint candidates ($i^+ \sim 26$) that lie at a similar distance from the millimeter emission peak COSBO-6S (6S.1 and 6S.2), and one faint possible counterpart to COSBO-6N (Fig. 5.8). Since we do not detect such optical counterparts with

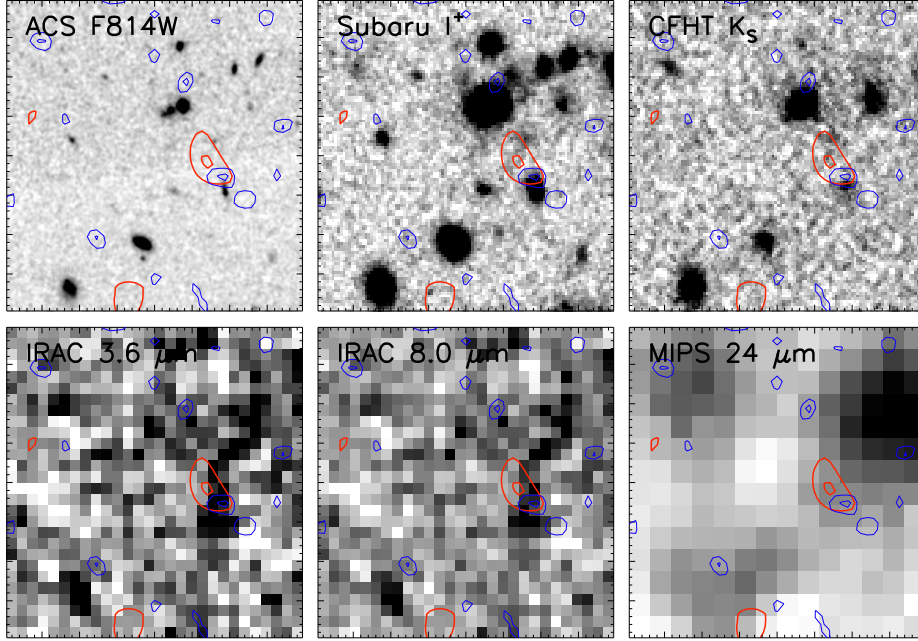


Figure 5.5: Multi-wavelength images of the field of COSBO-4 ($16'' \times 16''$). Background images are the HST ACS I, Subaru i^+ , CFHT K, IRAC $3.6 \mu\text{m}$, IRAC $8.0 \mu\text{m}$ and MIPS $24 \mu\text{m}$ bands. Red contours represent the continuum 1.3 mm S/N map at 2σ , 3σ and 4σ levels. Blue contours represent the continuum 1.4 GHz S/N map at 2σ , 3σ , 4σ and 5σ levels ($\sigma = 7 \mu\text{Jy}$).

our own photometry and given the faintness of such sources, we consider them as tentative associations.

Finally, the PdBI/VLA source COSBO-9 coincides with the position of a very faint optical counterpart ($i^+ \sim 28$; Figure 5.8), indicating that the emitting galaxy is strongly obscured.

5.3.3 Photometric redshifts

We computed optical/IR photometric redshifts using the HyperZ code (Bolzonella et al., 2000). It exploits a χ^2 minimization routine in order to find the best redshift, spectral template and extinction correction that best fit the photometric data points. For the COSBO 4, 6C and 9, we employed our own multi-wavelength photometry in the u^* , B , V_j , g^+ , r^+ , i^+ , i^* , z^+ , J , K_S and IRAC bands. For the other sources (COSBO 6S.1, 6S.2 and 6N), the COSMOS catalog only lists their photometry from the u^* to the K_S bands; and therefore these were used. We created a library of synthetic templates from the models of Bruzual & Charlot (2003). We included one Burst, three exponentially decaying and one constant star formation rate histories at 51 different ages, similar to the default templates from HyperZ. We searched for redshifts in the range $z = 0.5 - 6.0$ and allowed for the extinction to vary in the range $A_V = 0.0 - 2.5$. Photometric data points with errors < 0.01 magnitudes were forced to have a minimum error of 0.01. Sources that were not detected in a certain band were assigned with a zero flux and an error corresponding to the flux limit in that band.

Additionally, we used the radio to millimeter spectral index as an indicator of redshift. This method is based on the tight correlation observed between radio and far-IR emission in nearby star-forming galaxies (Condon, 1992, Chapter 1). Basically, it assumes the radio/far-IR SED

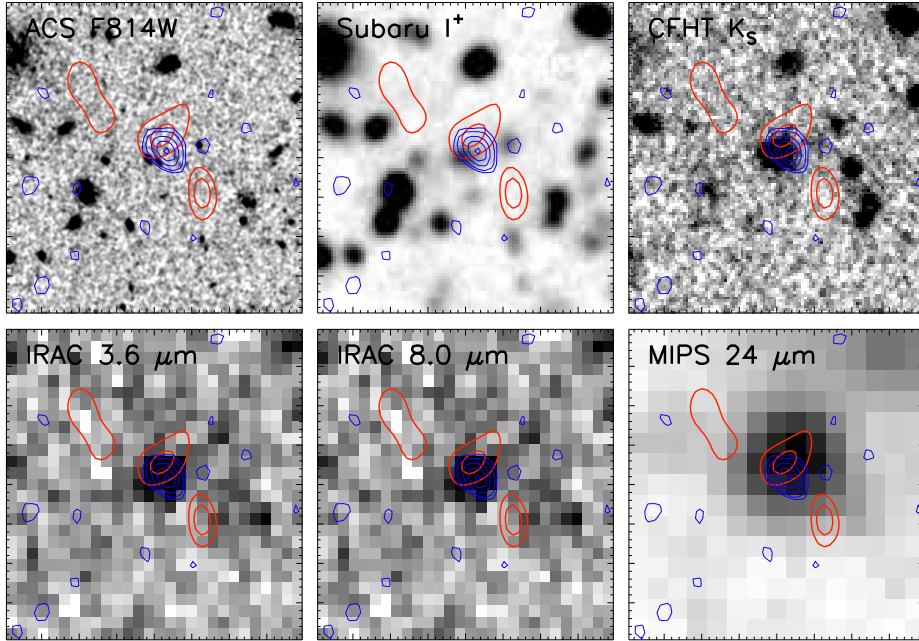


Figure 5.6: Multi-wavelength images of the field of COSBO-6 ($16'' \times 16''$). Background images are the HST ACS I, Subaru i^+ , CFHT K, IRAC $3.6 \mu\text{m}$, IRAC $8.0 \mu\text{m}$ and MIPS $24 \mu\text{m}$ bands. Red contours represent the continuum 1.3 mm S/N map at 2σ , 3σ and 4σ levels. Blue contours represent the continuum 1.4 GHz S/N map at 2σ , 3σ , 4σ and 5σ levels ($\sigma = 7 \mu\text{Jy}$).

of a typical starburst galaxy (i.e. Arp220) and uses it to predict the fluxes (, at 1.4 GHz and 250 GHz) at higher redshifts (Carilli & Yun, 1999). By comparing the observed fluxes with this model, it is possible to estimate the most likely redshift.

Figure 5.9 shows the best fit template models for the optical/IR photometric data points. All fits show a good agreement between the templates and the observed data. Major discrepancies are found for COSBO 6S.1, 6S.2 and 9, mainly due to their faintness and large errors. Because of the latter, these can only be detected in few optical bands, particularly COSBO-9.

Figure 5.10 shows the value of χ^2 as a function of redshift, for the optical counterparts to the PdBI sources. Lower values of χ^2 represent a better fit to the data, and thus a more likely redshift.

The χ^2 distribution for COSBO-4 indicates that its most likely redshift is $z = 3.2$. This estimate is in good agreement (within the errors) with the radio/millimeter photometric redshift, $z = 3.8^{+0.6}_{-0.5}$.

The strong decline in the χ^2 distribution of COSBO-6C implies an optical/IR redshift of 1.8, which is consistent with the radio/millimeter redshift estimate, $z = 1.4^{+0.2}_{-0.2}$. The agreement between both redshift estimates supports the reliability of the measured 1.3 mm flux towards COSBO-6C, noting its low signal to noise ratio. For the two optical associations to the southern millimeter detection (6S.1 and 6S.2), the primary solutions give low redshifts ($z = 0.6$) in agreement with the estimates listed in the COSMOS catalog (Mobasher et al., 2007). Nevertheless, the secondary solutions imply $z = 1.7$ and $z = 1.0$ for COSBO 6S.1 and 6S.2, respectively, indicating that a possible connection between the COSBO 6S.1 and 6C may exist. Furthermore, the most likely optical/IR redshift for COSBO-6N, $z = 1.3$, is similar to the redshift of 1.5 estimated by Mobasher et al. (2007) and supports the hypothesis of a forming SMG group at $z \sim 1.5$.

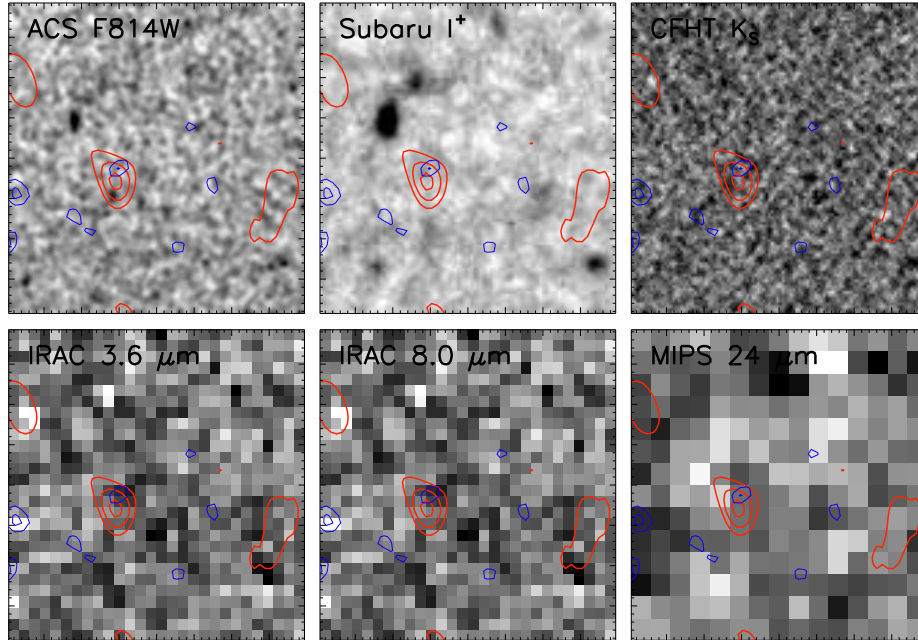


Figure 5.7: Multi-wavelength images of the field of COSBO-9 ($16'' \times 16''$). Background images are the HST ACS I, Subaru i^+ , CFHT K, IRAC $3.6 \mu\text{m}$, IRAC $8.0 \mu\text{m}$ and MIPS $24 \mu\text{m}$ bands. Red contours represent the continuum 1.3 mm S/N map at 2σ , 3σ and 4σ levels. Blue contours represent the continuum 1.4 GHz S/N map at 2σ , 3σ , 4σ and 5σ levels ($\sigma = 7 \mu\text{Jy}$).

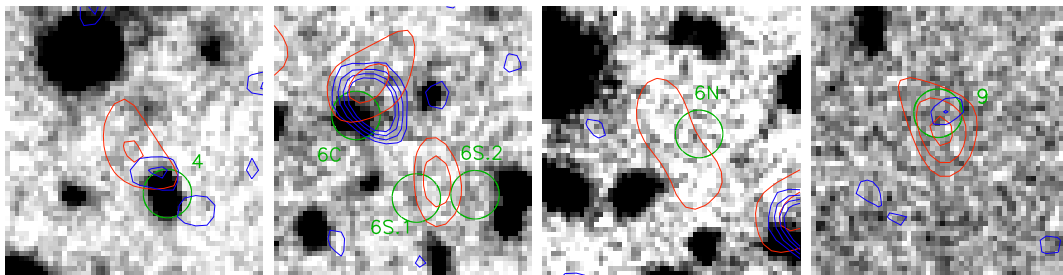


Figure 5.8: Close-up ($8'' \times 8''$) Subaru i^+ band image (background) around the 1.3 mm detections. Red contours represent the 1.3 mm PdBI continuum map at levels of 2σ , 3σ and 4σ . Blue contours show the 1.4 GHz VLA continuum map at levels of 2σ , 3σ , 4σ and 5σ . The positions of the likely counterparts are marked with green circles and labeled with their respective IDs.

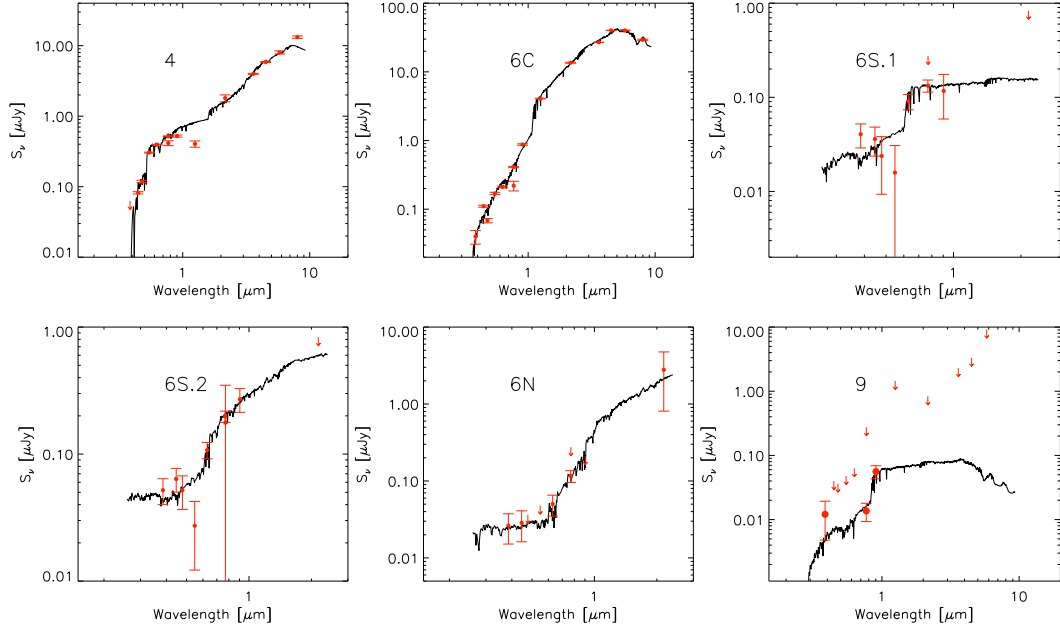


Figure 5.9: Optical and near-IR photometry for the likely counterparts to the millimeter sources. The black curves represent the best fitted template from the models of Bruzual & Charlot (2003).

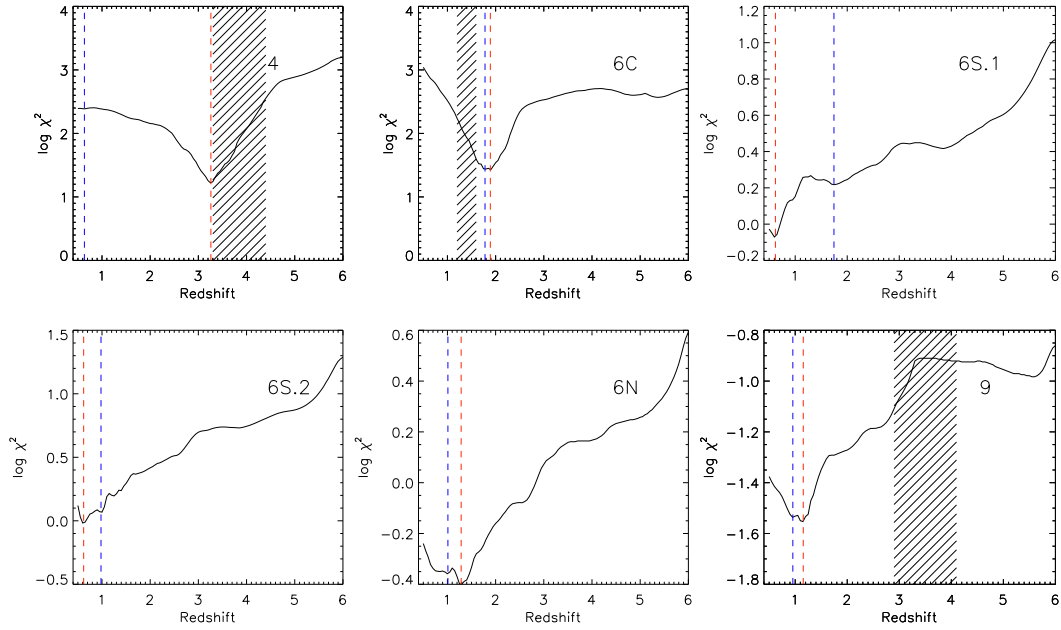


Figure 5.10: χ^2 distribution as a function of redshift for the likely optical counterparts to the millimeter sources. The vertical dashed red and blue lines represent the primary and secondary solutions (minima), respectively, derived from these distributions.

The optical counterpart to COSBO-9 is very faint and is thus only detected in three bands. The best fit solution indicates that this source is at $z \sim 1$. However, this is inconsistent with the radio photometric redshift, which suggests $z = 3.4_{-0.5}^{+0.7}$. The secondary solution implies $z = 5-6$, still inconsistent with the radio photometric redshift. Given that our optical/IR redshift estimates are very uncertain, we select the radio/millimeter estimate as the most likely value for the redshift of this source.

5.4 Discussion

5.4.1 Pinpointing the highest redshift SMGs

The acquisition of deep interferometric continuum maps has proven to be a crucial tool to identify the actual source of the emission in poor resolution bolometer millimeter maps (Dannerbauer et al., 2004; Younger et al., 2007).

Using the PdBI, we have located the position of two radio faint MAMBO sources in the COSMOS field. COSBO-4 and COSBO-9 are associated with faint radio emission which, due to its low signal to noise ($S/N \sim 3$), would not have been taken as a solid identification by itself. Faint optical counterparts were found to coincide with the radio emission, while no $24 \mu\text{m}$ counterparts were detected. Interestingly, the detection of COSBO-4 contradicts our previous result, where we associated its MAMBO emission with either of three possible $24 \mu\text{m}$ candidates, lying $\sim 7'' - 8''$ away from it (see Chapter 2). This indicates that $24 \mu\text{m}$ associations do not always provide the right counterparts. The lack of optical and IR sources in the field of COSBO-9 did not permit an initial identification of this source. A very faint optical source appears to be the most likely counterpart to the millimeter and radio emission.

The low flux levels detected at 1.3 mm with the PdBI compared with those measured at 1.2 mm with MAMBO suggest that flux boosting may have contributed to the strong MAMBO detections of COSBO-4 and COSBO-9.

Much controversy has arisen regarding the estimation of the redshift distribution of SMGs and, most importantly, the existence of a significant high redshift tail that would imply a larger median redshift for SMGs. Measurements of this high redshift tail impose important constraints to the modelling of the formation and evolution of SMGs (Baugh et al., 2005; Swinbank et al., 2008). Chapman et al. (2005) found that radio selected SMGs have a median spectroscopic redshift of 2.3, while recent studies based on photometric redshifts (Dye et al., 2008; Clements et al., 2008) agree that SMGs may typically lie at even lower redshifts, $z \sim 1.8 - 2.0$, despite the inclusion of radio undetected SMGs. Conversely, studies based on mid-IR spectroscopy have suggested that the median redshift for SMGs may be significantly larger, $z \sim 2.8$ (Menéndez-Delmestre et al., 2007; Valiante et al., 2007).

Studies of SMGs identified with millimeter interferometry, as in this work, reinforce this idea (Younger et al., 2007, 2008; Dannerbauer et al., 2008). The redshifts implied by the radio to millimeter spectral index and by the optical/near-IR photometry indicate that COSBO-4 and COSBO-9 lie at a larger redshift ($z > 3$) than that of typical SMGs. From the sample of 15 significant MAMBO sources from Bertoldi et al. (2007), five did not show a significant radio counterpart (including COSBO 4 and 9). Should all such MAMBO sources have similar redshifts, it would mean that at least 30% are located at larger redshifts than the radio-identified SMGs. Similar results were found by Dannerbauer et al. (2008) and Younger et al. (2007) in the GOODS-N and COSMOS-AzTEC fields. This questions current evolutionary models of SMGs (Swinbank et al., 2008) and suggests that the previously estimated median redshift of ≈ 2.3 is too low.

Our 1.3 mm observations can be used to provide a rough estimate of the dust masses and far-IR luminosities. If we assume an optically thin single component dust model, with a dust absorption coefficient given by equation 5.2, a spectral index $\beta = 2$, dust temperature $T_d = 30-70$ K, which is typical for SMGs and high redshift QSOs (Kovács et al., 2006; Beelen et al., 2006;

Omont et al., 2001), and a redshift between $z = 3-4$, we find dust masses of $(1.3-7.6) \times 10^8 M_\odot$ and $(0.9-5.6) \times 10^8 M_\odot$ for COSBO-4 and COSBO-9, respectively. This implies large amounts of dust and gas at about 1.5 to 2 Gyr after the Big Bang. Moreover, it implies far-IR luminosities ($50\mu\text{m}-1100\mu\text{m}$; Omont et al., 2001) of $(0.3-3.0) \times 10^{13} L_\odot$ and $(0.2-2.3) \times 10^{13} L_\odot$ for COSBO-4 and COSBO-9, respectively. Such luminosities suggest the presence of strong starburst activity for these $z > 3$ objects. Assuming a conversion factor between far-IR luminosity and star formation rate from Omont et al. (2001), we find star formation rates $> 500 M_\odot \text{ yr}^{-1}$.

Examples of high redshift ($z > 3$) galaxies with faint radio counterparts are also presented by Younger et al. (2007) and Dannerbauer et al. (2002, 2004, 2008). Such sources are not detected with ACS imaging, and have faint IRAC fluxes, albeit their higher (sub)millimeter fluxes, suggesting that brighter SMGs lie at larger redshifts.

5.4.2 A group of SMGs at $z = 1.5$?

There is increasing evidence suggesting that at least part of the SMG population may point at the early phases of massive galaxy clusters (Chapter 4). A prominent overdensity of high redshift *BzK* galaxies was found in the surroundings of COSBO-6. The spatial and redshift distribution of those *BzK* galaxies here indicated strong clustering on a scale of $\sim 10''$ and at a redshift of ~ 1.5 .

Although we had previously associated this MAMBO source with a significant radio source close to the millimeter emission peak, the PdBI imaging showed that this object is not the only one contributing to the millimeter emission. At least two other detections are found, being consistent with an actively interacting group of SMGs. The radio identified MAMBO source coincides with significant $24 \mu\text{m}$ emission, however, the other two millimeter detections could not be associated with radio or IR sources. Only faint optical sources were found as the most likely counterparts. For the southern millimeter detection (COSBO-6S), we found two possible optical counterparts (COSBO 6S.1 and 6S.2). COSBO-6S.1 has an optical/IR SED and χ^2 distribution consistent with the redshift of the galaxy group, $z \sim 1.5$. For the northern millimeter source (COSBO-6N) a faint optical counterpart was identified. Its optical photometry suggests $z \sim 1.3$, also consistent with the SMG group.

The detection of at least two millimeter sources embedded in a group of massive high-redshift, star forming *BzK* galaxies is evidence of merging activity and structure formation in the very early Universe. Assuming the model of dust emission presented above, we find that these SMGs have dust masses of $(0.9-3.3) \times 10^8 M_\odot$ and far-IR luminosities of $(0.1-1.5) \times 10^{13} L_\odot$, at $z = 1.5$. The high far-IR luminosities and thus the intense starburst activity present in these galaxies indicate that merger activity is taking place. This suggests that this system may not yet be very evolved, and therefore that the group of *BzK* galaxies is falling into the gravitational potential. Furthermore, it supports the possibility that the SMG phase is produced by the merger of starforming *BzK* galaxies at high redshifts (Takagi et al., 2008). It is interesting to note that the detection of such a group of SMGs may not be necessarily found on scales of a few arcseconds, as in this case. Large scale clustering, on arcminute scales, can also be found (Chapman et al., 2008) and it is possible that a mixture of both phenomena may co-exist. Nevertheless, it is still necessary to investigate the masses of such systems in order to assess whether they will evolve into massive galaxy clusters at later epochs.

Accurate spectroscopic redshifts will help to establish the connection between the group members and estimate the virial mass, in case of a virialized system. Deeper millimeter imaging will help to investigate the presence of other faint SMGs among the group members.

Properties of the molecular gas in a starbursting QSO

6.1 Introduction

Submillimeter blank field surveys have discovered a population of dust enshrouded high-redshift galaxies (Smail et al., 1997; Hughes et al., 1998; Eales et al., 1999) which are massive systems with huge molecular gas reservoirs and star formation at high rates (Neri et al., 2003; Greve et al., 2005; Solomon & Vanden Bout, 2005). Their faint X-ray emission (Alexander et al., 2005) suggests that most of the submillimeter output is not powered by AGN, but by massive star formation. These starbursting SMGs account for a substantial fraction of the far-IR background, and current models suggest this population may represent the formation of massive spheroidals at high-redshift (Dunlop, 2001).

In the local Universe, an evolutionary connection between starbursting ULIRGs and QSOs has been suggested (Sanders et al., 1988a) and discussed controversially (e.g. Sanders et al., 1988a,b; Genzel et al., 1998; Tacconi et al., 2002). This evolutionary cycle has found support from hydrodynamical simulations of galaxy formation (e.g. Di Matteo et al., 2005; Hopkins et al., 2005, 2006) and observations (Sanders et al., 1988a; Page et al., 2004; Stevens et al., 2005).

The ubiquitous presence of AGN activity in most SMGs (Alexander et al., 2005) suggests a close link between the AGN and starburst activity at redshifts $z \sim 1 - 3$. If a QSO is found to be far-IR luminous, it means that large amounts of gas and dust should still be present. Such a source may, in fact, be a good candidate for an object in the transition from a starburst to a QSO, in particular when it shows absorbed X-ray emission (Page et al., 2004; Stevens et al., 2005). Yet only a few high-redshift composite starburst/AGN have been studied in molecular and multi-wavelength continuum emission (Rowan-Robinson, 2000; Le Flo'c'h et al., 2007; Coppin et al., 2008).

Observations of CO in galaxies are important probes of the physical conditions of the cold and warm molecular gas in the galactic nuclei and disks. They provide estimates of the total amount of gas available to fuel starburst and/or AGN activity, and the CO line profile and intensity can be used to obtain important information about the galaxy kinematics, such as dynamical mass or size of the emitting region (Solomon et al., 1997; Solomon & Vanden Bout, 2005).

Because of their diagnostic value, great efforts have been made to observe CO emission lines in SMGs. These studies have benefited from deep radio continuum imaging (e.g. VLA 1.4 GHz) to locate the SMG accurately (Ivison et al., 2002, 2005, 2007), and from the determination of optical spectroscopic redshifts (e.g. Chapman et al., 2005). Due the small spectroscopic bandwidths of current (sub)millimeter telescopes and interferometers, this was necessary to permit the proper frequency tuning for line observations (e.g. of CO, [CI], [CII]). Yet only 19 SMGs

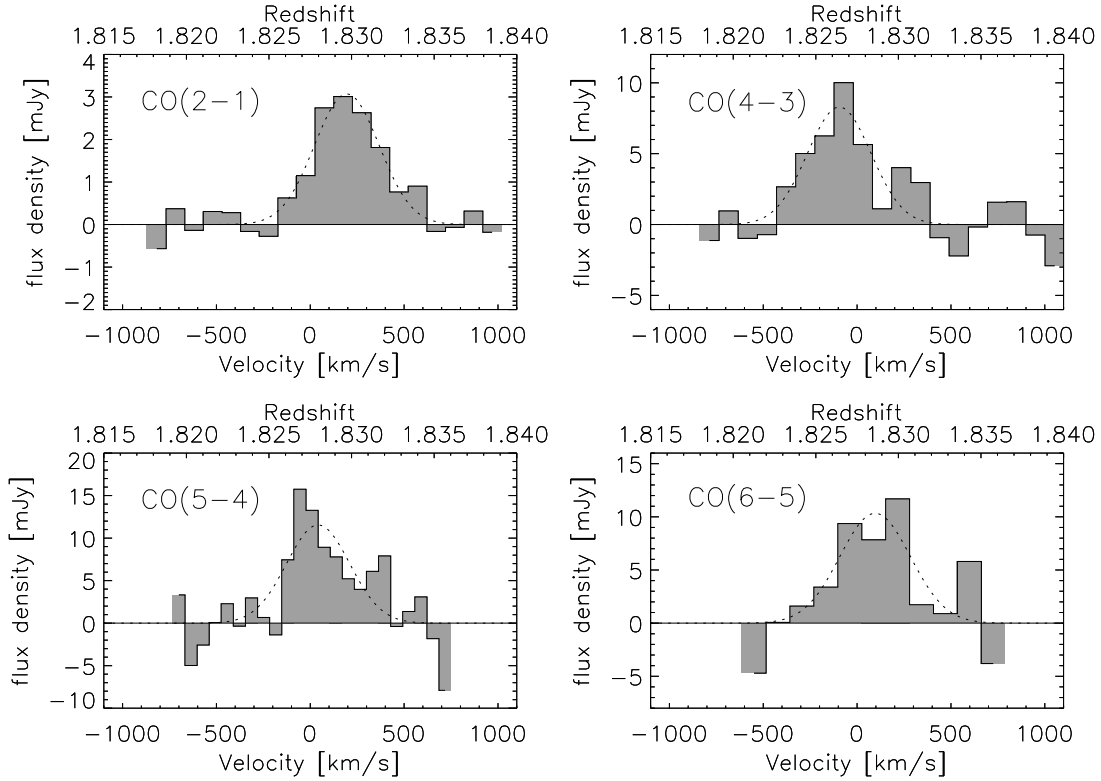


Figure 6.1: Observed spectra of the CO $J = 2-1, 4-3, 5-4$ and $6-5$ emission lines in $J100038+020822$, obtained with the IRAM 30m telescope. Gaussian fits to the spectra are shown as dotted lines. The velocity reference is at $z = 1.8275$.

have been reported in CO so far (Fraye et al., 1998, 1999; Andreani et al., 2000; Sheth et al., 2004; Hainline et al., 2004; Neri et al., 2003; Greve et al., 2005; Frayer et al., 2008; Coppin et al., 2008; Tacconi et al., 2008) and only a few have been observed in multiple molecular transitions to study the excitation conditions of their molecular gas reservoir (Solomon & Vanden Bout, 2005). Spatial structure and dynamics were studied for some SMGs through high resolution CO imaging (Tacconi et al., 2006, 2008). Overall, only ~ 50 high-redshift ($z > 1$) objects have been detected in CO, most of which are luminous, optically selected QSOs (Omont et al., 1996; Guilloteau et al., 1997, 1999; Carilli et al., 2002; Walter et al., 2003; Bertoldi et al., 2003; Beelen et al., 2004; Riechers et al., 2006; Carilli et al., 2007) and high-redshift radio galaxies (HzRG; De Breuck et al., 2003, 2005; Klamer et al., 2005; Papadopoulos et al., 2005).

In this Chapter, we report the detection of CO $2-1, 4-3, 5-4$, and $6-5$ line emission from a millimeter selected QSO in the COSMOS field, COSBO-11. Its CO line intensities and flux density ratios allow us to estimate its molecular gas content and its excitation conditions. Its spectral properties suggest that this object may be evolving from a starburst to a QSO.

After a description of the observations in Section 2, we present the molecular gas and dust properties of our source in Sections 6.3.1 to 6.3.4. We study its morphology and multi-wavelength properties in Sections 6.3.5, 6.3.6 and 6.3.7. We discuss the results in Section 4 and give a brief summary in Section 5.

Table 6.1: Observed line parameters for J100038.

Transition ^a	ν_{obs} ^b [GHz]	HPBW ^c [']	T_A^* ^d [mK]	T_{mb} ^e [mK]	S_ν ^f [mJy]	v_{FWHM} ^g [km s ⁻¹]	I_{CO} ^h [Jy km s ⁻¹]	L'_{CO} ⁱ 10 ¹⁰ [K km s ⁻¹ pc ²]	L_{CO} ^j 10 ⁸ [L _⊙]
CO 2 – 1	81.551	30.2	0.51	0.62	3.08	406 ± 31	1.33	5.6 ± 0.35	0.22 ± 0.01
CO 4 – 3	163.088	15.1	1.18	1.69	8.39	427 ± 73	3.81	4.0 ± 0.51	1.25 ± 0.16
CO 5 – 4	203.850	12.1	1.46	2.33	11.56	397 ± 161	4.87	3.3 ± 0.8	2.00 ± 0.49
CO 6 – 5	244.603	10	1.19	2.09	10.35	443 ± 75	4.86	2.3 ± 0.4	2.40 ± 0.47

Notes: ^a Observed frequency; ^b Half power beam width of the IRAM 30m telescope at the observed frequency; ^c Antenna temperature; ^d Main beam temperature; ^e Flux density; ^f CO line full width half maximum; ^g Integrated CO intensity; ^h CO luminosity; ⁱ Integrated CO luminosity.

6.2 Observations

6.2.1 Source selection

The COSBO source 11 (J100038.01+020822.4; hereafter: J100038) is one of the strongest millimeter selected sources in COSMOS (boosting corrected $S_{1.2\text{ mm}} = 4.6 \pm 0.9\text{ mJy}$).

It hosts an X-ray luminous ($L_X \sim 10^{44}\text{ erg s}^{-1}$), absorbed ($\log N(\text{H}) \sim 22 - 23\text{ cm}^{-2}$) AGN that classifies it as an obscured QSO (Brusa et al., 2007; Mainieri et al., 2007), and its optical spectrum is typical of a broad line (BL) AGN (Trump et al., 2007). The relatively faint 1.4 GHz radio emission ($S_{1.4\text{ GHz}} = 237 \pm 27\text{ }\mu\text{Jy}$) suggests that the millimeter emission arises from a starburst. In fact, the radio-to-millimeter flux ratio can be used as a redshift indicator (Carilli & Yun, 1999) that implies $z = 1.9$, which is consistent with the spectroscopic redshift. Since this is a millimeter selected QSO that has been detected in X-rays (Stevens et al., 2005), it likely constitutes a transitional case from SMG to QSO.

Three independent spectroscopic redshift measurements exist for J100038: 1.8325 ± 0.0023 (Trump et al., 2007), 1.825 ± 0.002 (Prescott et al., 2006) and 1.8289 ± 0.002 (Marco Scodreggio, priv. comm.), which we have averaged to $z = 1.8288 \pm 0.0037$.

6.2.2 CO observations

The CO observations were performed with the IRAM 30m telescope on Pico Veleta, Spain, during the winter 2006/2007 in good millimeter weather conditions (precipitable water vapor $< 5\text{ mm}$). We observed the CO 2 – 1 (redshifted to 81.551 GHz) and CO 5 – 4 (163.088 GHz) lines simultaneously using the A/B receiver configuration, and the CO 4 – 3 (203.850 GHz) and CO 6 – 5 (244.603 GHz) lines using the C/D receiver configuration.

The observations were centered on the optical Subaru i^+ band position of J100038 at $10^h 00^m 38.01^s +02^\circ 08' 22.6''$ (J2000). The optical position lies $0.04''$ away from the VLA 1.4 GHz position. The beam size of the IRAM 30m telescope at 200 GHz and 81 GHz is $12''$ and $30''$, respectively.

We observed in wobbler switching mode with a wobbler rate of 0.5 Hz and a wobbler throw of $60''$ in azimuth. Due to its proximity to the source, we used Saturn as main pointing and focus calibrator. The pointing was checked every hour and was stable within $3''$ during all runs.

Typical values for the system temperatures were $\sim 140\text{ K}$, 400 K , 460 K and 600 K for the 3 mm, 2 mm, and lower and higher 1 mm bands, respectively. We calibrated every 12 minutes with hot/cold absorbers and estimate the fluxes to be accurate to $\pm 10\%$ at 3 and 2 mm and 20% at 1 mm. As spectrometers we used the $512 \times 1\text{ MHz}$ filterbanks for the 3 mm receivers, and the $256 \times 4\text{ MHz}$ filterbanks for the 2 and 1 mm receivers (1 GHz bandwidth). We reduced the data using CLASS, removing scans with strongly distorted baselines, subtracted linear baselines in the remaining scans and rebinned the averaged spectra to velocity resolutions of 100, 120, 90 and 130 km s^{-1} for the CO 2 – 1, 4 – 3, 5 – 4 and 6 – 5 lines, respectively. This led to baseline antenna temperature (T_A^*) rms noise levels of 0.04, 0.17, 0.44 and 0.4 mK. To convert to main beam temperatures, T_{mb} , we multiply T_A^* by the ratio between the forward and beam efficiencies, $F_{\text{eff}}/B_{\text{eff}}$, at the observed frequencies. Flux densities were obtained using the conversion factor $S_\nu/T_{\text{mb}} = 4.95\text{ Jy/K}$ for the IRAM 30m telescope¹.

6.3 Results and Analysis

Figure 6.1 shows the resulting spectra and Table 6.1 summarizes the measured line parameters. The line profiles for the different transitions appear Gaussian and similar to each other, with

¹<http://www.iram.es/IRAMES/telescope.html>

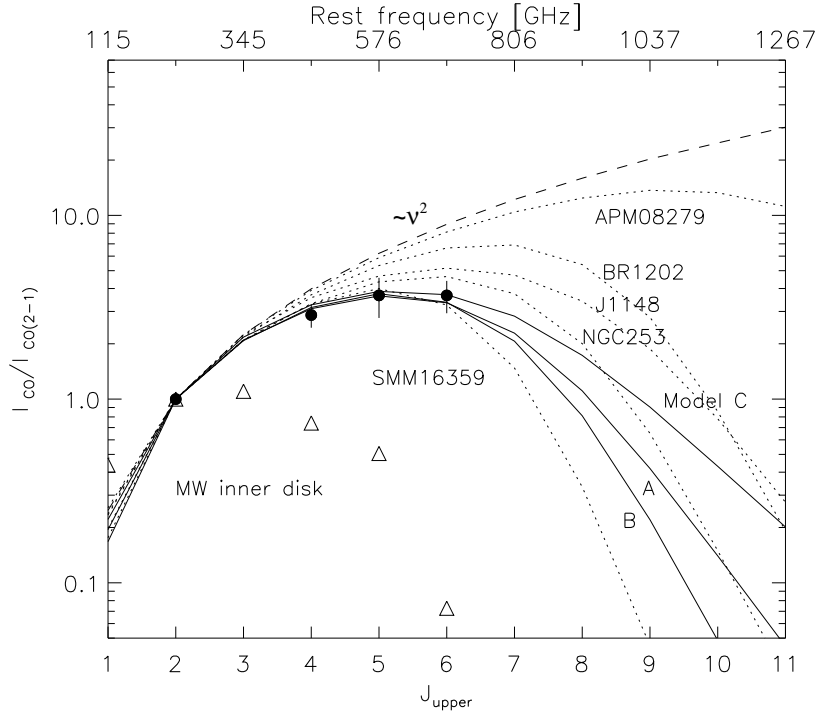


Figure 6.2: CO line SED: integrated line flux, I_{CO} , normalized to CO 2 – 1, vs. rotational quantum number. Filled squares mark the integrated line fluxes for J100038. Solid lines show LVG models A, B and C (see text). Dotted lines show the CO line SEDs for NGC253 (Güsten et al., 2006), SMM16359 (Weiß et al., 2005a), J1148 (Bertoldi et al., 2003), BR1202-0725 (Carilli et al., 2002; Riechers et al., 2006), and APM08279 (Weiß et al., 2007). Open triangles show the CO SED for the inner Milky Way (Fixsen et al., 1999). The dashed line shows the line flux increasing as ν^2 , which would be expected for optically thick local thermodynamical equilibrium (LTE) conditions.

no signs of velocity structure, as might be expected for a merger and is often found for SMGs (Greve et al., 2005; Weiß et al., 2005a). However, the signal to noise ratio is too low to examine the individual line profiles. Although the CO 4 – 3 line appears to be slightly shifted in velocity relative to the other lines, the line widths are very similar, with an average of $\Delta v_{\text{FWHM}} = 417 \pm 48$ km s⁻¹. The spectral energy distribution of the CO rotational emission (CO SED) peaks at the $J = 5 - 4$ transition (Fig. 2 and Table 6.1). Using the detected CO lines we estimate a systemic CO redshift $z = 1.8275 \pm 0.0013$, which we use throughout this work.

6.3.1 Large Velocity Gradient model

To study the molecular gas excitation in J100038 we compared the relative CO line intensities with those predicted by a single component large velocity gradient (LVG) model, assuming spherical geometry. We used the collision rates from Flower (2001) with an ortho-para H₂ ratio of 3 and a fixed CO abundance per velocity gradient of $[\text{CO}]/(\text{dv}/\text{dr}) = 10^{-5}$ pc (km s⁻¹)⁻¹ (e.g. Weiß et al., 2005b, 2007).

The best fit to the data is provided by a model with a kinetic temperature, T_{kin} of 95 K and an H₂ density, $n(\text{H}_2)$ of $10^{3.6}$ cm⁻³ (model A, Fig. 6.2). Similarly good fits are achieved with $T_{\text{kin}} = 60$ K and $n(\text{H}_2) = 10^{3.7}$ cm⁻³ (model B), or $T_{\text{kin}} = 200$ K and $n(\text{H}_2) = 10^{3.5}$ cm⁻³ (model

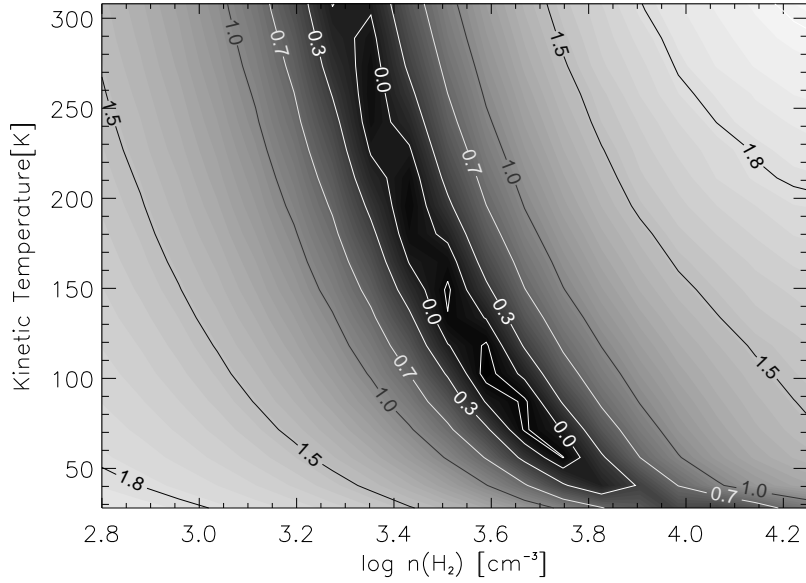


Figure 6.3: $\log\chi^2$ distribution for the single component LVG model as a function of T_{kin} and $n(\text{H}_2)$ with $[\text{CO}]/(\text{dv}/\text{dr}) = 10^{-5} \text{ pc (km s}^{-1}\text{)}^{-1}$. Best fits are provided for solutions with $\log_{10}\chi^2 < 0$.

C). They all show a peak in the CO SED at the $J = 5 - 4$ line, but predict different higher- J intensities.

Figure 6.3 shows the $\log_{10}\chi^2$ distribution as a function of the kinetic temperature and H_2 density. The temperature–density parameter space is degenerate at densities between $10^{3.0} \text{ cm}^{-3}$ and $10^{4.0} \text{ cm}^{-3}$. The most likely ranges for the kinetic temperature and the H_2 density are ~ 50 to 200 K and $10^{3.5}$ to $10^{4.0} \text{ cm}^{-3}$, respectively.

The CO abundance per velocity gradient relates to the line opacities predicted by the LVG models (Weiß et al., 2007). Higher values of $[\text{CO}]/(\text{dv}/\text{dr})$ correspond to higher opacities for the high- J transitions. From Figure 6.2 we see that all models predict optically thick conditions and thermalized emission in the $J_{\text{upper}} < 4$ lines, consistent with the line SED following ν^2 and supporting our CO column per velocity gradient selection.

Although the kinetic temperature is poorly constrained, the LVG modelling prediction for the CO $1 - 0$ line intensity does not strongly depend on the model chosen: $I_{\text{CO } 1-0} = 0.27 - 0.4 \text{ Jy km s}^{-1}$.

6.3.2 CO Size and Mass

The ratio between the brightness temperatures predicted by the LVG models, T_{b} , and the observed line temperatures, T_{mb} , yields an estimate of the CO emitting region size. The angular source size θ_{s} is related to the beam size θ_{b} through

$$\theta_{\text{s}} = \theta_{\text{b}} \times \left(\left[\frac{T_{\text{b}}}{(1+z)T_{\text{mb}}} \right] - 1 \right)^{-1/2}. \quad (6.1)$$

The source sizes we thereby compute for the different fit models (A, B and C) and line brightness temperatures agree well, $\theta_{\text{s}} \approx 0.17 - 0.20''$. At the source redshift ($z = 1.8275$), $1''$

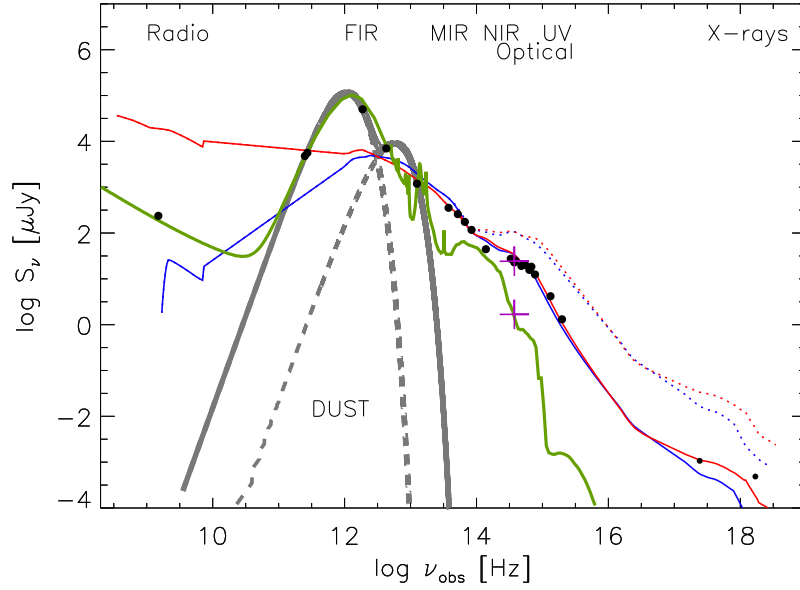


Figure 6.4: Spectral energy distribution (SED) for J100038. The photometric data points (filled circles) range from radio waves to X-rays. The lower purple cross shows the ACS I band flux derived for the host galaxy while the upper one shows the flux for the nucleus. The red and blue curves are the average radio-loud and radio-quiet QSO SEDs from Elvis et al. (1994). The dotted lines show the Elvis et al. (1994) models, not corrected for extinction, and the solid lines show the SEDs corrected with the Calzetti et al. (2000) extinction model. The green line shows the SED of the typical starburst galaxy Arp220. The thick gray lines show our two-component dust model.

corresponds to 8.44 kpc, so that the estimated source size lies in the range of 1.4 – 1.7 kpc.

The CO luminosity can be derived from the CO line intensity, following Solomon et al. (1997) as

$$L'_{\text{CO}} = 3.25 \times 10^7 S_{\text{CO}} \Delta v \nu_{\text{obs}}^{-2} D_L^2 (1+z)^{-3} \text{ K km s}^{-1} \text{ pc}^2 \quad (6.2)$$

where $S_{\text{CO}} \Delta v$ is the integrated CO line flux in Jy km s^{-1} , D_L is the luminosity distance in Mpc and ν_{obs} is the observed line frequency in GHz. Our predicted CO flux $I_{1-0} = S_{1-0} \Delta V = 0.27 - 0.4 \text{ Jy km s}^{-1}$ yields $L'_{1-0} = (4.5 - 6.7) \times 10^{10} \text{ K km s}^{-1} \text{ pc}^2$.

The CO 1–0 luminosity is commonly used to estimate the molecular gas mass. Adopting the conversion factor between CO luminosity and H_2 mass, $\alpha = 0.8 M_{\odot} (\text{K km s}^{-1} \text{ pc}^2)^{-1}$, that was derived for local ULIRGs (Downes & Solomon, 1998), we find an H_2 mass of $(3.6 - 5.4) \times 10^{10} M_{\odot}$.

From the size estimate of the dense gas region and the average CO line FWHM, $\Delta v = 417 \text{ km s}^{-1}$, we can estimate a dynamical mass contained in the emitting region. For a radius of 0.75 kpc we infer a dynamical mass $M_{\text{dyn}} = 3 \times 10^{10} \sin^{-2}(i) M_{\odot}$. For an average inclination angle $i = 30^\circ$, this leads to $1.2 \times 10^{11} M_{\odot}$, which agrees well with the CO luminous mass estimate. Assuming a disk-like geometry would lower the dynamical mass estimate by a factor $2/\pi$.

The molecular gas mass can thus account for a large fraction ($\approx 30 - 40\%$) of the dynamical mass out to 0.75 kpc. This result suggests a somewhat larger fraction than in local ULIRGs in which the molecular gas mass represents 16% of the dynamical mass in the nuclear regions

Table 6.2: Infrared and radio fluxes of J100038. †

Band	Flux density	Unit
IRAC 3.6 μm	116.1 ± 0.2	μJy
IRAC 4.5 μm	175 ± 0.4	μJy
IRAC 5.8 μm	258.1 ± 1.1	μJy
IRAC 8.0 μm	356.4 ± 2.3	μJy
MIPS 24 μm	1.43 ± 0.1	mJy
MIPS 70 μm	7 ± 2	mJy
MIPS 160 μm	50 ± 15	mJy
Bolocam 1.1 mm	5.6 ± 1.9	mJy
MAMBO 1.2 mm	4.8 ± 1.0	mJy
VLA 1.4 GHz	237 ± 37	μJy

† IRAC and MIPS aperture corrected (total) flux densities are from the S-COSMOS data (Sanders et al., 2007); Flux densities at 1.1 mm and 1.2 mm are from Aguirre et al. (2006) and Bertoldi et al. (2007), respectively; Radio flux is from VLA-COSMOS (Schinnerer et al., 2007).

(Downes & Solomon, 1998).

SMGs and high-redshift QSOs have typical H_2 masses, $M(\text{H}_2)$ of $(3.0 \pm 1.2) \times 10^{10} M_\odot$ within a 4 kpc diameter (Greve et al., 2005; Solomon & Vanden Bout, 2005), consistent with the value found in our source. Dynamical masses of SMGs and high-redshift QSOs range between 1.0 and $2.0 \times 10^{11} M_\odot$ (Greve et al., 2005; Tacconi et al., 2006; Solomon & Vanden Bout, 2005), which also agrees well with the result exposed above. We note that our dynamical mass estimate has been computed assuming a radius of 0.75 kpc unlike the case of typical SMGs and high-redshift QSOs, for which it is computed with a radius of 2 kpc. Scaling to this radius, i.e. adopting a continuous CO distribution, we find that the dynamical mass for J100038 would be $1.6 \times 10^{11} M_\odot$, still in agreement with values for SMGs and high-redshift QSOs.

6.3.3 Dust Continuum

To study the dust properties of J100038 we use a χ^2 minimization procedure to fit a two-component gray-body spectrum to the 5 IR photometric data points from 24 μm to 1.2 mm (observed frame). A single component gray-body spectrum does not provide a good approximation to all points. We do not assume optically thin emission (dust optical depth, $\tau_\nu \ll 1$) but use the complete expression for the flux density (see Weiß et al., 2007):

$$S_\nu = \frac{\Omega}{(1+z)^3} [B_\nu(T_{\text{dust}}) - B_\nu(T_{\text{BG}})] (1 - e^{-\tau_\nu}), \quad (6.3)$$

where $B_\nu(T)$ is the Planck function, T_{dust} is the dust temperature and T_{BG} is the cosmic background temperature at the source redshift, $T_{\text{BG}} = 2.73 \times (1+z)$ K. We define the apparent solid angle subtended by the source as $\Omega = \pi(d_0/D_A)^2$, with d_0 being the equivalent source size which we assume to be 1.5 kpc based on the derived CO size, and D_A the angular distance at the source redshift. The dust optical depth is

$$\tau_\nu = \frac{\kappa(\nu)M_{\text{dust}}}{D_A^2 \Omega}, \quad (6.4)$$

where M_{dust} refers to the dust mass, and the dust absorption coefficient has the form $\kappa(\nu) = \kappa_0(\nu/\nu_0)^\beta$. We adopt an emissivity index $\beta = 2.0$ (Priddey & McMahan, 2001) and $\kappa_0 = 0.4 \text{ cm}^2 \text{ g}^{-1}$ at 250 GHz (Kruegel & Siebenmorgen, 1994).

The best fitting model leads to a dominant cold component with $T_C = 42 \pm 5$ K, and a hot component with $T_H = 160 \pm 25$ K. We calculate a dust mass, M_C for the cold component of $(1.2 \pm 0.4) \times 10^9 M_\odot$; however the mass implied for the hot component is only $M_H = (4 \pm 2) \times 10^4 M_\odot$. Therefore, the cold dust component accounts for almost all the dust mass. We note that for a dust mass of $\sim 1 \times 10^9 M_\odot$ and a size of 1.5 kpc, the emission becomes optically thick ($\tau_\nu \geq 1$) at $\lambda \leq 130 \mu\text{m}$ (rest frame), supporting our model selection.

The far-IR luminosity can be computed from the modeled flux density as

$$L_{\text{FIR}} = 4\pi D_A^2 (1+z)^3 \int S_\nu d\nu. \quad (6.5)$$

Integrating from 50 to 1000 μm (Omont et al., 2001), we find $L_{\text{FIR}} = 8.5 \times 10^{12} L_\odot$. Although the contribution from hot dust is only $L_{\text{FIR, H}} = 5.1 \times 10^{10} L_\odot$, most of it is provided by the cold dust component with $L_{\text{FIR, C}} = 8.4 \times 10^{12} L_\odot$. We note that the selection of different integration limits implies different values for the luminosity, in particular for the hot dust component. If we integrate from 8 to 1000 μm (Sanders & Mirabel, 1996), we obtain $L_{\text{FIR}} = 1.3 \times 10^{13} L_\odot$, $L_{\text{FIR, c}} = 9.4 \times 10^{12} L_\odot$ and $L_{\text{FIR, h}} = 3.7 \times 10^{12} L_\odot$ for the total, cold and hot component luminosities, respectively.

A substantial difference seems to exist in the dust temperatures observed in SMGs ($T_{\text{dust}} \sim 35$ K; Kovács et al., 2006; Pope et al., 2006; Blain et al., 2004a) and high-redshift QSOs ($T_{\text{dust}} \sim 45$ K; Omont et al., 2003; Beelen et al., 2006; Wang et al., 2008). This difference could possibly be explained by the fact that starburst galaxies with warmer dust would have their dust emission shifted to shorter wavelengths making them more difficult to detect at submillimeter wavelengths (Blain et al., 2004a). If this difference is real, it would imply that the dust properties of J100038 are more consistent with high-redshift QSOs.

6.3.4 Star Formation Rates and Efficiencies

Assuming that the AGN does not contribute significantly to the heating of the cold and hot dust components and that most of the dust emission is produced by starburst activity, the far-IR luminosity implies an estimate for the SFR. Omont et al. (2001) found the following relation between the far-IR luminosity and the SFR,

$$\text{SFR} [M_\odot \text{ yr}^{-1}] = \delta \left(\frac{L_{\text{FIR}}}{10^{10} L_\odot} \right), \quad (6.6)$$

where δ is a function of the initial mass function (IMF) and vary in the range 0.8 – 3. For $\delta = 2$, we then find $\text{SFR} \approx 1700 M_\odot \text{ yr}^{-1}$, well in agreement with the value found using the IR based estimator from Kennicutt (1998), $\text{SFR} \approx 2150 M_\odot \text{ yr}^{-1}$.

The ratio between the far-IR luminosity and the CO luminosity can be interpreted as a star formation efficiency, $\text{SFE} = L_{\text{FIR}}/L'_{\text{CO}} = 130 - 190 L_\odot (\text{K km s}^{-1} \text{ pc}^2)^{-1}$, or in terms of the gas mass implied by the CO luminosity, $\text{SFE} = 160 - 235 L_\odot M_\odot^{-1}$.

This value is similar to the average value found for local ULIRGs, $\langle \text{SFE} \rangle = (180 \pm 160) L_\odot M_\odot^{-1}$ (Solomon et al., 1997), although it appears to be slightly lower than those obtained for SMGs, $\langle \text{SFE} \rangle = 450 \pm 170 L_\odot M_\odot^{-1}$ (Greve et al., 2005).

The luminosity ratio can also be interpreted as a gas depletion time, $\tau_{\text{SF}} = M(\text{H}_2)/\text{SFR} \approx 5 \times 10^{10} M_\odot / 1700 M_\odot \text{ yr}^{-1} = 30 \text{ Myr}$. Others (e.g. Greve et al., 2005) have estimated the gas depletion time in SMGs as $\sim 16 \text{ Myr}$, with a range of 10 – 100 Myr (Solomon & Vanden Bout, 2005), well in agreement with what we find for J100038, but shorter than that found in ULIRGs or normal spirals.

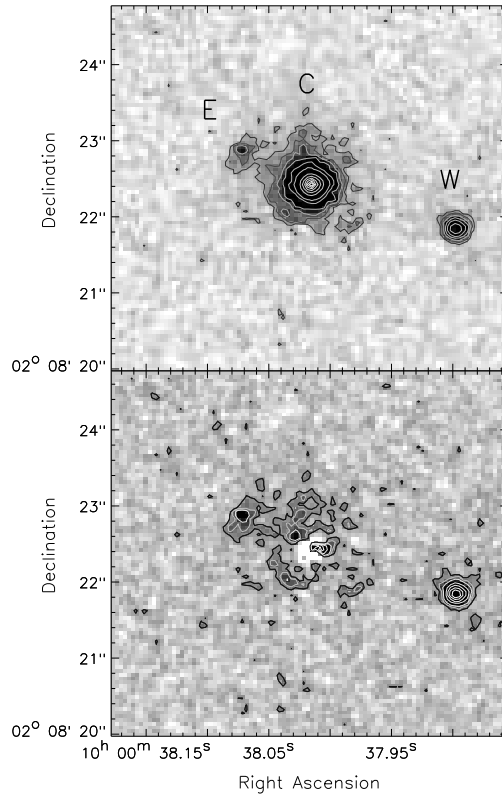


Figure 6.5: Optical morphology of J100038. The HST ACS I band image ($\lesssim 0.1''$ resolution) is shown with contours scaled in magnitude. The top panel shows the original image centered at the central component C, which coincides with the QSO and X-ray source. Two additional components are seen toward the east (E) and west (W). The bottom panel shows the nucleus subtracted HST ACS I image centered at the same position. In addition to the E and W components, patchy structure is seen in the central component.

6.3.5 Optical Morphology

The HST ACS I band image of J100038 (Figure 6.5) shows a complex morphology with three discernable components. For the bright central component C, Figures 6.4 and 6.6 show the SED and optical spectrum, respectively.

The western component is offset by $\sim 2''$ from the central source and shows no sign of a connection to it. Although the Subaru i^+ band images previously shown by Bertoldi et al. (2007) are only able to separate C and W (see also Chapter 2, the HST imaging interestingly shows a third eastern component (E)).

Since the three components are well aligned, it is suggestive that E and W could be gravitationally lensed images. It could also be possible that all three components are lensed images as in e.g. APM08279 (Weiß et al., 2007). However, the optical photometric redshift of 1.4 – 1.5 for W, which is resolved in all optical images (see Bertoldi et al., 2007), is consistent with that of C, with no significant secondary solution at higher redshift, thus ruling out the possibility that E and W is a background object lensed by C.

Imaging spectroscopy would much help to establish a dynamical relation between the three

components, which could support a merger history as the cause for the starburst and nuclear activity.

6.3.6 Spectral Energy Distribution

Figure 6.4 shows the J100038 spectral energy distribution from the radio regime to X-rays. For comparison, we show the (redshifted to $z = 1.83$) SED of the proto-typical starburst galaxy Arp220 (Silva et al., 1998), which fits well from radio to IR. The match strongly supports the conclusion that most of the radio to far-IR emission of J100038 is produced by star formation.

We also compare the observed photometry with the average QSO SEDs of Elvis et al. (1994). While the near to mid-IR photometry of J100038 is well matched by both the radio loud and radio quiet QSO templates, at higher frequencies we need to apply a reddening correction to obtain a good fit. Although the radio-loud model would fit the millimeter flux, it is clearly inconsistent with the low observed radio flux. To match the model at the higher frequencies, we applied an extinction correction based on the model of Calzetti et al. (2000) for starburst galaxies.

A correction with $A_V \approx 0.7$ yields a good match between the models and the UV/optical photometry, and for the radio-loud model even for the X-ray flux. Given the redshift ($z = 1.8275$) and the best fit reddened template, we derive an extinction corrected absolute magnitude in the Subaru V band, M_V of -24.2 magnitudes.

At near-IR and shorter wavelengths, the photometry corresponds to the central plus eastern component, but at longer wavelengths, the western component cannot be distinguished any longer. In the optical and radio regimes, the flux of component W is only 20% of that of C, but differential extinction could in principle be the cause of this difference.

Based on an empirical PSF created from isolated stars in the COSMOS field in the vicinity of J100038, Jahnke et al. (in preparation) studied the contribution from the AGN and host galaxy to the optical emission in J100038 (see also Jahnke et al., 2004). They find that the host galaxy is resolved and has irregular structure outside the central $0.5''$, where nuclear residuals might dominate, as shown in Figure 6.5.

The host galaxy contributes with a $\sim (8 \pm 2)\%$ to the total source flux. Therefore, most of the emission at optical wavelengths ($92 \pm 1\%$ of the total flux) arises from an unresolved point source, with $I_{\text{ACS,host}} = 23.07 \pm 0.1$ magnitudes for the host and $I_{\text{ACS,nucleus}} = 20.43 \pm 0.02$ magnitudes for the nucleus. This gives $I_{\text{ACS,total}} = 20.34 \pm 0.02$ magnitudes in total. Component E contributes a 0.8% to the total nucleus+host flux, $I_{\text{ACS,E}} = 25.6 \pm 0.2$.

Figure 6.4 shows the ACS I band fluxes for the host galaxy and nucleus. As mentioned above, the main flux contribution at this wavelength is provided by the latter. This is also true for the flux in the rest of the optical bands, however it is interesting to note that the I band flux density of the host galaxy component matches the optical emission of the Arp220 SED, suggesting that it is heavily absorbed by dust and hosts starburst activity.

6.3.7 Black Hole Mass Estimate

To estimate the mass of the central supermassive black hole one commonly assumes that the motion of the emitting gas around the black hole is virialized (Peterson & Wandel, 2000). Then the black hole mass is related to the Keplerian velocity of the broad-line region (BLR) gas, V_{BLR} , and to the BLR radius, R_{BLR} , through $M_{\text{BH}} \propto V_{\text{BLR}}^2 R_{\text{BLR}}$. The BLR velocity is proportional to the line width of the MgII line ($\text{FWHM}[\text{MgII}]$) and the BLR radius has been observed to correlate with the UV continuum emission at 3000 \AA (McLure & Jarvis, 2002). Combining these relations (see McLure & Dunlop, 2004),

$$\frac{M_{\text{BH}}}{M_{\odot}} = 3.2 \times \left(\frac{\lambda L_{3000}}{10^{37} \text{W}} \right)^{0.62} \left(\frac{\text{FWHM}[\text{MgII}]}{\text{km s}^{-1}} \right)^2, \quad (6.7)$$

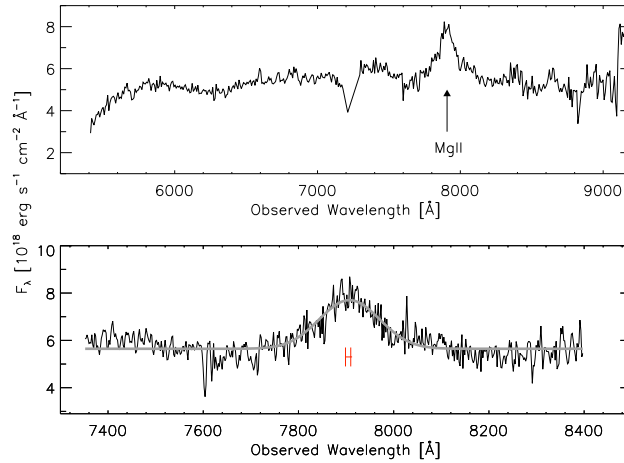


Figure 6.6: Top: optical Magellan spectrum of J100038 (Trump et al., 2007). The broad line at $\lambda \approx 7900$ Å is identified as MgII. Bottom: close-up of the MgII line. The smooth curve shows a Gaussian fit. The red horizontal error bar represents the position of the MgII line at the average CO redshift ($z = 1.8275$) and CO line width (~ 400 km s $^{-1}$).

where λL_{3000} is the luminosity at 3000 Å (rest frame). In the optical spectrum of J100038 (Trump et al., 2007), the MgII line is prominent and allows for an estimate of the black hole mass (Figure 6.6). Assuming a Gaussian shape for the MgII doublet we find a FWHM of 150.6 ± 37.8 Å or 5714 ± 1442 km s $^{-1}$. From the average radio-quiet QSO SED fit we estimate that the rest frame (extinction corrected) 3000 Å luminosity is 8.71×10^{38} W, resulting in a black hole mass of $M_{\text{BH}} = (1.7 \pm 0.8) \times 10^9 M_{\odot}$.

The maximum luminosity that can be reached by an accreting black hole of this mass, or Eddington limit, is $L_{\text{Edd}} = 5.6 \times 10^{13} L_{\odot}$. Assuming a typical QSO SED (Elvis et al., 1994), we obtain a bolometric luminosity of $L_{\text{bol}} \approx 3 \times 10^{13} L_{\odot} = 0.54 \times L_{\text{Edd}}$ which implies a moderate accretion rate (far from the Eddington limit).

6.4 Discussion

6.4.1 Comparison of Excitation Conditions

The observations of the CO lines in J100038 show that its molecular gas is somewhat less excited than observed in local starburst or high-redshift QSOs. We find that the turn-over of the CO line SED occurs between the CO 5–4 and CO 6–5 transitions whereas in most local starbursts/AGNs, or high-redshift QSOs studied to date, the peak of the CO line SED is typically located between the CO 6–5 and CO 7–6 transitions. Examples of such higher excitation CO emission in the local Universe are NGC253 (Güsten et al., 2006), M82 (Weiß et al., 2005b), and at high-redshift, J1148+5251 (Bertoldi et al., 2003; Walter et al., 2003), BR1202-0725 (Carilli et al., 2002; Riechers et al., 2006) and APM08279+5255 (Weiß et al., 2007). The only SMG for which the CO SED has been traced over its peak is J16359+6612 (Weiß et al., 2005a), which interestingly, shows a similar CO excitation to J100038. Other examples of lower excitation are found toward the centers of the local starburst/AGN of Circinus and NGC4945 (Hitschfeld et al., 2008), or in the main starburst region of the Antennae galaxy (Zhu et al., 2003). The lower excitation of the molecular gas observed in these cases, and in particular towards J100038, is likely produced by the relatively low H $_2$ density values ($n(\text{H}_2) < 10^4$ cm $^{-3}$). Furthermore, the best solution derived

Table 6.3: Summary of derived properties of J100038

Property	Name	Value
$M(\text{H}_2)$	Molecular Gas Mass ($10^{10} M_\odot$)	3.6 – 5.4
M_{dyn}	Dynamical Mass ($10^{10} \sin^{-2}(i) M_\odot$)	3.0
M_{dust}	Dust Mass ($10^9 M_\odot$)	1.2
SFR	Star Formation Rate ($10^3 M_\odot \text{ yr}^{-1}$)	1.7
SFE	Star Formation Efficiency ($L_\odot M_\odot^{-1}$)	190
τ_{SF}	Gas Depletion Lifetime (Myr)	30
M_V	Optical Absolute Magnitude	-24.2
M_{BH}	Black Hole Mass ($10^9 M_\odot$)	1.7

from the LVG analysis indicates a moderate kinetic temperature (~ 95 K), suggesting that the AGN does not contribute strongly to the heating of the molecular gas. Conversely, this may imply that most of the heating is produced by star formation, as it is also suggested by the similarity of molecular gas conditions ($T_{\text{kin}}, n(\text{H}_2)$) observed between J16359+6612 and J100038.

6.4.2 A Starburst-QSO Composite

The general picture for QSO and stellar spheroid formation is based on the merger of two gas-rich disk galaxies. The large amounts of gas and dust involved in these mergers provide the fuel for infrared luminous starbursts to occur, and the gas inflow into the inner regions of the galaxy likely feeds the central massive black hole (Mihos & Hernquist, 1994; Barnes & Hernquist, 1996). Observations of local ULIRGs indicate that the most luminous phase occurs close to the final stage of the merger, when both galaxy disks overlap (Sanders et al., 1988a,b; Veilleux et al., 1999).

When the central massive black hole has reached a sufficient size and luminosity, feedback from an active nucleus phase dissipates the dust (Di Matteo et al., 2005) and an optically luminous QSO emerges. As the gas is being expelled, the feeding of the QSO ceases, stopping its activity, and the system relaxes into a spheroidal galaxy hosting a (quiescent) supermassive black hole at its center (Hopkins et al., 2006).

One important question in galaxy evolution is whether this scenario connecting gas-rich starburst galaxies and optically bright QSOs constitutes a rule for most of these systems or whether it is a phenomenon that applies only to the most luminous and massive objects. This evolutionary connection has been studied with vast supporting evidence in the local Universe (e.g. Sanders et al., 1988a). However, for the crucial epoch of star formation and QSO activity ($1 < z < 3$) only a few studies have so far been undertaken. The study of submillimetre (Page et al., 2004; Stevens et al., 2005) and CO line (Coppin et al., 2008) emission of absorbed and unabsorbed high-redshift QSOs indicates that the QSO phase could be preceded by a SMG starburst phase and suggests that submillimetre selected QSOs represent ideal objects for studying these transitional cases at $z > 1$.

J100038 appears to be in a transition between the starburst and QSO phases, as a comparison of its properties to those of a sample of typical SMGs (Greve et al., 2005) and QSOs (Solomon & Vanden Bout, 2005) shows. We start by describing its QSO properties followed by the features that classify this source as a starburst galaxy.

J100038 shows an optical spectrum typical of a Type-1 AGN (Figure 6.6) with a prominent MgII broad emission line. It is relatively luminous at optical wavelengths ($M_V \sim -24$ magnitudes, extinction corrected), shows mild optical extinction with $A_V \sim 1$ and its X-ray emission indicates it is a heavily absorbed QSO ($\log N(\text{H}) = 22 - 23 \text{ cm}^{-2}$). Moreover, its optical to mid-IR SED resembles that of typical QSOs (Figure 6.4), well in agreement with Elvis et al. (1994) templates.

In addition, we derived a diameter of ~ 1.5 kpc for the CO line emitting region. This size is consistent with values observed in high-redshift QSOs which range between 1 and 3 kpc (Walter et al., 2004; Solomon & Vanden Bout, 2005; Maiolino et al., 2007) and similar to those found in local ULIRGs (~ 0.5 kpc; Downes & Solomon, 1998; Soifer et al., 2000), but smaller than the diameters for the CO emitting region in SMGs ($\lesssim 4$ kpc; Tacconi et al., 2006).

On the other hand, J100038 shows distinctive features of on-going starburst activity. The optical morphology of J100038 seen in the HST imaging is suggestive of a recent merger event (Figure 6.5). While most of the emission is concentrated in the point-like central source (C), the faint emission from the eastern source (E) may be indicative of a tidal tail, hinting at a past interaction or merger, although it could also imply the influence of gravitational lensing. The low number density of HST I -band sources in the surroundings of J100038, $\rho(I < 25.5) = 62 \text{ arcmin}^{-2}$, implies that the probability of chance association between E and C is only 4.1%. If both sources (E and C) are physically related, the projected distance between them would be 7.5 kpc. A large fraction of the optical emission from the host galaxy in J100038 could still be absorbed by surrounding dust (Jahnke et al, in prep.), and could be hiding the actual link to the eastern component. We note that the optical emission of the host galaxy is consistent with the obscured SED of the prototypical local starburst galaxy Arp220. Indeed, the optical morphology of this system is strikingly similar to that observed in local ULIRG/PG-QSOs (IRAS 05189-2524; Sanders et al., 1988b; Surace et al., 1998). Furthermore, the far-IR to radio SED of J100038 agrees very well with that of Arp220 (Figure 6.4), and does not follow the typical behavior of radio-loud or radio-quiet QSOs at these wavelengths. In fact, its radio to far-IR spectral index, when used as a redshift indicator results in $z = 1.9$ (Bertoldi et al., 2007), a strong indication that the far-IR and radio emission are both produced by star formation. As mentioned before, the analysis of the molecular gas physical conditions suggest that the AGN plays a moderate role in the gas heating and hints that the heating may actually be dominated by starforming regions.

All the evidence exposed permits to well fit J100038 in the Sanders et al. scenario. Studies of these transitional cases in the local Universe have found that about 30 – 50% of the most luminous ULIRGs ($L_{\text{FIR}} > 10^{12.3} L_{\odot}$) show broad emission lines (Veilleux et al., 1999) and the presence of compact nuclei in 40% of all ULIRGs (Scoville et al., 2000; Soifer et al., 2000) as well as large molecular gas reservoirs (Evans et al., 2002, 2005), even in the late stages of this evolutionary sequence. All these properties apply to J100038. Furthermore, the presence of both starburst and QSO attributes imprinted in the galaxy SEDs have largely been observed in nearby objects, constituting the basis of this evolutionary scenario (Sanders et al., 1988a,b, 1989). These templates compare favorably with the SED observed for J100038, strongly suggesting that this object is evolving from a starburst to a QSO. In fact, it is possible to classify it in a stage between the “warm ULIRG” and the “infrared excess” QSO phases following the mentioned scenario (Sanders, 2004).

Summary and Outlook

7.1 Summary

About a decade ago, extragalactic surveys with large submillimeter bolometer cameras discovered a population of dust obscured galaxies at high redshifts. The large IR luminosities and molecular gas reservoirs show that these so-called submillimeter galaxies (SMGs) are undergoing an intense burst of star formation. An important fraction of the stars and light emission in the Universe are produced in these systems. These SMGs play an important role in the stellar and structure build up of the Universe, and their abundance and epoch of formation place important constraints on models of galaxy evolution.

In this Thesis, we have investigated the properties and the evolutionary context in which SMGs can be placed. For this, we have used millimeter bright sources detected in the MAMBO survey of the COSMOS field (COSBO).

In Chapter 2, we introduced our millimeter observations, described the careful selection of counterparts to the MAMBO sources and studied their contribution to the cosmic background radiation. The inner $20' \times 20'$ of the COSMOS field was observed with the MAMBO instrument at the IRAM 30 m telescope to an rms noise level of 1 mJy per $11''$ beam (see Bertoldi et al., 2007). We found fifteen millimeter sources with $S/N > 4$, eleven of which could be associated with faint radio counterparts. The four significant MAMBO detections with no radio association can be associated with faint MIPS and IRAC sources, however, as it is shown in Chapter 5, these are not necessarily the actual infrared counterparts. Ten lower significance ($S/N = 3.5 - 4.0$) MAMBO sources were identified based on a radio source association within $5''$ from the MAMBO peak. Two faint MAMBO sources were selected based on the association with a significant Bolocam source.

Using deep HST ACS imaging, we were able to locate two faint point sources that lie close to bright, low-redshift elliptical galaxies. They are the most likely counterparts to the millimeter emission, based on their association with radio sources. These objects are possibly affected by gravitational lensing and would have been wrongly associated with the bright optical sources without the help of the high resolution HST images.

We performed a stacking analysis in order to quantify the contribution of faint radio and $24 \mu\text{m}$ sources to the millimeter background radiation. We inferred average 1.2 mm fluxes of radio and $24 \mu\text{m}$ sources of $401 \pm 64 \mu\text{Jy}$ and $384 \pm 71 \mu\text{Jy}$, respectively, which translates into a contribution to the 1.2 mm background of $1.02 \pm 0.16 \text{ Jy deg}^{-2}$ and $0.49 \pm 0.09 \text{ Jy deg}^{-2}$, respectively. This is comparable to the total contribution from the significant MAMBO sources, 0.65 Jy deg^{-2} . Including MAMBO, radio and IR sources, we resolve about 12% of the cosmic background at this wavelength.

In Chapter 3, we studied the properties of the COSBO SMGs. From their optical and near-

IR colors, we found that there is a large overlap between the SMGs and the high-redshift, star forming *BzK* galaxies. About 70% of our SMGs can be classified as high redshift star-forming *BzK* galaxies. In fact, this suggests that the *BzK* color selection criterion could be efficiently used to pre-select SMGs when there are ambiguous radio or 24 μm counterparts. Based on two independent mid-IR color criteria, we separated those MAMBO galaxies that appear to be dominated by obscured and unobscured AGN activity from those purely powered by star formation. We find that about 35% of our MAMBO galaxies can be classified as AGN, in agreement with prior results from deep X-ray imaging of SCUBA galaxies.

We used the radio and millimeter flux densities to obtain estimates of the redshift of the MAMBO sources, based on the correlation between far-IR and radio luminosity of star forming galaxies in the local Universe. Using the optical and IR photometry from the COSMOS survey, we computed photometric redshifts based on χ^2 minimization procedure. From our radio/millimeter and optical/IR based estimates, we find a median redshift of 2.6 and of 2.3, respectively. As suggested by the radio to millimeter flux densities, the four COSBO sources that did not show significant radio counterparts are likely to lie at redshifts > 3 (see also Chapter 5).

We computed stellar masses using SED fits to the photometric data points. We find that MAMBO galaxies are very massive systems with an average stellar mass of $10^{11.4 \pm 0.4} M_{\odot}$. This estimate is in agreement with previous estimates for SCUBA galaxies. Furthermore, SMGs appear to have systematically larger masses than the bulk of galaxies at redshift $z = 1.5 - 2.5$. This suggests that SMGs may be among the most massive systems at high redshifts.

In Chapter 4, we studied the environments of COSBO sources and searched for those that could be involved in the formation of galaxy proto-clusters. We generated a multi-wavelength catalog of *K*-band selected galaxies and created density maps of low-redshift ($z < 1.4$) and high-redshift ($z > 1.4$) *BzK* galaxies in the COSBO field. We found that some COSBO sources appear to be located in extended overdensities of low-redshift galaxies. This could imply that at least some of these SMGs are gravitationally lensed by foreground galaxies. Furthermore, we found that four COSBO sources are located at the center of significant overdensities of high-redshift galaxies. The associations of the COSBO sources and the density peaks appear to be real, as suggested by the low probability of chance association. Two of these overdensities turned out to be the strongest high-redshift galaxy density peaks in the COSBO field. Such concentrations of galaxies are compact, with a typical radius of $\sim 10''$. The overdensities can be identified with concentrations of red galaxies in optical true color images.

The color magnitude diagrams of these four proto-cluster candidates suggest that the surrounding high-redshift *BzK* galaxies and their associated COSBO sources do not have similar colors, as is typically the case for galaxy clusters. Nevertheless, the associated SMGs are amongst the brightest *K*-band selected galaxies in these structures. Photometric redshifts from our *K*-band selected catalog indicate that the galaxies in the surroundings of these SMGs are likely at the same redshift, particularly for the second most prominent overdensity around COSBO-6, for which the redshifts from the COSMOS catalog are consistent with a strong overdensity of galaxies at $z \sim 1.8$. The significance of the observed overdensities indicate that these groups are real, representing substantial evidence of clustering around SMGs.

In Chapter 5, we report on IRAM PdBI 1.3 mm imaging to locate the position of COSBO-4 and COSBO-9, for which no significant ($> 4\sigma$) radio counterparts were found in the VLA 1.4 GHz map. We also studied the millimeter emission from COSBO-6, which is embedded in a significant overdensity of high-redshift star-forming *BzK* galaxies. We find that COSBO-4 and COSBO-9 are each associated with a single PdBI 1.3 mm detection ($> 3.5\sigma$). Nevertheless, their flux densities at 1.3 mm are about a factor of 2 lower than what we would expect from their fluxes at 1.2 mm. We attributed this difference to flux boosting in the MAMBO 1.2 mm maps. COSBO-6 is associated with three PdBI 1.3 mm sources. The integrated 1.3 mm flux density over the whole region occupied by these PdBI sources is in good agreement with the value expected from the integrated MAMBO 1.2 mm flux.

The PdBI 1.3 mm detections of COSBO-4 and COSBO-9 coincide with $\sim 3\sigma$ radio peaks in the VLA 1.4 GHz map. The radio to millimeter spectral index imply redshifts of 3.8 and 3.4 for COSBO-4 and COSBO-9, respectively. COSBO-4 could be identified with a faint optical source in the HST ACS images. Its optical/IR photometric redshift of 3.2, is in agreement with the radio/millimeter redshift estimate. COSBO-9 could be identified with a very faint optical counterpart that was only detected in the COSMOS catalog at $i^+ \sim 28$ magnitudes. The optical/IR photometric redshift indicates either $z \sim 1$ or $z \sim 5 - 6$. Since only 3 photometric data points are available for this source, a redshift estimate is very uncertain. The detection of these two millimeter sources, which are most likely at $z > 3$, suggest that a substantial fraction of SMGs have redshifts higher than the bulk of this population ($z \sim 1 - 3$) and imply that the study of SMGs at higher redshifts is still incomplete.

From the three PdBI 1.3 mm detections associated with COSBO-6, only one (COSBO-6C) can be associated with radio emission above the 3σ level. Its radio to millimeter spectral index implies a redshift of ~ 1.4 . This source is associated with a relatively bright optical source with photometric redshift ≈ 1.8 , consistent with the radio estimate. The likely optical counterparts for the other PdBI detections are faint and their optical/IR redshifts are not as well constrained as for the radio detected source (COSBO-6C). For the northern PdBI source (COSBO-6N), the optical photometric redshift is ~ 1.3 , similar to the photometric redshift derived for COSBO-6C, but in disagreement with the optical photometric redshift derived for the southern source, $z \sim 0.5$. The detection of at least two millimeter sources related in space is consistent with the clustering of high-redshift *BzK* galaxies at $z \sim 1.5$. It indicates that these galaxies are in an active star formation phase, likely being part of mergers.

In Chapter 6, we report the detection of four CO lines toward COSBO-11 (J100038+020822), a millimeter bright AGN at $z = 1.8275$. We used the IRAM 30 m telescope to observe the ^{12}CO $J = 2-1, 4-3, 5-4$ and $6-5$ emission lines. The CO SED shows a peak in the CO $5-4$ transition and LVG modeling of the CO SED yields molecular gas (H_2) densities in the range $10^{3.5-4.0} \text{ cm}^{-3}$ and kinetic temperatures between 50 K and 200 K. This source appears to be less excited than other known high-redshift QSOs (e.g., J1148+5251, BR1202-0725, APM08279+5255) but more similar to what is found for the only SMG studied in several CO transitions to date, J16359+6612. The CO emission seems to be concentrated in the central kpc, as the comparison of the predicted brightness temperatures and the observed main beam temperatures shows. The implied molecular gas mass of $(3.6 - 5.4) \times 10^{10} M_\odot$ could account for a substantial fraction of the implied dynamical mass within this radius (< 0.75 kpc).

Assuming a two-component gray-body far-IR spectrum, we derive a dust mass of $1.2 \times 10^9 M_\odot$, and a dominant cold dust component with $T_d = 42 \pm 4$ K. The broad MgII line seen in the optical spectrum of this MAMBO galaxy allowed us to estimate the central black hole mass to $1.7 \times 10^9 M_\odot$.

Although the molecular gas and dust properties are similar to those of typical SMGs and some ULIRGs, the SED from the X-rays to the mid-IR is typical of a QSO. The optical morphology associated with this system is complex, showing evidence of a possible interaction or merger. Its shared properties of starburst and AGN suggests that this composite galaxy fits into the evolutionary scenario from starburst to QSOs proposed by Sanders et al. (1988a).

7.2 Perspectives

Despite the great advances achieved in the understanding of the nature of SMGs, there are still a number of questions to be answered to place SMGs into an evolutionary context.

An important step is to observe larger contiguous areas of the sky at submillimeter wavelengths that allow to get statistically more significant samples of SMGs. Our ongoing LABOCA survey of the COSMOS field (P.I.: F. Bertoldi) is expected to map a total area of $\sim 1 \text{ deg}^2$ and detect

~ 100 bright SMGs. This survey will allow studies of the correlation strength of SMGs and the comparison with the large scale structure at high redshift as traced by other classes of galaxies (e.g. *BzK*, EROs). This will bring more conclusive evidence on how SMGs are related to local spheroidals and to their environment. By tracing the bright end of the SMG luminosity function, it will be possible to shed light on the role that AGN accretion has in setting a limit to the maximum luminosity that starburst galaxies can have and to probe whether brighter SMGs are significantly more distant than the average SMG (Ivison et al., 2002; Younger et al., 2007).

The measurement of spectroscopic redshifts for SMGs is crucial to study the nature of this population. Our MAMBO galaxies and the high-redshift *BzK* galaxies in the most crowded environments around them are currently being targeted with Keck spectroscopy. This will allow studies of the properties of the COSBO sources in greater detail, such as accurate measures of their stellar masses and redshifts. Also, it will permit to further quantify the clustering of the *BzK* galaxies around SMGs and thus obtain a more complete description of their relation to local ellipticals. Accurate redshifts will allow follow-up searches for bright CO or atomic lines, probing the molecular gas properties in these sources.

For the 12 brightest COSBO sources we will obtain Spitzer mid-IR spectroscopy (P.I.: C. Carilli). The PAH emission features present in the mid-IR spectra of starburst galaxies can provide accurate redshifts (or lower limits) in order to verify the high redshift tail of SMGs and to study their dominant power source, whether starburst or AGN activity.

We recently obtained deep CO $J = 1 - 0$ and continuum imaging the COSBO-11 using the VLA (P.I.: M. Aravena). The measured intensity of the CO $1 - 0$ line yields a direct estimate of the amount of molecular gas present in this object and can be used to further constrain our modeling of the CO SED, and therefore the properties of the molecular gas. High-resolution imaging of the CO $5 - 4$ line with the PdBI will allow to resolve the gas distribution in the inner regions of this starburst/QSO and to reveal whether interaction with a possible companion galaxy is taking place.

For seven significant MAMBO sources (and six Bolocam sources), deep $350 \mu\text{m}$ maps were obtained with the SHARC-II instrument on the CSO (P.I.: J. Aguirre). In combination with deep MIPS $70 \mu\text{m}$ and $160 \mu\text{m}$ along with the $1200 \mu\text{m}$ flux densities and spectroscopic redshifts, this will permit to study the dust properties (temperature and masses) on a significant sample of SMGs.

We will continue the interferometric imaging of our COSBO sources. Using the Submillimeter Array (SMA), three significant COSBO sources that did not show any significant VLA 1.4 GHz radio counterpart (COSBO 1, 14 and 15) will be observed at $870 \mu\text{m}$ (P.I.: G. Fazio). This will allow further progress in the detection of dust obscured galaxies that possibly lie at the highest redshifts and their study through the multi-wavelength COSMOS dataset.

References

- Alexander, D. M., Bauer, F. E., Brandt, W. N., et al. 2003, *AJ*, 125, 383
- Alexander, D. M., Bauer, F. E., Chapman, S. C., et al. 2005, *ApJ*, 632, 736
- Almaini, O. 2002, in *Astronomical Society of the Pacific Conference Series*, Vol. 283, *A New Era in Cosmology*, ed. N. Metcalfe & T. Shanks, 377–+
- Altieri, B., Metcalfe, L., Kneib, J. P., et al. 1999, *A&A*, 343, L65
- Andreani, P., Cimatti, A., Loinard, L., & Röttgering, H. 2000, *A&A*, 354, L1
- Aravena, M., Bertoldi, F., Schinnerer, E., et al. 2008, *A&A*, 491, 173
- Aretxaga, I., Hughes, D. H., Coppin, K., et al. 2007, *MNRAS*, 379, 1571
- Armand, C., Milliard, B., & Deharveng, J. M. 1994, *A&A*, 284, 12
- Ashby, M. L. N., Dye, S., Huang, J.-S., et al. 2006, *ApJ*, 644, 778
- Barger, A. J., Cowie, L. L., & Richards, E. A. 2000, *AJ*, 119, 2092
- Barger, A. J., Cowie, L. L., Sanders, D. B., et al. 1998, *Nature*, 394, 248
- Barnes, J. E. & Hernquist, L. 1996, *ApJ*, 471, 115
- Baugh, C. M., Lacey, C. G., Frenk, C. S., et al. 2005, *MNRAS*, 356, 1191
- Beelen, A., Cox, P., Benford, D. J., et al. 2006, *ApJ*, 642, 694
- Beelen, A., Cox, P., Pety, J., et al. 2004, *A&A*, 423, 441
- Beelen, A., Omont, A., Bavouzet, N., et al. 2008, *A&A*, 485, 645
- Bernstein, R. A., Freedman, W. L., & Madore, B. F. 2002, *ApJ*, 571, 56
- Berta, S., Lonsdale, C. J., Siana, B., et al. 2007, *A&A*, 467, 565
- Bertin, E. 2006, in *Astronomical Society of the Pacific Conference Series*, Vol. 351, *Astronomical Data Analysis Software and Systems XV*, ed. C. Gabriel, C. Arviset, D. Ponz, & S. Enrique, 112–+
- Bertin, E. & Arnouts, S. 1996, *A&AS*, 117, 393
- Bertin, E., Mellier, Y., Radovich, M., et al. 2002, in *Astronomical Society of the Pacific Conference Series*, Vol. 281, *Astronomical Data Analysis Software and Systems XI*, ed. D. A. Bohlender, D. Durand, & T. H. Handley, 228–+
- Bertoldi, F., Carilli, C., Aravena, M., et al. 2007, *ApJS*, 172, 132
- Bertoldi, F., Carilli, C. L., Menten, K. M., et al. 2000, *A&A*, 360, 92
- Bertoldi, F., Cox, P., Neri, R., et al. 2003, *A&A*, 409, L47
- Best, P. N. 2000, *MNRAS*, 317, 720
- Best, P. N. 2002, *MNRAS*, 336, 1293

- Best, P. N., Lehnert, M. D., Miley, G. K., & Röttgering, H. J. A. 2003, *MNRAS*, 343, 1
- Blain, A. W., Chapman, S. C., Smail, I., & Ivison, R. 2004a, *ApJ*, 611, 52
- Blain, A. W., Chapman, S. C., Smail, I., & Ivison, R. 2004b, *ApJ*, 611, 725
- Blain, A. W. & Longair, M. S. 1993, *MNRAS*, 265, L21
- Blain, A. W., Smail, I., Ivison, R. J., & Kneib, J.-P. 1999, *MNRAS*, 302, 632
- Blain, A. W., Smail, I., Ivison, R. J., Kneib, J.-P., & Frayer, D. T. 2002, *Phys. R.*, 369, 111
- Bolzonella, M., Miralles, J.-M., & Pelló, R. 2000, *A&A*, 363, 476
- Borys, C., Chapman, S., Halpern, M., & Scott, D. 2003, *MNRAS*, 344, 385
- Borys, C., Smail, I., Chapman, S. C., et al. 2005, *ApJ*, 635, 853
- Bouwens, R. J., Illingworth, G. D., Rosati, P., et al. 2003, *ApJ*, 595, 589
- Bouwens, R. J., Thompson, R. I., Illingworth, G. D., et al. 2004, *ApJL*, 616, L79
- Brodwin, M., Brown, M. J. I., Ashby, M. L. N., et al. 2006, *ApJ*, 651, 791
- Brusa, M., Zamorani, G., Comastri, A., et al. 2007, *ApJS*, 172, 353
- Bruzual, G. & Charlot, S. 2003, *MNRAS*, 344, 1000
- Calzetti, D., Armus, L., Bohlin, R. C., et al. 2000, *ApJ*, 533, 682
- Capak, P., Aussel, H., Ajiki, M., et al. 2007, *ApJS*, 172, 99
- Cappelluti, N., Hasinger, G., Brusa, M., et al. 2007, *ApJS*, 172, 341
- Carilli, C. L., Bertoldi, F., Rupen, M. P., et al. 2001, *ApJ*, 555, 625
- Carilli, C. L., Kohno, K., Kawabe, R., et al. 2002, *AJ*, 123, 1838
- Carilli, C. L., Neri, R., Wang, R., et al. 2007, *ApJL*, 666, L9
- Carilli, C. L. & Yun, M. S. 1999, *ApJL*, 513, L13
- Castellano, M., Salimbeni, S., Trevese, D., et al. 2007, *ApJ*, 671, 1497
- Chabrier, G. 2003, *PASP*, 115, 763
- Chapman, S. C., Blain, A. W., Ibata, R., et al. 2008, *ArXiv e-prints*
- Chapman, S. C., Blain, A. W., Ivison, R. J., & Smail, I. R. 2003, *Nature*, 422, 695
- Chapman, S. C., Blain, A. W., Smail, I., & Ivison, R. J. 2005, *ApJ*, 622, 772
- Chapman, S. C., Scott, D., Borys, C., & Fahlman, G. G. 2002, *MNRAS*, 330, 92
- Cimatti, A., Daddi, E., Mignoli, M., et al. 2002, *A&A*, 381, L68
- Clements, D. L., Vaccari, M., Babbedge, T., et al. 2008, *MNRAS*, 387, 247
- Coleman, G. D., Wu, C.-C., & Weedman, D. W. 1980, *ApJS*, 43, 393
- Condon, J. J. 1992, *ARAA*, 30, 575
- Connolly, A. J., Szalay, A. S., Dickinson, M., Subbarao, M. U., & Brunner, R. J. 1997, *ApJL*, 486, L11+
- Coppin, K., Chapin, E. L., Mortier, A. M. J., et al. 2006, *MNRAS*, 372, 1621
- Coppin, K., Swinbank, M., Neri, R., et al. 2008, *ArXiv e-prints*, 806
- Cowie, L. L., Barger, A. J., Fomalont, E. B., & Capak, P. 2004, *ApJL*, 603, L69

- Cowie, L. L., Barger, A. J., & Kneib, J.-P. 2002, *AJ*, 123, 2197
- Cowie, L. L., Songaila, A., & Barger, A. J. 1999, *AJ*, 118, 603
- Cowie, L. L., Songaila, A., Hu, E. M., & Cohen, J. G. 1996, *AJ*, 112, 839
- Cram, L. E. 1998, *ApJL*, 506, L85
- Croft, S., Kurk, J., van Breugel, W., et al. 2005, *AJ*, 130, 867
- Daddi, E., Cimatti, A., & Renzini, A. 2000, *A&A*, 362, L45
- Daddi, E., Cimatti, A., Renzini, A., et al. 2004, *ApJ*, 617, 746
- Daddi, E., Dickinson, M., Morrison, G., et al. 2007, *ApJ*, 670, 156
- Dale, D. A., Gil de Paz, A., Gordon, K. D., et al. 2007, *ApJ*, 655, 863
- Dannerbauer, H., Daddi, E., Onodera, M., et al. 2006, *ApJL*, 637, L5
- Dannerbauer, H., Lehnert, M. D., Lutz, D., et al. 2002, *ApJ*, 573, 473
- Dannerbauer, H., Lehnert, M. D., Lutz, D., et al. 2004, *ApJ*, 606, 664
- Dannerbauer, H., Walter, F., & Morrison, G. 2008, *ApJL*, 673, L127
- De Breuck, C., Downes, D., Neri, R., et al. 2005, *A&A*, 430, L1
- De Breuck, C., Neri, R., & Omont, A. 2003, *New Astronomy Review*, 47, 285
- Di Matteo, T., Springel, V., & Hernquist, L. 2005, *Nature*, 433, 604
- Dickinson, M., Papovich, C., Ferguson, H. C., & Budavári, T. 2003, *ApJ*, 587, 25
- Dole, H., Le Floc'h, E., Pérez-González, P. G., et al. 2004, *ApJS*, 154, 87
- Downes, A. J. B., Peacock, J. A., Savage, A., & Carrie, D. R. 1986, *MNRAS*, 218, 31
- Downes, D. & Solomon, P. M. 1998, *ApJ*, 507, 615
- Dressler, A. 1980, *ApJ*, 236, 351
- Dunlop, J. S. 2001, *New Astronomy Review*, 45, 609
- Dwek, E. & Arendt, R. G. 1998, *ApJL*, 508, L9
- Dwek, E., Arendt, R. G., Hauser, M. G., et al. 1998, *ApJ*, 508, 106
- Dwek, E. & Krennrich, F. 2005, *ApJ*, 618, 657
- Dye, S., Eales, S. A., Aretxaga, I., et al. 2008, *MNRAS*, 433
- Eales, S., Lilly, S., Gear, W., et al. 1999, *ApJ*, 515, 518
- Eales, S., Lilly, S., Webb, T., et al. 2000, *AJ*, 120, 2244
- Egami, E., Dole, H., Huang, J.-S., et al. 2004, *ApJS*, 154, 130
- Elston, R., Rieke, G. H., & Rieke, M. J. 1988, *ApJL*, 331, L77
- Elston, R. J., Gonzalez, A. H., McKenzie, E., et al. 2006, *ApJ*, 639, 816
- Elvis, M., Wilkes, B. J., McDowell, J. C., et al. 1994, *ApJS*, 95, 1
- Evans, A. S., Mazzarella, J. M., Surace, J. A., et al. 2005, *ApJS*, 159, 197
- Evans, A. S., Mazzarella, J. M., Surace, J. A., & Sanders, D. B. 2002, *ApJ*, 580, 749
- Fabian, A. C., Smail, I., Iwasawa, K., et al. 2000, *MNRAS*, 315, L8

- Fazio, G. G., Ashby, M. L. N., Barmby, P., et al. 2004, *ApJS*, 154, 39
- Ferrarese, L. & Merritt, D. 2000, *ApJL*, 539, L9
- Finkbeiner, D. P., Davis, M., & Schlegel, D. J. 2000, *ApJ*, 544, 81
- Finoguenov, A., Guzzo, L., Hasinger, G., et al. 2007, *ApJS*, 172, 182
- Fixsen, D. J., Bennett, C. L., & Mather, J. C. 1999, *ApJ*, 526, 207
- Fixsen, D. J., Cheng, E. S., Gales, J. M., et al. 1996, *ApJ*, 473, 576
- Fixsen, D. J., Dwek, E., Mather, J. C., Bennett, C. L., & Shafer, R. A. 1998, *ApJ*, 508, 123
- Flores, H., Hammer, F., Thuan, T. X., et al. 1999, *ApJ*, 517, 148
- Flower, D. R. 2001, *Journal of Physics B Atomic Molecular Physics*, 34, 2731
- Fontana, A., Salimbeni, S., Grazian, A., et al. 2006, *A&A*, 459, 745
- Franx, M., Labbé, I., Rudnick, G., et al. 2003, *ApJL*, 587, L79
- Frayer, D. T., Ivison, R. J., Scoville, N. Z., et al. 1999, *ApJL*, 514, L13
- Frayer, D. T., Ivison, R. J., Scoville, N. Z., et al. 1998, *ApJL*, 506, L7
- Frayer, D. T., Koda, J., Pope, A., et al. 2008, *ApJL*, 680, L21
- Gallego, J., Zamorano, J., Aragon-Salamanca, A., & Rego, M. 1996, *ApJL*, 459, L43+
- Gebhardt, K., Bender, R., Bower, G., et al. 2000, *ApJL*, 539, L13
- Genzel, R., Lutz, D., Sturm, E., et al. 1998, *ApJ*, 498, 579
- Gialalisco, M., Dickinson, M., Ferguson, H. C., et al. 2004a, *ApJL*, 600, L103
- Gialalisco, M., Ferguson, H. C., Koekemoer, A. M., et al. 2004b, *ApJL*, 600, L93
- Gladders, M. D. 2002, PhD thesis, AA(Department of Astronomy and Astrophysics, University of Toronto)
- Gladders, M. D. & Yee, H. K. C. 2000, *AJ*, 120, 2148
- Glazebrook, K., Abraham, R. G., McCarthy, P. J., et al. 2004, *Nature*, 430, 181
- Glenn, J., Ade, P. A. R., Amarie, M., et al. 2003, in Presented at the Society of Photo-Optical Instrumentation Engineers (SPIE) Conference, Vol. 4855, Millimeter and Submillimeter Detectors for Astronomy. Edited by Phillips, Thomas G.; Zmuidzinas, Jonas. Proceedings of the SPIE, Volume 4855, pp. 30-40 (2003)., ed. T. G. Phillips & J. Zmuidzinas, 30–40
- Gorjian, V., Wright, E. L., & Chary, R. R. 2000, *ApJ*, 536, 550
- Grazian, A., Salimbeni, S., Pentericci, L., et al. 2007, *A&A*, 465, 393
- Greve, T. R., Bertoldi, F., Smail, I., et al. 2005, *MNRAS*, 359, 1165
- Greve, T. R., Ivison, R. J., Bertoldi, F., et al. 2004, *MNRAS*, 354, 779
- Greve, T. R., Pope, A., Scott, D., et al. 2008, *ArXiv e-prints*, 806
- Guilloteau, S., Omont, A., Cox, P., McMahon, R. G., & Petitjean, P. 1999, *A&A*, 349, 363
- Guilloteau, S., Omont, A., McMahon, R. G., Cox, P., & Petitjean, P. 1997, *A&A*, 328, L1
- Güsten, R., Philipp, S. D., Weiß, A., & Klein, B. 2006, *A&A*, 454, L115
- Guzzo, L., Cassata, P., Finoguenov, A., et al. 2007, *ApJS*, 172, 254
- Haarsma, D. B., Partridge, R. B., Windhorst, R. A., & Richards, E. A. 2000, *ApJ*, 544, 641

- Haig, D. J., Ade, P. A. R., Aguirre, J. E., et al. 2004, in Presented at the Society of Photo-Optical Instrumentation Engineers (SPIE) Conference, Vol. 5498, Millimeter and Submillimeter Detectors for Astronomy II. Edited by Jonas Zmuidzinas, Wayne S. Holland and Stafford Withington Proceedings of the SPIE, Volume 5498, pp. 78-94 (2004)., ed. C. M. Bradford, P. A. R. Ade, J. E. Aguirre, J. J. Bock, M. Dragovan, L. Duband, L. Earle, J. Glenn, H. Matsuhara, B. J. Naylor, H. T. Nguyen, M. Yun, & J. Zmuidzinas, 78-94
- Hainline, L. J., Scoville, N. Z., Yun, M. S., et al. 2004, *ApJ*, 609, 61
- Hall, P. B. & Green, R. F. 1998, *ApJ*, 507, 558
- Hall, P. B., Sawicki, M., Martini, P., et al. 2001, *AJ*, 121, 1840
- Hasinger, G., Cappelluti, N., Brunner, H., et al. 2007, *ApJS*, 172, 29
- Hatziminaoglou, E., Pérez-Fournon, I., Polletta, M., et al. 2005, *AJ*, 129, 1198
- Hauser, M. G., Arendt, R. G., Kelsall, T., et al. 1998, *ApJ*, 508, 25
- Hickox, R. C., Jones, C., Forman, W. R., et al. 2007, *ApJ*, 671, 1365
- Hitschfeld, M., Aravena, M., Kramer, C., et al. 2008, *A&A*, 479, 75
- Högbom, J. A. 1974, *A&AS*, 15, 417
- Holland, W. S., Robson, E. I., Gear, W. K., et al. 1999, *MNRAS*, 303, 659
- Hopkins, A. M., Connolly, A. J., Haarsma, D. B., & Cram, L. E. 2001, *AJ*, 122, 288
- Hopkins, P. F., Hernquist, L., Cox, T. J., et al. 2005, *ApJ*, 630, 705
- Hopkins, P. F., Hernquist, L., Cox, T. J., et al. 2006, *ApJS*, 163, 1
- Hu, E. M. & Ridgway, S. E. 1994, *AJ*, 107, 1303
- Hughes, D. H., Serjeant, S., Dunlop, J., et al. 1998, *Nature*, 394, 241
- Ilbert, O., Arnouts, S., McCracken, H. J., et al. 2006, *A&A*, 457, 841
- Ilbert, O., Capak, P., Salvato, M., et al. 2008, *ArXiv e-prints*
- Intema, H. T., Venemans, B. P., Kurk, J. D., et al. 2006, *A&A*, 456, 433
- Iverson, R. J., Dunlop, J. S., Smail, I., et al. 2000a, *ApJ*, 542, 27
- Iverson, R. J., Greve, T. R., Dunlop, J. S., et al. 2007, *MNRAS*, 380, 199
- Iverson, R. J., Greve, T. R., Serjeant, S., et al. 2004, *ApJS*, 154, 124
- Iverson, R. J., Greve, T. R., Smail, I., et al. 2002, *MNRAS*, 337, 1
- Iverson, R. J., Smail, I., Barger, A. J., et al. 2000b, *MNRAS*, 315, 209
- Iverson, R. J., Smail, I., Dunlop, J. S., et al. 2005, *MNRAS*, 364, 1025
- Iverson, R. J., Smail, I., Le Borgne, J.-F., et al. 1998, *MNRAS*, 298, 583
- Iwata, I., Ohta, K., Tamura, N., et al. 2003, *PASJ*, 55, 415
- Jahnke, K., Sánchez, S. F., Wisotzki, L., et al. 2004, *ApJ*, 614, 568
- Jenkins, A., Frenk, C. S., Pearce, F. R., et al. 1998, *ApJ*, 499, 20
- Kajisawa, M., Kodama, T., Tanaka, I., Yamada, T., & Bower, R. 2006, *MNRAS*, 371, 577
- Kawara, K., Sato, Y., Matsuhara, H., et al. 1998, *A&A*, 336, L9
- Kennicutt, Jr., R. C. 1998, *ARAA*, 36, 189
- Klamer, I. J., Ekers, R. D., Sadler, E. M., et al. 2005, *ApJL*, 621, L1

- Kneib, J.-P., van der Werf, P. P., Kraiberg Knudsen, K., et al. 2004, MNRAS, 349, 1211
- Knudsen, K. K., Barnard, V. E., van der Werf, P. P., et al. 2006, MNRAS, 368, 487
- Knudsen, K. K., van der Werf, P. P., & Kneib, J.-P. 2008, MNRAS, 384, 1611
- Kodama, T., Tanaka, I., Kajisawa, M., et al. 2007, MNRAS, 377, 1717
- Koekemoer, A. M., Aussel, H., Calzetti, D., et al. 2007, ApJS, 172, 196
- Kovács, A., Chapman, S. C., Dowell, C. D., et al. 2006, ApJ, 650, 592
- Kreysa, E., Gemuend, H.-P., Gromke, J., et al. 1998, in Presented at the Society of Photo-Optical Instrumentation Engineers (SPIE) Conference, Vol. 3357, Proc. SPIE Vol. 3357, p. 319-325, Advanced Technology MMW, Radio, and Terahertz Telescopes, Thomas G. Phillips; Ed., ed. T. G. Phillips, 319-325
- Krugel, E. & Siebenmorgen, R. 1994, A&A, 288, 929
- Kurk, J. D., Pentericci, L., Overzier, R. A., Röttgering, H. J. A., & Miley, G. K. 2004a, A&A, 428, 817
- Kurk, J. D., Pentericci, L., Röttgering, H. J. A., & Miley, G. K. 2004b, A&A, 428, 793
- Lacy, M., Storrie-Lombardi, L. J., Sajina, A., et al. 2004, ApJS, 154, 166
- Lagache, G. & Puget, J. L. 2000, A&A, 355, 17
- Lampton, M., Deharveng, J. M., & Bowyer, S. 1990, in IAU Symposium, Vol. 139, The Galactic and Extragalactic Background Radiation, ed. S. Bowyer & C. Leinert, 449-452
- Larson, R. B., Tinsley, B. M., & Caldwell, C. N. 1980, ApJ, 237, 692
- Laurent, G. T., Aguirre, J. E., Glenn, J., et al. 2005, ApJ, 623, 742
- Le Floch, E., Willmer, C. N. A., Noeske, K., et al. 2007, ApJL, 660, L65
- Lehnert, M. D. & Heckman, T. M. 1996, ApJ, 472, 546
- Lilly, S. J., Eales, S. A., Gear, W. K. P., et al. 1999, ApJ, 518, 641
- Lilly, S. J., Le Fevre, O., Hammer, F., & Crampton, D. 1996, ApJL, 460, L1+
- Lilly, S. J., Le Fevre, O., Renzini, A., et al. 2007, ApJS, 172, 70
- Lim, J. & Ho, P. T. P. 1999, ApJL, 510, L7
- Lutz, D., Valiante, E., Sturm, E., et al. 2005, ApJL, 625, L83
- Madau, P., Ferguson, H. C., Dickinson, M. E., et al. 1996, MNRAS, 283, 1388
- Mainieri, V., Hasinger, G., Cappelluti, N., et al. 2007, ApJS, 172, 368
- Maiolino, R., Neri, R., Beelen, A., et al. 2007, A&A, 472, L33
- Matarrese, S., Coles, P., Lucchin, F., & Moscardini, L. 1997, MNRAS, 286, 115
- Mather, J. C., Fixsen, D. J., Shafer, R. A., Mosier, C., & Wilkinson, D. T. 1999, ApJ, 512, 511
- McCarthy, P. J., Persson, S. E., & West, S. C. 1992, ApJ, 386, 52
- McLeod, K. K. & Rieke, G. H. 1994, ApJ, 431, 137
- McLeod, K. K., Rieke, G. H., & Storrie-Lombardi, L. J. 1999, ApJL, 511, L67
- McLure, R. J. & Dunlop, J. S. 2004, MNRAS, 352, 1390
- McLure, R. J. & Jarvis, M. J. 2002, MNRAS, 337, 109
- Menéndez-Delmestre, K., Blain, A. W., Alexander, D. M., et al. 2007, ApJL, 655, L65
- Mihos, J. C. & Hernquist, L. 1994, ApJL, 431, L9

- Miley, G. & De Breuck, C. 2008, *A&A R.*, 1
- Mobasher, B., Capak, P., Scoville, N. Z., et al. 2007, *ApJS*, 172, 117
- Mortier, A. M. J., Serjeant, S., Dunlop, J. S., et al. 2005, *MNRAS*, 363, 563
- Mullis, C. R., Rosati, P., Lamer, G., et al. 2005, *ApJL*, 623, L85
- Murthy, J., Hall, D., Earl, M., Henry, R. C., & Holberg, J. B. 1999, *ApJ*, 522, 904
- Neri, R., Genzel, R., Ivison, R. J., et al. 2003, *ApJL*, 597, L113
- Omont, A., Beelen, A., Bertoldi, F., et al. 2003, *A&A*, 398, 857
- Omont, A., Cox, P., Bertoldi, F., et al. 2001, *A&A*, 374, 371
- Omont, A., Petitjean, P., Guillobeau, S., et al. 1996, *Nature*, 382, 428
- Overzier, R. A., Bouwens, R. J., Cross, N. J. G., et al. 2008, *ApJ*, 673, 143
- Overzier, R. A., Miley, G. K., Bouwens, R. J., et al. 2006, *ApJ*, 637, 58
- Overzier, R. A., Röttgering, H. J. A., Rengelink, R. B., & Wilman, R. J. 2003, *A&A*, 405, 53
- Page, M. J., Stevens, J. A., Ivison, R. J., & Carrera, F. J. 2004, *ApJL*, 611, L85
- Papadopoulos, P. P., Greve, T. R., Ivison, R. J., & De Breuck, C. 2005, *A&A*, 444, 813
- Papovich, C., Dole, H., Egami, E., et al. 2004, *ApJS*, 154, 70
- Peacock, J. A. 1999, *Cosmological Physics* (Cosmological Physics, by John A. Peacock, pp. 704. ISBN 052141072X. Cambridge, UK: Cambridge University Press, January 1999.)
- Pérez-González, P. G., Rieke, G. H., Villar, V., et al. 2008, *ApJ*, 675, 234
- Peterson, B. M. & Wandel, A. 2000, *ApJL*, 540, L13
- Pettini, M., Kellogg, M., Steidel, C. C., et al. 1998, *ApJ*, 508, 539
- Polletta, M., Tajer, M., Maraschi, L., et al. 2007, *ApJ*, 663, 81
- Pope, A., Scott, D., Dickinson, M., et al. 2006, *MNRAS*, 370, 1185
- Pozzetti, L., Madau, P., Zamorani, G., Ferguson, H. C., & Bruzual A., G. 1998, *MNRAS*, 298, 1133
- Prescott, M. K. M., Impey, C. D., Cool, R. J., & Scoville, N. Z. 2006, *ApJ*, 644, 100
- Priddey, R. S. & McMahon, R. G. 2001, *MNRAS*, 324, L17
- Puget, J.-L., Abergel, A., Bernard, J.-P., et al. 1996, *A&A*, 308, L5+
- Reddy, N. A., Erb, D. K., Steidel, C. C., et al. 2005, *ApJ*, 633, 748
- Riechers, D. A., Walter, F., Carilli, C. L., et al. 2006, *ApJ*, 650, 604
- Rix, H.-W., Barden, M., Beckwith, S. V. W., et al. 2004, *ApJS*, 152, 163
- Rosati, P., Borgani, S., & Norman, C. 2002, *ARAA*, 40, 539
- Rosati, P., Stanford, S. A., Eisenhardt, P. R., et al. 1999, *AJ*, 118, 76
- Roussel, H., Sauvage, M., Vigroux, L., & Bosma, A. 2001, *A&A*, 372, 427
- Rowan-Robinson, M. 2000, *MNRAS*, 316, 885
- Sánchez, S. F. & González-Serrano, J. I. 1999, *A&A*, 352, 383
- Sánchez, S. F. & González-Serrano, J. I. 2002, *A&A*, 396, 773
- Sanders, D. B. 2004, *Advances in Space Research*, 34, 535

- Sanders, D. B. & Mirabel, I. F. 1996, *ARAA*, 34, 749
- Sanders, D. B., Phinney, E. S., Neugebauer, G., Soifer, B. T., & Matthews, K. 1989, *ApJ*, 347, 29
- Sanders, D. B., Salvato, M., Aussel, H., et al. 2007, *ApJS*, 172, 86
- Sanders, D. B., Soifer, B. T., Elias, J. H., et al. 1988a, *ApJ*, 325, 74
- Sanders, D. B., Soifer, B. T., Elias, J. H., Neugebauer, G., & Matthews, K. 1988b, *ApJL*, 328, L35
- Santos, M. R., Ellis, R. S., Kneib, J.-P., Richard, J., & Kuijken, K. 2004, *ApJ*, 606, 683
- Saunders, W., Rowan-Robinson, M., Lawrence, A., et al. 1990, *MNRAS*, 242, 318
- Schechter, P. 1976, *ApJ*, 203, 297
- Schinnerer, E., Smolčić, V., Carilli, C. L., et al. 2007, *ApJS*, 172, 46
- Schlegel, D. J., Finkbeiner, D. P., & Davis, M. 1998, *ApJ*, 500, 525
- Schneider, P., Ehlers, J., & Falco, E. E. 1992, *Gravitational Lenses (Gravitational Lenses, XIV, 560 pp. 112 figs.. Springer-Verlag Berlin Heidelberg New York. Also Astronomy and Astrophysics Library)*
- Scott, K. S., Austermann, J. E., Perera, T. A., et al. 2008, *MNRAS*, 268
- Scott, S. E., Fox, M. J., Dunlop, J. S., et al. 2002, *MNRAS*, 331, 817
- Scoville, N. 2003, *Journal of Korean Astronomical Society*, 36, 167
- Scoville, N., Abraham, R. G., Aussel, H., et al. 2007a, *ApJS*, 172, 38
- Scoville, N., Aussel, H., Benson, A., et al. 2007b, *ApJS*, 172, 150
- Scoville, N., Aussel, H., Brusa, M., et al. 2007c, *ApJS*, 172, 1
- Scoville, N. Z., Evans, A. S., Thompson, R., et al. 2000, *AJ*, 119, 991
- Sheth, K., Blain, A. W., Kneib, J.-P., et al. 2004, *ApJL*, 614, L5
- Silva, L., Granato, G. L., Bressan, A., & Danese, L. 1998, *ApJ*, 509, 103
- Smail, I., Ivison, R. J., & Blain, A. W. 1997, *ApJL*, 490, L5+
- Smail, I., Ivison, R. J., Blain, A. W., & Kneib, J.-P. 2002, *MNRAS*, 331, 495
- Smail, I., Ivison, R. J., Gilbank, D. G., et al. 2003, *ApJ*, 583, 551
- Smail, I., Ivison, R. J., Owen, F. N., Blain, A. W., & Kneib, J.-P. 2000, *ApJ*, 528, 612
- Smith, G. P., Treu, T., Ellis, R. S., Moran, S. M., & Dressler, A. 2005, *ApJ*, 620, 78
- Smolcic, V., Schinnerer, E., Zamorani, G., et al. 2008, *ArXiv e-prints*
- Soifer, B. T., Neugebauer, G., Matthews, K., et al. 2000, *AJ*, 119, 509
- Solomon, P. M., Downes, D., Radford, S. J. E., & Barrett, J. W. 1997, *ApJ*, 478, 144
- Solomon, P. M. & Vanden Bout, P. A. 2005, *ARAA*, 43, 677
- Stanev, T. & Franceschini, A. 1998, *ApJL*, 494, L159+
- Stanford, S. A., Eisenhardt, P. R., Brodwin, M., et al. 2005, *ApJL*, 634, L129
- Stanford, S. A., Elston, R., Eisenhardt, P. R., et al. 1997, *AJ*, 114, 2232
- Stanford, S. A., Romer, A. K., Sabirli, K., et al. 2006, *ApJL*, 646, L13
- Steidel, C. C., Adelberger, K. L., Giavalisco, M., Dickinson, M., & Pettini, M. 1999, *ApJ*, 519, 1
- Steidel, C. C., Adelberger, K. L., Shapley, A. E., et al. 2000, *ApJ*, 532, 170

- Steidel, C. C., Adelberger, K. L., Shapley, A. E., et al. 2003, *ApJ*, 592, 728
- Steidel, C. C., Giavalisco, M., Dickinson, M., & Adelberger, K. L. 1996, *AJ*, 112, 352
- Stern, D., Eisenhardt, P., Gorjian, V., et al. 2005, *ApJ*, 631, 163
- Stetson, P. B. 1987, *PASP*, 99, 191
- Stevens, J. A., Ivison, R. J., Dunlop, J. S., et al. 2003, *Nature*, 425, 264
- Stevens, J. A., Page, M. J., Ivison, R. J., et al. 2005, *MNRAS*, 360, 610
- Surace, J. A., Sanders, D. B., Vacca, W. D., Veilleux, S., & Mazzarella, J. M. 1998, *ApJ*, 492, 116
- Swinbank, A. M., Chapman, S. C., Smail, I., et al. 2006, *MNRAS*, 371, 465
- Swinbank, A. M., Edge, A. C., Smail, I., et al. 2007, *MNRAS*, 379, 1343
- Swinbank, M., Lacey, C., Smail, I., et al. 2008, *ArXiv e-prints*
- Tacconi, L. J., Genzel, R., Lutz, D., et al. 2002, *ApJ*, 580, 73
- Tacconi, L. J., Genzel, R., Smail, I., et al. 2008, *ArXiv e-prints*, 801
- Tacconi, L. J., Neri, R., Chapman, S. C., et al. 2006, *ApJ*, 640, 228
- Takagi, T., Ono, Y., Shimasaku, K., & Hanami, H. 2008, *ArXiv e-prints*, 806
- Tan, J. C., Silk, J., & Balland, C. 1999, *ApJ*, 522, 579
- Taniguchi, Y., Scoville, N., Murayama, T., et al. 2007, *ApJS*, 172, 9
- Thompson, D., Beckwith, S. V. W., Fockenbrock, R., et al. 1999, *ApJ*, 523, 100
- Thompson, T. A., Quataert, E., & Murray, N. 2005, *ApJ*, 630, 167
- Toller, G., Tanabe, H., & Weinberg, J. L. 1987, *A&A*, 188, 24
- Trump, J. R., Impey, C. D., McCarthy, P. J., et al. 2007, *ApJS*, 172, 383
- Valiante, E., Lutz, D., Sturm, E., et al. 2007, *ApJ*, 660, 1060
- van Dokkum, P. G., Förster Schreiber, N. M., Franx, M., et al. 2003, *ApJL*, 587, L83
- Veilleux, S., Sanders, D. B., & Kim, D.-C. 1999, *ApJ*, 522, 139
- Venemans, B. P., Röttgering, H. J. A., Miley, G. K., et al. 2005, *A&A*, 431, 793
- Venemans, B. P., Röttgering, H. J. A., Miley, G. K., et al. 2007, *A&A*, 461, 823
- Venemans, B. P., Röttgering, H. J. A., Overzier, R. A., et al. 2004, *A&A*, 424, L17
- Véron-Cetty, M. P. & Véron, P. 2000, *A&A R.*, 10, 81
- Voss, H., Bertoldi, F., Carilli, C., et al. 2006, *A&A*, 448, 823
- Walter, F., Bertoldi, F., Carilli, C., et al. 2003, *Nature*, 424, 406
- Walter, F., Carilli, C., Bertoldi, F., et al. 2004, *ApJL*, 615, L17
- Wang, R., Wagg, J., Carilli, C. L., et al. 2008, *AJ*, 135, 1201
- Webb, T. M., Eales, S. A., Lilly, S. J., et al. 2003, *ApJ*, 587, 41
- Webb, T. M. A., Yee, H. K. C., Ivison, R. J., et al. 2005, *ApJ*, 631, 187
- Weiß, A., Downes, D., Neri, R., et al. 2007, *A&A*, 467, 955
- Weiß, A., Downes, D., Walter, F., & Henkel, C. 2005a, *A&A*, 440, L45

- Weiß, A., Kovács, A., Güsten, R., et al. 2008, *A&A*, 490, 77
- Weiß, A., Walter, F., & Scoville, N. Z. 2005b, *A&A*, 438, 533
- Williams, R. E., Blacker, B., Dickinson, M., et al. 1996, *AJ*, 112, 1335
- Wilson, G., Huang, J.-S., Fazio, G. G., et al. 2007, *ApJL*, 660, L59
- Wilson, G., Huang, J.-S., Pérez-González, P. G., et al. 2004, *ApJS*, 154, 107
- Wilson, G. W., Austermann, J. E., Perera, T. A., et al. 2008, *MNRAS*, 386, 807
- Wright, E. L. & Johnson, B. D. 2001, *ArXiv Astrophysics e-prints*
- Wright, E. L. & Reese, E. D. 2000, *ApJ*, 545, 43
- Younger, J. D., Fazio, G. G., Huang, J.-S., et al. 2007, *ApJ*, 671, 1531
- Younger, J. D., Fazio, G. G., Wilner, D. J., et al. 2008, *ArXiv e-prints*
- Zhu, M., Seaquist, E. R., & Kuno, N. 2003, *ApJ*, 588, 243
- Zirm, A. W., Stanford, S. A., Postman, M., et al. 2008, *ArXiv e-prints*, 802

Acknowledgments

It would have been impossible to go through my doctoral studies without the support of many wonderful people. Here, I would like to thank all of them.

First of all, I would like to thank my parents, Nora and Julio, and my whole family for their unconditional support to become an astronomer. *Gracias mamá y papá por el apoyo incondicional en este difícil camino para ser astrónomo. Gracias por el amor y los valores que me han dado. Gracias también a mi núcleo familiar, mi abuelita Nora, y a mis tíos Pepe, Gabriel (Lilo) y Daniel.*

Perhaps more important has been the support from my wife, Constanza. Her unlimited love, patience, loyalty and tenderness has strongly motivated me all the way to the end.

I am very grateful to Frank Bertoldi for his patience and guidance throughout these important years of my life. Thanks for your open mind, clever ideas and strong motivation.

I would like to give special thanks to Gabriele Breuer, Christina Stein-Schmitz and Eduardo Ros. You have made my life in Bonn much easier. I really appreciate your kindness, infinite patience and support.

Thanks to my collaborators in the COSMOS team, particularly to Eva Schinnerer, Chris Carilli, Mara Salvato and Karl Menten. Thanks to Henry J. McCracken for providing me the K-band data used in part of this Thesis. Thanks to Knud Jahnke for the nucleus-subtracted ACS images of J100038. Thanks to Axel Weiss, Christian Henkel and Martin Müller for instructing me on single dish telescope observations. I would also like to thank to the NANTEN2 team, in particular to Marc Hitschfeld and Carsten Kramer.

It is very important for me to thank my dear friends Timo Anguita, Paola Caprile and Paula Jofré-Pfeil. I thank you very much for your advice, unconditional support and friendship. I appreciate very much our years in Germany, our “jugos” and all that we have lived together that has certainly shaped our lives.

Many thanks to my friends C. W. Martin “the boy” Nord, Alexandre “high-Z rider” Beelen, Kaustuv Basu, Diego Garcia-Appadoo, Catherine Vlahakis, Frederic Schuller and Florian Pacaud. You have certainly made my years in Bonn lovely. Thanks Martin for being my boy from the beginning. Thanks Alex for your friendship, and for instructing me on millimeter interferometer observations.

I would also like to thank to my friends Chris Puetz and Nikhil Jethava, for backing me in difficult times. Thanks to Yahya Orr, Schech Bashir Dultz, Chadigah Kissel, Karimah Stauch and the whole Tariqa As-safina.

Many thanks to the computer managers, cleaning ladies and to all the AIFA people.

I was supported for this research through a stipend from the International Max-Planck Research School (IMPRS) for Radio and Infrared Astronomy at the Universities of Bonn and Cologne.

Curriculum Vitae

Personal

Name: Manuel Alejandro Aravena Aguirre.

Place of birth: Santiago, Chile.

Education

(2005 – Today) Doctoral studies at the Argelander Institute für Astronomie of the Rheinischen-Friedrich-Wilhelms Universität Bonn. Supervisor: Prof. Dr. Frank Bertoldi.

(2001 – 2005) Diploma studies at the Department of Astronomy and Astrophysics of the Pontificia Universidad Católica de Chile. Thesis title: *Determination of the star-formation history of the Universe in the MUSYC survey*. Graduated with “highest distinction”. Supervisors: Prof. Dr. Francisco Castander and Prof. Dr. Leopoldo Infante.

(1997 – 2000) High-school studies at the Santa Maria La Florida school in Santiago, Chile.

Grants, Awards, Honors

(2005) International Max-Planck Research School doctoral studentship for doctoral studies. Max-Planck Society (Bonn, Germany).

(2004) Latin-European Network for Astronomy and Cosmology fellowship for collaboration visit to the Instituto de Estudios Espaciales de Catalunya (Barcelona, Spain).

(2001) *Padre Hurtado* scholarship for academic excellence (Santiago, Chile).

(2001) *Juan Gomez Millas* scholarship for university studies (Santiago, Chile).

Publications

- Aravena, M.**, Bertoldi, F., Schinnerer, E., et al. 2007, *Properties of the Molecular Gas in a Starbursting QSO at $z = 1.83$ in the COSMOS field*, A&A, 491, 173.
- Bertoldi, F., Carilli, C., **Aravena, M.**, et al. 2007, *COSBO: The MAMBO 1.2 mm Imaging Survey of the COSMOS Field*, ApJS, 172, 132
- Hitschfeld, M., **Aravena, M.**, Kramer, C., et al. 2008, *^{12}CO 4–3 and [CI] 1–0 in the centers of NGC4945 and Circinus*, A&A, 479, 75
- Kramer, C., Cubick, M., Roellig, M., Sun, K., Yonekura, Y., **Aravena, M.**, et al. 2008, *Clumpy photon-dominated regions in Carina. I. [CI] and mid-J CO lines in two 4'x4' fields*, A&A, 477, 547
- Pineda, J. L., Mizuno, N., Stutzki, J., Cubick, M., **Aravena, M.**, et al. 2008, *Submillimeter Line Emission from LMC N159W: a Dense, Clumpy PDR in a Low Metallicity Environment*, A&A, 482, 197

Erklärung

Ich versichere, daß ich diese Arbeit selbständig verfaßt und keine anderen als die angegebenen Quellen und Hilfsmittel benutzt sowie Zitate kenntlich gemacht habe.